

**BROADBAND MICROWAVE SPECTROSCOPY OF LIGNIN, BIOFUELS
AND THEIR PYROLYSIS INTERMEDIATES**

by

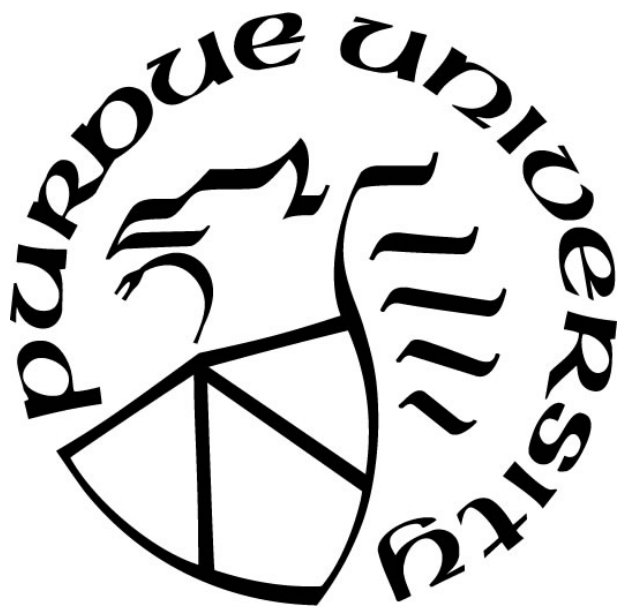
Alicia O. Hernandez-Castillo

A Dissertation

Submitted to the Faculty of Purdue University

In Partial Fulfillment of the Requirements for the degree of

Doctor of Philosophy



Department of Chemistry

West Lafayette, Indiana

December 2018

THE PURDUE UNIVERSITY GRADUATE SCHOOL
STATEMENT OF COMMITTEE APPROVAL

Dr. Timothy S. Zwier, Chair

Department of Chemistry

Dr. Adam Wasserman

Department of Chemistry

Dr. Shelley Claridge

Department of Chemistry

Dr. Libai Huang

Department of Chemistry

Approved by:

Dr. Christine A. Hrycyna

Head of the Graduate Program

*La science, mon garçon, est faite d'erreurs,
mais ce sont des erreurs qu'il est utile de faire,
parce qu'elles conduisent peu à peu à la vérité.*

Jules Verne

ACKNOWLEDGMENTS

This work wouldn't have been possible without the guidance and encouragement of Dr. Zwier. Thank you for your genuine interest in my success as a researcher. I would also like to thank Dr. John Stanton and Dr. Francis Robicieux, you have been wonderful collaborators, and I have learned much from you. And of course, I would like to thank former and current members of the Zwier research group.

Thanks to all the departmental staff. Rob Reason, Betty Dexter, Betty Hatfield, Debbie Packer, Darci DeCamp, Suzy Gustafson, and Trisha Herrera you are undoubtedly the wheels and engine that keep the department running. I would also like to thank James Zimmerman for your help in developing the temperature controller. I must also acknowledge Randy, for his patience with all my designs and for the assistance and new ideas for the microreactor.

Apart from the people associated with Purdue, many other people in my life were instrumental in supporting me during my time here:

I would like to begin thanking Jorge Campos, for first introducing me to the world of quantum mechanics, the impact you have had on my career is invaluable. Without your friendship, advice, and kicks to reality I wouldn't be here. Thanks for never letting me give up and being a source of balance in my life. Next, I must thank Andrea Chapela for all your support, the life lessons, the postcards, and being the best friend one can ask for. Nina Castro, thank you for the endless conversations, the innumerable hours that you spent listening to my presentations, the advice, and for being a source of constant support. I must also express my full-hearted gratitude to my partner in crime, Natalia Chapela, your contribution to this journey has been indispensable, and I hope we get to have more adventures together. I am also very grateful to Emilio, Helena, Leti, Viole, Kelsi, Otto, Mike, Andres, Adrian, Sarah, Joe, Pat, Dan, and Kate. Thank you for the great times and lively conversations. This could not have been done without all of you.

Last, but certainly not least, I would like to thank my family, their support has been immeasurable. To my grandmother Alicia, you taught me to never give up, and your unwavering encouragement and love is a perpetual source of strength. To my aunt Martha, for always pushing me to be a better person. And especially to my mom Silvia, words simply can't express how much I owe you, your support during this journey has been beyond measure. Your passion for life and work ethic have been an inspiration for me, and your enthusiasm for learning is something I will

always try to emulate. Thank you for nurturing my curious nature. Most importantly I would like to thank Captain Hooke, there is no way I would have made it without your unconditional love and the constant reminders that ‘no matter what’ there is always a reason to wag your tail. Thanks for making sure I know that no matter how *ruff* the day is, you will always find a way to make me smile. I love you!

TABLE OF CONTENTS

LIST OF TABLES	9
LIST OF FIGURES	11
ABSTRACT	16
CHAPTER 1. INTRODUCTION	18
1.1 Renewable Fuels	18
1.2 The Role of Reactive Intermediates in Combustion	19
1.3 Organization of Thesis	21
1.4 References	23
CHAPTER 2. EXPERIMENTAL METHODS	24
2.1 Supersonic Jet Expansion	24
2.2 Flash Pyrolysis	25
2.3 Vacuum Chambers	27
2.4 Diagnosis	29
2.4.1 Broadband Chirped-Pulse Fourier Transform Microwave Spectroscopy	29
2.4.2 Photoionization Time-of-flight Mass Spectrometry (PIMS)	33
2.5 Computational Methods	34
2.6 References	36
CHAPTER 3. STRONG FIELD COHERENCE BREAKING (SFCB)	38
3.1 Introduction	38
3.2 Experimental Methods	40
3.3 Method Development	40
3.3.1 Multiple selective-excitation (MSE)	44
3.3.2 Tailored sequential chirps (TSC)	48
3.4 Results and Discussion	48
3.4.1 ¹³ C-benzonitrile	48
3.4.2 (E)- and (Z)-phenylvinyl nitrile	50
3.4.3 Methyl butyrate (MB)	54
3.5 Conclusion	67
3.6 References	68

CHAPTER 4. SINGLE FREQUENCY MICROWAVE PULSES IN THE STRONG FIELD REGIME	72
4.1 Introduction	72
4.2 Experimental Methods.....	74
4.3 Results and Discussion.....	74
4.3.1 Collisions.....	79
4.3.2 Rabi Cycles	82
4.3.3 Theoretical Models.....	88
4.4 Conclusions	91
4.5 References	92
CHAPTER 5. SPECTROSCOPIC CHARACTERIZATION OF MODEL AROMATIC SUBSTITUENTS OF LIGNIN BY BROADBAND CHIRPED-PULSE MICROWAVE SPECTROSCOPY	94
5.1 Introduction	94
5.2 Experimental Methods.....	95
5.3 Results	95
5.3.1 Guaiacol	95
5.3.2 2,6-dimethoxyphenol (Syringol).....	99
5.3.3 4-methyl guaiacol (4-MG)	102
5.3.4 4-vinyl guaiacol (4-VG).....	105
5.4 Discussion.....	109
5.5 Conclusions	111
5.6 References	113
CHAPTER 6. BROADBAND MICROWAVE SPECTROSCOPY OF 2-FURANYLOXY RADICAL.....	115
6.1 Introduction	115
6.2 Experimental Methods.....	116
6.3 Results	117
6.4 Discussion.....	122
6.5 Conclusion.....	126
6.6 References	127

CHAPTER 7. CHARACTERIZATION OF RESONANCE-STABILIZED RADICALS USING A MASS-CORRELATED BROADBAND MICROWAVE SPECTROMETER	128
7.1 Introduction	128
7.2 Structural Characterization of Phenoxy Radical	128
7.2.1 Experimental Methods	130
7.2.2 Results	131
7.2.3 Molecular Structure.....	138
7.3 Molecular Parameters of <i>o</i> -Hydroxy Phenoxy Radical.....	141
7.3.1 Experimental Methods	142
7.3.2 Results	142
7.4 Discussion and Conclusions	147
7.5 References	149
APPENDIX.....	151
VITA.....	165
PUBLICATION.....	166

LIST OF TABLES

Table 3.1: Experimental best-fit and theoretical calculated spectroscopic parameters for E/Z-PVN.	53
Table 3.2: The rotational constants A, B, C (in GHz), dipole moment components μ_a , μ_b , μ_c (in Debye), and relative energies E_{rel} (in $\text{kJ}\cdot\text{mol}^{-1}$) of the indicated conformers of MB calculated at the MP2/6-311++G(d,p) and B2PLYP-D3BJ/aug-cc-PVTZ levels of theory. The dipole moment components are with respect to the principal axes of inertia. All energies are electronic energies including vibrational zero-point correction and are relative to the lowest energetic conformer ($g_{\pm,a}$) with its absolute energy of $E + ZPE = -345.988667$ and -346.734269 Hartrees at the MP2 and B2PLYP-D3BJ levels of theory, respectively.	59
Table 3.3: Molecular parameters of conformers ($g_{\pm,a}$) and (a,a) of methyl butyrate obtained from the best fits to the frequencies.....	63
Table 3.4: Comparison between theoretical and experimental Boltzmann distributions. The theoretical values were calculated at the DFT B2PLYP-D3BJ/aug-cc-pVTZ level of theory.	66
Table 4.1: List of transitions modulated by a single frequency pulse, they match the numbers in Figure 4.7. The number in orange indicate that those transitions were modulated with a 500 ns SFP. The transitions indicated in green correspond to those modulated by a 1000 ns pulse. The blue numbers are associated with those transitions that were modulated by a 1500 SFP.	85
Table 5.1: List of spectroscopic parameters used to fit guaiacol and its isotopomers. The atoms follow the numbering label showed in red in Figure 5.1.	97
Table 5.2: Comparison of experimental and calculated geometrical parameters for guaiacol. The standard deviation of the fit was 0.0047 \AA . The atoms follow the numbering label showed in red in Figure 5.1.	98
Table 5.3: Experimental rotational parameters for syringol.	101
Table 5.4: Comparison of internal rotation barriers for the hydroxyl group in phenol derivatives.	102
Table 5.5: Molecular parameters of 4-methyl guaiacol. All parameters refer to the principal axis system. Watson's A reduction and I' representation were used. The rotational constant of methyl rotor, F_0 , was fixed at 158 GHz.	105
Table 5.6: Molecular parameters for <i>syn</i> - and <i>anti</i> -4-vinyl guaiacol.....	107
Table 6.1: Experimental best-fit and theoretical calculated spectroscopic parameters for 2-furanyloxy radical.	122

Table 6.2: Principal bond lengths and angles of the precursor (2-methoxy furan) and the 2-furanyloxy radical. Structures determined at ANO0/CCSD(T) level of theory.	123
Table 6.3: Spectroscopic constants (A-Reduction, I ^r representation) for 2-methoxy furan. The experimental constants were taken from the previous work of J.A. Beukes ¹³	124
Table 7.1: Experimental best-fit and calculated spectroscopic parameters for phenoxy radical.	134
Table 7.2: Experimental best fit of the spectroscopic parameters for isotopomers of phenoxy radical.....	136
Table 7.3: Experimental best fit of the spectroscopic parameters for phenoxy-2,3,4,5,6-d5 radical and the ¹³ C isotopomers of phenoxy-2,3,4,5,6-d5 radical present in 2% natural abundance. ...	137
Table 7.4: Principal bond lengths and angles of phenoxy radical.	139
Table 7.5: Experimental best fit of the spectroscopic parameters for <i>o</i> -hydroxy phenoxy radical.	144

LIST OF FIGURES

- Figure 2.1: Flash pyrolysis micro-reactor assembly used to thermally decompose samples entrained in buffer gas. 26
- Figure 2.2: Schematic circuit to resistively heat the SiC micro-reactor. 27
- Figure 2.3: Schematic diagram of the chamber that can be used for both microwave spectroscopy and photoionization TOF mass detection. 28
- Figure 2.4: Schematic diagram of the CP-FTMW electronics for broadband acquisition over the 2-18 GHz frequency region. Components unique to the 2-8 GHz region are shown in blue, while those used only in the 8-18 GHz frequency range are indicated in red. 31
- Figure 3.1: Schematic diagram for SFCB scheme..... 42
- Figure 3.2: Intensity of the 40,4-30,3 transition of benzonitrile resulting from a 1 μ s broadband chirp (8-18 GHz) followed by a SFP resonant with the 40,4-30,3 transition at 10855.233 MHz. (a) Taken with the TWTA power set at 1%. (b) Taken with the TWTA set at 100%. 43
- Figure 3.3: ((a) and (b)): Broadband CP-FTMW spectra of benzonitrile over the 8-18 GHz region, comparing the spectra following 900 ns chirps with the frequency swept up from 8 to 18 GHz (black) and down from 18 to 8 GHz (red), with TWTA gain at (a) 1% and (b) 100% of full power. ((c) and (d)): Difference spectra from an 8-18 GHz chirp (800 ns duration) with and without a resonant pulse (100 ns) following the broadband sweep, centered in frequency at the $J_{KaKc}=4_{0,4}-3_{0,3}$ transition (10855.233 MHz). The TWTA gain in (c) is 1% and (d) 100% of full power. Only the directly connected transitions appear in (c), while additional transitions appear under SFCB conditions in (d). The transitions shown here are above median noise level. 45
- Figure 3.4: Line picking scheme to establish the multiple pulses sequence originally employed in the SFCB/MSE method. 46
- Figure 3.5: (a) The 8-18 GHz pure rotational spectrum of benzonitrile recorded with a 900 ns chirped pulse at 100% TWTA gain level. The inset is an expanded view (13.35-13.45 GHz) illustrating the relative line intensities of the ^{13}C and parent transitions. The arrow indicates the transition due to [$2\text{-}^{13}\text{C}$] benzonitrile used for excitation via the resonant pulse. The green spectrum is scaled 7 \times with labels identifying the isotopologues present in the expanded region, (1) [$1\text{-}^{13}\text{C}$] benzonitrile and (2) [$2\text{-}^{13}\text{C}$] benzonitrile. (b) Experimental lines modulated by more than 40% in the SFCB difference spectrum using the MSE sequence (green) with SFP frequencies marked with an asterisk, compared to the simulated stick spectra (black). The rotational constants used for the prediction in black were taken from Casado et al³³. 49
- Figure 3.6: Broadband CP-FTMW spectra over the 8-18 GHz region of (E)- and (Z)-PVN, comparing the spectra with the frequency swept up from 8 to 18 GHz (black) and down from 18-8 GHz (red), with TWTA gain at (a) 10% and (b) 100% of full power. Experimental conditions: 1 μ s long chirped pulse, 250 000 averages, 16 μ s molecular FID collection. 51

Figure 3.7: Experimental lines modulated more than 10% in the SFCB difference spectrum compared to the simulated stick spectra for (a) (Z)-PVN and (b) (E)-PVN. Experimental conditions: 1 μ s 8-18 GHz chirp, 50 ns gap, and 3×100 ns SFPs on the frequencies labeled by asterisks and 100% TWTA gain level. 52

Figure 3.8: (a) The experimental 8-18 GHz broadband microwave spectrum of a mixture of (E)- and (Z)-PVN (black), and the final fit for both structural isomers overlaid on top of one another. (b) Expanded view of 9.5-10.5 GHz with the assignments overlaid. 54

Figure 3.9: Optimized geometries of the assigned conformers of MB calculated at B2PLYP-D3BJ/aug-cc-pVTZ level of theory. Upper trace: front view, lower trace: view along the C₄-O₅ bond. A tilt angle of the ethyl group ($\Theta=180^\circ-|\varphi_2|=15^\circ$), relative to the C₄, O₅, O₆, C₇ plane, was calculated for the more stable conformer (g^\pm , a) (lower left). 55

Figure 3.10: Potential energy of MB for conformational analysis. Here four stable conformers were found: 1=(g^+ ,a), 2=(g^+ , g^+), 3=(a, g^-), 4=(a,a), 5=(a, g^+), 6=(g^- , g^-), 7=(g^- ,a). Conformer 1 and 7; 2 and 6; and 3 and 5 are enantiomers. This surface was obtained by rotating the dihedral angles $\varphi_1=\angle(C_1,C_2,C_3,C_4)$ (rotation about C₂-C₃ bond) and $\varphi_2=\angle(C_2,C_3,C_4,O_6)$ (rotation about the C₃-C₄ bond). Calculations were performed at the B2PLYP-D3BJ/aug-cc-pVTZ level of theory. The absolute energy of the lowest conformation is $E=346.95152$ Hartree. Dash lines indicate the minimum energy pathway shown in Figure 3.14. 56

Figure 3.11: The trans conformers of methyl butyrate in order of their energies relative to that of the most stable conformer (g^\pm ,a) calculated at the MP2/6-311++G(d,p) level with and without zero point energy correction as well as at the B2PLYP-D3BJ/aug-cc-pVTZ level (for values see Table 3.2). 57

Figure 3.12: 8-18 GHz CP-FTMW rotational spectrum of MB. (a) 10% TWTA gain level and 1.5×10^6 acquisitions. (b) 100% TWTA gain and 75000 acquisitions using TSC with different sweep rates covering 8-18 GHz sweeping up (black) or down (red) in frequency; where $\alpha_1=14.3$ GHz/ μ s for the 8.0-13.0 GHz region, $\alpha_2=2.0$ GHz/ μ s for the 13.0-15.0 GHz region, and $\alpha_3=20.0$ GHz/ μ s for the 15.0-18.0 GHz region. 58

Figure 3.13: Experimental lines modulated more than 20% in the SFCB(TSC)/MSE difference spectrum compared with the simulated stick spectra for the two most abundant conformers of MB. 61

Figure 3.14: (a) A cut along φ_1 through the (a,a) and (g^\pm ,a) minima. (b) A cut along φ_2 through the (g^\pm , g^\pm) and (g^\pm ,a) minima. (c) A cut along φ_2 through the (a, g^\pm) and (a,a) minima. The barrier heights are indicated in blue and in red the relative energies. The numbers in black indicate which minima it is referring according to Figure 3.10. 64

Figure 3.15: (a) The rotational temperature for (g^\pm ,a) is estimated to be about 0.84 (± 0.19) K. (b) The rotational temperature for (a,a) is estimated to be about 0.35 (± 0.08) K. 65

Figure 4.1: PVN single frequency pulses. The modulated transitions by a single frequency pulse probing the $2_{2,1}-1_{1,0}$ Z-PVN transition are shown in blue. The modulated transitions by a single

frequency pulse probing the $11_{1,11}-10_{1,10}$ E-PVN transition are shown in red. In black a PVN spectrum taken in the linear fast passage (10% TWTA gain) is shown. 75

Figure 4.2: Comparison of spectra following single-frequency pulses as a function of detuning from resonance. The blank is shown in red. 78

Figure 4.3: Comparison of single frequency pulse spectra taken at different backing pressures with He as carrier gas. 79

Figure 4.4: Intensity of the the $2_{1,1}-1_{1,0}$ Z-PVN transition vs time after the pulse triggers. The red dotted line indicates the intensity of the probed transition when the single frequency spectrum was taken at Δt_{optim} . The green dotted line is the intensity of the probed transition at $\Delta t_{\text{optim}}+400\mu\text{s}$. The blue dotted line is the intensity of the probed transition at $\Delta t_{\text{optim}}+800\mu\text{s}$ 80

Figure 4.5: Broadband spectrum and single frequency pulse spectrum taken at two different sample holder temperatures. The blue spectra were taken at 39 °C (VP=0.057 torr and C= $\sim 5 \times 10^{-3}\%$) and the green spectra were taken at 115 °C (VP=2.52 torr and C=0.2%). 81

Figure 4.6: Single frequency pulse probing the $9_{0,9}-8_{0,8}$ Z-PVN transition. a) Spectrum taken at 10% TWTA gain (20 W, 3500 V/m). b) Spectrum taken at 100% TWTA gain (200 W, 11000 V/m). 83

Figure 4.7: Comparison of single frequency pulse spectra taken at different SFP durations. The numbers match the transitions in Table 4.1. 84

Figure 4.8: Energy diagrams for the off-resonant modulated transitions. a) Z-PVN energy diagram for the SFP at $8_{0,8}-9_{0,9}$. b) E-PVN energy diagram for the SFP at $7_{0,7}-8_{0,8}$ 87

Figure 5.1: Broadband spectrum of guaiacol over the 2-18 GHz range. The 2-8 GHz frequency region was recorded heating the sample holder to 110 °C with the sample entrained in 1.03 bar of He, and 30 FIDs recorded per gas pulse. For the 8-18 GHz frequency region the sample was heated to 105°C. The rotational temperature was determined to be 1.56 ± 0.12 K. The blank subtracted experimental spectrum is shown in black and the simulated spectrum is illustrated in red. The inset show transitions due to the isotopic species in natural abundance. 96

Figure 5.2: a) Broadband spectrum of syringol from 2-18 GHz. The 2-8 GHz frequency region was recorded heating the sample holder to 148 °C with the sample entrained in 2.75 bar of He, collecting 30 FIDs per gas pulse. For the 8-18 GHz frequency region the sample was heated to 130 °C. The rotational temperature of syringol following supersonic expansion was determined to be 1.7 ± 0.3 K. b) Close-up view of the $8_{3,6}-7_{3,5}$, $8_{4,5}-7_{4,4}$, and $8_{4,4}-7_{4,3}$ transitions showing their tunneling splitting due to the internal rotation of the hydroxyl group. See text for further discussion. 100

Figure 5.3: A window of about 20 MHz taken from the 8-18 GHz spectrum of 4-MG, highlighting the $7_{0,7}-6_{1,6}$ and $7_{1,7}-6_{0,6}$ transitions, which are split by 1.3 and 2.1 MHz, respectively, due to methyl internal rotation. The spectrum was recorded by heating the sample holder to 123 °C with the sample entrained in 0.7 bar of He, accumulating 20 FIDs per gas pulse. The rotational temperature was determined to be 1.79 ± 0.3 K. 103

Figure 5.4: Experimental lines modulated in the SFCB difference spectrum compared to the simulated stick spectra for a) *syn*-4-VG and b) *anti*-4-VG. Experimental conditions: 1 μ s 8-18 GHz chirp, 50 ns gap and 3×100 ns single frequency pulses on frequencies labeled with asterisks, 100% TWTA gain level. The spectrum was recorded with the sample heated to 193 °C and entrained in 0.7 bar He. The timing of the experiment was set to record 30 FIDs per gas pulse. 108

Figure 5.5: Summary of the calculated molecular geometries for: a) guaiacol, b) syringol, c) 4-MG, d) *anti*-4-VG, and e) *syn*-4-VG, all computed at the B2PLYP-D3BJ/aug-cc-pVTZ level of theory. 110

Figure 6.1: Intensities of the $1_{1,1}-0_{0,0}$ and $2_{0,2}-1_{0,1}$ rotational transitions of the 2-furanyloxy radical as a function of the micro-reactor wall temperature. 119

Figure 6.2: a) Broadband rotational spectrum of the 2-8 GHz (in blue) and 8-18 GHz (in black) regions of the pyrolysis of 2-methoxy furan, recorded at microtubular reactor temperatures of 850 K and 900 K, respectively. The simulated spectrum of the 2-furanyloxy radical at a rotational temperature of 2 K is shown as inverted sticks (red) below the rotational spectrum. b) Broadband spectrum with the precursor and other pyrolysis products removed in order to highlight the transitions of the radical and remaining transitions not assigned. c) Splitting of the $2_{0,2}-1_{0,1}$ transition due to spin-rotation coupling. A splitting of 3.4 MHz is observed between the $5/2-3/2$ and $3/2-1/2$ transitions. d) Spin-rotation splitting of the $7_{2,5}-7_{2,6}$ transition, with a splitting between $15/2-15/2$ and $13/2-13/2$ transitions of 9.8 MHz. 121

Figure 6.3: Heavy atom atomic spin densities calculated for 2-furanyloxy radical at the ANO1/CCSD(T) level of theory. Spin densities are indicated in red. 125

Figure 7.1: a) Optimized structure of phenoxy radical. The color and numbering scheme are consistent with those in Tables 7.1, 7.2, 7.3, and 7.4. b) Resonance structures of phenoxy radical. 130

Figure 7.2: Unimolecular products from the pyrolysis of anisole using a pulsed flow heated SiC reactor, temperatures indicated are the measured reactor wall-temperature. a) Mass spectra recorded at different temperatures. b) $3_{0,3}-2_{0,2}$ rotational transition of phenoxy radical. 132

Figure 7.3: a) Spin-rotation splitting of the $3_{0,3}-2_{0,2}$ transition due to spin-rotation coupling. b) Spin-rotation splitting of the $6_{2,4}-6_{2,5}$ transition. 133

Figure 7.4: Spin-rotation splitting of the $4_{0,4}-3_{0,3}$ transition of fully deuterated phenoxy radical due to spin-rotation coupling: a) all ^{12}C phenoxy-2,3,4,5,6- d_5 radical. b) phenoxy-2,3,4,5,6- d_5 radical with ^{13}C in the C(2) or C(6) positions, and c) phenoxy-2,3,4,5,6- d_5 radical with ^{13}C in the C(3) or C(5) positions. 138

Figure 7.5: Molecular geometry of: a) phenoxy radical, b) benzene, and c) phenol²⁴. 139

Figure 7.6: Heavy atom atomic spin densities calculated for phenoxy radical at the ANO0/CCSD(T) level of theory. 140

Figure 7.7: Mass spectra resulting from heating a mixture of *o*-guaiacol imbedded in Ar in a SiC micro-reactor. Temperatures indicated are the measured reactor wall-temperature..... 143

Figure 7.8: a) Section of the broadband rotational in the 8-18 GHz frequency region, recorded at microtubular reactor temperature of 820 K. The sample holder was heated to 95 °C with the sample entrained in 1.30 bar of He, and 30 FIDs recorded per gas pulse. The simulated spectrum of *o*-hydroxy phenoxy radical at a rotational temperature of 2 K is shown as inverted sticks (blue) below the rotational spectrum. b) Optimized structure of *o*-hydroxy phenoxy radical. Spin densities calculated at the ANO0/CCSD(T) level of theory are indicated in red. 145

Figure 7.9: CP-FTMW spectra in small frequency regions around microwave transitions due to a) vinylacetylene and b) cyclopentadienone. 146

ABSTRACT

Author: Hernandez-Castillo, Alicia, O. PhD

Institution: Purdue University

Degree Received: December 2018

Title: Broadband Microwave Spectroscopy of Lignin, Biofuels, and Their Pyrolysis Intermediates.

Committee Chair: Timothy S. Zwier

The chemical complexity of hydrocarbon fuels and the fast-expanding list of potential plant-derived biofuels pose a challenge to the scientific community seeking to provide a molecular understanding of their combustion. More refined spectroscopic tools and methodologies must be developed to selectively detect and characterize the widening array of fuel components and combustion reactive intermediates. The direct relationship between molecular structure and rotational frequencies makes rotational spectroscopy highly structural specific; therefore, it offers a powerful means of characterizing pyrolysis intermediates. This thesis describes experimental work using broadband microwave spectroscopy to address a number of challenging problems in the spectroscopy of gas complex mixtures.

Usually, the observed rotational spectra contain contributions from many distinct species, creating a complicated spectrum with interleaved transitions that make spectral assignment challenging. To assist with the process, a protocol called “strong-field coherence breaking” (SFCB) has been developed. It exploits multi-resonance effects that accompany sweeping the microwave radiation under strong-field conditions to output a set of transitions that can confidently be assigned to a single component in a mixture, thereby reducing the spectral assignment time.

The broadband chirped pulse Fourier transform microwave (CP-FTMW) spectra of guaiacol, syringol, 4-methyl guaiacol, 4-vinyl guaiacol were recorded under jet-cooled conditions over the 2-18 GHz frequency range. Using data from the ^{13}C isotopomers the r_0 structure of guaiacol was determined by means of a Kraitchman analysis. The tunneling due to OH hindered rotation was observed in syringol and the V_2 barrier was deduced to be 50% greater than phenol’s barrier. This is due to the intramolecular H-bonding between the hydroxy and the methoxy groups. The internal rotation barrier for the methyl group for 4-methyl guaiacol was also determined. Moreover, the spectral assignment of the two conformers of 4-vinyl guaiacol was sped-up by using SFCB. The

main structural insight from these lignin-related molecules was that polar substituents dictate the magnitude and type of structural shift that occurs relative to that of the unsubstituted aromatic ring.

In the next part of my work, the pyrolysis of 2-methoxy furan was carried out over the 300-1600 K temperature range, with microwave detection in the 2-18 GHz frequency range, using high-temperature flash pyrolysis micro-reactor coupled with a supersonic expansion. The SFCB technique was used to analyze and speed up the line assignment. The 2-furanyloxy radical, a primary, resonance-stabilized radical formed by loss of a methyl group in the pyrolysis of 2-methoxy furan, was detected and its molecular parameters were determined.

Finally, a unique setup that combines the high-resolution spectroscopic data provided by chirped pulse Fourier transform microwave (CP-FTMW) spectroscopy with photoionization mass spectra from a vacuum ultraviolet (VUV) time-of-flight mass spectrometer (TOF-MS) was used to find optimal conditions to detect reactive intermediates and make full assignments for the microwave spectra of phenoxy radical and *o*-hydroxy phenoxy radical over the 2-18 GHz range. Phenoxy radical was generated through the pyrolysis of anisole and allyl phenyl ether. Using a combination of data from ^{13}C isotopomers and fully deuterated phenoxy radical, in combination with high level ab initio calculations, a near-complete r_0 structure for the radical was obtained. The structural data point to the radical being a primarily carbon-centered rather than oxygen-centered radical. Using guaiacol as precursor, we studied the spectroscopy of the *o*-hydroxy phenoxy radical, whose structural data is compared with that of phenoxy to understand the role played by the hydroxyl group in modifying the resonance stabilization of the radical.

CHAPTER 1. INTRODUCTION

1.1 Renewable Fuels

Combustion of fossil fuels - coal, oil, and natural gas – account for about 85% of the energy consumed worldwide.¹ The rapid worldwide increase in the consumption of fossil fuels to meet energy demand suggests that the depletion of petroleum and natural gas reserves is unavoidable. Therefore, the limited fossil resources and climate impacts due to carbon dioxide emissions have made it critical that we find ways to produce and use renewable, carbon-neutral fuels. The first generation of biofuels converted sugars and starch to ethanol; nonetheless, compared with petroleum-based fuels, ethanol is much less dense in energy.² Also, due to its polar molecular structure ethanol is hydroscopic and forms an azeotrope with water. Butanol has also been considered as a candidate for biofuel since it has a longer chain and it has a higher energy density. Ultimately, fuels derived from sugar and starch are disruptive to the food chain; thus, they are not sustainable in the long run.

Biomass is a term used for plant-based materials that are not used for food, and it is one of the few renewable natural resources that can be utilized to reduce both the number of fossil fuels burned and several greenhouse gases formed during fossil fuel combustion processes. Biomass-based fuels form a closed, carbon-neutral cycle, where the excess CO₂ from combustion can be recycled through the growth of renewable biomass. Among the benefits of using biomass instead of fossil fuels are its better greenhouse gas balance, an enhanced energy supply security (if biomass is produced and burned in the same region), and its status as a renewable source for carbon-based fuels.³ However, separation of most biomass waste is a complicated process that involves organic solvents. In order for bio-based chemical production to be self-sustainable, these solvents must also be bio-based and can't be derived from crude oil.⁴

Various types of biomass feedstocks are available for the production of biofuels. Sugars and vegetable oils are considered as “first generation” biofuels, whereas lignocellulosic biomass and residues from agriculture and forestry are considered “second generation” biofuels.⁵ With the goal of producing fuels derived from the inedible portion of plants, there have been several improvements in the past few years in thermochemical and biochemical processes to convert lignocellulosic biomass to fuels. For thermochemical processing of the whole feedstock, the raw

material is mechanically processed, and it is introduced into a reactor where it undergoes gasification (some oxygen) or pyrolysis (no oxygen) to make intermediates which can be turned into desirable end-products. Thermochemical technologies can convert biomass to fuels in a matter of seconds, which gives them an advantage over enzyme-catalyzed processes; however, they require large capital and transportation costs to handle the quantity of feedstock needed for operation.⁶

Numerous factors need to be considered when creating a renewable and cost-competitive bio-based fuel. Any potential biofuel should ideally possess similar properties to gasoline or diesel, since that will allow them to be efficiently distributed and stored using existing infrastructure, and possibly burned in existing engines. It is also important to consider any potential environmental consequences associated with producing or distributing the fuels. Many different molecules can potentially be used as fuels that can be synthesized from lignocellulosic biomass, ranging from; alkylated furans and furanic ethers to alkyl ethers and lactones. However, it is likely that the ideal fuel will be a blend of different molecules, and in any case, if these molecules are to be part of the future fuels, it is important to understand both their pyrolysis and combustion in considerable detail. As with petroleum-based fuels, identifying pathways that produce harmful emissions is particularly important, and this necessitates a fundamental understanding of the elementary reaction steps involved, including identifying important reactive intermediates involved.

1.2 The Role of Reactive Intermediates in Combustion

Clean-burning, renewable, oxygenated fuels such as alcohols, ethers, and alkyl ethers are considered to be possible replacements for conventional gasoline and diesel fuels. The chemical complexity of the fast-expanding list of potential plant-derived biofuels poses a challenge to the scientific community that seeks to provide a molecular-scale understanding of their combustion. Experimental data on the reaction pathways, kinetics, and product branching ratios of individual reaction steps can help the development of accurate combustion models. In order to predict the combustion behavior of more complex fuels, more refined spectroscopic tools and methodologies are needed to selectively detect and characterize the widening array of fuel components and combustion reactive intermediates. Moreover, the full array of combustion fuels currently includes oxygenated fuels, which increases the challenge associated with modeling the reaction pathways associated with combustion.

Resonantly-stabilized radicals (RSRs) play a particularly important role in many contexts of combustion since, due to their unusual stability, pathways that form them are thermodynamically preferred. Since RSRs can build up in concentration and participate in various radical recombination reactions, they are believed to play an important role in the growth of polycyclic aromatic hydrocarbon (PAH) and ultimately soot.^{7, 8} One of the main differences between petroleum and renewable raw materials is that the latter has a higher oxygen content; therefore, characterization of the stabilities and structures of oxygenated RSRs could have important implications for the combustion of biofuels.

Practical combustion devices are turbulent in nature, and comprehensive chemical kinetics modeling is challenging in this type of environments; therefore, practical combustion devices are not well suited for direct investigation of complex chemical reaction mechanisms. Kinetic models of combustion chemistry are best explored in well-characterized combustion environments such as laminar flames, shock tubes, jet-stirred reactors, flow reactors, and non-premixed counter-flow diffusion flames.⁹ Flame-sampling molecular-beam mass spectrometry enables the quantitative detection of both radical and stable reaction intermediates without prior knowledge of their identities; thus, it has had an enormous impact on our understanding of fundamental chemical combustion processes.

Since the reaction pathways can differ between isomeric forms the inclusion of isomer-specific data in the combustion models is another important factor in developing combustion models. Flame-sampling vacuum ultraviolet (VUV) photoionization mass spectrometry (PIMS) has been used for quantitative measurements of the concentrations of isomer pairs of importance in hydrocarbon combustion.¹⁰ Double-resonance laser-based methods for isomer-specific spectroscopy and dynamics have been previously used to study molecules that contain aromatic moieties as well as resonance-stabilized radicals. However, some important intermediates in combustion are not easily accessible by these laser-based methods.

The direct relationship between molecular structure and rotational frequencies makes rotational spectroscopy, also known as microwave spectroscopy, highly structure-specific; therefore, it offers a powerful means of characterizing reactive intermediates. Indeed, microwave spectroscopy offers extraordinary resolution, with more than one million resolution elements typical (kHz out of GHz). The revolutionary technique of chirped-pulse Fourier transform microwave spectroscopy (CP-FTMW), first demonstrated by Pate and coworkers in 2008, uses

broadband excitation and detection to record microwave spectra over large spectral ranges in a relatively short amount of time. Yet, despite these considerable advantages, the technique does have certain limitations. For instance, the molecular sample must possess a permanent dipole moment, since molecules without a permanent dipole moment would not be susceptible to the initial polarizing field. Furthermore, if the gas mixture contains contributions from many distinct species, the resulting microwave spectrum is complicated by interleaved transitions from each molecular component, making spectral assignment challenging.

In this thesis, CP-FTMW spectroscopy will be on display as a general and powerful detection method for neutral molecules and reactive intermediates relevant to combustion chemistry. To assist with the analysis, a protocol called ‘strong-field coherence breaking’ (SFCB) has been developed. This method exploits multi-resonance effects that accompany sweeping the microwave radiation under strong-field conditions to output a set of transitions that can confidently be assigned to a single component in a mixture, thereby reducing the spectral assignment time. Furthermore, a heated microreactor for flash pyrolysis has been used as a source for key pyrolysis intermediates at well-defined reactor wall temperatures.

1.3 Organization of Thesis

The overall goal of this thesis is to obtain the rotational molecular parameters of a series of stable molecules and reactive intermediates of relevance to biomass-derived fuel combustion processes. Chapter 2 describes the experimental methods, vacuum chambers, and spectroscopy techniques used to obtain the spectra presented in the following chapters.

As previously mentioned the modern developments in broadband microwave techniques have immensely reduced the data acquisition time, while creating a need for high-speed data analysis procedures. Chapter 3 describes a new microwave-microwave double resonance method to perform single conformer/isomer microwave spectroscopy in complex chemical mixtures, thereby reducing the time required for spectral assignment. This strong-field coherence breaking (SFCB) method combines selective excitation schemes possible in chirped pulse microwave spectroscopy with multi-resonance effects observed upon sweeping the polarizing microwave field at high powers that enter the rapid adiabatic passage regime. While developing this method, new phenomena were observed even for simpler experiments employing monochromatic microwave

pulses capable of driving resonant transitions through many Rabi cycles. Chapter 4 focuses on the theoretical and experimental discoveries associated with these high-field, resonant excitations.

The ultraviolet and infrared spectroscopy of guaiacol, syringol, 4-methyl guaiacol, and 4-vinyl guaiacol have been previously studied by laser-based double resonance techniques. Nonetheless, no high-resolution data on these molecules existed. Chapter 5 focuses on the study of aromatic portions of lignin monomers, this series of molecules were studied using CP-FTMW spectroscopy under jet-cooled conditions over the 2-18 GHz frequency range.

In order to record the broadband microwave spectra of the RSR 2-furanyloxy over the 2-18 GHz range a flash pyrolysis source attached to a pulsed valve was used. Chapter 6 discusses the pyrolysis of 2-methoxyfuran, a second-generation biofuel, at a series of temperature ranging from 300-1600 K. The molecular parameters of the 2-furanyloxy radical were determined using CP-FTMW spectroscopy combined with strong field coherence breaking, the first such application of the method to free radicals.

Phenoxy radical is an important intermediate in the oxidation of many aromatic compounds. Surprisingly, prior to our work, there are no previous high-resolution data on the radical, and therefore no accurate experimental characterization of its structure. Chapter 7 provides such a detailed characterization, leading to a full determination of its structure to high accuracy based on a series of studies of isotopically labeled forms of the radical. To generate this RSR, the pyrolysis of anisole and allyl phenyl ether were carried out, and a combination of CP-FTMW spectroscopy and VUV time-of-flight mass spectrometry (TOF-MS) was used to determine its molecular parameters. Furthermore, as a direct follow-up to this work, using this same set-up the pyrolysis of *o*-guaiacol was carried out, leading to the spectroscopic characterization of the *o*-hydroxy phenoxy radical, formed by loss of methyl radical from the guaiacol precursor.

Finally, a description of the Matlab programs used through the different experimental and analysis stages of this work is described in the Appendix.

1.4 References

1. Hansen, N.; Cool, T. A.; Westmoreland, P. R.; Kohse-Höinghaus, K., Recent contributions of flame-sampling molecular-beam mass spectrometry to a fundamental understanding of combustion chemistry. *Progress in Energy and Combustion Science* **2009**, *35*, 168-191.
2. Savage, N., The ideal biofuel. *Nature* **2011**, *474*, S9-S11.
3. Haro, P.; Ollero, P.; Villanueva Perales, Á. L.; Vidal-Barrero, F., Potential routes for thermochemical biorefineries. *Biofuel. Bioprod. Bior.* **2013**, *7*, 551-572.
4. Tuck, C. O.; Perez, E.; Horvath, I. T.; Sheldon, R. A.; Poliakoff, M., Valorization of biomass: Deteriving more value from waste. *Science* **2012**, *337*, 695-699.
5. Graça, I.; Lopes, J. M.; Cerqueira, H. S.; Ribeiro, M. F., Bio-oils Upgrading for Second Generation Biofuels. *Ind. Eng. Chem. Res.* **2013**, *52*, 275-287.
6. Mettler, M. S.; Vlachos, D. G.; Dauenhauer, P. J., Top ten fundamental challenges of biomass pyrolysis for biofuels. *Energy & Environmental Science* **2012**, *5*.
7. Liu, R.; Morokuma, K.; Mebel, A. M.; Lin, M. C., Ab Initio Study of the Mechanism for the Thermal Decomposition of the Phenoxy Radical. *J. Phys. Chem.* **1996**, *100*, 9314-9322.
8. Goulay, F.; Osborn, D. L.; Taatjes, C. A.; Zou, P.; Meloni, G.; Leone, S. R., Direct detection of polyynes formation from the reaction of ethynyl radical (C₂H) with propyne (CH₃-C[triple bond]CH) and allene (CH₂=C=CH₂). *Phys Chem Chem Phys* **2007**, *9*, 4291-300.
9. Simmie, J. M., Detailed chemical kinetic models for the combustion of hydrocarbon fuels. *Progress in Energy and Combustion Science* **2003**, *29*, 599-634.
10. Cool, T. A.; Nakajima, K.; Mostefaoui, T. A.; Qi, F.; McIlroy, A.; Westmoreland, P. R.; Law, M. E.; Poisson, L.; Peterka, D. S.; Ahmed, M., Selective detection of isomers with photoionization mass spectrometry for studies of hydrocarbon flame chemistry. *The Journal of Chemical Physics* **2003**, *119*, 8356-8365.

CHAPTER 2. EXPERIMENTAL METHODS

This chapter outlines the experimental apparatus and techniques employed to identify and characterize various chemical species including reactive intermediates. The experimental methods are coupled with a supersonic expansion which is first described, followed by the details of the flash pyrolysis microreactor used during this work to produce and characterize transient species. In Section 2.3 a brief description of the vacuum chambers is given; and Section 2.4 contains the details of the two different diagnostic techniques used to probe the molecules: chirped pulse Fourier transform microwave (CP-FTMW) spectroscopy and photoionization time-of-flight (TOF) mass spectrometry. At the end of the chapter the computational methods used to complement the experimental results are discussed. In the chapters that follow, experimental protocols used in unique circumstances will be described.

2.1 Supersonic Jet Expansion

All experiments were carried out utilizing a supersonic jet expansion. This is a powerful technique for cooling gas phase molecules to low temperatures where they can be interrogated by a range of detection schemes. A supersonic expansion is created by pulsing a high-pressure buffer gas (typically several bar He, Ne, or Ar) through a small orifice (500-1000 μm diameter) into vacuum. During the expansion, the random, thermal motion of the atoms is turned into directed motion along the expansion axis. The width of the velocity distribution shrinks dramatically during this process, so that in that moving frame of reference, the buffer gas atoms has translational temperatures well below 1 K. When a molecular sample is entrained in this buffer gas expansion, its internal energy is removed by collisions with the cold buffer gas, cooling the molecule into its zero-point vibrational level.¹⁻³ Collisions between the buffer gas and the molecular sample help transfer the internal energy of the thermalized molecule into translational energy of the collisional partner, funneling down the Boltzmann population of the sample.³ As a result, this simplifies the spectra and provides a medium for detailed spectroscopic interrogation in the gas phase.² Jet-cooled molecules typically have internal temperatures of 10-20 K, 1-5 K and $< 1\text{K}$ for the vibrational, rotational and translational degrees of freedom, respectively.

The collision frequency is at its maximum nearest the exit of the nozzle,² as the gas expands the collision rate drops nearly quadratically with distance from the nozzle orifice, generating a collisionless environment downstream where the molecular sample and the buffer gas atoms travel unidirectionally and at the same velocity. It is in this region that the spectroscopic interaction with the isolated molecules occur. For the time-of-flight mass spectrometer the free jet expansion is skimmed, forming a molecular beam of the coldest part of the expansion.

2.2 Flash Pyrolysis

Flash pyrolysis is the direct thermal decomposition of molecules or mixtures in the absence of oxygen. In contrast to an electric discharge, pyrolysis provides temperature-dependent control over the production of transient species when they can be produced from an appropriate precursor. The microreactor is an adapted version of Peter Chen's hyperthermal nozzle⁴, which was originally designed as a source to produce radicals and other reactive intermediates⁵⁻⁷. In order to study thermal decomposition mechanisms of molecules relevant to biomass pyrolysis⁸⁻¹¹ and potential biofuels¹² the Chen nozzle was modified by the Ellison group at Boulder¹³. The microreactor offers a short residence time which diminishes bimolecular chemistry and allows the identification of unimolecular reaction schemes. The residence time is short enough that it is possible to detect radicals and other reactive intermediates.

To couple the flash pyrolysis microreactor with a broadband CP-FTMW spectrometer the design used in the Ellison's group was modified. The schematics of this design are shown in Figure 2.1. It consists of a 2 mm ID X 5 mm OD X 3.5 cm long silicon carbide (SiC) tube (Saint-Gobain Ceramics, Hexoloy SE). The SiC tube is mounted inside an alumina tube to reduce radiative heat loss. The tubular reactor is inserted into a copper heatsink and held concentric with a faceplate of a pulsed valve (General Valve, Series 9) outfitted with a 1 mm diameter nozzle orifice. Two sets of perpendicular set screws are used to hold the SiC and alumina tubes separately in place. The electrical current used to heat the SiC tube is provided through copper wires connected to molybdenum clips that hold two carbon discs, which are themselves in direct contact with the SiC tube. About two-thirds of the full length of the reactor is resistively heated, and the temperature of the outer wall is measure by a tungsten/rhenium type C thermocouple. A water-cooled copper heat sink is placed concentrically between the SiC tube and the valve faceplate to prevent the pulsed valve from getting heated by the micro-reactor. The maximum practical operable temperature of

the micro-reactor is about 1900 K. Upon exiting the reactor, the molecules are immediately jet-cooled, quenching further reactions and cooling the internal degrees of freedom for spectroscopic interrogation.

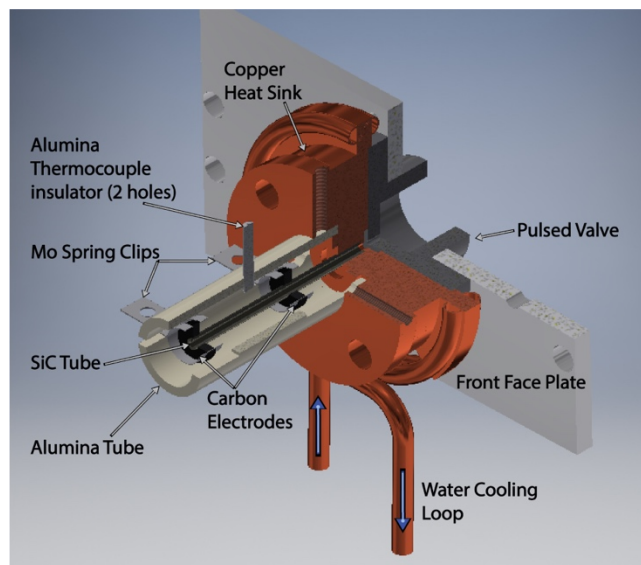


Figure 2.1: Flash pyrolysis micro-reactor assembly used to thermally decompose samples entrained in buffer gas.

There are two common failure modes for the micro-reactor upon heating to pyrolysis temperatures: the thermocouple breaks or the resistance of the SiC becomes too small. First, the thermocouple can easily break. After the thermocouple has been used at high T, it becomes rather brittle, and once it has been heated several times any movement of the junction will break it. Second, the resistance of the SiC tube can become too small, making it impossible to reach high temperatures or to even control the temperature. The optimal resistance for stable operation should be between 500 and 3000 ohms.

As mentioned before, the micro-reactor is resistively heated. In order to control the current flow through the SiC tube, the tube is incorporated into a circuit (Figure 2.2) consisting of a set of 6 light bulbs (250 watt) wired in parallel with one another, but in series with the SiC tube and controller. The power is provided and controlled by a 120 VAC source (typically a Variac). By adding bulbs in a parallel circuit, the net resistance of the bulbs decreases and the circuit current increases at a set source voltage, resulting in a temperature increase of the SiC tube. The Mo clip

closest to the pulse valve should be connected to neutral (white cable) and the hot side (black cable) should be connected to the Mo clip farther from the valve.

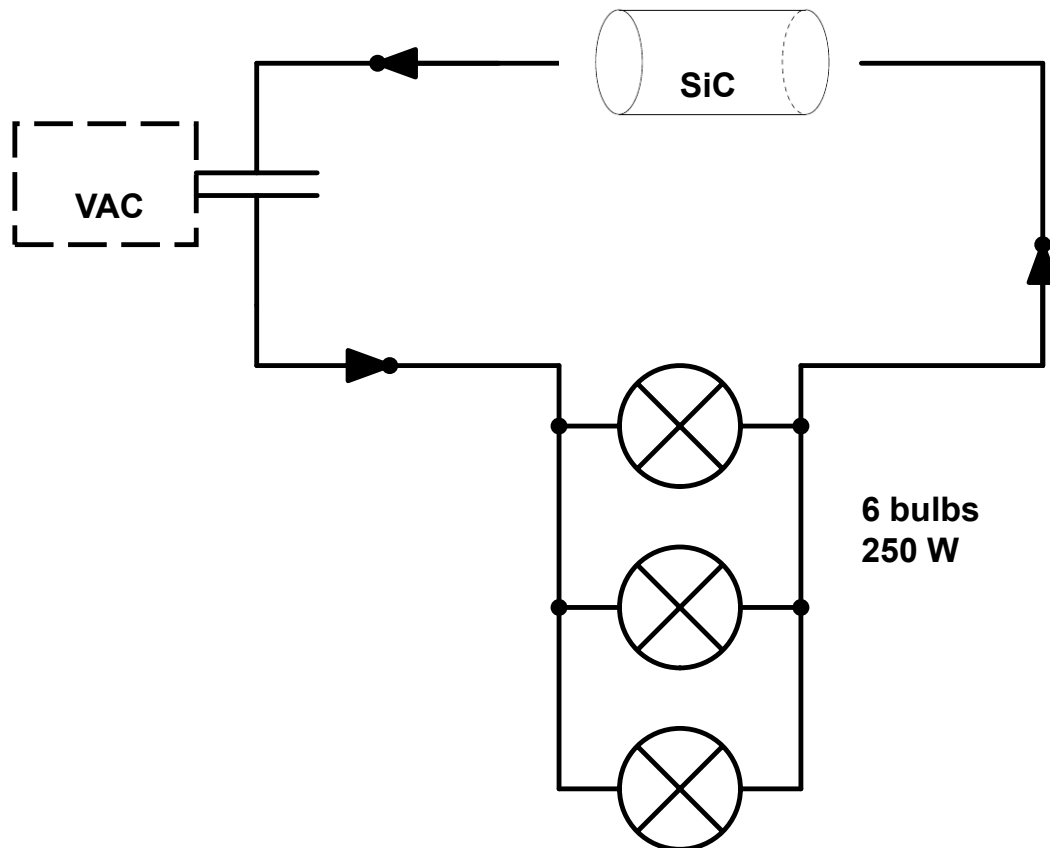


Figure 2.2: Schematic circuit to resistively heat the SiC micro-reactor.

2.3 Vacuum Chambers

There were two stainless steel vacuum chambers used for these experiments. In both cases the section of the chamber used to acquire the ground state microwave spectra were lined with a broadband microwave absorber backed with metal shielding (Emerson & Cuming ECCOSORB HR-25/ML) to reduce spurious reflection noise from the polarizing microwave pulse. The chambers were evacuated through two diffusion pumps (Varian VHS 10), the pump closest to the interrogation section of the chamber is fitted with a water baffle (Varian F8600310) to reduce backflow of the pump oil from the hot jet assembly. These pumps are backed up by a roughing pump (Alcatel 2063) and roots blower (BOC Edwards EH 500).

For some of the experiments a chamber originally designed by Brian Dian¹⁴ was used. The chamber was maintained at an unloaded pressure of $\sim 10^{-6}$ torr and an average operating pressure of $\sim 10^{-5}$ torr. The sample is introduced into the chamber using a pulsed valve (General Valve, Series 9) with a 1 mm orifice operating at 10 Hz. The pulse valve is placed perpendicular to the polarizing pulse to minimize Doppler effects and it is designed so that the valve is attached to a bracket that enables the flow to be adjusted from outside the chamber. Upon exiting the valve orifice, the sample undergoes supersonic expansion, cooling the molecules to the ground vibrational state.

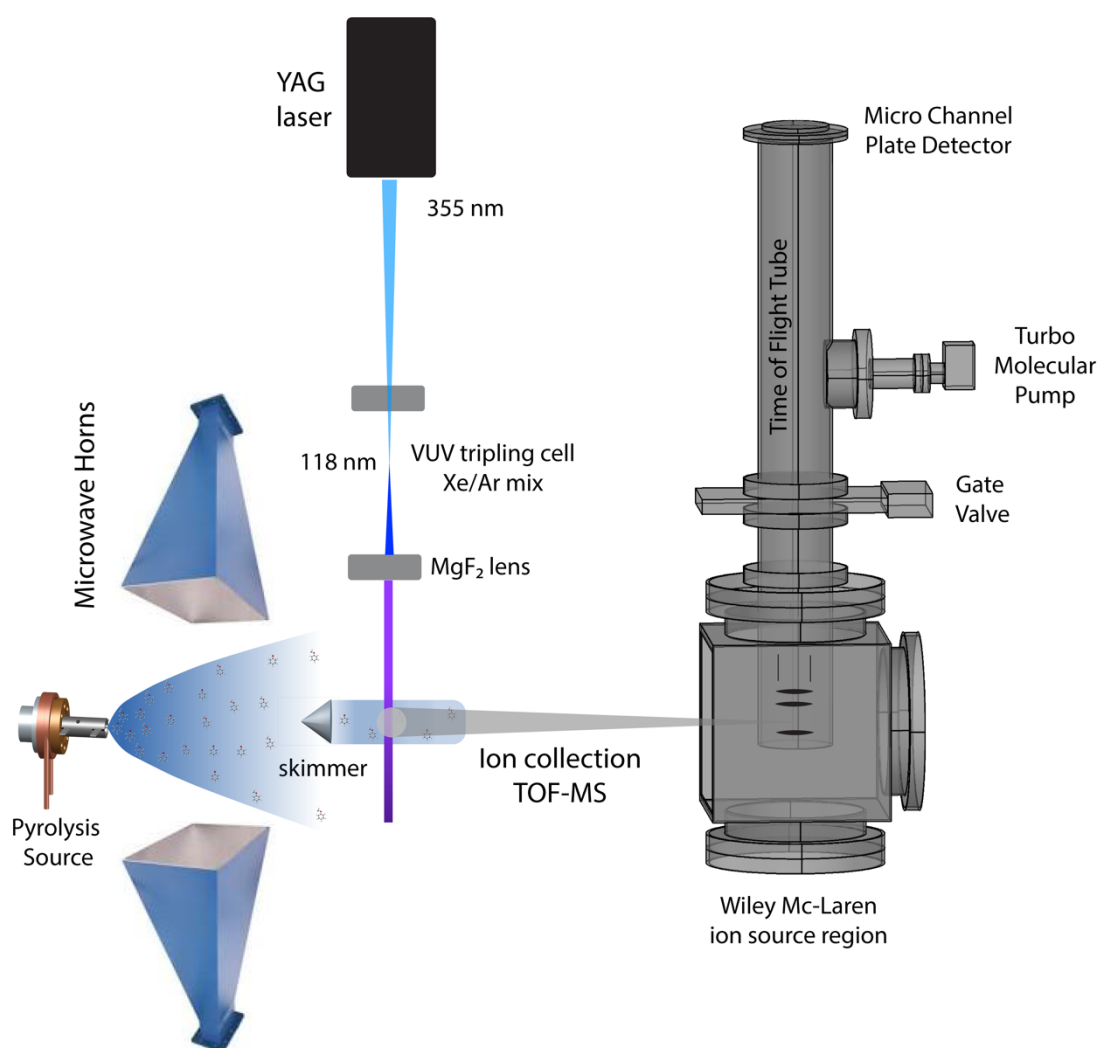


Figure 2.3: Schematic diagram of the chamber that can be used for both microwave spectroscopy and photoionization TOF mass detection.

Dr. Brian Hays designed an extension to the original chamber¹⁵, the current chamber can be used to simultaneously record a CP-FTMW spectrum and carry out photoionization TOF-MS detection. It consists of a rectangular stainless-steel chamber (60 cm x 30 cm x 30 cm) with two sets of flanges on each side. The base pressure of the chamber is $\sim 10^{-5}$ torr and maintains an operating pressure of $\sim 10^{-4}$ torr when the pulsed valve is operating. The valve is now supported by a bracket mounted on the end flange of a 12 cm nipple. The gaseous sample is interrogated first by microwave radiation. The interaction region between the microwave pulse and the sample molecules is dictated by the size of the microwave antennas (16 cm x 16.4 cm). After measuring the rotational spectrum, the expansion gas travels further downstream and goes through a 2 mm skimmer, forming a molecular beam. Here it is introduced into a 0.9 m Wiley-McLaren time-of-flight mass spectrometer. The TOF tube is evacuated by a 350 L/s turbo pump (Osaka Vacuum TG350F) backed by a roughing pump (Alcatel 2010I). The standing and operating pressures of this section of the chamber are 10^{-9} torr and 10^{-7} torr respectively.

Figure 2.3 shows a schematic diagram of the chamber. VUV photoionization TOF mass spectrometry provides the molecular formulae of the mixture components; nonetheless, the chemical structure of the molecular components is often not uniquely prescribed by the molecular formulae. Therefore, by having a complementary high-resolution method, such as CP-FTMW spectroscopy, it is possible to determine the gas phase structure, extending and speeding the analysis of complex gas mixtures.

2.4 Diagnosis

Molecules exiting the microreactor are probed by a CP-FTMW/TOF spectrometer that incorporates the capabilities to acquire simultaneous rotational and mass spectra under identical conditions. This section provides further details of the experimental apparatus and techniques employed. The unique experimental protocols applied in specific circumstances will be described in the respective chapters.

2.4.1 Broadband Chirped-Pulse Fourier Transform Microwave Spectroscopy

In this work CP-FTMW spectroscopy was used to obtain high-resolution ground state rotational spectra. Many neutral molecules and reactive intermediates have substantial dipole moments, making them good candidates for detection by rotational spectroscopy. The power of

this type of spectroscopy is the shape sensitive nature of the technique, since the spectrum is dependent on the moments of inertia of a molecule, any difference in atomic position for each isomer will generate a completely unique spectrum.

The moment of inertia is a tensor that determines the torque needed for an angular acceleration about a rotational axis. However, it is possible to define three mutually perpendicular rotational axes (*a*-axis, *b*-axis, and *c*-axis) that intersect at the center of mass of the molecule and calculate the moment of inertia about each axis separately. The frequencies of the rotational transitions observed are inherently related to the moments of inertia in the molecular frame of reference. In this frame, the moments of inertia about the *a*, *b*, and *c*-axes are labeled I_a , I_b , and I_c , where the labeling convention is that $I_a \leq I_b \leq I_c$. The rotational constants (*A*, *B* and *C*) of a molecule are then defined in terms of these moments of inertia as follows:

$$A = \frac{h}{8\pi^2 c I_a}, B = \frac{h}{8\pi^2 c I_b}, C = \frac{h}{8\pi^2 c I_c}$$

where c is the speed of light and h is Planck's constant.^{16, 17}

Light-induced transitions between rotational levels are dipole-allowed whenever the molecules of interest have a permanent dipole moment. CP-FTMW spectroscopy utilizes high-speed digital electronics to produce a broadband, chirped microwave pulse, typically of 1 μ s or shorter, that linearly sweeps the desired frequency region. Thus, in a short timeframe it is possible to probe a bandwidth of more than 10 GHz. Chirped pulse instruments can independently control the pulse power and the frequency bandwidth. The sweep range of the pulse, $\Delta\omega$, is a function of the sweep rate and the pulse duration, t_{pulse} ($\Delta\omega = \alpha \cdot t_{pulse}$). The frequency independent electric field, $E(t)$, produced by a chirped pulse, is defined by the peak electric field, E_{max} , the initial frequency parameter, ω_0 , and the linear sweep rate, α : $E(t) = E_{max} e^{i(\omega_0 t + \frac{1}{2}\alpha t^2)}$. The relationship between molecular signal strength for a given rotational transition and the bandwidth of the polarizing pulse in a linear frequency sweep is advantageous, since, as is shown in the following equation, the molecular signal decreases with the square root of the sweep rate,

$$S \propto \omega \cdot \mu^2 \cdot E_{pulse} \cdot \Delta N_0 \cdot \left(\frac{\pi}{\alpha}\right)^{\frac{1}{2}}$$

this equation shows that the molecular signal, S , is dependent on the frequency, ω , the transition dipole moment, μ , the electric field, E_{pulse} , and the population difference, ΔN_0 .^{18, 19}

The main components of the Purdue CP-FTMW spectrometer are shown in Figure 2.4. All polarizing microwave pulses were produced using a 10 GS/s arbitrary waveform generator (AWG, Tektronix AWG7101) that can be programmed to produce single frequency pulses or linear frequency sweeps up to 5GHz, producing an output intensity up to 1 V peak to peak. The AWG output is directed through a 5 GHz low-pass filter (Lorch 10LP-5000-S, 164 MHz) to reject high frequency harmonics. The AWG outputs an electric field that is frequency dependent, decreasing in intensity at higher frequencies. As a result, these uneven pulses were leveled using a preamplifier (Mini-Circuits ZX60-6013E-S+ 6000MHz, +14.2 dB gain). The pre-amplifier output is then multiplied by either a quadrupler (Phase One PS06-0161) for the 8-18 GHz frequency region or by a doubler (TRW Microwave RX8008) for the frequency region from 2-8 GHz. Final waveforms are power controlled with a step attenuator (Weinschel AF117A-69-11) and, for the 8-18 GHz frequency range, these are fed into a 200 W traveling wave-tube amplifier (TWTA, Amplifier Research 200T8G18A). In the case of the 2-8 GHz frequency range the waveforms are amplified by a 13 W solid state amplifier (Mercury Systems L0208-41 T113). The amplified pulses are sent into a vacuum chamber through a gain antenna (Seatite; Q-par Antennas QWH-SL-2-18-S-HG-R).

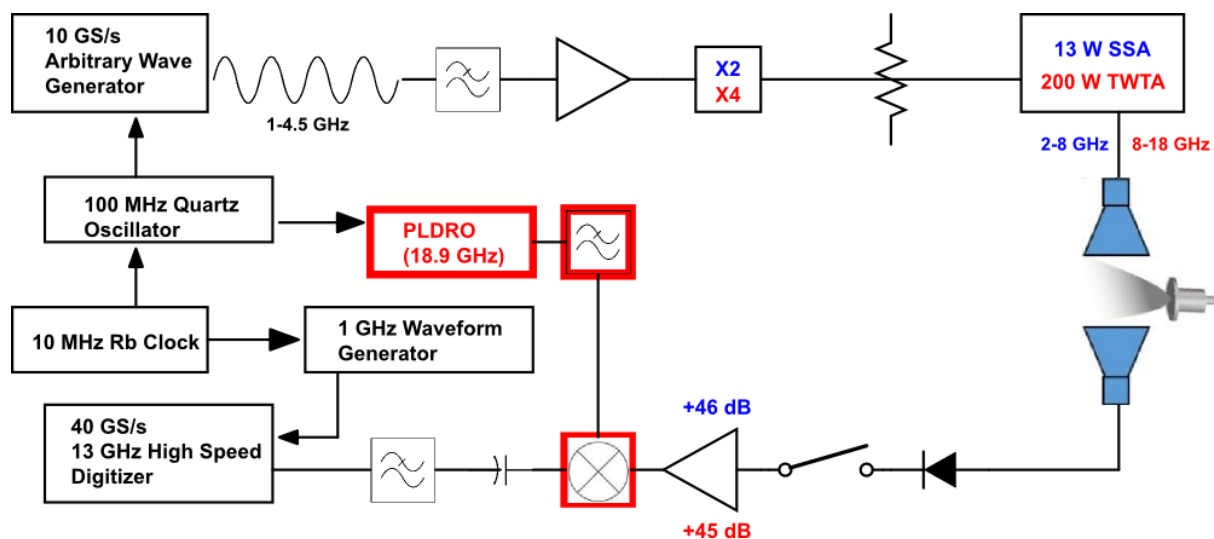


Figure 2.4: Schematic diagram of the CP-FTMW electronics for broadband acquisition over the 2-18 GHz frequency region. Components unique to the 2-8 GHz region are shown in blue, while those used only in the 8-18 GHz frequency range are indicated in red.

The broadcasted, high-power microwave pulse polarizes the molecular sample, which then undergoes free induction decay (FID) with a dephasing (T_2) time of about 15 μ s. The FID signal is collected with a second gain antenna and passed through a PIN diode limiter (Advanced Control Components ACLS 4619F-C36-1K, 1 kW peak power for 1 μ s pulse) and a reflective single pole single throw (SPST) switch (Advanced Technical Materials A1517D isolation 80 dB, 2-18 GHz). The switch remains closed during the polarizing pulse and the initial noise decay of the system. This combination protects the amplifier and high-speed digitizer from the high-power polarizing chirp. The FID collection is initiated \sim 60 ns after the high-power chirp, which incorporates the switching speed of the switch and a buffer. In the 8-18 GHz frequency region the collected molecular FID is amplified by a +45 dB gain low noise amplifier (Miteq AMF-6F-06001800-15-10P) and down-converted using a triple balanced mixer (Miteq TB044LW1) with a phase-locked dielectric resonator oscillator (PLDRO, Microwave Dynamics PLO-1000-18.9) operating at 18.9 GHz. For mixing purity, the PLDRO output is filtered with an 18.9 GHz cavity bandpass filter (Lorch 7CF7-18900/100S, (50 MHz at 3 dB)). In the case of the 2-8 GHz frequency region the FID is amplified by a +46 dB gain low noise amplifier (Miteq AMF-5F-02000800-15-10P). The mixed low-frequency band (0.4-11.4 GHz) or the amplified frequencies (2-8 GHz) are transmitted through a DC block (MCL 15542 BLK-18) and a 12 GHz low pass filter (Lorch 7LA-12000-S, (92.54 MHz)). Finally, the molecular free induction decay (FID) is phase coherently averaged and digitized in the time domain with a 13 GHz, 40 GS/s real-time digitizer (Guzik ADC6131). In order to average in the time domain, phase stability is essential; therefore, the PLDRO and the AWG are synchronized to a 100 MHz phase-locked loop (Wenzel Associates 501-10137B). This loop is driven by a 10 MHz Rb-disciplined crystal oscillator (Sandford Research Systems FS725). The phase drift of the oscillators and the amplifiers is sensitive to temperature variations, which is minimized by locating these components on water-cooled copper blocks for temperature stabilization. Additionally, a power supply constructed by the Purdue Amy Facility provides power to the PLDRO, amplifiers (excluding the TWTA and the 13 W Solid State Amplifier), quadrupler, quartz oscillator and the switch.

The general experimental timing scheme is controlled by the two marker channels of the AWG, enabling multiple chirp/FID detections in a single gas pulse. The AWG output is routed through two pulse-delay generators (Berkeley Nucleonics Corp. Model #555 and 557), one of

which is used to control the delays between the gas pulse and the chirp sequence. The other delay generator sets the timings of the TWTA amplification and the fast PIN switch.

The real-time digitizer used to capture the molecular FID signal achieves its 40 GS/s digitization rate using 160 separate internal ADC chips interleaved with one another, where each individual chip makes an acquisition every 4 ns. These ADC chips are not perfectly matched, producing baseline shifts between them. This causes the appearance of spurious lines at 250 MHz intervals in the frequency domain. Therefore, a custom Matlab routine was written to attenuate these lines. This routine determines the offset of each individual ADC chip by calculating the average of the last 150 points acquired by each respective ADC chip in the data set; that is, at the end of each FID collection time window. The Matlab routine then subtracts each ADC's baseline offset from all points acquired by that ADC to obtain a properly baseline-corrected FID. Then the data is converted to the frequency domain. A second custom Matlab program is also used to apply the fast Fourier transform (fft) to the time domain data. The data is first filtered with a Kaiser-Bessel^{18, 20} function to suppress side lobes.

There are two main sources of noise in the CP-FTMW spectrometer. One is due to residual ringdown of the polarizing pulse, this comes from reflections propagating through the stainless-steel chamber that have not been totally suppressed by the Eccosorb. The other source of noise comes from spurious peaks from the electronic components. To identify this noise in the frequency spectrum, in addition to acquiring a molecular FID, it is necessary to acquire a background spectrum. Usually during the data analysis, the background subtracted spectrum is used.

2.4.2 Photoionization Time-of-flight Mass Spectrometry (PIMS)

Time-of-flight mass spectrometry was used to determine the molecular weights of the components of gas phase mixtures. This technique is considered “soft” ionization because it ionizes a molecule close to its ionization threshold, reducing or even eliminating fragmentation of ions compared to electron impact ionization.^{21, 22}

After the expansion is skimmed, the molecular beam travels into the Wiley McLaren²³ type ion source region. The cold molecules are ionized with vacuum ultraviolet (VUV) radiation. The 118.2 nm (10.487 eV) light is generated using the output of a pulsed neodymium-doped yttrium aluminum garnet (Nd:YAG) laser (fundamental wavelength 1064 nm). In the Nd:YAG laser, a portion of the 1064 nm fundamental is frequency tripled to 355 nm. Then about 30 mJ of 355 nm

light is focused into a Xenon:Argon (Xe:Ar) gas cell, where a small fraction of the incoming light is tripled again to generate the 9th harmonic of the Nd:YAG at 118.2 nm. The VUV cell is 31 cm long and has a gas manifold attached to an inlet port to allow for the introduction of argon and xenon to produce the tripling medium. A vessel attached to the base of the VUV cell allows for the placement of dry ice to ensure better mixing of the gas by convection. A MgF₂ lens (148 mm focal length, 2.5 cm diam) affixed to the end of the VUV tube is used to separate the 355 nm light from the VUV radiation. The tripling cell has a total cell pressure of ~110 Torr, and uses a 1:10, Xe:Ar, ratio.

Molecules with ionization thresholds less than 10.487 eV are ionized by single-photon ionization. Photoionization occurs between the repeller plate and the draw-out-grid, which are separated from one another by 2 cm. Typical operating voltages of +3000 V and +2750 V are placed on repeller and draw-out grid, respectively. The ion packet is steered and focused by an Einzel lenses operating at +1750 V before striking an 18 mm dual chevron microchannel plate (MCP) (Jordan TOF Products, Inc. C0701) with typical front-surface potential at -2500 V. The current pulses from the mass-resolved photoions are amplified a second time by a factor of 25 in a fast amplifier (Stanford Research Systems SR445) before being displayed on a 3.5 GHz, 40 GS/s digital phosphor oscilloscope (Tektronix DPO 7354C). In this set-up the AWG serves as the master clock for all the components involved in the experiment, including the digital delay generator that triggers the Nd:YAG laser.

2.5 Computational Methods

As an aid to the analysis of the experimental spectra, *ab initio* calculations were carried out. To determine the optimized ground-state geometries, MP2 and DFT calculations were employed using Gaussian09²⁴. Since microwave data rely heavily on a close correspondence between calculated and experimental rotational constants, for each molecule different levels of theory with different basis sets were explored to determine which one yield rotational constants that are in close agreement with the experiment. The B2PLYP functional, including Grimme's dispersion correction²⁵ and a Becke-Johnson damping²⁶, with the correlation consistent basis set aug-cc-pVTZ, was determined to give excellent agreement between experiment and theory. Harmonic frequency calculations were used to confirm that the calculated structures were true minima.

The radicals were studied computationally in collaboration with John Stanton at the University of Florida, using the CFOUR suite of programs. The study was done using coupled-cluster theory at the CCSD(T) level²⁷. First, the economical ANO0 basis set^{28, 29} was used in conjunction with CCSD(T) to obtain the structure, harmonic frequencies and the cubic anharmonic force field, as well as the dipole moment and unpaired spin densities. The harmonic frequencies and cubic force constants, together with the equilibrium structure, provide the necessary input to compute the centrifugal distortion constants as well as the rotation-vibration interaction constants at the level of the second-order vibrational perturbation theory (VPT2)³⁰. The latter corrections account for differences between the simple equilibrium rotational constants (A_e , B_e , C_e), which are inversely proportional to the inertial tensor, and the vibrational ground state values (A_0 , B_0 , C_0) that are measured experimentally. Then using the considerably larger cc-pCVTZ basis³¹, the equilibrium structure was obtained to provide a good estimate of A_e , B_e and C_e . Augmentation of these by the vibrational corrections computed with ANO0/CCSD(T) yield theoretical estimates that are in good agreement with the experimental values. Finally, the electronic spin-rotation tensor was computed analytically at the ANO0/CCSD(T) level using the approach outlined by Tarczay *et. al.*³².

To locate conformational minima and to better understand the potential energy landscape, for molecules such as methyl butyrate, a relaxed two-dimensional potential energy surface (2D-PES) was also calculated using Gaussian09. The 2D-PES pictorializes the inherent conformational preferences, and this can give information on the observed conformers in case of having collisional removal of population during the supersonic expansion.

In some cases, it was necessary to determine the barrier to internal rotation of the methyl group. This is done by rotating the methyl group and varying the dihedral angle in 10° increments, while other parameters are optimized. The level of theory used depended on the size of the molecule.

2.6 References

1. Levy, D. H., The Spectroscopy of Very Cold Gases. *Science* **1981**, *214*, 263-269.
2. Lubman, D. M.; Rettner, C. T.; Zare, R. N., How Isolated Are Molecules in a Molecular Beam? *J. Phys. Chem.* **1982**, *86*, 1129-1135.
3. Smalley, R. E.; Wharton, L.; Levy, D. H., Molecular Optical Spectroscopy with Supersonic Beams and Jets. *Accounts Chem. Res.* **1977**, *10*, 139-145.
4. Chen, P.; Colson, S. D.; Chupka, W. A.; Berson, J. A., Flash Pyrolytic Production of Rotationally Cold Free Radicals in a Supersonic Jet. Resonant Multiphoton Spectrum of the $3p2A2'' \leftarrow X2A2''$ Origin Band of CH₃. *J. Phys. Chem.* **1986**, *90*, 2319-2321.
5. Jochowitz, E. B.; Zhang, X.; Nimlos, M. R.; Varner, M. E.; Stanton, J. F.; Ellison, G. B., Propargyl Radical: Ab Initio Anharmonic Modes and the Polarized Infrared Absorption Spectra of Matrix-Isolated HCCCH₂. *J. Phys. Chem. A* **2005**, *109*, 3812-3821.
6. Rohrs, H. W.; Wickham-Jones, C. T.; Ellison, G. B.; Berry, D.; Argrow, B. M., Fourier transform infrared absorption spectroscopy of jet-cooled radicals. *Review of Scientific Instruments* **1995**, *66*, 2430-2441.
7. Zhang, X.; Friderichsen, A. V.; Nandi, S.; Ellison, G. B.; David, D. E.; McKinnon, J. T.; Lindeman, T. G.; Dayton, D. C.; Nimlos, M. R., Intense, hyperthermal source of organic radicals for matrix-isolation spectroscopy. *Review of Scientific Instruments* **2003**, *74*, 3077-3086.
8. Jarvis, M. W.; Daily, J. W.; Carstensen, H.-H.; Dean, A. M.; Sharma, S.; Dayton, D. C.; Robichaud, D. J.; Nimlos, M. R., Direct Detection of Products from the Pyrolysis of 2-Phenethyl Phenyl Ether. *J Phys Chem* **2011**, *115*, 428-438.
9. Scheer, A. M.; Mukarakate, C.; Robichaud, D. J.; Ellison, G. B.; Nimlos, M. R., Radical Chemistry in the Thermal Decomposition of Anisole and Deuterated Anisoles: An Investigation of Aromatic Growth. *J. Phys. Chem. A* **2010**, *114*, 9043-9056.
10. Scheer, A. M.; Mukarakate, C.; Robichaud, D. J.; Nimlos, M. R.; Ellison, G. B., Thermal Decomposition Mechanisms of the Methoxyphenols: Formation of Phenol, Cyclopentadienone, Vinylacetylene, and Acetylene. *J. Phys. Chem. A* **2011**, *115*, 1381-1389.
11. Vasilioiu, A. K.; Kim, J. H.; Ormond, T. K.; Piech, K. M.; Urness, K. N.; Scheer, A. M.; Robichaud, D. J.; Mukarakate, C.; Nimlos, M. R.; Daily, J. W.; Guan, Q.; Carstensen, H. H.; Ellison, G. B., Biomass pyrolysis: thermal decomposition mechanisms of furfural and benzaldehyde. *J Chem Phys* **2013**, *139*, 104310.
12. Urness, K. N.; Guan, Q.; Troy, T. P.; Ahmed, M.; Daily, J. W.; Ellison, G. B.; Simmie, J. M., Pyrolysis Pathways of the Furanic Ether 2-Methoxyfuran. *J Phys Chem A* **2015**, *119*, 9962-77.
13. Guan, Q.; Urness, K. N.; Ormond, T. K.; David, D. E.; Barney Ellison, G.; Daily, J. W., The properties of a micro-reactor for the study of the unimolecular decomposition of large molecules. *Int. Rev. Phys. Chem.* **2014**, *33*, 447-487.
14. Shirar, A. J.; Wilcox, D. S.; Hotopp, K. M.; Storck, G. L.; Kleiner, I.; Dian, B. C., Impact of Molecular Conformation on Barriers to Internal Methyl Rotation: The Rotational Spectrum of m-Methylbenzaldehyde. *J. Phys. Chem. A* **2010**, *114*, 12187-12194.
15. Fritz, S. M.; Hays, B. M.; Hernandez-Castillo, A. O.; Abeysekera, C.; Zwier, T. S., Multiplexed characterization of complex gas-phase mixtures combining chirped-pulse Fourier transform microwave spectroscopy and VUV photoionization time-of-flight mass spectrometry. *Review of Scientific Instruments* **2018**, *89*.
16. Gordy, W.; Cook, R. L., *Microwave Molecular Spectra*. John Wiley & Sons Inc.: 1984.
17. Townes, C. H.; Schawlow, A. L., *Microwave Spectroscopy*. Dover Publications: 1975.

18. Brown, G. G.; Dian, B. C.; Douglass, K. O.; Geyer, S. M.; Shipman, S. T.; Pate, B. H., A broadband Fourier transform microwave spectrometer based on chirped pulse excitation. *Rev Sci Instrum* **2008**, *79*, 053103.
19. McGurk, J. C.; Schmalz, T. G.; Flygare, W. H., Fast passage in rotational spectroscopy: Theory and experiment. *The Journal of Chemical Physics* **1974**, *60*, 4181-4188.
20. Harris, F. J., On the Use of Windows for Harmonic Analysis with the Discrete Fourier Transform. *Proc. IEEE* **1978**, *66*.
21. Cao, L.; Muhlberger, F.; Adam, T.; Streibel, T.; Wang, H. Z.; Kettrup, A.; Zimmermann, R., Resonance-Enhanced Multiphoton Ionization and VUV-Single Photon Ionization as Soft and Selective Laser Ionization Methods for On-Line Time-of-Flight Mass Spectrometry: Investigation of the Pyrolysis of Typical Organic Contaminants in the Steel Recycling Process. *Anal. Chem.* **2003**, *75*, 5639-5645.
22. Shi, Y. J.; Lipson, R. H., An overview of organic molecule soft ionization using vacuum ultraviolet laser radiation. *Canadian Journal of Chemistry* **2005**, *83*, 1891-1902.
23. Wiley, W. C.; McLaren, I. H., Time-of-Flight Mass Spectrometer with Improved Resolution. *Review of Scientific Instruments* **1955**, *26*, 1150-1157.
24. Frisch, M. J.; Trucks, G. W.; Schlegel, H. B.; Scuseria, G. E.; Robb, M. A.; Cheeseman, J. R.; Scalmani, G.; Barone, V.; Petersson, G. A.; Nakatsuji, H.; Caricato, X. L., M.; Marenich, A.; Bloino, J.; Janesko, B. G.; Gomperts, R.; Mennucci, B.; Hratchian, H. P.; Ortiz, J. V.; Izmaylov, A. F.; Sonnenberg, J. L.; Williams-Young, D.; Ding, F.; Lipparini, F.; Egidi, F.; Goings, J.; Peng, B.; Petrone, A.; Henderson, T.; Ranasinghe, D.; Zakrzewski, V. G.; Gao, J.; Rega, N.; Zheng, G.; Liang, W.; Hada, M.; Ehara, M.; Toyota, K.; Fukuda, R.; Hasegawa, J.; Ishida, M.; Nakajima, T.; Honda, Y.; Kitao, O.; Nakai, H.; Vreven, T.; Throssell, K.; Montgomery, J. A.; Peralta, J., J. E. ; Ogliaro, F.; Bearpark, M.; Heyd, J. J.; Brothers, E.; Kudin, K. N.; Staroverov, V. N.; Keith, T.; Kobayashi, R.; Normand, J.; Raghavachari, K.; Rendell, A.; Burant, J. C.; Iyengar, S. S.; Tomasi, J.; Cossi, M.; Millam, J. M.; Klene, M.; Adamo, C.; Cammi, R.; Ochterski, J. W.; Martin, R. L.; Morokuma, K.; Farkas, O.; Foresman, J. B.; Fox, D. J., *Gaussian, Inc, Wallingford CT* **2016**.
25. Grimme, S., Semiempirical hybrid density functional with perturbative second-order correlation. *J Chem Phys* **2006**, *124*, 034108.
26. Grimme, S.; Ehrlich, S.; Goerigk, L., Effect of the damping function in dispersion corrected density functional theory. *J Comput Chem* **2011**, *32*, 1456-65.
27. Raghavachari, K.; Trucks, G. W.; Pople, J. A.; Head-Gordon, M., A Fifth-Order Perturbation Comparison of Electron Correlation Theories. *Chem Phys Lett* **1989**, *157*, 479-483.
28. Almlöf, J.; Taylor, P. R., General contraction of Gaussian basis sets. I. Atomic natural orbitals for first- and second-row atoms. *J. Chem. Phys.* **1987**, *86*, 4070-4077.
29. McCaslin, L.; Stanton, J., Calculation of fundamental frequencies for small polyatomic molecules: a comparison between correlation consistent and atomic natural orbital basis sets. *Mol. Phys.* **2013**, *111*, 1492-1496.
30. Mills, I. M., In *Molecular Spectroscopy: Modern Research*, Rao, K. N.; Mathews, C. W., Eds. Academic Press: New York, 1972; p 115.
31. Woon, D. E.; Dunning, T. H., Gaussian basis sets for use in correlated molecular calculations. V. Core-valence basis sets for boron through neon. *J. Chem. Phys.* **1995**, *103*, 4572-4585.
32. Tarasay, G.; Szalay, P. G.; Gauss, J., First-Principles Calculation of Electron Spin-Rotation Tensor. *J. Phys. Chem. A.* **2010**, *114*, 9246-9252.

CHAPTER 3. STRONG FIELD COHERENCE BREAKING (SFCB)

3.1 Introduction

In many important circumstances (e.g., photochemical product analysis, pyrolysis, and combustion), it is possible to encounter complex gas-phase mixtures that have a number of unique molecular components whose identities and abundances must be determined. Even in pure samples containing a single chemical component, if the molecule is large enough, it can possess several distinct conformational and/or structural isomers, each with their unique properties and spectral signatures;¹ these contribute to the spectrum via transitions that are interspersed amongst each other, making it hard to assign individual transitions to particular components of the mixture. This has fueled much effort towards the development of methods for isomer-specific spectroscopy. Double resonance methods to carry out isomer-specific spectroscopy in the optical and infrared regions have been used for many years; with one light source tagging a ground state level of a single isomer by selectively removing population from it, while a second tuned light source probes the changes induced in the spectral intensities by the first. In the gas phase, optical-optical², IR-IR³, and IR-optical methods⁴⁻⁶ have been devised.

The direct relationship between molecular structure and rotational frequencies makes rotational spectroscopy highly structurally specific and an important tool for analyzing chemically complex structures and mixtures. Gas-phase microwave experiments routinely achieve frequency resolution better than 10 kHz, therefore, a typical broadband spectrum covering 8-18 GHz contains (10 GHz/10 kHz) 10^6 resolution elements.⁷ Thus, a chemical species can be unambiguously identified even in complex mixtures; and since the pattern of frequencies is directly related to the molecular geometry, the spectrum can be directly compared with theoretical structure calculations. The rotational transitions of a molecule can be fit to obtain highly accurate rotational constants, while intensities report on the populations of the levels and the projections of the permanent dipole moment on the inertial axes of the molecule.⁸ Shifts and splittings due to the centrifugal distortion, nuclear quadrupole coupling, tunneling, or other large amplitude motions of specific functional groups all add to the richness of the structural data.

However, the extremely high resolution and precision of microwave spectroscopy are also a hindrance, since this generates complex spectra. Rotational transitions due to different

components of a mixture show up intersected amongst one another, and this is a challenge especially when the determination of the chemical composition of the gas mixture is itself the research problem of primary interest. The broadband capability and rapid data acquisition of Chirped-Pulse Fourier transform microwave (CP-FTMW) spectroscopy⁹ has enabled many advances in microwave double-resonance techniques that can facilitate the analysis of congested rotational spectra.¹⁰ For example, microwave three-wave mixing can differentiate two chiral enantiomers;¹¹ infrared-microwave (IR-MW)¹² has been used to study kinetics of conformational isomerization,¹³ and UV-microwave (UV-MW) techniques can extract single-species rotational spectra using rotationally resolved electronic spectra^{14, 15}.

Coherence transfer techniques like microwave-radio frequency (MW-RF) double resonance gives information about the connectivity of rotational energy levels, by modulating the MW transitions with an interacting RF pulse.^{16, 17} The coherence-breaking null scheme, in which laser excitation out of a single rovibronic level occurs between two oppositely phased composite millimeter-wave pulses, has successfully demonstrated the ability to rapidly analyze dense, congested regions in an optical spectrum of a small molecule.¹⁸ McCarthy and co-workers have introduced a powerful method for “spectral taxonomy” of multi-component mixtures that combines broadband microwave spectroscopy with fast acquisition of line-by-line double resonance spectra that determine line connectivity using a computer-controlled cavity microwave spectrometer.¹⁰ Techniques like selective-excitation CP-FTMW¹⁹ have demonstrated the ability to selectively modulate intensities of rotational transitions that share a common rotational energy level. The technique uses a broadband chirp to create the molecular transient absorption, and a narrowband pulse to selectively disrupt specific coherences between rotational transitions that share common energy levels in the molecular free induction decay. Finally, two-dimensional CP-FTMW spectroscopy has already been explored,²⁰ but currently remains an undeveloped area of research; its development will not only help diagnose and disentangle complex spectra, but it could enable new experiments such as time-resolved tracking of the moments of inertia of coherent states.

Here, a new method is introduced, using the same CP-FTMW hardware to extract from a congested spectrum a subset of transitions ascribable to single-components of the mixture, thereby greatly simplifying line assignments. A procedure is introduced that leads to selection of three transition frequencies that can be incorporated as a set of resonant sequential single-frequency

microwave pulses that follow the broadband chirped-pulse excitation, resulting in a reduction of the coherent signal from a set of transitions associated to the compound of interest.

3.2 Experimental Methods

For this study, commercial samples of the molecules (benzonitrile (98%, Sigma Aldrich), a commercial mixture of (E)- and (Z)-phenylvinyl nitrile (PVN) (97%, Alfa Aesar), and methyl butyrate (MB) (99%, Sigma-Aldrich)) were used without any further purification. The liquid samples were inserted into a stainless-steel sample holder, located immediately behind the pulse valve. The (E)- and (Z)-PVN mixture was heated to ~ 80 °C to obtain sufficient vapor pressure. The samples were entrained in helium gas at a 0.69 bar backing pressure. A home-made pulsed valve driver powered the solenoid valve triggered externally at a 10 Hz repetition rate. The experiments were performed with the chamber originally designed by Brian Dian described in section 2.3, and the lay out of the main components is described in section 2.4.1. The timing scheme was matched to the width of the gas pulse in order to collect a set of 25 FIDs in a single pulse, each FID was 16 μ s.

Ab initio and DFT calculations on (E)/(Z)- PVN and MB were initially performed using Gaussian 09 suite²¹ at the MP2/aug-cc-pVTZ and M06-2X/6-311+g(d) levels of theory for PVN and MB respectively. The calculated rotational constants were used to predict the line frequencies and compared directly to experimental observations. More details on the computational studies of MB are given on section 3.3.3.

3.3 Method Development

Fast passage excitation in chirped pulse spectroscopy can be considered as a transient absorption during the excitation pulse and a subsequent transient emission.^{9, 22} Considering a simple case in which the frequency of a pulse of microwave radiation is swept from well below to well above a single molecular rotational transition. The Rabi frequency for the transition between the two energy levels is given by

$$\Omega_0 = \left[\left| \frac{\vec{\mu} \cdot \vec{E}_{pulse}}{\hbar} \right| + \Delta^2 \right]^{\frac{1}{2}}$$

where μ is the transition dipole moment, E_{pulse} is the electric field strength of the microwave field, and Δ is the detuning of the excitation pulse from resonance frequency. If the linear sweep rate ($\alpha = \frac{\partial}{\partial t} \Delta\omega_{ab}$) is much faster than the Rabi frequency ($\alpha \gg \Omega_0^2$), the coupling between the molecules and the polarizing electric field via the rotational transient dipole moment is small. In this weak coupling limit, referred to as the linear fast passage (LFP) regime, radiation that sweeps from low-to-high or high-to-low frequencies produces a coherence between the two rotational states.²³ The maximum coherence is achieved with a $\pi/2$ excitation pulse in the Bloch sphere representation. Population analysis is possible in this regime because the signal scales linearly with the population difference, which is governed by a Boltzmann distribution.

However, as Schnell and co-workers have recently highlighted, the high power TWTAs used in CP-FTMW spectrometers have allowed the exploration of rapid adiabatic passage (RAP) effects in rotational spectroscopy.²⁴ In this regime, a strong coupling ($\alpha \ll \Omega_0^2$) is created,^{25, 26} inducing significant population transfer between two diabatic states, leading in the RAP limit to a π -pulse excitation in the Bloch sphere representation that creates a population inversion between the two states. Therefore, a linear broadband excitation sweep in the strong field limit can alter the relative line intensities from what would be expected based on a Boltzmann distribution. A linear excitation sweep, from low to high frequency will excite low-J states at the beginning of the sweep and higher J states later. If a near π -pulse excitation is achieved, the population transfer induced in the two rotational states will propagate up the ladder in subsequent excitations, moving population to higher J-levels that are subsequently involved in transitions at higher frequency, leading to multi-resonance excitation effects.^{24, 27-29}

Strong coupling between the polarizing electric field and the molecular rotational dipole is a primary prerequisite for the SFCB method. As demonstrated in previous work,²⁴ operation in either of the two coupling regimes can be achieved by controlling the polarizing electric field strength of the microwave radiation via the gain on the TWT amplification stage. In the LFP regime, the line intensities will be independent of the direction of the chirp (low-to-high frequency, or high-to-low); however, in the RAP regime, population transfer during the chirp will be significant, resulting in different intensities when the chirp occurs in one direction or the other. As Figure 3.3(a) illustrates for benzonitrile, a CP-FTMW spectrum recorded with 1% TWT gain, in the LFP regime, shows no difference between spectra recorded with an 8→18 GHz or an 18→8

GHz sweep. However, at 100% TWTA gain (Figure 3.3(b)), large differences in intensity between the two scans are observed, indicating effects characteristic of the RAP regime.

In its simplest form, the SFCB method involves three fundamental steps (Figure 3.1):

1. A second spectrum is recorded after excitation with the same high power linear broadband chirp (8-18 GHz), followed by a single-frequency pulse (or pulses), also at high power, whose frequency is resonant with a transition(s). The resultant molecular FID is collected at the end of the selective frequency pulse.
2. A high-power broadband linear chirp is used to record a CP-FTMW spectrum.
3. A difference spectrum is constructed between scans 1 and 2 in the frequency domain. When the difference is taken, some of the transitions increase in intensity and some decrease. The absolute value of the intensities is plotted.

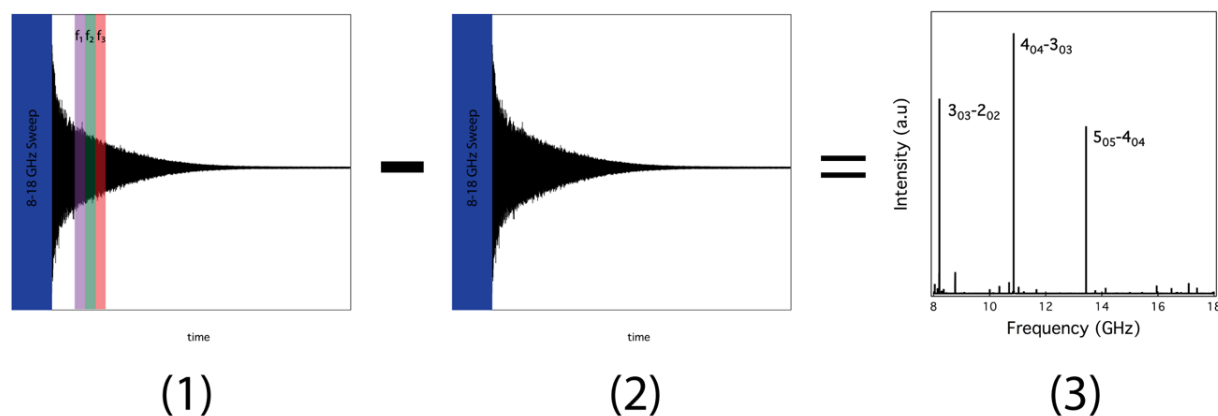


Figure 3.1: Schematic diagram for SFCB scheme.

In order to obtain difference spectra of the highest selectivity, we explored a range of time delays and pulse durations for the single-frequency pulse(s) in benzonitrile, to establish parameters that work best. The $J_{K_a K_c}=4_{0,4}-3_{0,3}$ ($\nu=10855.233$ MHz) rotational transition of benzonitrile was chosen for the selective single-frequency pulse. We explicitly looked for pulse durations that minimized the intensity of the transition on which the single frequency pulse (SFP) is resonant. Under the conditions where the broadband chirp (1 μ s; 8-18 GHz) was followed by a SFP it was possible to reduce the transition intensity up to 97% at 1% TWTA power and 98% at 100% TWTA power. For the reduced power condition (TWTA 1%) the pulse length where the was 35 ns, Figure 3.3(a). At 100% TWTA the lowest line intensity was reached with a pulse length of 20 ns (Figure

3.3(b)), as we increased the pulse length there was no significant change in the depletion of the transition. However, using longer pulse durations can reduce edge effects.³⁰

When searching for conditions to use for the broadband chirp followed by a SFP we explicitly looked for pulse durations that minimized the intensity of the transition on which the SFP is resonant (Figure 3.2). Focusing on the $J_{k_{akc}}=4_{0,4}-3_{0,3}$ transition, when the TWTA power was 1% the intensity of the transition decreased by $\sim 97\%$ with a pulse duration of 35 ns, whereas when the TWTA was 100% the intensity decreased by about 98% at a pulse length of 20 ns. However, at 100% TWTA gain (Figure 3.2(b)) when we increase the pulse length we didn't observe any significant change in the intensity. Both the time delay and single pulse(s) duration must be on time scales fast compared to the relaxation times (T_1, T_2) of the pulsed transition in order to create multi-level modulation in the FID from the broadband pulse.

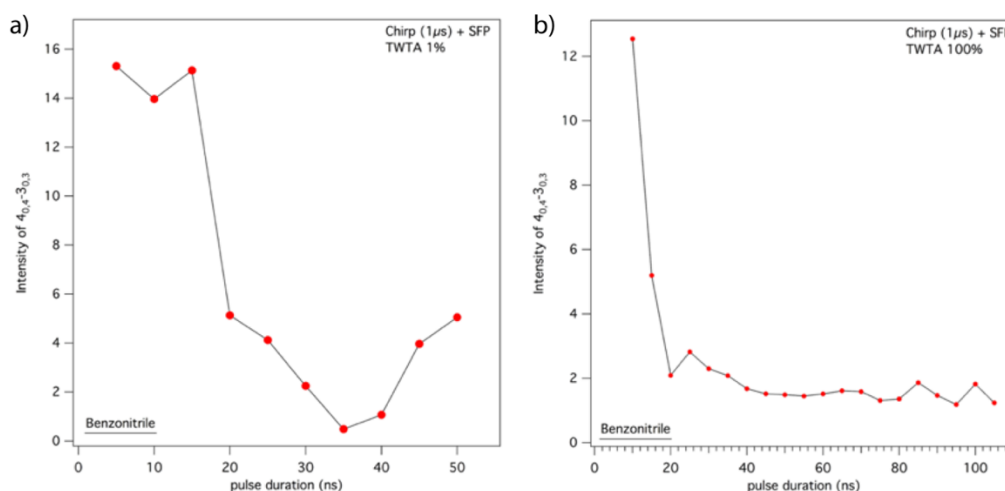


Figure 3.2: Intensity of the $4_{0,4}-3_{0,3}$ transition of benzonitrile resulting from a 1μ s broadband chirp (8-18 GHz) followed by a SFP resonant with the $4_{0,4}-3_{0,3}$ transition at 10855.233 MHz. (a) Taken with the TWTA power set at 1%. (b) Taken with the TWTA set at 100%.

For benzonitrile, the method was tested in both coupling regimes, with its optimal selective frequency pulse duration and gap. The difference spectra obtained under weak coupling (LFP) and strong coupling (RAP) regimes are shown in Figures 3.3(c) and 3.3(d) respectively. The resulting difference spectrum in the LFP regime (Figure 3.3(c)) is just as anticipated, based on the selective-excitation CP-FTMW technique,¹⁹ with intensity changes induced in $2_{0,2}\rightarrow 3_{0,3}$ and $4_{0,4}\rightarrow 5_{0,5}$ transitions that share a rotational level with the $3_{0,3}\rightarrow 4_{0,4}$ transition on which the single-frequency

coherence breaking pulse is resonant. Meanwhile in the RAP regime (Figure 3.3(d)), other transitions had their intensities modulated, even those that have no shared rotational energy level with the $3_{0,3} \rightarrow 4_{0,4}$ transition used as SFP. The stability and the reproducibility were checked between scans to make sure the modulation was not due to experimental uncertainty. The ability to create modulation of a large fraction of the rotation transitions of the molecule in the 8-18 GHz frequency region, by just placing a single selective excitation pulse after the broadband chirp is unique and demonstrates the advantage of operating in the strong field limit when seeking to obtain isomer-specific spectra. All difference spectra taken in this work were obtained by using the custom made Matlab program described in Appendix A.2, the program also selects the transitions whose modulated intensity is greater than or equal to a set percentage and their absolute intensity is higher than an established threshold.

3.3.1 Multiple selective-excitation (MSE)

The test molecule benzonitrile has its total dipole moment (μ) fixed along a single rotational axis (*a*-axis). Since, a-type rotational transitions therefore dominate the spectrum in its 8-18 GHz range, most of these transitions can be modulated with the SFCB method by exciting a single a-type coherence-breaking transition. However, most molecules do not have this advantage. Therefore, the SFCB method was modified by implementing a refinement involving a Multiple Selective-Excitation (MSE) sequence, where instead of a single selective pulse, multiple successive SFPs are used to disrupt coherences. To find the frequencies required for the MSE scheme that would sensitively modulate the intensities of a large fraction of the rotational transitions due to a single isomer or molecular component in a mixture, we initially developed a line picking scheme based purely on a series of experiments with SFPs. However, with increased experience, the selection criteria for the resonant frequencies was refined.

During the development of the SFCB method, it became clear that the single-frequency pulses themselves modulate a number of connected and non-connected transitions due to the isomer selected by the resonant pulse, even in the absence of the broadband chirped-pulse. Careful tests were carried out to ensure that these modulations were not due to any noise associated with the microwave electronics or the high power TWTA. Optimum operating conditions were chosen by varying the input power to the TWTA to make sure that no transition was modulated in intensity when the frequency of the resonant pulse was shifted 10 MHz off-resonance from the most intense

transition chosen for MSE. Further explanation of the effects produced by SFPs is described in Chapter 4.

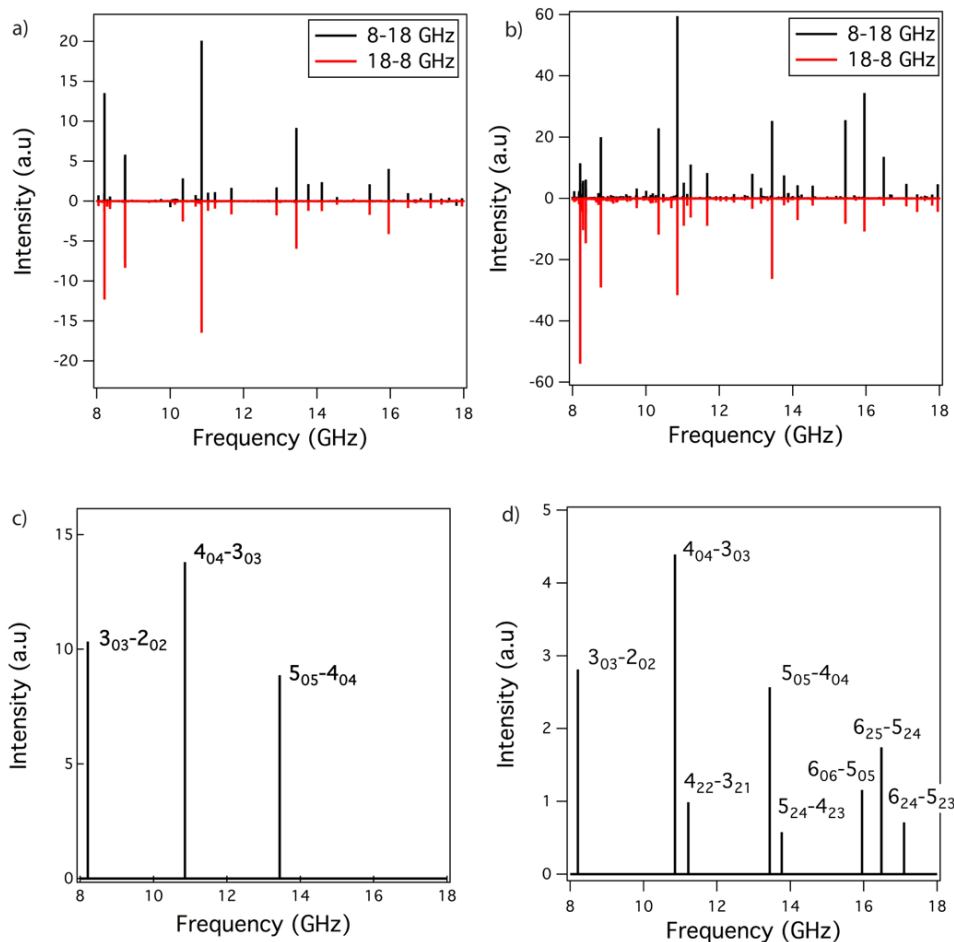


Figure 3.3: ((a) and (b)): Broadband CP-FTMW spectra of benzonitrile over the 8-18 GHz region, comparing the spectra following 900 ns chirps with the frequency swept up from 8 to 18 GHz (black) and down from 18 to 8 GHz (red), with TWTA gain at (a) 1% and (b) 100% of full power. ((c) and (d)): Difference spectra from an 8-18 GHz chirp (800 ns duration) with and without a resonant pulse (100 ns) following the broadband sweep, centered in frequency at the $J_{KaKc}=4_{0,4}-3_{0,3}$ transition (10855.233 MHz). The TWTA gain in (c) is 1% and (d) 100% of full power. Only the directly connected transitions appear in (c), while additional transitions appear under SFCB conditions in (d). The transitions shown here are above median noise level.

The MSE sequence initially implemented, consisted of the sequential application of single frequency pulses at three frequencies (ν_1, ν_2, ν_3), producing a difference spectrum that modulated a sufficient number of lines in a particular isomer to greatly aid the assignment. The three frequencies in the MSE sequence were chosen using a selection algorithm illustrated in Figure 3.4.

In step 1 the most intense line in the LFP spectrum is chosen as the first frequency (ν_1) pulse, and a FID is collected following a high-power, single-frequency selective pulse at frequency ν_1 , leading to the appearance of multiple transitions. In step 2 the spectrum from the previous step is compared to the LFP broadband spectrum, and a transition that is intense in the broadband spectrum but comparatively weak in the ν_1 spectrum is chosen as ν_2 . Having made this choice for ν_2 , a single-frequency spectrum at ν_2 is obtained as in step 1. In step 3 the same two criteria are used to choose an initial transition at frequency ν_3^i that appears is weak in ν_2 but is relatively intense in the broadband spectrum. This frequency ν_3^i is subsequently used as the basis for a single-frequency pulse spectrum at ν_3^i . Since selective excitation of transitions due to a single isomer is key to the proper choice of frequencies, the final value for the frequency ν_3 is made after viewing all three single-frequency excitation spectra. The final value for the frequency ν_3 is then chosen by identifying a transition that is the most intense line in the broadband spectrum modulated in all three single-frequency spectra.

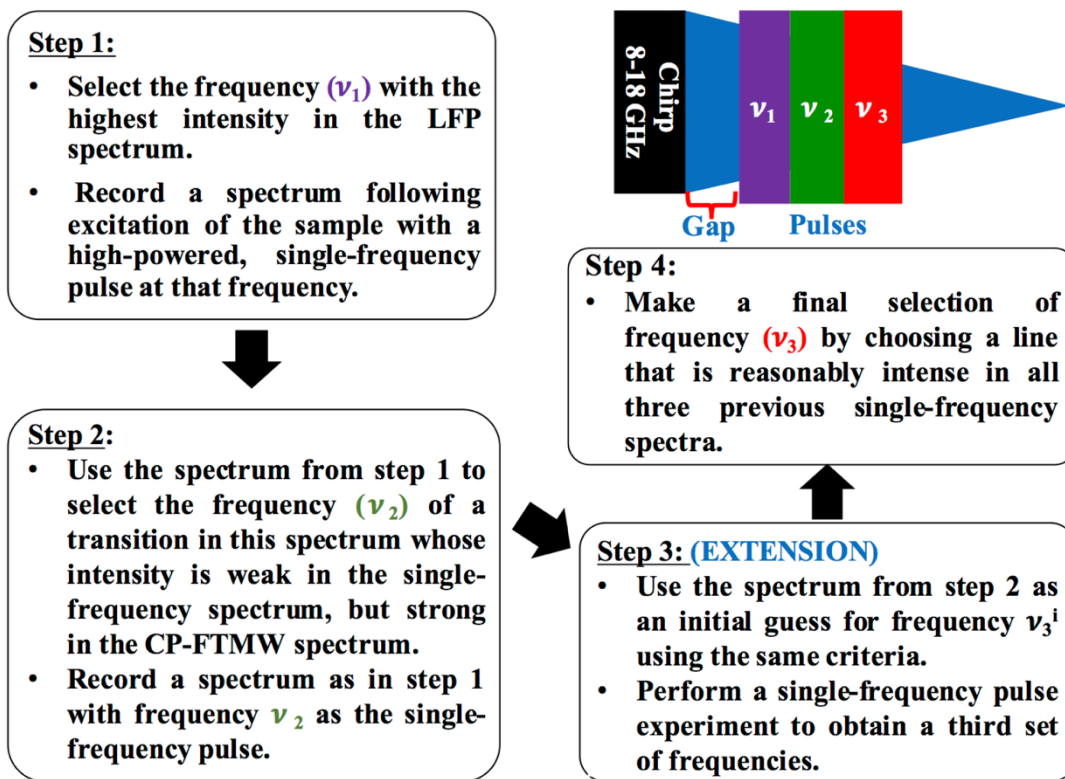


Figure 3.4: Line picking scheme to establish the multiple pulses sequence originally employed in the SFCB/MSE method.

This step-wise routine increases the probability of picking frequencies capable of modulating larger number of transitions in the final difference spectrum. It also provides a tier of validation that all the selected frequencies for the MSE scheme are exciting energy levels of the same species irrespective of their relative abundance. However, as more complex spectra were studied there was a need to modify the line picking scheme previously described³¹.

The new line picking scheme involves stepwise repetition of SFCB while incorporating an additional SFP in each step. A broadband sweep followed by a SFP (ν_1) targeting the most intense line in the LFP spectrum is probed, then a difference spectrum is acquired by subtracting the broadband spectrum with and without the SFP and the magnitude of this difference spectrum is plotted. Using the criteria previously described, we chose a second SFP (ν_2), which will modulate a complementary set of transitions. This, in turn, enables determination of ν_3 by looking at the magnitude of the difference spectrum. The process of adding SFPs can continue until a sufficient number of lines are modulated that will allow a preliminary fit to be obtained.

The main considerations to consider are:

1. It is important to make sure that the resonant transition is at least 10 MHz from another transition, that way the wings of the SFP won't have a significant overlap and reduce selectivity.
2. The frequencies of the SFP are typically chosen so these are not at the ends of the broadband frequency range being acquired, that way it is more likely that the directly connected transitions will be in the same frequency range, and therefore be detected.
3. If possible, we try to choose a transition that is weak in the difference spectrum but strong under LFP conditions. As a strong transition under LFP conditions, the transition will possess a big transition moment and therefore its choice as an SFP will modulate a large number of transitions. At the same time, the weak intensity in the difference spectrum increases the chances that the transition is not directly connected to the transition(s) previously used, and hence will produce complementary transitions in the final SFCB spectrum.

Having made this choice of frequencies for the SFPs, the single isomer microwave spectrum for the component in the mixture originally identified with the transition at frequency ν_1 is carried out using a broadband chirp followed by the set of sequential SFPs. In our experience, three SFPs is

typically sufficient for the purpose of obtaining a preliminary fit. Having obtained this difference spectrum, the same series of steps can be carried out beginning with the next-most intense transition not appearing in the initial SFCB/MSE spectrum. This process can continue until all transitions of interest have been accounted for.

3.3.2 Tailored sequential chirps (TSC)

As previously described, creating a strong coupling between the molecular transitions and the microwave electric field is vital for the SFCB method. However, in most CP-FTMW spectrometers the maximum attainable electric field is limited by the available amplification power of the TWTA. Therefore, for the same linear broadband sweep rate (α), a molecule with a small dipole moment may have no or few transitions that experience strong coupling with the electric field. To circumvent this experimental limitation, and still implement SFCB, a new Tailored Sequential Chirps (TSC) scheme was introduced. Employing TSC, the entire 8-18 GHz frequency range is swept in segments, with different tailored linear sweep rates chosen to vary the sweep rate in each segment. Region(s) of the spectrum in which a majority of the transitions are comparatively weak are candidates for interrogation at a slower sweep rate. In addition, more congested regions of the spectrum, where assignment is challenging, also benefit from a slower sweeping rate, this brings more transitions in that region into the strong coupling regime, so they gain intensity in the SFCB/MSE spectrum, which facilitates line assignment.

3.4 Results and Discussion

3.4.1 ¹³C-benzonitrile

While benzonitrile has no conformational or structural isomers, it does have in natural abundance the presence of a set of five isotopologues, differing from the all ¹²C parent in having a single ¹³C atom in any of the six positions (four inequivalent) in the aromatic ring, or a seventh in the nitrile group. These isotopologues have different rotational constants than the all ¹²C molecule, appearing just to the low-frequency side of those main transitions, as illustrated by the dotted lines and inset in Figure 3.5(a). Since the ¹³C isotope is present in 1% natural abundance compared to ¹²C, the transitions due to the isotopologues are often difficult to identify with certainty in the spectrum since they appear with such low intensity. Their identification is valuable

in that it pins down the position of the ^{13}C -substituted atoms in the molecular framework to high accuracy via Kraitchmann analysis.³²

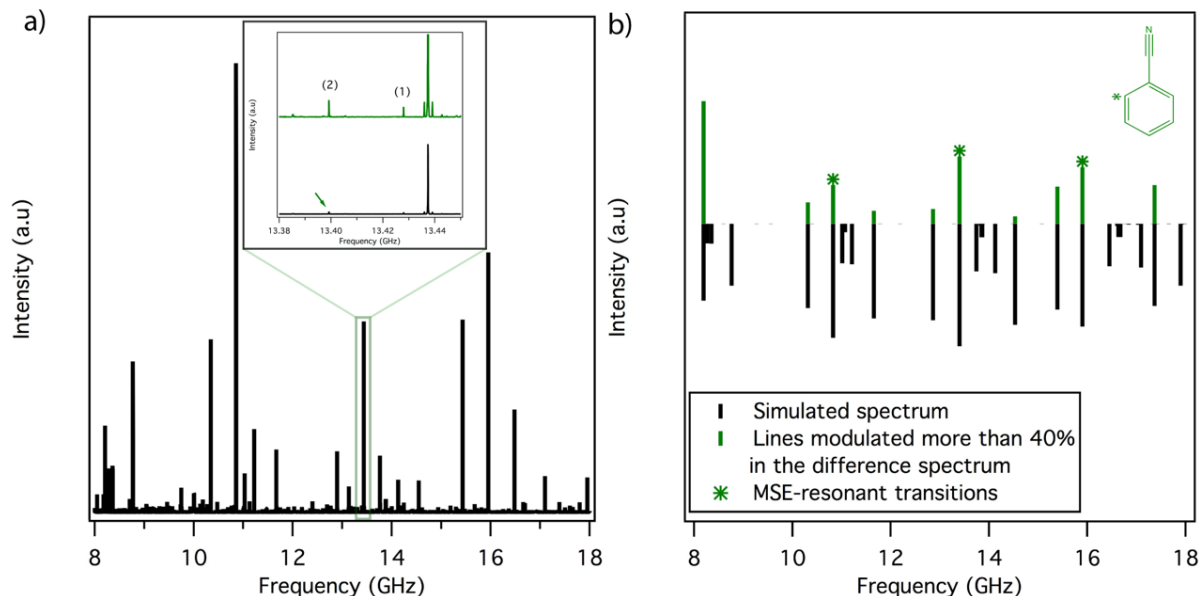


Figure 3.5: (a) The 8-18 GHz pure rotational spectrum of benzonitrile recorded with a 900 ns chirped pulse at 100% TWTA gain level. The inset is an expanded view (13.35-13.45 GHz) illustrating the relative line intensities of the ^{13}C and parent transitions. The arrow indicates the transition due to $[2\text{-}^{13}\text{C}]$ benzonitrile used for excitation via the resonant pulse. The green spectrum is scaled $7\times$ with labels identifying the isotopologues present in the expanded region, (1) $[1\text{-}^{13}\text{C}]$ benzonitrile and (2) $[2\text{-}^{13}\text{C}]$ benzonitrile. (b) Experimental lines modulated by more than 40% in the SFCB difference spectrum using the MSE sequence (green) with SFP frequencies marked with an asterisk, compared to the simulated stick spectra (black). The rotational constants used for the prediction in black were taken from Casado et al³³.

In benzonitrile, by symmetry, ^{13}C substitution at the 2- and 6- positions has equivalent rotational constants, as do the 3- and 5- substituted pair. We chose the $[2\text{-}^{13}\text{C}]$ isotopologue to illustrate the technique's sensitivity and capability to selectively identify low intensity transitions in a dense spectrum. The initial signal intensity of the transitions due to $[2\text{-}^{13}\text{C}]$ benzonitrile was $\sim 2\%$ of those due to the parent molecule. The SFCB scheme was implemented with MSE using three transitions due to the $[2\text{-}^{13}\text{C}]$ isotopologue chosen with the initial line picking scheme described in section 3.2.1. The resulting difference spectrum with the modulated ^{13}C lines is shown in Figure 3.5(b). As anticipated by symmetry, only a-type rotational transitions were observed for $[2\text{-}^{13}\text{C}]$ benzonitrile. The SFCB scan used a linear broadband chirp (8-18 GHz) of 1000 ns duration, with a 50 ns gap followed by three 150 ns selective pulses. The selected frequencies for the MSE

scheme were 15900.31, 13399.19, and 10828.94 MHz. A custom Matlab routine described in Appendix A.2, was used to extract from the experimental difference spectrum those transitions that were modulated more than 40% compared to the original 8-18 GHz sweep. The choice of a 40% threshold was made to avoid false positives in the difference spectrum due to intensity fluctuations from changing experimental conditions (e.g., those associated with gas flow fluctuations). The method selectively modulated 10 transitions due to the [2-¹³C] isotopologue, with no interference from transitions due to the all ¹²C isotopologue, despite the fact that these transitions are 50 times more intense. This demonstrates the SFCB's future potential to selectively modulate low abundance isotopes, or minor isomer/conformers concealed in a highly congested spectrum.

3.4.2 (E)- and (Z)-phenylvinyl nitrile

(E)- and (Z)-PVN are structural isomers of one another, and of the simplest polyaromatic nitrogen heterocycle quinoline. These molecules have extensive absorptions in the UV and have been postulated as intermediates along photochemical pathways that lead to nitrogen heteroaromatics.^{34, 35} Their isomer-specific vibronic spectroscopy has been studied previously by the Zwier group in some detail in the ultraviolet, motivated by their potential relevance to such heteroaromatic formation in Titan's atmosphere, one of the moons of Saturn.³⁵ The microwave spectra of these isomers have not been recorded previously; therefore it offered an opportunity to implement the method "blind". Furthermore, PVN served as a good model in that the two isomers have significantly different dipole moments that are distributed along more than one rotational axis.

Figure 3.6 compares the rotational spectra of (E)- and (Z)-PVN recorded in the frequency range of 8-18 GHz sweeping up (black) and down (red) in frequency, in both the strong and weak field coupling regimes. The spectrum recorded with the TWTA gain level at 10% is shown in Figure 3.6(a), demonstrating operation in the LFP regime, with relative intensities maintained irrespective of the sweep direction. However, at 100% TWTA gain level, Figure 3.6(b) clearly shows the line intensity patterns change with the direction of the linear frequency sweep; therefore, it is possible to access the strong field regime. In this case, the original line picking sequence, Figure 3.4, was implemented to determine the selective frequencies required for the MSE scheme. Step 1 was

initiated using the most intense line (10052.50 MHz) in the 8-18 GHz LFP spectrum (10%, TWTA). The selected MSE frequencies were: 10052.50, 16400.12, and 8203.63 MHz.

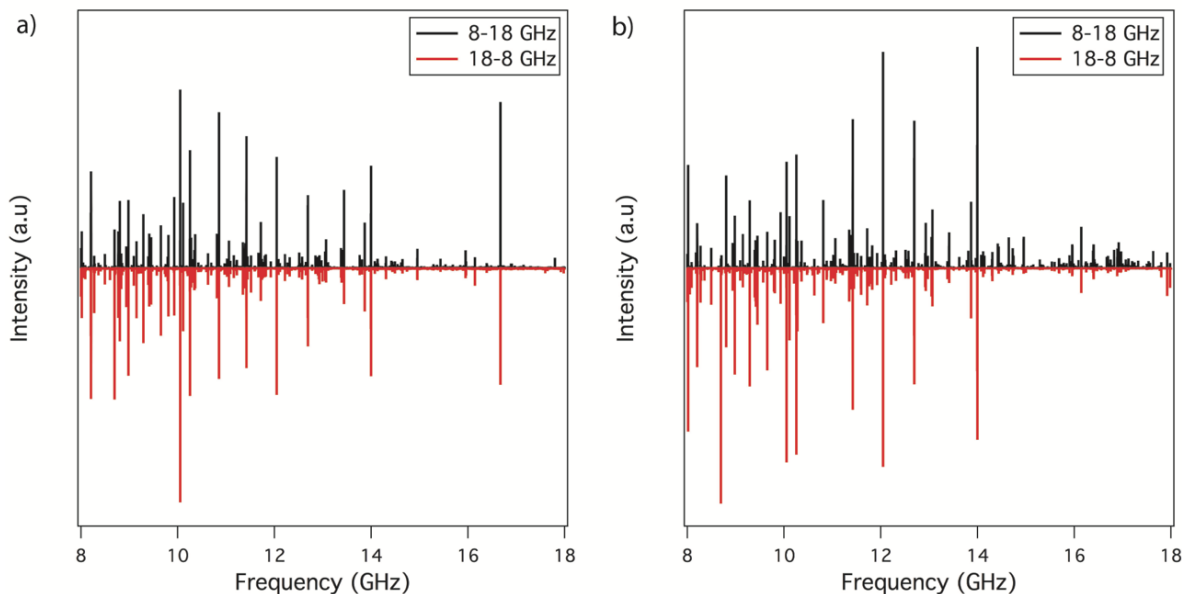


Figure 3.6: Broadband CP-FTMW spectra over the 8-18 GHz region of (E)- and (Z)-PVN, comparing the spectra with the frequency swept up from 8 to 18 GHz (black) and down from 18-8 GHz (red), with TWTA gain at (a) 10% and (b) 100% of full power. Experimental conditions: 1 μ s long chirped pulse, 250 000 averages, 16 μ s molecular FID collection.

Since the end result of the SFCB method is a difference spectrum, it is important to assess the level of stability in the CP-FTMW spectrum. In PVN, these intensity fluctuations ($\pm 1.5\%$) were assessed via single 8-18 GHz chirp scans immediately before and after the SFCB scans. Using the same custom Matlab routine previously mentioned, 93 transitions had their intensities modulated more than 10% compared to the 8-18 GHz sweep in the absence of the MSE, as shown in Figure 3.7(a). The transitions were compared to the predicted spectra and the modulated transitions were determined to belong exclusively to the (Z)-PVN isomer.

The rotational transitions obtained through the initial SFCB/MSE run were compared with the 8-18 GHz LFP rotational spectrum, and the method was implemented a second time on the remaining unassigned transitions, using the same pulse durations and time delay conditions. The second set of selective frequencies was 10624.97 MHz, the strongest line in the LFP spectrum not previously modulated, 16697.08 MHz and 8016.88 MHz. The difference spectrum was plotted, and a set of 32 transitions were modulated more than 10%. These transitions matched the (E)

isomer predictions (Figure 3.7(b)). The set of transitions obtained through the SFCB/MSE difference spectra were used for the initial rigid rotor fits of both isomers. The clear differentiation between the two frequency sets reduced the spectral fitting time. The method's isomer specificity enabled the assignment of transitions and provided an extra level of confidence when assigning transitions from higher J-levels with low intensity.

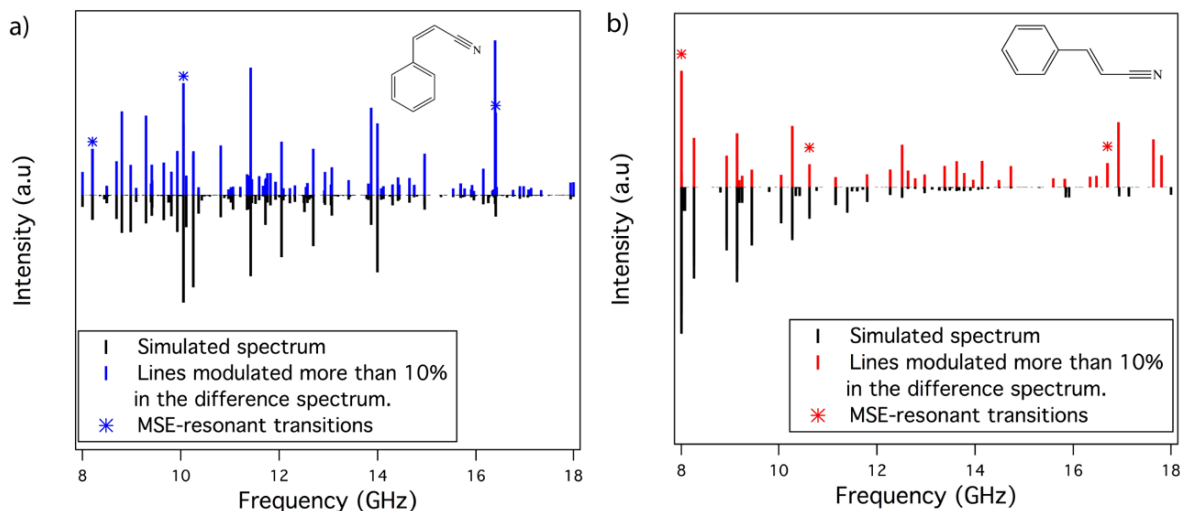


Figure 3.7: Experimental lines modulated more than 10% in the SFCB difference spectrum compared to the simulated stick spectra for (a) (Z)-PVN and (b) (E)-PVN. Experimental conditions: 1 μ s 8-18 GHz chirp, 50 ns gap, and 3 \times 100 ns SFPs on the frequencies labeled by asterisks and 100% TWTA gain level.

The ^{14}N nuclei possess a quadrupole moment arising from its nuclear spin \mathbf{I} being greater than $\frac{1}{2}(\mathbf{I}=1)$. This causes splitting of the rotational transitions. The spectral transitions were fit to Watson's semi-rigid Hamiltonian (A-reduction, I'-representation) while accounting for hyperfine interaction using the CALPGM³⁶ program suite, with the PIFORM program used to format outputs from the spectral fitting. The experimental rotational constants, centrifugal distortion constants, and nuclear quadrupole coupling constants are listed in Table 3.1, where they are compared to the predictions of calculations at the MP2/aug-cc-pVTZ level of theory. The calculated values are in good agreement with the constants obtained experimentally. The fit for both isomers is reported with one sigma uncertainty for the last digit and overlaid on the 8-18 GHz LFP spectrum in Figure 3.8. Remaining features in the spectrum were identified as arising from incomplete subtraction of spurious lines arising from electronic noise and reflections.

Table 3.1: Experimental best-fit and theoretical calculated spectroscopic parameters for E/Z-PVN.

	Z-PVN		E-PVN	
	Experimental	Theoretical	Experimental	Theoretical
A (MHz)	3122.8826(13) ^a	3124.3392	5102.4108(20)	5125.1298
B (MHz)	873.25109(62)	880.2379	607.51435(69)	608.1963
C (MHz)	683.73089(43)	687.7546	543.21036(62)	543.6783
Δ_J (kHz)	0.0790(33)	-	0.0118(17)	-
Δ_{JK} (kHz)	-0.288(18)	-	-	-
Δ_K (kHz)	0.738(88)	-	-	-
δ_J (kHz)	0.0185(14)	-	-	-
δ_K (kHz)	0.257(80)	-	-	-
χ_{aa} (MHz)	1.147(30)	1.027	-3.839(123)	-3.48
$\chi_{bb}-\chi_{cc}$ (MHz)	-5.291(12)	-5.008	-0.192(4)	-0.352
μ_a (D)	-	2.68	-	-5.01
μ_b (D)	-	2.83	-	0.63
μ_c (D)	-	0.00	-	0.00
Δ (uÅ ²) ^b	-1.415	-1.070	-0.571	0.000
σ (kHz) ^c	35	-	36	-
N ^d	321	-	204	-

^a Standard error in parentheses in units of the last digit. ^b Zero-point inertial defect. ^c One sigma standard deviation on the fit. ^d Number of fitted transitions.

Previous LIF and UV-UV hole burning studies³⁴ of the ground S_0 and S_1 excited states of (E)- and (Z)-PVN showed both isomers to be planar in the S_0 state, based on selection rules followed by the vibronic transitions involving out-of-plane vibrations. The inertial defect ($\Delta = I_0^c - I_0^b - I_0^a$) is a spectroscopic test for planarity,³⁷ and was calculated for both isomers. The experimental inertial defects (Δ) for both isomers are negative but small. Similar molecules that are planar on a vibrationally averaged basis also show non-negligible negative inertial defects in the ground vibrational state, due to the presence of a low-frequency out-of-plane vibration.³⁸ In

(E)- and (Z)-PVN, the lowest frequency vibrational mode involves an out-of-plane torsion of the vinylcyanide substituent relative to the ring, with frequencies of 18.5 and 48 cm^{-1} , respectively. Thus, the small negative inertial defect is consistent with both isomers of PVN being planar but floppy.

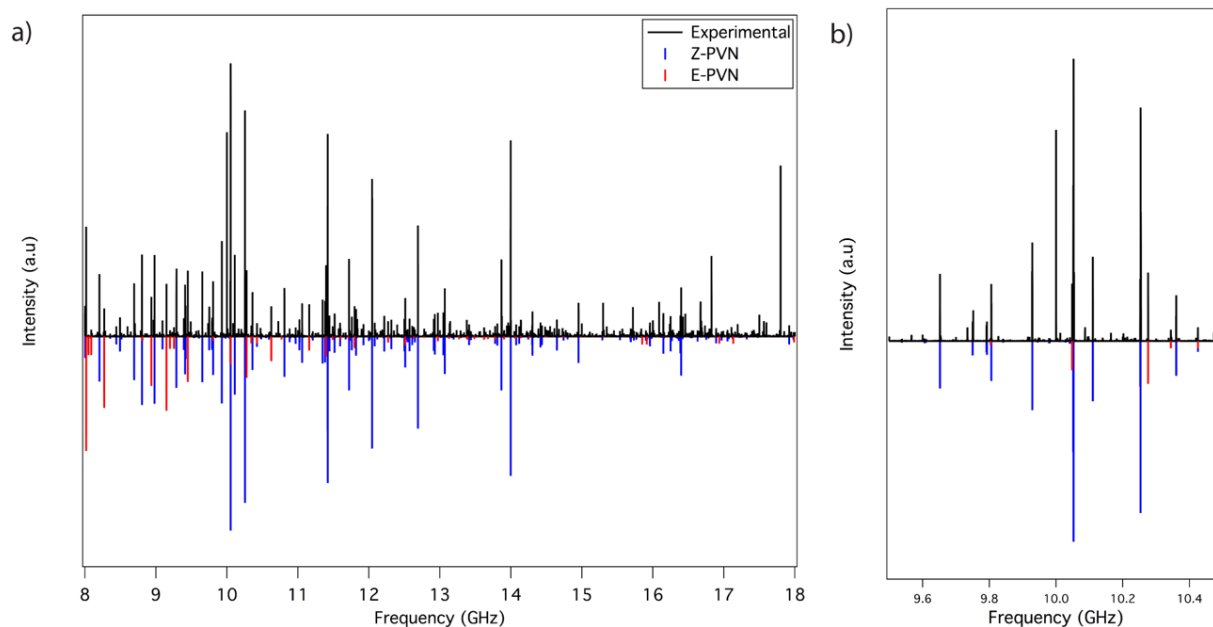


Figure 3.8: (a) The experimental 8-18 GHz broadband microwave spectrum of a mixture of (E)- and (Z)-PVN (black), and the final fit for both structural isomers overlaid on top of one another. (b) Expanded view of 9.5-10.5 GHz with the assignments overlaid.

3.4.3 Methyl butyrate (MB)

Methyl esters of fatty acids are important components of biologically-derived diesel fuel (“biodiesel”), produced by reacting vegetable oils or animal fats with an alcohol.³⁹ By comparison with petroleum diesel, which contains straight-chain alkanes, the alkyl chains in the fatty acids serving as a source of biodiesel are a mixture of straight-chain, branched-chain, and with partial unsaturation.⁴⁰ Not surprisingly, the combustion chemistry of fatty acid methyl esters will thus have reactions characteristic of the long alkyl or alkenyl “tail” and methyl ester “head” groups. While the alkyl chains are common to petroleum diesel, the presence of the ester functional group complicates the combustion chemistry of biodiesel. Methyl butyrate ($\text{CH}_3\text{-CH}_2\text{-CH}_2\text{-C(=O)-O-CH}_3$), combines the methyl ester with an alkyl chain just long enough to capture some of the key

features anticipated for the combustion chemistry of longer-chain methyl esters. As a result, MB serves in combustion studies as a model system.^{41, 42}

MB has an alkyl chain sufficiently long to support conformational isomers. As a result, the inherent conformational preferences of gas phase methyl butyrate are important to understand. Since the rotations of the two methyl groups in MB do not create new conformations, the conformational landscape is completely defined by three dihedral angles $\varphi_1 = \angle(C_1, C_2, C_3, C_4)$, $\varphi_2 = \angle(C_2, C_3, C_4, O_6)$, and $\varphi_3 = \angle(C_3, C_4, O_6, C_7)$, corresponding to the rotations about the C₂-C₃, C₃-C₄, and C₄-O₆ bonds, Figure 3.9 shows the atom numbering. The rotation about C₄-O₆ bond by varying the dihedral angle φ_3 results in *trans* ($\varphi_3=180^\circ$) and *cis* ester ($\varphi_3=0^\circ$) conformations. It is known that only *trans* esters can be observed in a supersonic expansion⁴³⁻⁴⁵, where the rotational temperature is very low, approximately 2 K, this is because *cis* esters are much higher in energy (often more than 25 kJ mol⁻¹). Hence, we only took the *trans* conformers into consideration.

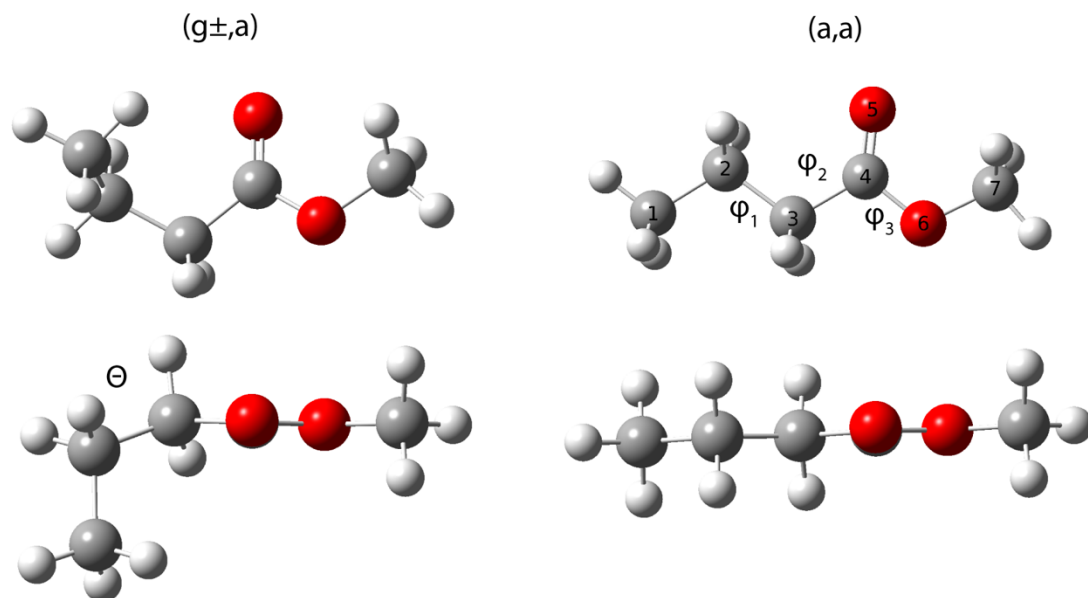


Figure 3.9: Optimized geometries of the assigned conformers of MB calculated at B2PLYP-D3BJ/aug-cc-pVTZ level of theory. Upper trace: front view, lower trace: view along the C₄-O₅ bond. A tilt angle of the ethyl group ($\Theta=180^\circ-|\varphi_2|=15^\circ$), relative to the C₄, O₅, O₆, C₇ plane, was calculated for the more stable conformer (*g±*, *a*) (lower left).

To locate the conformational minima and to better understand the potential energy landscape, a relaxed two-dimensional potential energy surface (2D-PES) was calculated. The angles (φ_1 , φ_2) were varied over a grid of points separated by 15° while optimizing all other coordinates. DFT calculations were employed with B2PLYP-D3BJ/aug-cc-pVTZ level of theory. The result is shown in Figure 3.10. Four conformers of MB were identified on the PES, and the structures were also optimized at the MP2/6-311++G(d,p) level of theory. The optimized geometries are illustrated in Figure 3.11 in order of their energies relative to the most stable conformer. Harmonic frequency calculations at both levels of theory confirm that these structures are true minima. The conformers are named according to the conformational arrangement of φ_1 and φ_2 dihedral angles. Using **a** for antiperiplanar conformations (torsional angles between -150° and $+150^\circ$), **g \pm** is used for *gauche* conformations ($\pm 30^\circ$ to $\pm 90^\circ$).

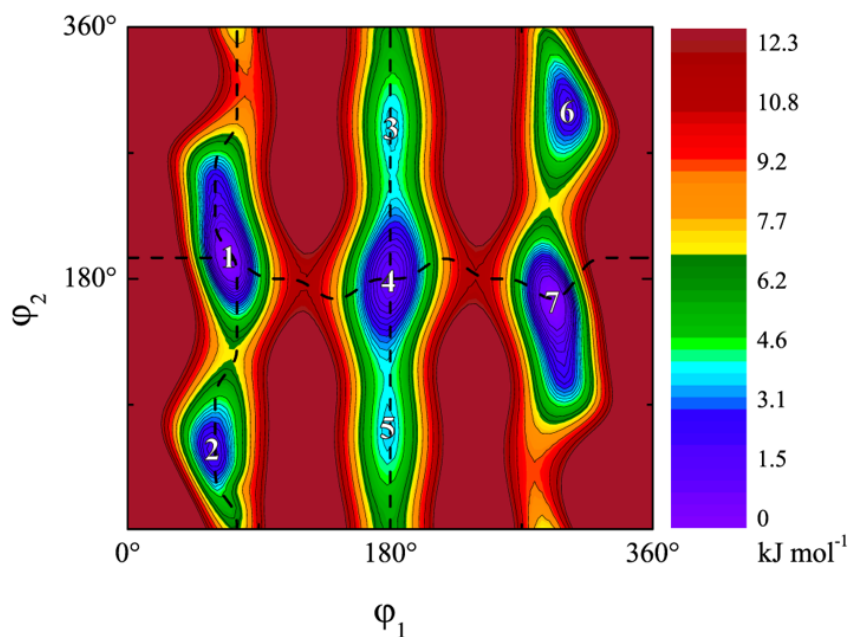


Figure 3.10: Potential energy of MB for conformational analysis. Here four stable conformers were found: 1=(g+,a), 2=(g+,g+), 3=(a,g-), 4=(a,a), 5=(a,g+), 6=(g-,g-),7=(g-,a). Conformer 1 and 7; 2 and 6; and 3 and 5 are enantiomers. This surface was obtained by rotating the dihedral angles $\varphi_1=\angle(C_1,C_2,C_3,C_4)$ (rotation about C_2-C_3 bond) and $\varphi_2=\angle(C_2,C_3,C_4,O_6)$ (rotation about the C_3-C_4 bond). Calculations were performed at the B2PLYP-D3BJ/aug-cc-pVTZ level of theory. The absolute energy of the lowest conformation is $E=346.95152$ Hartree. Dash lines indicate the minimum energy pathway shown in Figure 3.14.

Only conformer **(a, a)** located at $(\varphi_1, \varphi_2) = (180.0^\circ, 180.0^\circ)$ has C_s symmetry; all the other conformers **(g \pm , a)**, **(g \pm , g \pm)**, and **(a, g \pm)**, possess C_1 symmetry and exist in what are essentially enantiomeric pairs by virtue of the direction of curvature of the alkyl chain, though there are no chiral centers. The enantiomers have the same electronic energy and rotational constants, and therefore cannot be distinguished under our measurement conditions. The global minimum, **(g \pm , a)**, is calculated to have $(\varphi_1, \varphi_2) = (\mp 68.5^\circ, \pm 158.7^\circ)$ and has the propyl methyl group tilted out of the molecular frame spanned by the C₄, O₅, O₆, C₇ atoms that make up the methyl ester. The two other conformers, **(g \pm , g \pm)**, and **(a, g \pm)**, both have $\varphi_2 \approx \pm 60^\circ$.

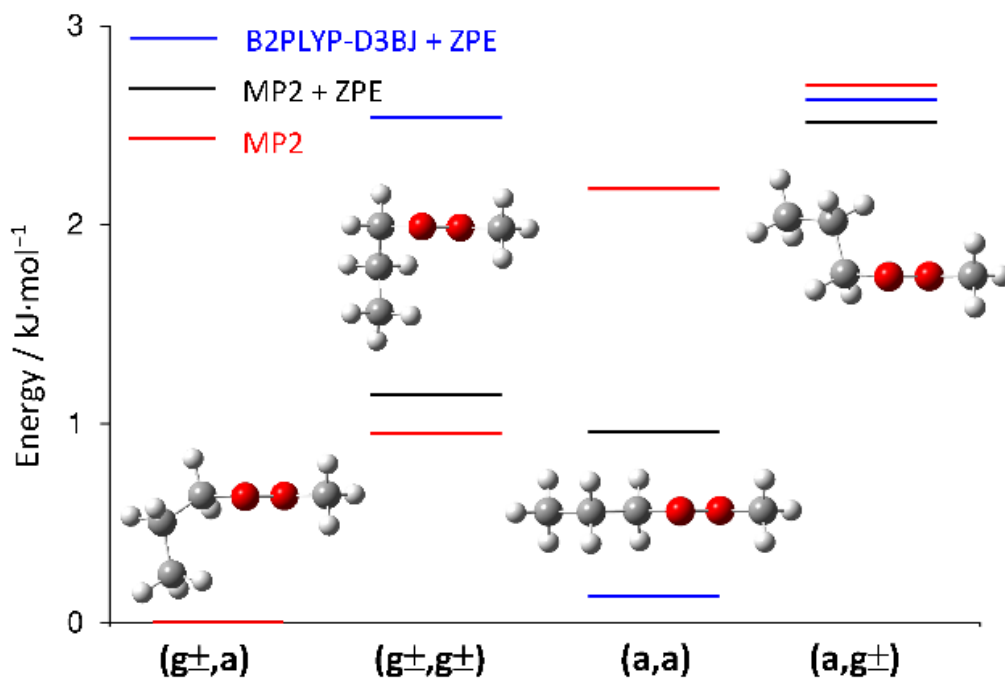


Figure 3.11: The trans conformers of methyl butyrate in order of their energies relative to that of the most stable conformer (g \pm ,a) calculated at the MP2/6-311++G(d,p) level with and without zero point energy correction as well as at the B2PLYP-D3BJ/aug-cc-pVTZ level (for values see Table 3.2).

The four conformers previously mentioned have a total dipole moment less than 1.7 D; therefore, in order to apply the SFCB method it was necessary to incorporate TSC to deconvolute the spectrum. The first set of TSC was designed focusing on the congested Q-branch region in the 13-15 GHz region, which contained many weak transitions (Figure 3.12(a)). To bring this region into the RAP regime, segments of 8-13, 13-15, and 15-18 GHz were chosen, with durations of 350,

1000, and 140 ns respectively. This set of conditions resulted in relative sweep rates of 7:1:10 in the three frequency regions. Strong-field conditions were achieved, this is shown in Figure 3.12(b), where the spectrum chirping up (black) is compared with that chirping down (red), showing clear intensity changes. The TSC set covered the entire 8-18 GHz region, promoting strong coupling of the maximum number of rotational transitions with the polarizing electric field. The selective frequencies, for the MSE scheme, were determined using the original line picking scheme; and it was initiated with the most intense line, at 10059.87 MHz, the following steps of the scheme output the set of frequencies 10059.87, 12682.25, and 15264.19 MHz, denoted with asterisks in the spectrum of Figure 3.13(a).

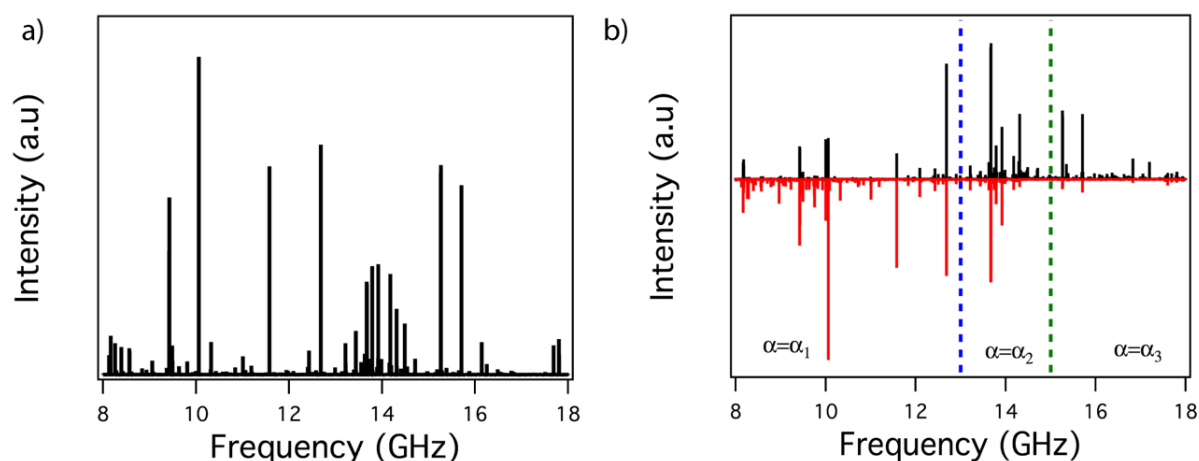


Figure 3.12: 8-18 GHz CP-FTMW rotational spectrum of MB. (a) 10% TWTA gain level and 1.5X10⁶ acquisitions. (b) 100% TWTA gain and 75000 acquisitions using TSC with different sweep rates covering 8-18 GHz sweeping up (black) or down (red) in frequency; where $\alpha_1=14.3$ GHz/ μ s for the 8.0-13.0 GHz region, $\alpha_2=2.0$ GHz/ μ s for the 13.0-15.0 GHz region, and $\alpha_3=20.0$ GHz/ μ s for the 15.0-18.0 GHz region.

The difference spectrum obtained from the SFCB(TSC)/MSE method with 100% TWTA gain (Figure 3.13(a)) employed a modulation level above 20% as threshold, producing a set of 47 lines. These transitions were assigned to the lowest energy conformer, ($\mathbf{g}\pm, \mathbf{a}$), which has a total dipole moment of 1.474 D and a mixed set of *a*- and *b*-type transitions. A preliminary assignment was done with the *SPFIT/SPCAT* suite of programs³⁶ using a Watson-A reduced Hamiltonian. And a refinement of the fit was done through the inclusion of centrifugal distortion constants. However, for this molecule all rotational lines in the spectrum are split into two torsional components, called

A and E species, due to the internal rotation of the methoxy methyl group. Therefore, the Hamiltonian can be written as $H = H_{rot} + H_{cd} + H_i$, where H_{rot} refers to the rigid rotor Hamiltonian, H_{cd} is the Hamiltonian associated with the centrifugal part, and H_i is the internal rotation of the methyl top.⁴⁶

Table 3.2: The rotational constants A, B, C (in GHz), dipole moment components μ_a , μ_b , μ_c (in Debye), and relative energies $E_{rel.}$ (in $\text{kJ}\cdot\text{mol}^{-1}$) of the indicated conformers of MB calculated at the MP2/6-311++G(d,p) and B2PLYP-D3BJ/aug-cc-PVTZ levels of theory. The dipole moment components are with respect to the principal axes of inertia. All energies are electronic energies including vibrational zero-point correction and are relative to the lowest energetic conformer ($g\pm, a$) with its absolute energy of $E + ZPE = -345.988667$ and -346.734269 Hartrees at the MP2 and B2PLYP-D3BJ levels of theory, respectively.

Conf.	MP2/6-311++G(d,p)				B2PLYP-D3BJ/aug-cc-PVTZ			
	($g\pm, a$)	(a, a)	($g\pm, g\pm$)	($a, g\pm$)	($g\pm, a$)	(a, a)	($g\pm, g\pm$)	($a, g\pm$)
<i>A</i>	5.521	8.339	4.251	6.134	5.935	8.388	4.323	6.307
<i>B</i>	1.452	1.198	1.703	1.306	1.426	1.198	1.667	1.291
<i>C</i>	1.414	1.076	1.572	1.180	1.351	1.076	1.551	1.174
μ_a	0.239	-0.067	-0.606	0.646	-0.386	0.103	-0.503	-0.511
μ_b	1.621	-1.756	-1.792	-1.963	1.554	-1.708	-1.790	-1.904
μ_c	-0.593	-0.001	-1.073	-0.305	0.557	0.000	-0.950	-0.245
$E_{rel.}$	0	0.96	1.15	2.51	0	0.13	2.54	2.63

The rotational energy levels associated with the A and E internal rotor levels have different nuclear spin symmetry, and therefore do not interconvert during the collisional cooling in the supersonic expansion. In principle, the SFCB method could be used to selectively modulate transitions due to either A or E methyl rotor levels, aiding in their assignment. However, due to their close proximity (typical splittings <2 MHz), selective excitation of only A or E levels was not possible. Nonetheless, characteristic patterns of transitions appeared close to those of the A levels, suggesting themselves as the E level components of the same rotational transitions. The program *XIAM*⁴⁷ was then used to predict the methyl rotor splittings of the E internal rotor level due to internal rotation-overall rotation coupling, using the rotational constants and centrifugal

distortion constants of the A levels as starting parameters. The barrier to hindered rotation of the methoxy methyl group was set to 420 cm^{-1} , which is approximately the barrier found for methyl acetate⁴⁸ and methyl propionate⁴⁹. The angles between the internal rotor axis and the principal axes were set based on the calculated geometry of conformer (**g±, a**). Finally, it was possible to assign 35 A and 32 E lines, with a standard deviation of 29 kHz, in the 8-18 GHz broadband spectrum. Using the prediction from this fit, high resolution measurements were performed in the frequency range 2-26.5 GHz. These measurements were recorded in collaboration with the Lam Nguyen using a molecular jet FTMW spectrometer located in LISA, at Universite Paris-Est Creteil, Universite Paris, France.⁵⁰ The high-resolution measurements led to an expanded assignment of 53 A and 60 E lines and reduced the standard deviation of the fits to 4 kHz (Table 3.3). The rotational constants calculated are in close agreement with the experimental ones, with deviations of less than 1% typical.

The second set of TSC focused on the remaining intense unassigned lines, with chosen frequency bandwidths of 8-9.5, 9.5-16.5, and 16.5-18 GHz with a duration of 100, 1300, and 100 ns, respectively. The frequencies used in the MSE sequence were 9427.38, 11578.06, and 13671.63 MHz. For this TSC set the SFCB(TSC)/MSE method was implemented under the same experimental conditions, and the difference spectrum shown in Figure 3.13(b) was obtained. The Matlab routine with 20% modulation threshold outputs 18 lines. The (**g±, a**) and (**a, a**) conformers are very close in energy; therefore, the next conformer we considered was (**a, a**). Noticing that the experimental conformer-specific transitions from SFCB(TSC)/MSE matched the pattern of the calculated 8-18 GHz microwave spectrum for this conformer, a preliminary assignment of the A species as a rigid rotor was made. In the broadband spectrum, the splittings due to internal rotation of the methoxy methyl group were resolved, with splittings of approximately 2 MHz in the low-frequency region. The program *XIAM* was used to assign the transitions associated with the E internal rotor levels in the same manner as done for conformer (**g±, a**). In the broadband scan a total of 32 A and E *a*-type R-branch transitions with $K_a=0,1$ were assigned and fitted to a standard deviation of 41 kHz. Additional high-resolution scans in the region 20-23 GHz were carried out that detected transitions that could be assigned as *b*-type Q-branch transitions with $K_a=2\leftarrow 1$. In total 42 A transitions and 43 E transitions were assigned involving transitions up to $J=15$, with a standard deviation of 7.8 kHz on the fit (Table 3.3).

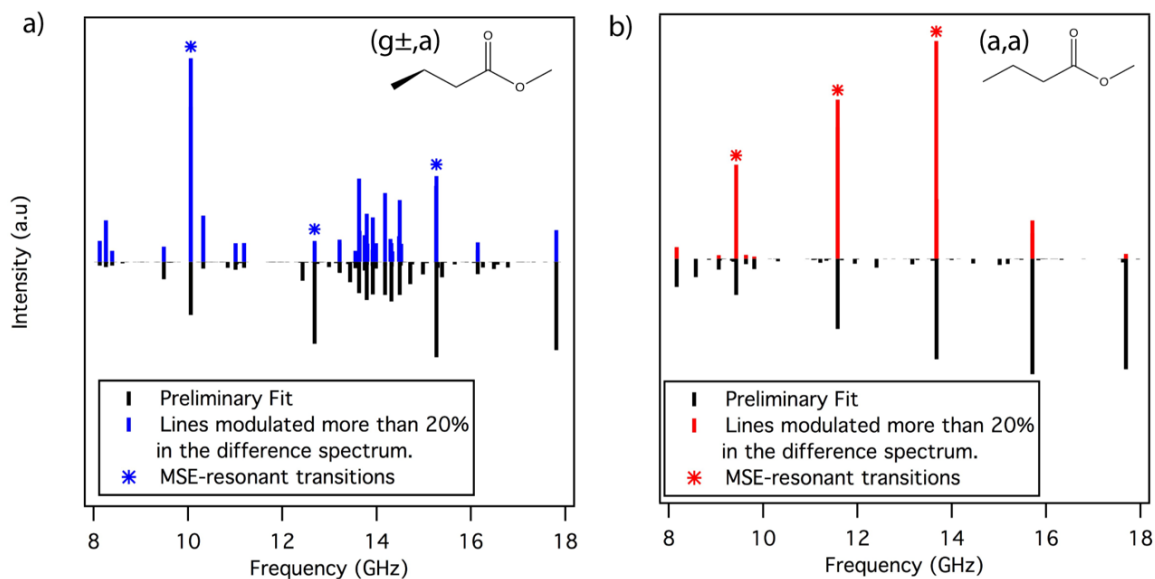


Figure 3.13: Experimental lines modulated more than 20% in the SFCB(TSC)/MSE difference spectrum compared with the simulated stick spectra for the two most abundant conformers of MB.

Some c -type transitions involving E internal rotor levels were observable, it is known that for the E species, such forbidden transitions can be observed, as previously found in e.g. ethyl acetate⁴³, vinyl acetate⁵¹, and butadienyl acetate⁴⁴. In the case of rigid rotors and the A species of molecules with internal rotation, the K_a , K_c pseudo quantum numbers can be used to derive the symmetry and thereby the selection rules. This is no longer true for the E species, here these quantum numbers just give the order of the energy levels and do not contain any symmetry information. Consequently, c -type transitions may be found even if no c dipole moment component is present.

The rotational constants obtained at MP2/6-311++G(d,p) level of theory are in poor agreement with experiment, with a deviation between experiment and theory of almost 9% in the A rotational constant. This is a likely consequence of the relatively flat-bottomed potential along the φ_2 dihedral angle, which makes the optimized structure sensitive to the shape of this well and thus the level of theory. By carrying out geometry optimizations using a range of computational methods and basis sets, it was noticed that the A rotational constant of conformer $(g\pm, a)$ varies widely with level of theory, while it stays nearly constant for the (a, a) conformer. More specifically the dihedral angle φ_1 varies by no more than 1° (between 69° and 70°), the φ_2 dihedral

angle varies from 146° to 169° . Furthermore, initially, it was anticipated that the tilt angle $\Theta=180^\circ - |\varphi_2|$ of the C(2) carbon atom of the ethyl group relative to the C₃-C₄-O₆ plane would be near zero degrees, so that only the propyl methyl group would be out of plane. This type of symmetry breaking has frequently occurred in quantum chemical calculations on other esters previously studied, for example in ethyl pivalate⁵² and ethyl valerate⁵³; we noticed that the largest deviations between calculated and experimental values are observed when diffuse functions are included in the MP2 calculations. The most likely cause for this is the large intramolecular basis-set superposition error that plagues MP2 calculations without sufficient diffuse basis functions^{54, 55}. For the basis set sizes explored the addition of the diffuse functions decreases the agreement with experiment, but their removal reaches the correct answer for the wrong reason.

MB has an alkyl chain of sufficient length to produce a total of seven low-lying conformational minima: the single **(a, a)** minimum, and three enantiomeric pairs **(g \pm , a)**, **(g \pm , g \pm)**, and **(a, g \pm)**. In the pure alkyl chain analog pentane, a similar set of two torsional coordinates would give rise to a total of nine minima, with each torsion occurring in a threefold potential. In MB, the two “missing” minima are in the upper left and lower right corners of the 2D surface in Figure 3.10, associated with the **(g \pm , g \mp)** pair. Figure 3.14 presents three minimum-energy pathways on the 2D surface. Figure 3.14(a) shows a cut along φ_1 through the **(a, a)** and **(g \pm , a)** minima. These minima are nearly isoenergetic and contain all the observed population in this corridor at the nominally “*anti*” φ_2 configuration, which places the first two carbon atoms of the propyl chain near the plane of the ester group. The barriers to hindered rotation of the alkyl chain about φ_1 are more than 10 kJ mol⁻¹ (900 cm⁻¹). The other two minimum energy pathways involve motion primarily along the φ_2 coordinate. The 2D surface is much softer along φ_2 than φ_1 , creating long troughs along this coordinate. Figure 3.14(b) is the minimum energy pathway nominally associated with the *gauche* propyl chain conformations. A slice of the 2D surface along φ_2 with the propyl chain in the fully-extended “*anti*” configuration ($\varphi_1=180^\circ$) is shown in Figure 3.14(c). Its shape is very much like that involving the ethyl group in methyl propionate⁴⁹, with a single deep **(a, a)** minimum and two secondary minima near the perpendicular configuration, whose exact location and barrier height are sensitive to the level of theory employed.

Table 3.3: Molecular parameters of conformers ($\mathbf{g}\pm,\mathbf{a}$) and (\mathbf{a},\mathbf{a}) of methyl butyrate obtained from the best fits to the frequencies.

	($\mathbf{g}\pm,\mathbf{a}$)	(\mathbf{a},\mathbf{a})
A (MHz) ^a	6.05932256(59)	8.3497791(19)
B (MHz)	1.42134885(29)	1.19776069(25)
C (MHz)	1.33334892(33)	1.07654609(23)
Δ_I (kHz)	0.6018(37)	0.0495(12)
Δ_{JK} (kHz)	-5.930(15)	0.428(18)
Δ_K (kHz)	51.785(52)	9.01(36)
δ_j (kHz)	-0.13468(33)	0.00480(15)
δ_k (kHz)	12.289(57)	-
F_0 (GHz) ^b	158	158
I_α ($\text{u}\text{\AA}^2$) ^c	3.199	3.199
V_3 (cm^{-1})	419.447(59)	420.184(71)
s^d	34.28326	33.74637
$\angle(i,a)$ ($^\circ$)	30.528(54)	19.848(88)
$\angle(i,b)$ ($^\circ$)	59.521(98)	70.153(88)
$\angle(i,c)$ ($^\circ$)	88.4(20)	90.0 ^e
σ (kHz) ^f	4.0	8.5
N_A/N_E ^g	54/59	42/44

^a All parameters refer to the principal axis system. Watson's A reduction in the I representation was used. ^b Fixed to a reasonable value often obtained for a methyl group. ^c Moment of inertia of the internal rotor, derived from its rotational constant F_0 . ^d Reduced barrier $s=4V_3/9F$. ^e Fixed due to symmetry. ^f Standard deviation of the fit. ^g Number of the A (N_A) and E (N_E) species lines.

The ($\mathbf{g}\pm, \mathbf{a}$) minima has the $\text{C}_2\text{-C}_3$ bond nearly in-plane (out-of-plane tilt angle of about 15°) on the oxygen side of the C=O group, with the terminal methyl group of the alkyl chain nearly

perpendicular to that plane. It is noteworthy that this configuration places one of the CH bonds of C(2) so that it interacts with the carbonyl oxygen, forming a weak $\text{CH}\cdots\text{O}=\text{C}$ hydrogen bond. In so doing, it forms a five-membered H-bonded ring, much as occurs in peptides between adjacent NH and C=O groups in β -sheet secondary structure where it takes on a configuration closer to that of a free alkyl chain⁵⁶.

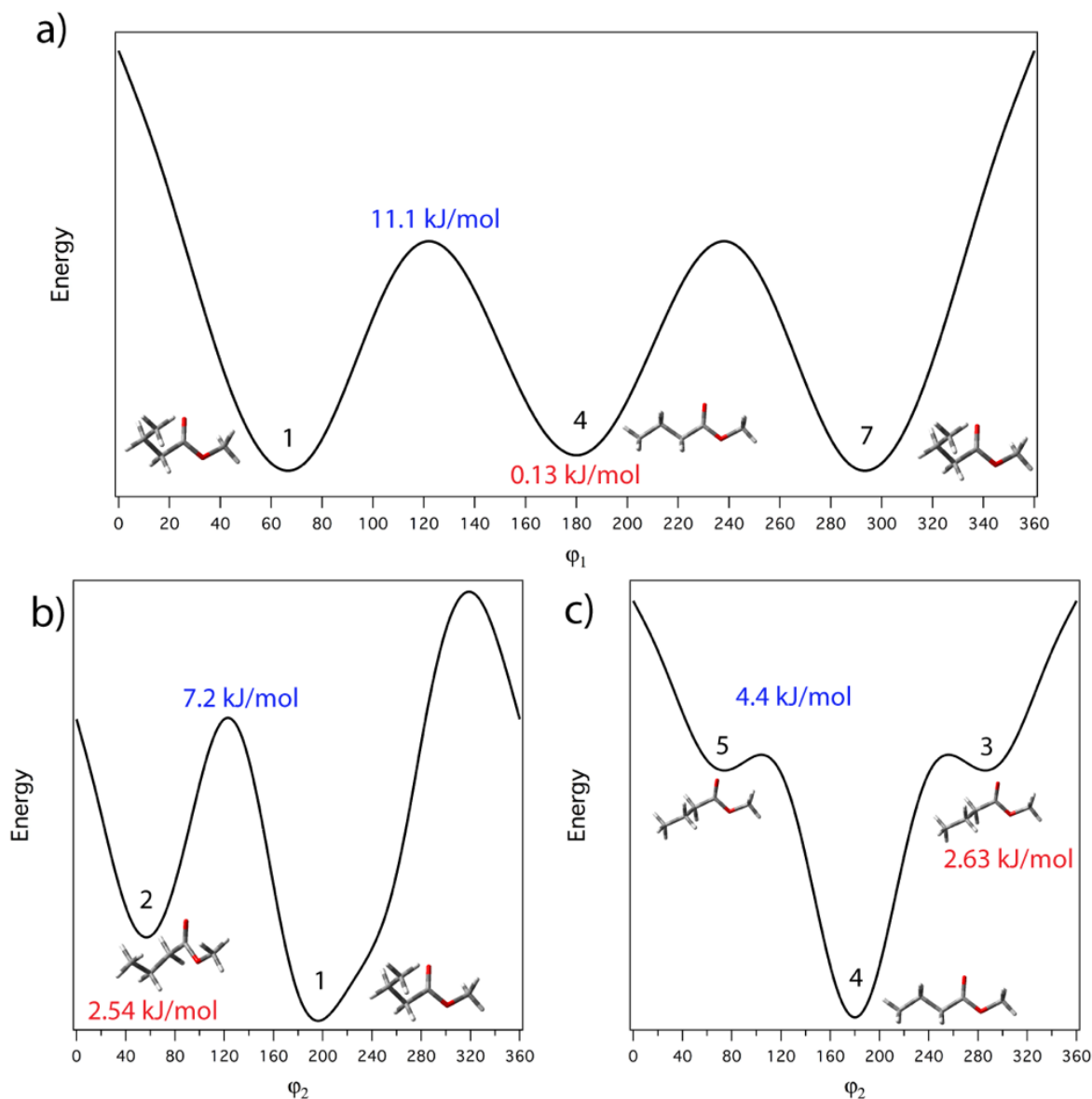


Figure 3.14: (a) A cut along ϕ_1 through the (a,a) and (g^\pm ,a) minima. (b) A cut along ϕ_2 through the (g^\pm , g^\pm) and (g^\pm ,a) minima. (c) A cut along ϕ_2 through the (a, g^\pm) and (a,a) minima. The barrier heights are indicated in blue and in red the relative energies. The numbers in black indicate which minima it is referring according to Figure 3.10.

The shape of the PES presented in Figure 3.10 and the potential energy curves Figure 3.14 also help explain why only two of the four stable conformational minima are observed downstream in the expansion. The rotational temperature was determined with a Boltzmann plot by using the relationship between the integrated line intensities (W) and corresponding lower state energy (E_i) (Figure 3.15).⁵⁷ Interestingly, best-fits to the rotational temperatures for the two conformers (0.86 ± 0.19 K vs. 0.35 ± 0.08 K), indicating some conformer specificity to the collisional cooling, with conformer (**a, a**) being more efficiently cooled than (**g \pm , a**).

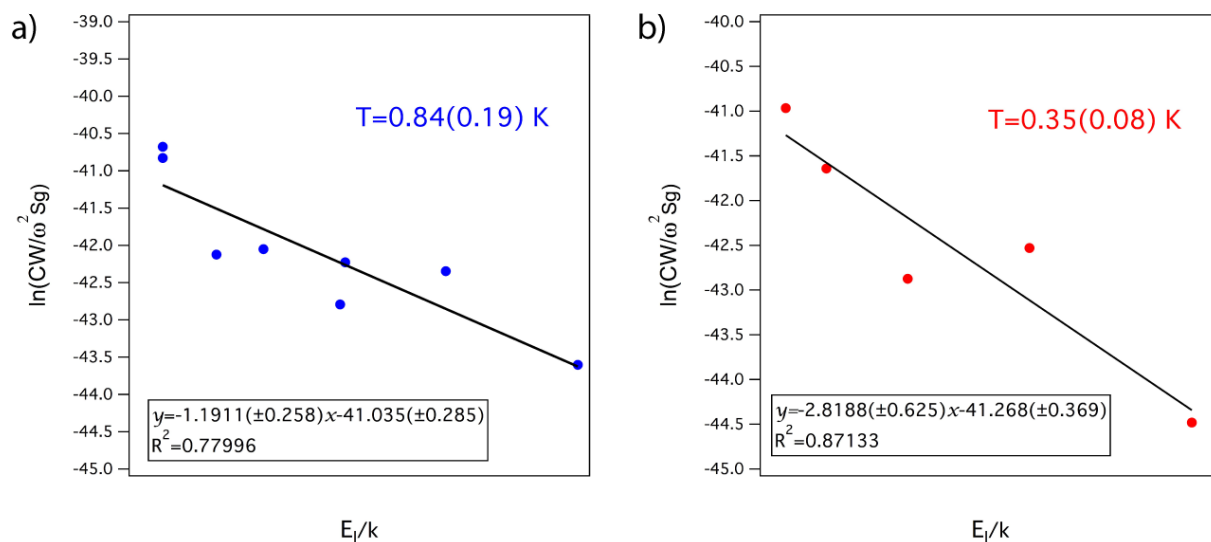


Figure 3.15: (a) The rotational temperature for (**g \pm , a**) is estimated to be about $0.84 (\pm 0.19)$ K. (b) The rotational temperature for (**a, a**) is estimated to be about $0.35 (\pm 0.08)$ K.

Using the experimental rotational temperatures and the relationship between experimental integrated line intensities and column densities to obtain fractional abundances.⁵⁸ The percent abundances were $41\pm 4\%$ (**a, a**) and $59\pm 6\%$ (**g \pm , a**) (Table 3.4). Based on the experimental signal-to-noise ratio, it was possible to place upper bounds on the percent populations of (**g \pm , g \pm)** and (**a, g \pm)** of less than 0.1%. By comparison, using the calculated relative free energies of the four conformers at the pre-expansion temperature (300 K), the percent populations of the (**g \pm , g \pm)** and (**a, g \pm)** conformers are predicted to be within a factor of 0.3-0.6 of the population of the most abundant (**g \pm , a**) conformer, and therefore these should have been easily detectable. Nonetheless, there are many examples in the literature of collisional removal of population of secondary minima during the supersonic expansion process if the barrier of isomerization to a lower-energy minimum

is small compared to the average internal energy initially available to the conformer⁵⁹. Indeed, as Figure 3.14 shows, the barrier separating the $(\mathbf{a}, \mathbf{g}\pm)$ from the (\mathbf{a}, \mathbf{a}) is predicted to be only 370 cm^{-1} (4.4 kJ mol^{-1}), a value small enough that the $(\mathbf{a}, \mathbf{g}\pm)$ population can be completely transferred into (\mathbf{a}, \mathbf{a}) during the collisional cooling in the expansion. Similarly, the barrier separating $(\mathbf{g}\pm, \mathbf{g}\pm)$ from $(\mathbf{g}\pm, \mathbf{a})$ is 602 cm^{-1} (7.2 kJ mol^{-1}), significantly smaller than the average internal energy available to the conformers prior to the expansion ($E_{\text{ave}} \approx 1900 \text{ cm}^{-1}$).

Table 3.4: Comparison between theoretical and experimental Boltzmann distributions. The theoretical values were calculated at the DFT B2PLYP-D3BJ/aug-cc-pVTZ level of theory.

	Experimental abundance / % ^a	Boltzmann Population Ratio (300 K) / %	
		B2PLYP-D3BJ/aug-cc-pVTZ	MP2/6-311++G(d,p)
(\mathbf{a}, \mathbf{a})	41(4)	21.7	14.6
$(\mathbf{g}\pm, \mathbf{a})$	59(6)	45.8	42.8
$(\mathbf{g}\pm, \mathbf{g}\pm)^b$	< 0.1	16.5	27.0
$(\mathbf{a}, \mathbf{g}\pm)^b$	< 0.1	15.9	15.6

^a Experimental abundances of (\mathbf{a}, \mathbf{a}) and $(\mathbf{g}\pm, \mathbf{a})$ were derived using the experimental temperatures from the Boltzmann plot (Figure 3.15). Errors denote 1σ uncertainty in the last digit. ^b Calculated percent populations for these non-observed conformers are based on an average of the rotational temperatures of the observed conformers (0.595 K). The percentages for all conformers except (\mathbf{a}, \mathbf{a}) were multiplied by a factor of 2 to account for the enantiomeric pairs.

The RRKM rate constants for the $(\mathbf{g}\pm, \mathbf{g}\pm) \rightarrow (\mathbf{g}\pm, \mathbf{a})$ isomerization at this initial energy is $k(E_{\text{ave}}) \approx 1 \times 10^8 \text{ s}^{-1}$, a rate sufficient to enable collisional relaxation into the $(\mathbf{g}\pm, \mathbf{a})$ minimum. In contrast, the barriers separating the $(\mathbf{g}\pm, \mathbf{a})$ and (\mathbf{a}, \mathbf{a}) minima are 928 cm^{-1} (11.1 kJ mol^{-1}), with an isomerization rate of approximately $1 \times 10^6 \text{ s}^{-1}$, so that population initially residing in one of the vertical troughs is incapable of isomerizing into the other in the time scale of the cooling, and is thus trapped in the (\mathbf{a}, \mathbf{a}) or $(\mathbf{g}\pm, \mathbf{a})$ wells. Thus, the final population in the (\mathbf{a}, \mathbf{a}) well should be the sum of the room temperature populations in the (\mathbf{a}, \mathbf{a}) and $(\mathbf{a}, \mathbf{g}\pm)$ wells (38%), while the final $(\mathbf{g}\pm, \mathbf{a})$ is the sum of the initial $(\mathbf{g}\pm, \mathbf{g}\pm)$ and $(\mathbf{g}\pm, \mathbf{a})$ populations. The predictions of the B2PLYP-D3BJ calculations (Table 3.4) are in excellent agreement with experiment ($(\mathbf{a}, \mathbf{a}) + (\mathbf{a}, \mathbf{g}\pm) = 38\%$ calculated vs. 41% experiment; $(\mathbf{g}\pm, \mathbf{g}\pm) + (\mathbf{g}\pm, \mathbf{a}) = 62\%$ calculated vs. 59% experiment).

3.5 Conclusion

A new SFCB analysis method that can dissect congested rotational spectra into sub-sets of transitions due to particular components of a mixture was developed, simplifying line assignments. The method incorporates a unique combination of broadband CP-FTMW and MSE while operating in the strong field coupling regime to differentiate conformer/isomer transitions. The ability of the method to obtain isomer specific microwave spectra was demonstrated for isotopomers, structural isomers and conformational isomers, illustrating a range of circumstances in which the method will be useful. The method's high selectivity even in the face of potential interferences from transitions more than 50 times more intense was demonstrated on [2-¹³C] benzonitrile as a proof of concept. Next the SFCB/MSE method was used to differentiate and assign the microwave spectra of the two structural isomers (E)- and (Z)-PVN. The isomer-specific output frequencies were used as starting points for the line assignments, which greatly reduced the analysis time. Finally, in order to extend the method and create strong field coupling with transitions that have a low transient dipole moment, TSC were introduced to reach the RAP regime on weak transitions that potentially have smaller transition dipole moments, by slowing the sweep rate that interrogates them. The SFCB(TSC)/MSE method successfully produced sets of conformer specific rotational lines for the two observed MB conformers. Both conformers have A/E splittings in the microwave spectrum due to the methyl ester that could be fitted within a simple 1D hindered rotor model to obtain threefold barriers to methyl internal rotation of about 420 cm⁻¹.

In many ways, the broadband CP-FTMW technology has revolutionized the field of rotational spectroscopy by introducing rapid data acquisition time. Nevertheless, for chemists to fully utilize the technology, high-speed, cost effective analysis techniques are vital, that enable its practitioners to quickly identify transitions due to single components of complex gas-phase mixtures and draw structural inferences about them. The SFCB method makes use of tailored excitation pulses using standard CP-FTMW hardware and incorporates them into a scheme that produces single-isomer microwave spectra with a sufficient number of transitions so that preliminary assignments are possible on short time scales. Taken as a whole, we see great potential for the SFCB method as a useful tool in modern high-speed rotational spectroscopy to selectively "light up" conformer/isomer transitions in a highly congested system, speeding line assignments, and providing the ability to address chemically challenging environments in a more effective way.

3.6 References

- Zwier, T. S., Laser Spectroscopy of Jet-Cooled Biomolecules and Their Water-Containing Clusters: Water Bridges and Molecular Conformation. *J. Phys. Chem. A* **2001**, *105*, 8827-8839.
- Bernheim, R. A.; Gold, L. P.; Kelly, P. B.; Kittrell, C.; Veirs, D. K., Pulsed Optical-Optical Double Resonance Spectroscopy of Gerade-Excited Electronic States in Li₂. *Physical Review Letters* **1979**, *43*, 123-125.
- Elliott, B. M.; Relph, R. A.; Roscioli, J. R.; Bopp, J. C.; Gardenier, G. H.; Guasco, T. L.; Johnson, M. A., Isolating the spectra of cluster ion isomers using Ar-"tag"-mediated IR-IR double resonance within the vibrational manifolds: Application to NO₂-*H₂O. *J Chem Phys* **2008**, *129*, 094303.
- Walther, T.; Bitto, H.; Minton, T. K.; Huber, J. R., UV-IR double-resonance spectroscopy of jet-cooled propynal detected by the fluorescence dip method. *Chem Phys Lett* **1994**, *231*, 64-69.
- Page, R. H.; Shen, Y. R.; Lee, Y. T., Infrared-ultraviolet double resonance studies of benzene molecules in a supersonic beam. *The Journal of Chemical Physics* **1988**, *88*, 5362-5376.
- Hippler, M.; Pfab, R.; Quack, M., Isotopomer-Selective Overtone Spectroscopy of Jet-Cooled Benzene by Ionization Detected IR + UV Double Resonance: The N₂ CH Chromophore Absorption of ¹²C₆H₆ and ¹³C₁₂C₅H₆ near 6000 cm⁻¹. *J. Phys. Chem. A* **2003**, *107*, 10743-10752.
- Park, G. B.; Field, R. W., Perspective: The first ten years of broadband chirped pulse Fourier transform microwave spectroscopy. *J Chem Phys* **2016**, *144*, 200901.
- Townes, C. H.; Schawlow, A. L., *Microwave Spectroscopy*. Dover Publications: 1975.
- Brown, G. G.; Dian, B. C.; Douglass, K. O.; Geyer, S. M.; Shipman, S. T.; Pate, B. H., A broadband Fourier transform microwave spectrometer based on chirped pulse excitation. *Rev Sci Instrum* **2008**, *79*, 053103.
- Crabtree, K. N.; Martin-Drumel, M. A.; Brown, G. G.; Gaster, S. A.; Hall, T. M.; McCarthy, M. C., Microwave spectral taxonomy: A semi-automated combination of chirped-pulse and cavity Fourier-transform microwave spectroscopy. *J Chem Phys* **2016**, *144*, 124201.
- Patterson, D.; Doyle, J. M., Sensitive chiral analysis via microwave three-wave mixing. *Phys Rev Lett* **2013**, *111*, 023008.
- Twagirayezu, S.; Clasp, T. N.; Perry, D. S.; Neill, J. L.; Muckle, M. T.; Pate, B. H., Vibrational Coupling Pathways in Methanol As Revealed by Coherence-Converted Population Transfer Fourier Transform Microwave Infrared Double-Resonance Spectroscopy. *J Phys Chem A* **2010**, *114*, 6818-6828.
- Dian, B. C.; Brown, G. G.; Douglass, K. O.; Pate, B. H., Measuring Picosecond Isomerization Kinetics via Broadband Microwave Spectroscopy. *Science* **2008**, *320*.
- Berden, G.; Meerts, W. L.; Kreiner, W., High-resolution laser-induced fluorescence and microwave-ultraviolet double resonance spectroscopy on 1-cyanonaphthalene. *Chem Phys* **1993**, *174*, 247-253.
- Nakajima, M.; Sumiyoshi, Y.; Endo, Y., Development of microwave-optical double-resonance spectroscopy using a Fourier-transform microwave spectrometer and a pulsed laser. *Review of Scientific Instruments* **2002**, *73*, 165-171.
- Heineking, N.; Stahl, W.; Dreizler, H., Radiofrequency Microwave Double Resonance Experiments in Fourier Transform Technique. *Z. Naturforsch* **1988**, *43a*, 280-282.

17. Wodarczyk, F. J.; Wilson, E. B., Radio Frequency-Microwave Double Resonance as a Tool in the Analysis of Microwave Spectra. *J. Mol. Spec.* **1971**, *37*, 445-463.
18. Park, G. B.; Womack, C. C.; Whitehill, A. R.; Jiang, J.; Ono, S.; Field, R. W., Millimeter-wave optical double resonance schemes for rapid assignment of perturbed spectra, with applications to the C (1)B(2) state of SO₂. *J Chem Phys* **2015**, *142*, 144201.
19. Shipman, S. T.; Pate, B. H., New Techniques in Microwave Spectroscopy. In *Handbook of High-Resolution Spectroscopy*, Wiley: 2011; pp 801-827.
20. Wilcox, D. S.; Shirar, A. J.; Williams, O. L.; Dian, B. C., Additional conformer observed in the microwave spectrum of methyl vinyl ketone. *Chemical Physics Letters* **2011**, *508*, 10-16.
21. Frisch, M. J.; Trucks, G. W.; Schlegel, H. B.; Scuseria, G. E.; Robb, M. A.; Cheeseman, J. R.; Scalmani, G.; Barone, V.; Petersson, G. A.; Nakatsuji, H.; Caricato, X. L., M.; Marenich, A.; Bloino, J.; Janesko, B. G.; Gomperts, R.; Mennucci, B.; Hratchian, H. P.; Ortiz, J. V.; Izmaylov, A. F.; Sonnenberg, J. L.; Williams-Young, D.; Ding, F.; Lipparini, F.; Egidi, F.; Goings, J.; Peng, B.; Petrone, A.; Henderson, T.; Ranasinghe, D.; Zakrzewski, V. G.; Gao, J.; Rega, N.; Zheng, G.; Liang, W.; Hada, M.; Ehara, M.; Toyota, K.; Fukuda, R.; Hasegawa, J.; Ishida, M.; Nakajima, T.; Honda, Y.; Kitao, O.; Nakai, H.; Vreven, T.; Throssell, K.; Montgomery, J. A.; Peralta, J., J. E.; Ogliaro, F.; Bearpark, M.; Heyd, J. J.; Brothers, E.; Kudin, K. N.; Staroverov, V. N.; Keith, T.; Kobayashi, R.; Normand, J.; Raghavachari, K.; Rendell, A.; Burant, J. C.; Iyengar, S. S.; Tomasi, J.; Cossi, M.; Millam, J. M.; Klene, M.; Adamo, C.; Cammi, R.; Ochterski, J. W.; Martin, R. L.; Morokuma, K.; Farkas, O.; Foresman, J. B.; Fox, D. J., *Gaussian, Inc, Wallingford CT* **2016**.
22. McGurk, J. C.; Schmalz, T. G.; Flygare, W. H., Fast passage in rotational spectroscopy: Theory and experiment. *The Journal of Chemical Physics* **1974**, *60*, 4181-4188.
23. Schmalz, T. G.; Flygare, W. H., *Coherent Transient Microwave Spectroscopy and Fourier Transform Methods*. Springer: 1978.
24. Schmitz, D.; Alvin Shubert, V.; Betz, T.; Schnell, M., Multi-resonance effects within a single chirp in broadband rotational spectroscopy: The rapid adiabatic passage regime for benzonitrile. *Journal of Molecular Spectroscopy* **2012**, *280*, 77-84.
25. Vitanov, N. V.; Halfmann, T.; Shore, B. W.; Bergmann, K., LASER-INDUCED POPULATION TRANSFER BY ADIABATIC PASSAGE TECHNIQUES. *Annu. Rev. Phys. Chem.* **2001**, *52*, 763-809.
26. Liedenbaum, C.; Stolte, S.; Reuss, J., Inversion Produced and Reversed by Adiabatic Passage. *Phys. Rep.* **1989**, *178*, 1.
27. Grabow, J.-U., Fourier Transform Microwave Spectroscopy Measurement and Instrumentation. In *Handbook of High-Resolution Spectroscopy*, Wiley, Ed. 2011; p 723.
28. Balling, P.; Maas, D. J.; Noordam, L. D., Interference in climbing a quantum ladder system with frequency-chirped laser pulses. *Physical Review A* **1994**, *50*, 4276-4285.
29. Maas, D. J.; Rella, C. W.; Antoine, P.; Toma, E. S.; Noordam, L. D., Population transfer via adiabatic passage in the rubidium quantum ladder system. *Phys Rev A* **1999**, *59*, 1374-1381.
30. Park, G. B.; Field, R. W., Edge effects in chirped-pulse Fourier transform microwave spectra. *Journal of Molecular Spectroscopy* **2015**, *312*, 54-57.
31. Fritz, S. M.; Hernandez-Castillo, A. O.; Abeysekera, C.; Hays, B. M.; Zwier, T. S., Conformer-specific microwave spectroscopy of 3-phenylpropionitrile by strong field coherence breaking. *J. Mol. Spec.* **2018**, *349*, 10-16.
32. Kraitchman, J., Determination of Molecular Structure from Microwave Spectroscopic Data. *American Journal of Physics* **1953**, *21*, 17-24.

33. Casado, J.; Nygaard, L.; Sorensen, G. O., Microwave Spectra of Isotopic Benzonitriles. Refined Molecular Structure of Benzonitrile. *J. Mol. Spec.* **1971**, *8*, 211-224.
34. Mehta-Hurt, D. N.; Korn, J. A.; Navotnaya, P.; Parobek, A. P.; Clayton, R. M.; Zwier, T. S., The spectroscopy and photochemistry of quinioline structural isomers: (E)- and (Z)-phenylvinyl nitrile. *J Chem Phys* **2015**, *143*, 074304.
35. Cable, M. L.; Horst, S. M.; Hodyss, R.; Beauchamp, P. M.; Smith, M. A.; Willis, P. A., Titan tholins: simulating Titan organic chemistry in the Cassini-Huygens era. *Chem Rev* **2012**, *112*, 1882-909.
36. Pickett, H. M., The Fitting and Prediction of Vibration-Rotation Spectra with Spin Interactions. *J. Mol. Spec.* **1991**, *148*, 371-377.
37. Watson, J. K. G., Approximations for the inertial defects of planar molecules. *The Journal of Chemical Physics* **1993**, *98*, 5302-5309.
38. Oka, T., On negative inertial defect. *J. Mol. Spec.* **1995**, *352/353*, 225-233.
39. Li, X.; Xu, X.; You, X.; Truhlar, D. G., Benchmark Calculations for Bond Dissociation Enthalpies of Unsaturated Methyl Esters and the Bond Dissociation Enthalpies of Methyl Linolenate. *J Phys Chem A* **2016**, *120*, 4025-36.
40. Kohse-Hoinghaus, K.; Osswald, P.; Cool, T. A.; Kasper, T.; Hansen, N.; Qi, F.; Westbrook, C. K.; Westmoreland, P. R., Biofuel combustion chemistry: from ethanol to biodiesel. *Angew Chem Int Ed Engl* **2010**, *49*, 3572-97.
41. Westbrook, C. K.; Pitz, W. J.; Curran, H. J., Chemical Kinetic Modeling Study of the Effects of Oxygenated Hydrocarbons on Soot Emissions from Diesel Engines. *J. Phys. Chem. A.* **2006**, *110*, 6912-6922.
42. Gaïl, S.; Thomson, M. J.; Sarathy, S. M.; Syed, S. A.; Dagaut, P.; Diévert, P.; Marchese, A. J.; Dryer, F. L., A wide-ranging kinetic modeling study of methyl butanoate combustion. *Proceedings of the Combustion Institute* **2007**, *31*, 305-311.
43. Jelisavac, D.; Cortés Gómez, D. C.; Nguyen, H. V. L.; Sutikdja, L. W.; Stahl, W.; Kleiner, I., The microwave spectrum of the trans conformer of ethyl acetate. *Journal of Molecular Spectroscopy* **2009**, *257*, 111-115.
44. Jabri, A.; Van, V.; Nguyen, H. V.; Stahl, W.; Kleiner, I., Probing the Methyl Torsional Barriers of the E and Z Isomers of Butadienyl Acetate by Microwave Spectroscopy. *Chemphyschem* **2016**, *17*, 2660-5.
45. Oki, M.; Nakanishi, H., Conformations of the Ester Group. *Bull. Chem. Soc. Japan* **1970**, *43*, 2558-2566.
46. Kleiner, I., Asymmetric-top molecules containing one methyl-like internal rotor: Methods and codes for fitting and predicting spectra. *Journal of Molecular Spectroscopy* **2010**, *260*, 1-18.
47. Hartwig, H.; Dreizler, H., The Microwave Spectrum of trans-2,3-Dimethyloxirane in Torsional Excited States. *Z. Naturforsch* **1996**, *51a*, 923-932.
48. Nguyen, H. V. L.; Kleiner, I.; Shipman, S. T.; Mae, Y.; Hirose, K.; Hatanaka, S.; Kobayashi, K., Extension of the measurement, assignment, and fit of the rotational spectrum of the two-top molecule methyl acetate. *Journal of Molecular Spectroscopy* **2014**, *299*, 17-21.
49. Nguyen, H. V. L.; Stahl, W.; Kleiner, I., Structure and rotational dynamics of methyl propionate studied by microwave spectroscopy. *Molecular Physics* **2012**, *110*, 2035-2042.
50. Grabow, J. U.; Stahl, W.; Dreizler, H., A multioctave coaxially oriented beam-resonator arrangement Fourier-transform microwave spectrometer. *Review of Scientific Instruments* **1996**, *67*, 4072-4084.

51. Nguyen, H. V.; Jabri, A.; Van, V.; Stahl, W., Methyl internal rotation in the microwave spectrum of vinyl acetate. *J Phys Chem A* **2014**, *118*, 12130-6.
52. Mouhib, H.; Zhao, Y.; Stahl, W., Two conformers of ethyl pivalate studied by microwave spectroscopy. *Journal of Molecular Spectroscopy* **2010**, *261*, 59-62.
53. Mouhib, H.; Stahl, W., Conformational analysis of green apple flavour: the gas-phase structure of ethyl valerate validated by microwave spectroscopy. *Chemphyschem* **2012**, *13*, 1297-301.
54. Balabin, R. M., Enthalpy difference between conformations of normal alkanes: effects of basis set and chain length on intramolecular basis set superposition error. *Molecular Physics* **2011**, *109*, 943-953.
55. Holroyd, L. F.; van Mourik, T., Insufficient description of dispersion in B3LYP and large basis set superposition errors in MP2 calculations can hide peptide conformers. *Chemical Physics Letters* **2007**, *442*, 42-46.
56. Fricke, H.; Funk, A.; Schrader, T.; Gerhards, M., Investigation of Secondary Structure Elements by IR/UV Double Resonance Spectroscopy: Analysis of an Isolated *J. Am. Chem. Soc* **2008**, *130*, 4692-4698.
57. Oldham, J. M.; Abeysekera, C.; Joalland, B.; Zack, L. N.; Prozument, K.; Sims, I. R.; Park, G. B.; Field, R. W.; Suits, A. G., A chirped-pulse Fourier-transform microwave/pulsed uniform flow spectrometer. I. The low-temperature flow system. *J Chem Phys* **2014**, *141*, 154202.
58. Abeysekera, C.; Joalland, B.; Ariyasingha, N.; Zack, L. N.; Sims, I. R.; Field, R. W.; Suits, A. G., Product Branching in the Low Temperature Reaction of CN with Propyne by Chirped-Pulse Microwave Spectroscopy in a Uniform Supersonic Flow. *J Phys Chem Lett* **2015**, *6*, 1599-604.
59. Zhang, D.; Bocklitz, S.; Zwier, T. S., Broadband Microwave Spectroscopy of Prototypical Amino Alcohols and Polyamines: Competition between H-Bonded Cycles and Chains. *J Phys Chem A* **2016**, *120*, 55-67.

CHAPTER 4. SINGLE FREQUENCY MICROWAVE PULSES IN THE STRONG FIELD REGIME

4.1 Introduction

The majority of spectroscopic studies employing Fourier transform microwave techniques are based on the interaction of molecular two-level systems with a microwave radiation field. The theoretical description is based on the density matrix formalism, which models the sample of rotating molecules as an ensemble of two-level systems.¹ The evolution in time of a gaseous molecular ensemble is usually treated considering a homogeneous z-polarized field, and its description is based on the optical Bloch equations. These equations describe the time-evolution of the diagonal and off-diagonal density matrix elements corresponding to the populations N_a and N_b of the two levels and their two-level coherence.²⁻³

When electromagnetic radiation interacts with a molecule through a two-level electric dipole interaction, a macroscopic polarization is produced which has a relaxation time of T_2 , and a non-thermal equilibrium population distribution is produced which decays with a relaxation time of T_1 .⁴⁻⁵ Transient experiments normally involve observing the effects of bringing an ensemble of two-level quantum-mechanical systems into or out of resonance with high-power radiation on timescales short relative to the relaxation processes in the two-level system.⁶ All transient phenomena involve the interplay of the polarization and population differences through their coupling with the electric field. Transient experiments on rotational states are classified as those involving coherent absorption and coherent spontaneous emission. In magnetic resonance, transient nutation is used to describe transient absorption, and free induction decay is used to describe spontaneous coherent transient emission.⁷

Chirped-pulse Fourier transform microwave (CP-FTMW) spectroscopy, first implemented in the Pate laboratory⁸, has since become widely used by the spectroscopy community.⁹ An important advance of CP-FTMW spectroscopy compared to previous experiments, such as Stark sweeping, is that it is possible to perform a broadband chirped pulse excitation on a time scale shorter than the transient emission time. In a standard CP-FTMW experiment, after the transient absorption, the polarization of the molecular ensemble is observed in the absence of external electromagnetic fields (in the absence of the polarization pulse). Thus, the molecular coherence

causes transient emission that propagate in the same direction as the electromagnetic pulse driving the transient absorption.¹

Excitation that occurs under fast passage conditions in which the microwave frequency is swept over the absorption profile, produces transient absorption during the sweep, followed by transient emission after the sweep.¹⁰⁻¹¹ Depending on the experimental conditions, a large change in population difference of the states in resonance or the coherence of the two-level ensemble can be achieved. Therefore, the coupling of the molecules to the electric field is particularly important, and it is characterized by the Rabi frequency of the population oscillating between the two states of the resonance. When there is strong coupling with the electric field, as often is utilized in atomic physics, the process is known as rapid adiabatic passage (RAP) and is a well-known technique to selectively prepare atoms in specific states using, for example, chirped lasers.¹²

Since its invention, the method of CP-FTMW spectroscopy has been used to study a wide range of molecules and clusters and to probe chemical kinetics and reaction dynamics¹³⁻¹⁴. The full power of the method is also being put to use in double-resonance experiments¹⁵⁻¹⁶ and in coherent techniques based on the application of frequency-agile pulse sequences¹⁷⁻¹⁸. Using standard hardware available in CP-FTMW, in Chapter 3 an experimental method was described that selectively modulates the intensities of a set of transitions due to a single component in a gas phase mixture¹⁹. The algorithm originally devised to produce the set of transitions involved first probing the sample with one or more single-frequency microwave pulses in the strong field regime, where a phenomenon not previously described in the literature was observed.

Even though the molecular response to microwave pulses in the strong field regime have not been previously explored in a systematic way, there are simpler systems where interaction of quantum systems with a strong oscillating electric field have been modeled.²⁰ For example, in atomic cavity quantum electrodynamics (QED), an isolated atom interacts with an electric field, giving rise to coherent oscillations of a single excitation between the atom and the cavity at the vacuum Rabi frequency, which can be observed when the Rabi frequency exceeds the rates of relaxation and decoherence of both the atom and the field.²¹ Furthermore, the interaction of a strong E-field and the quantum system is also important in the time domain signals creating in Rydberg atoms in three-dimensional microwave cavities,^{18, 22-23} or in alkali atoms exposed to radiation in very small optical cavities where the spacing between vacuum levels is large²⁴.

This Chapter will focus on the experimental and theoretical discoveries associated with application of (nearly) monochromatic microwave pulses resonant with molecular rotational transitions, operating in the strong field regime. A set of experiments that helped characterize the observed phenomena are described, including the effect that collisions, pulse length, and amplitude of the microwave field have on the off-resonant modulated transitions. Finally, the different attempts to model the phenomena are described.

4.2 Experimental Methods

A commercial mixture of (E)- and (Z)-phenylvinyl nitrile (PVN (97%, Alfa Aesar) was used without any further purification. The liquid sample was inserted into a stainless-steel sample holder, located immediately behind the pulse valve, and was heated to ~ 80 °C using a heating rope to obtain sufficient vapor pressure. The experiments were performed with the chamber originally designed by Brian Dian described in section 2.3, for which the lay out of the main components is described in section 2.4.1. For the theoretical modeling of the phenomena a series of Matlab and Fortran programs were written in collaboration with Dr. Francis Robicheaux.

The data recorded for these set of experiments was done using a sinusoidal single frequency pulse (SFP) in combination with a window function. Tukey, Kaiser Gaussian and rectangular window functions were used. The first step was to record an 8-18 GHz weak field spectrum and select a transition to probe. The chosen transition was interrogated with a single frequency microwave pulse and the resultant FID was collected. It is important to notice that the SFPs need to be longer than 100 ns to avoid edge effects²⁵.

4.3 Results and Discussion

When resonantly exciting a molecular rotational transition with a single frequency pulse under full power conditions on our traveling wave-tube analyzer (TWTA), we noticed early in our investigations that coherent signals were produced from a set of conformer specific transitions, not just from the transition resonantly excited. Figure 4.1 illustrates this behavior using PVN as a test molecule, taking advantage of its large dipole moment to obtain strong signals with comparatively little signal averaging. Initially, it was expected that when sending a SFP, only the probe frequency would show up in the resultant spectrum. However, when the frequency of the excitation pulse

was fixed on the $2_{2,1}-1_{1,0}$ (10052.500 MHz) transition of Z-PVN, application of a 1 μ s long pulse at 100% TWTA power (200 W) produces a Fourier-transformed signal that contained 13 transitions belonging to Z-PVN (shown in blue in Figure 4.1), while no transitions associated with E-PVN appeared. Alternatively, when the same experiment was carried out with the single-frequency pulse (SFP) resonant a transition in E-PVN (the $11_{1,11}-10_{1,10}$ at 12270.313 MHz), an analogous 1 μ s pulse at 100% TWTA power produces a set of five isomer specific transitions shown in red.

Even though the transition dipole moment of the Z-PVN probe transition is smaller than that used for E-PVN, the number of transitions appearing above the noise level in Z-PVN is almost three times greater than in E-PVN. Admittedly, since the E-PVN was present in the mixture in $\sim 10\%$ abundance relative to Z-PVN, this difference could have been primarily due to signal-to-noise issues; nevertheless, the very appearance of this large number of off-resonant transitions in the molecular FID called for further exploration, especially since the signals are isomer-specific, and hence not likely due to some artifact, at least not in its entirety.

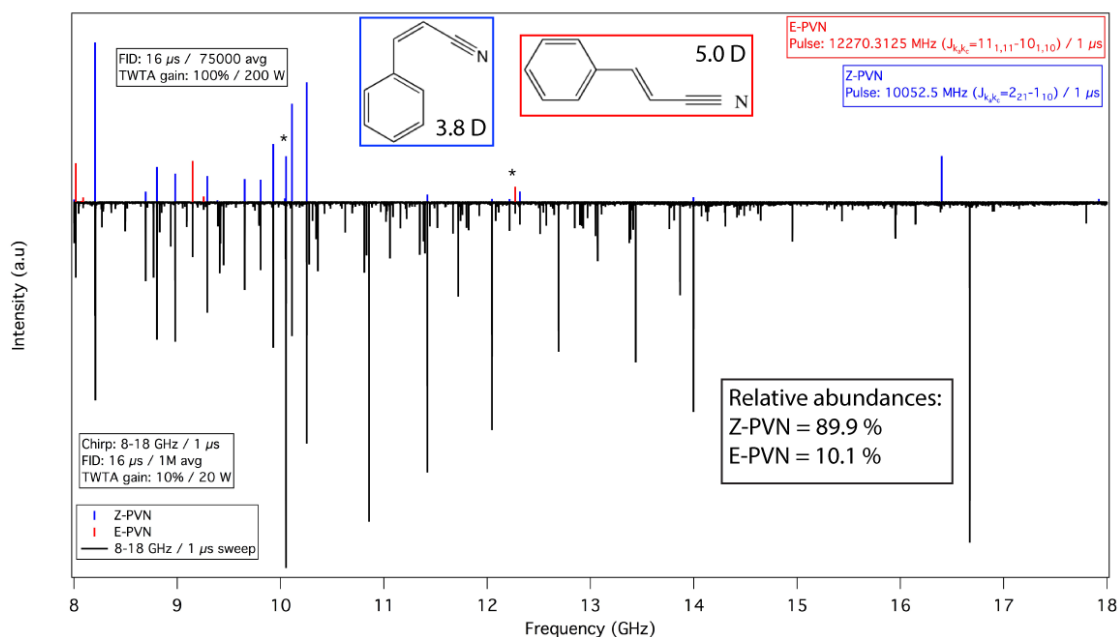


Figure 4.1: PVN single frequency pulses. The modulated transitions by a single frequency pulse probing the $2_{2,1}-1_{1,0}$ Z-PVN transition are shown in blue. The modulated transitions by a single frequency pulse probing the $11_{1,11}-10_{1,10}$ E-PVN transition are shown in red. In black a PVN spectrum taken in the linear fast passage (10% TWTA gain) is shown.

Windowing functions:

The spectra obtained in Figure 4.1 used ‘square’ or ‘rectangular’ pulses in that the input to the arbitrary wave form generator (AWG) involved application of a single frequency pulse. Such pulses have wings in frequency space, which could lead to poor spectral isolation and the possibility that low-intensity spectral wings to the pulse could provide the frequencies needed to excite the other molecular transitions. Notably, this simple ‘explanation’ wouldn’t account for the species specificity that we previously mentioned. Nevertheless, it was important to test if by using cleaner pulses the phenomenon was still present. To do so, we initially applied a Gaussian window function to the SFP, with coefficients computed using the following equation:

$$\omega(n) = e^{-1/2 \left(\alpha \frac{n}{\frac{N-1}{2}} \right)^2} = e^{-n^2/2\sigma^2},$$

where $-(N-1)/2 \leq n \leq (N-1)/2$ and α is inversely proportional to the standard deviation (σ) of a Gaussian random variable.²⁶ Therefore, a larger value of α produces a narrower window. When using this window function a decrease in intensity was observed in the overall spectrum; nonetheless, as long as α was smaller than 3, the number and pattern of off-resonant transitions appearing in the strong-field SFP experiment remained the same. Once the single frequency pulse was too narrow in time, the resulting spectrum slowly shifted towards that expected for a SFP in the weak field regime, with transition intensity present in fewer transitions with less intensity, until only the resonant transition appears in the spectrum.

A Kaiser window was also used on the single frequency pulses. The coefficients of the Kaiser window were computed by

$$\omega(n) = \frac{I_0 \left(\pi \alpha \sqrt{1 - \left(\frac{2n}{N-1} - 1 \right)^2} \right)}{I_0(\pi \alpha)}, \quad 0 \leq n \leq N$$

where I_0 is the zeroth-order modified Bessel function of the first kind and the length is $N+1$.²⁶ The sidelobe attenuation governed by the choice of α is defined in Matlab via the following relationship:

$$\beta = \begin{cases} 0.1102(\alpha - 8.7) & \alpha > 50 \\ 0.5842(\alpha - 21)^{0.4} + 0.07886(\alpha - 21) & 50 \geq \alpha \geq 21 \\ 0 & \alpha < 21 \end{cases}$$

therefore, by increasing β the main lobe widens and the amplitude of the sidelobes decreases, thus the attenuation increases.²⁷ A series of scans were recorded with β chosen in the range 3 to 15 in increments of 2; however, no change was observed in the SFP spectra.

Finally, a tapered cosine or Tukey window was applied as a third test of its effects on the SFP signals. In the Tukey window, the frequency-dependent amplitude $\omega(n)$ is defined by the following equation:

$$\omega(n) = \begin{cases} 1/2 \left\{ 1 + \cos \left(\frac{2\pi}{r} \left[n - \frac{r}{2} \right] \right) \right\} & 0 \leq n < \frac{r}{2} \\ 1 & \frac{r}{2} \leq n < 1 - \frac{r}{2} \\ 1/2 \left\{ 1 + \cos \left(\frac{2\pi}{r} \left[n - 1 + \frac{r}{2} \right] \right) \right\} & 1 - \frac{r}{2} \leq n \leq 1 \end{cases}$$

where r is the ratio of cosine-tapered section length to the entire window length. Thus, a Tukey window is a rectangular window with the first and last $r/2$ percent of the samples equal to parts of a cosine. If $r=0$ the end result is a rectangular window, and if $r=1$ then for practical purposes a Hann window is being applied.²⁸ A series of scans was carried out in which the SFP signal was collected for excitation pulses in which r was increased from 0.25 to 0.75 in increments of 0.1. Again, there was no noticeable change in the number or pattern of the modulated transitions with change in r . We conclude on the basis of these tests that any frequency broadening present when using a rectangular single-frequency pulse was not the reason for the off-resonant modulated transitions observed when pumping a transition with a single frequency pulse.

The tests of different window functions also showed clearly that, as the length of the SFP is shortened, adding a window function made the resonant frequency more selective. Moreover, adding a Tukey window reduced the leakage just as effectively as a Kaiser or Gaussian window, without a big loss in S/N. Therefore, for the rest of the experiments presented in this chapter a Tukey window was used.

Off-resonant output from the TWTA:

It is well known that there are noise sources associated with the microwave components, particularly the TWTA. In order to make sure that the observed phenomenon was not due to electronic noise or power noise from the TWTA, the intensity of the different non-resonant transitions was measured as a function of detuning from resonance. Figure 4.2 shows the effects of varying excitation frequency from resonance for both a Z-PVN ($6_{1,6}$ - $5_{0,5}$, 9921.90 MHz) and an E-PVN ($8_{1,7}$ - $7_{1,6}$, 9448.75 MHz) transition. For these tests a $1\mu\text{s}$ SFP was used, with the TWTA set to full power. For E-PVN, all resonant and non-resonant molecular signal was lost when the pulse was 15 MHz off-resonance; whereas for Z-PVN, detuning of only 10 MHz off-resonance

was sufficient. This is consistent with the larger transition dipole moment present in E-PVN relative to Z-PVN. We conclude on this basis that resonant excitation of a molecular transition is essential for observation of the non-resonant signal from other molecular transitions, and that the drop-off in non-resonant signal depends sensitively on the inherent transition strength of the resonant (or near-resonant) transition.

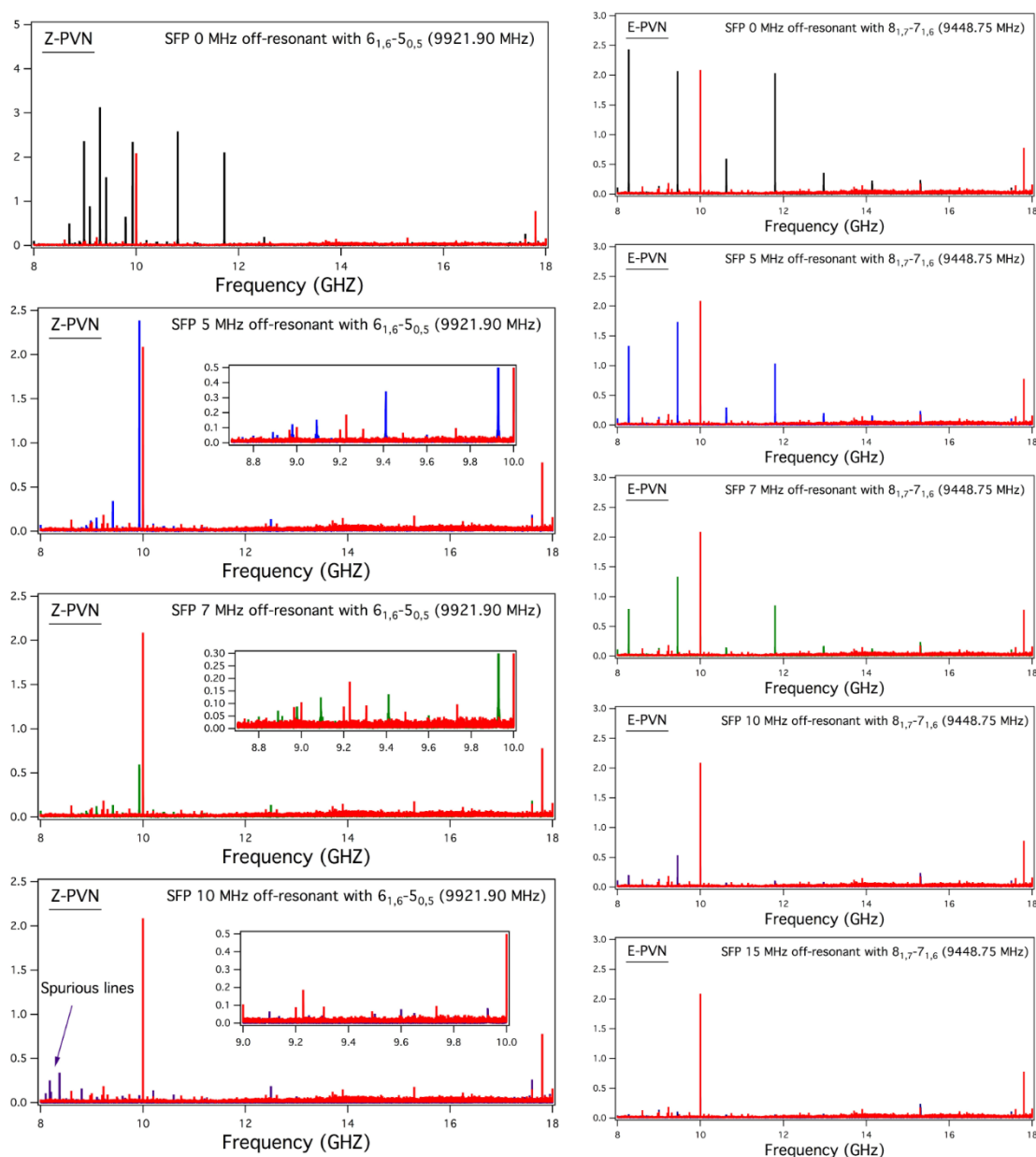


Figure 4.2: Comparison of spectra following single-frequency pulses as a function of detuning from resonance. The blank is shown in red.

4.3.1 Collisions

Another hypothesis for the appearance of these non-resonant transitions is that collisions with the buffer gas or between PVN molecules could induce coherence transfer. At first, this is an odd hypothesis, since collisions are typically thought of as destroying coherences. Nonetheless, the role played by collisions is important to establish. To establish this role, a series of tests were performed, including changing the backing pressure, the carrier gas, the temperature of the sample holder, and the timing when the FID was collected. These tests were also carried out using PVN as the test molecule, and with the TWTA set to full power (200 W). The $2_{1,1}-1_{1,0}$ (10052.50 MHz) transition of Z-PVN was used to probe if by changing the backing pressure there was a change in the intensity or number of off-resonant transitions that appear following SFP excitation. Using He as carrier gas, the backing pressure was increased from 5 to 35 psig (0.34 to 2.41 bar) in intervals of 10 psig. Figure 4.3 shows that no significant change was observed as the backing pressure was increased. The same 13 transitions appeared in the SFP spectrum in each case with relative intensities virtually unchanged. The same lack of change was observed when changing the carrier gas from helium to neon.

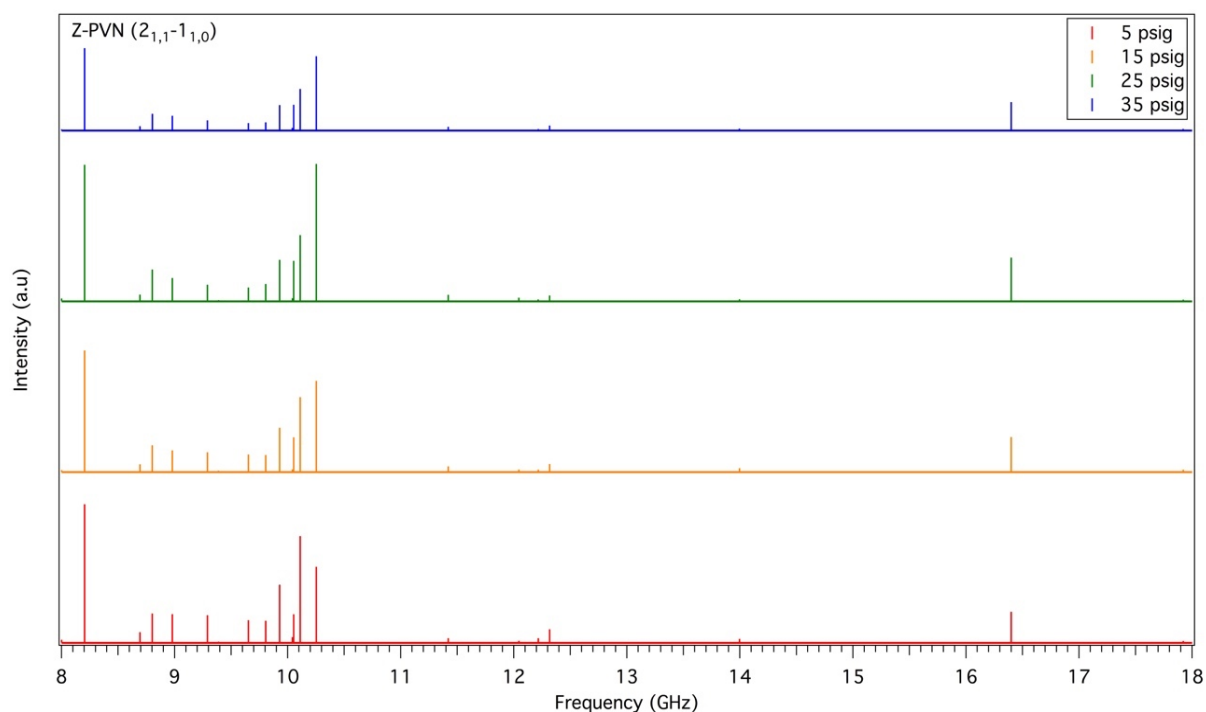


Figure 4.3: Comparison of single frequency pulse spectra taken at different backing pressures with He as carrier gas.

As the molecules exit the nozzle and undergo a supersonic free jet expansion, they undergo many collisions with the buffer gas; nonetheless, as the adiabatic expansion progresses the expanding gas becomes so rarefied that it is possible to achieve a collision-free environment on the timescale of the molecular FID collection. During a typical experiment in which 25 FIDs are recorded per gas pulse, the delay Δt between opening the pulsed valve and initiating the SFP produced maximum signal at $\Delta t_{\text{optim}}=885 \mu\text{s}$. However, to address if all the off-resonant transitions appearing in the SFP spectrum are present regardless of which segment of the gas pulse is probed, we recorded SFP spectra at three different time delays (Δt_{optim} , $\Delta t_{\text{optim}}+400\mu\text{s}$, and $\Delta t_{\text{optim}}+800\mu\text{s}$) of the expansion while collecting only a single FID per gas pulse, as illustrated in Figure 4.4. Using a $1\mu\text{s}$ rf excitation pulse resonant with the $2_{1,1}-1_{1,0}$ Z-PVN transition, at time Δt_{optim} , 13 transitions were modulated, while at the other two timings only 5 transitions were observed. Nonetheless, since the signal was lower at these time delays in the gas pulse and the missing transitions were small even at Δt , the results of this test are hard to interpret conclusively.

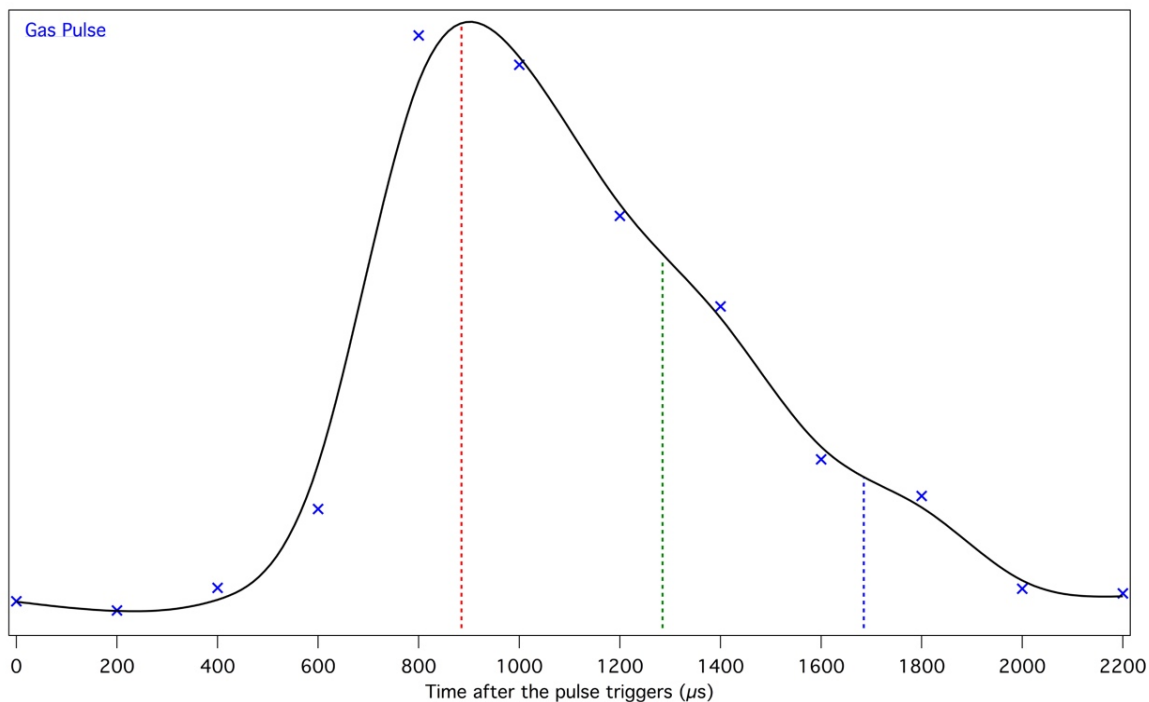


Figure 4.4: Intensity of the the $2_{1,1}-1_{1,0}$ Z-PVN transition vs time after the pulse triggers. The red dotted line indicates the intensity of the probed transition when the single frequency spectrum was taken at Δt_{optim} . The green dotted line is the intensity of the probed transition at $\Delta t_{\text{optim}}+400\mu\text{s}$. The blue dotted line is the intensity of the probed transition at $\Delta t_{\text{optim}}+800\mu\text{s}$.

The previous experiments all point to the conclusion that collisions between the carrier gas and the interrogated molecules don't play a major role in the observed phenomena. Even though the molecules responsible for the microwave signal (PVN in this case) are entrained in the carrier gas at a low concentration, we also checked whether PVN-PVN collisions might contribute to the off-resonant transitions observed in the SFP experiments. To that end, the $9_{0,9}-8_{0,8}$ rotational transition of Z-PVN at 13069.37 MHz was probed with a 1 μ s single frequency pulse at two different temperatures (39 °C and 115 °C), the PVN sample entrained in 1.38 bar of He. At 39 °C PVN's vapor pressure is ~ 0.057 torr; therefore, its percentage concentration in the expansion was $\sim 5 \times 10^{-3}\%$. At 115 °C the concentration was nearly 40 times larger ($\sim 0.2\%$) since at this temperature PVN's vapor pressure is ~ 2.52 torr. Figure 4.5 shows that although the absolute intensity of the transitions grew commensurately with the increase in vapor pressure, the number and pattern of the modulated transitions stayed unchanged. On this basis and the previous backing pressure studies, it seems unlikely that molecule-carrier gas or molecule-molecule collisions could play a meaningful role in contributing to the presence and intensity of off-resonant molecular transitions.

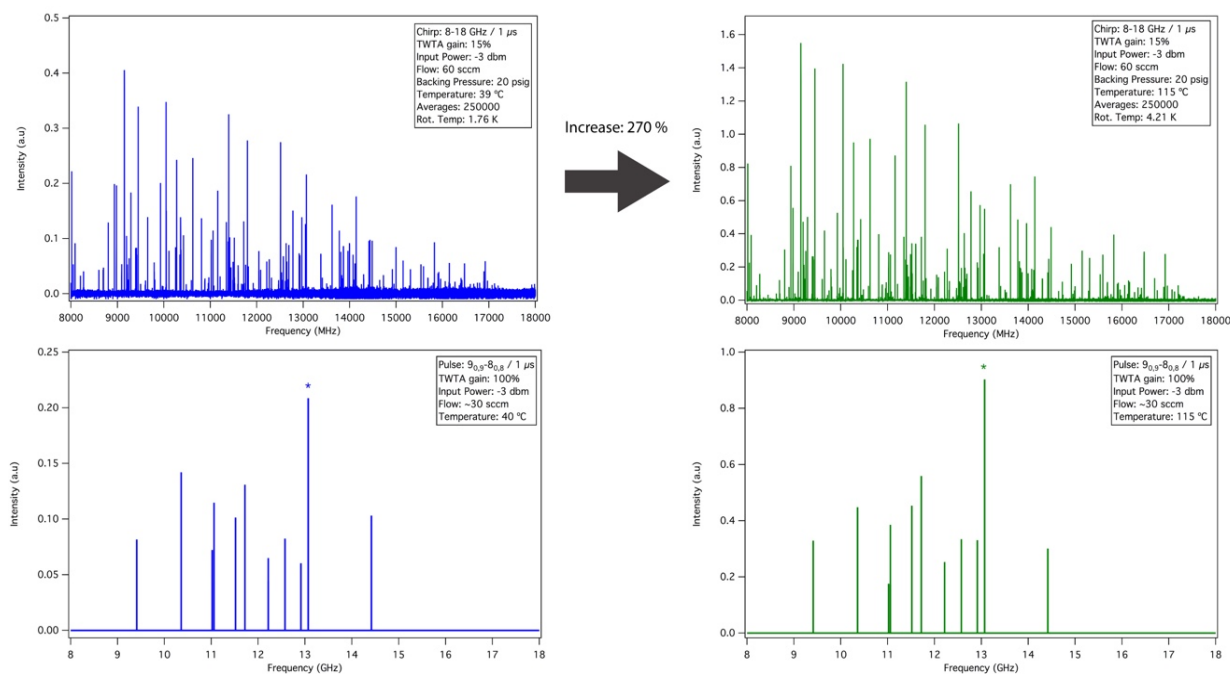


Figure 4.5: Broadband spectrum and single frequency pulse spectrum taken at two different sample holder temperatures. The blue spectra were taken at 39 °C (VP=0.057 torr and $C \sim 5 \times 10^{-3}\%$) and the green spectra were taken at 115 °C (VP=2.52 torr and $C=0.2\%$).

4.3.2 Rabi Cycles

When a two-level system interacts with an oscillatory driving field, it will cyclically absorb and re-emit photons Rabi cycle occurring at the Rabi frequency. This is the frequency of fluctuations in the populations of the two levels involved in the system and is proportional to the strength of the coupling of the molecular transition with the amplitude of the electric field. The Rabi frequency is defined as:

$$\Omega_i = \frac{\mu_i E_0}{\hbar}$$

where μ_i is the transition dipole moment for transition i and E_0 is the electric field amplitude. In order to evaluate Ω_i for a given resonant molecular transition, the correct dipole transition matrix element μ_i has to be calculated. SPCAT, a program from Pickett's suite of programs²⁹ can output the reduced transition matrix element. Using the Wigner-Eckart theorem, it is possible to relate the expectation value of an operator with the reduced matrix element for that operator. This theorem concerns matrix elements of frequent occurrence in perturbation theory and in the theory of emission and absorption of radiation, and it allows the determination of the selection rules for the matrix element that follow from rotational invariance.³⁰

The transition matrix element for an electric dipole transition is proportional to $\langle e | \mathbf{E} \cdot \mathbf{r} | g \rangle$ where $|e\rangle$ and $|g\rangle$ are described by a set of angular momentum quantum numbers. So, for instance, a transition between two atomic quantum states would have $|g\rangle = |l', m_l'\rangle$ and $\langle e| = \langle l, m_l|$. Therefore,

$$\langle l, m_l | \mathbf{E} \cdot \mathbf{r} | l', m_l' \rangle = E_0 \sum_{\rho} (-1)^{\rho} \varepsilon_{\rho} \langle l, m_l | r_{-\rho} | l', m_l' \rangle$$

where $r_{-\rho}$ is a component of a vector and can be evaluated using the relationship for expectation values of a tensor operator,

$$\langle l, m_l | T_{kq} | l', m_l' \rangle = (-1)^{l-m} (l || T_k || l') \begin{pmatrix} l & k & l' \\ -m & q & m' \end{pmatrix}$$

In this expression, the quantity in parentheses is the Wigner 3j symbol and $(l || T_k || l')$ is the reduced matrix element. The 3j symbol is related to the usual Clebsch-Gordon coefficient that couple two angular momenta j_1 and j_2 to produce a total angular momentum j by

$$(j_1 j_2 m_1 m_2 | j_1 j_2 j m) = (-1)^{-j_1+j_2-m} \sqrt{2j+1} \begin{pmatrix} j_1 & j_2 & j \\ m_1 & m_2 & -m \end{pmatrix}$$

In our experiments the polarization of the electric field is assumed to be along the z-direction; that is, $-m = 0$.³¹ The Matlab program that uses the previously described formalism to convert the SPCAT output (reduced matrix elements) into the transition dipole moments is described in Appendix A.3.

The SFP only modulates off-resonant transitions when the oscillating electric field is relatively strong and can couple with the transition dipole moment of the transition. Thus, it is interesting to assess experimentally the number and quantum state make-up of the transitions that appear in the SFP spectrum as a function of TWTA power (or more precisely, electric field strength) and in pulse length, which is related to the number of Rabi cycles driven by the resonant microwave pulse. Figure 4.6 presents a series of SFP spectra recorded with increasing microwave power (or equivalent, electric field strength). Clearly, the number of transitions appearing in the SFP spectrum increases with rf power. More specifically, as Figure 4.6a illustrates, with a $1\mu\text{s}$ SFP resonant with the $9_{0,9}-8_{0,8}$ rotational transition in Z-PVN, only the resonant transition appears in the spectrum with 10% of the full power of the TWTA (~ 20 W, 3500 V/m). However, at full TWTA power (100%, 200 W, 11000 V/m) there are 11 transitions contributing to the spectrum (Figure 4.6b). Note that, as the labels in the spectra indicate, the powers available in the TWTA, when concentrated on a single resonant microwave transition, constitute conditions in which the transition is undergoing 26 to 83 Rabi cycles during the $1\mu\text{s}$ rf pulse. These are decidedly different conditions than is the norm under linear fast passage conditions.

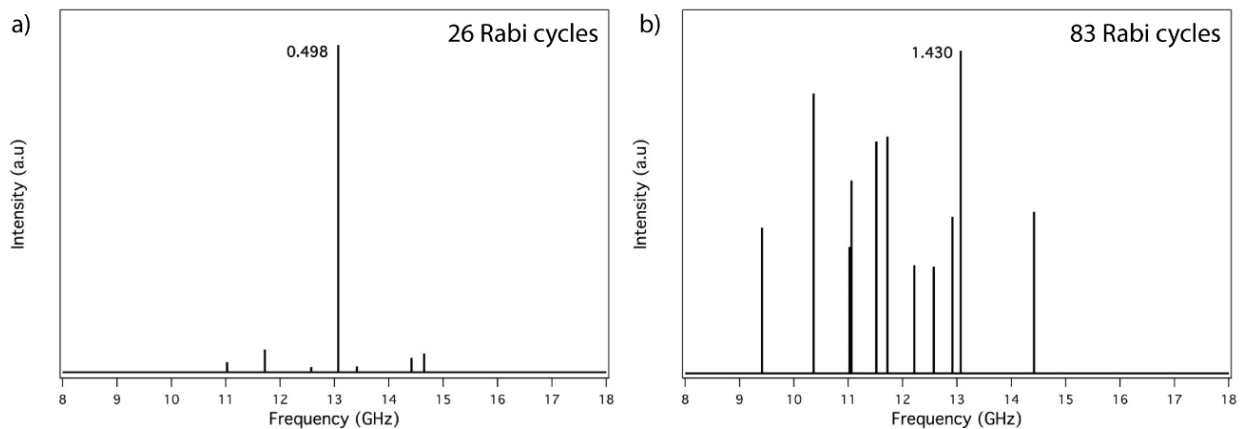


Figure 4.6: Single frequency pulse probing the $9_{0,9}-8_{0,8}$ Z-PVN transition. a) Spectrum taken at 10% TWTA gain (20 W, 3500 V/m). b) Spectrum taken at 100% TWTA gain (200 W, 11000 V/m).

To explore this general phenomenon further, a series of SFPs experiments were conducted in which the TWTA power was increased systematically. These were performed when probing three different transitions for Z-PVN and two different transitions for E-PVN. In each case, the same behavior was observed, in which the number of transitions appearing in the SFP spectrum increased systematically as the power increased until a saturation point, where only the intensity pattern slightly changed. This saturation point was reached faster by those transitions with a bigger transition dipole moment; however, it is also possible that at stronger electric fields the modulated transitions are outside the detected frequency range.

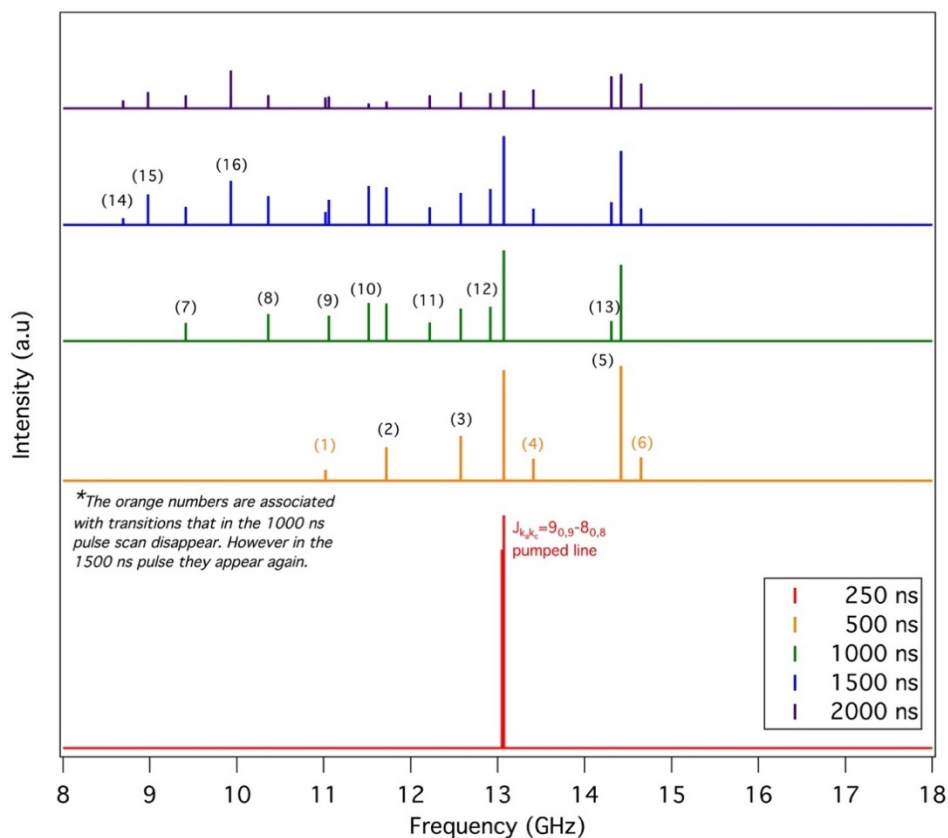


Figure 4.7: Comparison of single frequency pulse spectra taken at different SFP durations. The numbers match the transitions in Table 4.1.

Since changing the pulse length also varies the number of Rabi cycles experienced by the resonant two-level system, a series of experiments were carried out for both PVN isomers, where the length of the SFP was systematically increased at fixed TWTA power (in the strong field regime). Since in both isomers of PVN α -type transitions are allowed and strong, we chose a

resonant frequency associated with an *a*-type transition in both isomers in order to reduce the number of variables in the measurements.

For Z-PVN the $9_{0,9}$ - $8_{0,8}$ transition at 13069.37 MHz was used as the resonant ‘drive’ transition, and SFP spectra were recorded for rf pulse lengths of 250, 500, 1000, 1500, and 2000 ns. It is important to point out that in each case a Tukey window with $r=0.3$ was used when generating the pulses. The results from these series of experiments are illustrated in Figure 4.7. When the pulse length is 250 ns, only the resonant transition appears in the spectrum, but increases systematically as the pulse length increases, reaching as many as 16 new transitions at a pulse length of 1500 ns. Interestingly, between 1500 and 2000 ns, no more new transitions appear, and in fact, the overall intensity decreased somewhat. One possible explanation for this intensity loss could be that a 2000 ns pulse might be so long that the contributions from some transitions to the molecular FID could start to decay before the FID is recorded.

Table 4.1: List of transitions modulated by a single frequency pulse, they match the numbers in Figure 4.7. The number in orange indicate that those transitions were modulated with a 500 ns SFP. The transitions indicated in green correspond to those modulated by a 1000 ns pulse. The blue numbers are associated with those transitions that were modulated by a 1500 SFP.

	Transition		Transition
1	$8_{0,8}$ - $7_{1,7}$	9	$7_{1,7}$ - $6_{0,6}$
2	$8_{0,8}$ - $7_{0,7}$	10	$8_{1,8}$ - $7_{1,7}$
3	$9_{0,9}$ - $8_{1,8}$	11	$8_{1,8}$ - $7_{0,7}$
4	$9_{1,9}$ - $8_{0,8}$	12	$9_{1,9}$ - $8_{1,8}$
5	$10_{0,10}$ - $9_{0,9}$	13	$10_{1,10}$ - $9_{1,9}$
6	$10_{1,10}$ - $9_{0,9}$	14	$6_{1,6}$ - $5_{1,5}$
7	$7_{0,7}$ - $6_{1,6}$	15	$6_{0,6}$ - $5_{0,5}$
8	$7_{0,7}$ - $6_{0,6}$	16	$6_{1,6}$ - $5_{0,5}$

Table 4.1 shows a list of transitions appearing in the SFP spectrum, indicating which new transitions appear at each step. To better understand this data, Figure 4.8a provides the energy diagram of the observed transitions at each step, with the number of Rabi cycles indicated as labels. As can be seen, a 500 ns-length SFP would induce about 48 Rabi cycles in the resonant transition, leading to the presence of six new off-resonant transitions. It is important to highlight that all of the new transitions appearing in the 500 ns SFP spectrum share a lower or upper energy level with the pumped transition. Increasing the length to 1000 ns adds a new set of 7 transitions, and at 1500 ns there are three more off-resonant transitions. It is important to note that at every stage, the new transition(s) that appear share an energy level with either the pumped transition or an off-resonant transition previously induced. Moreover, even though the transition dipole moment of the transitions between lower energy levels (smaller $J_{K_aK_c}$) is smaller, these transitions seem to be more likely to be present in the SFP spectrum than those between higher energy levels. We tentatively conclude based on this observation that the population in the energy levels play a significant role, with larger populations (determined by the rotational Boltzmann distribution in the expansion) producing detectable molecular coherences more readily than those with smaller populations.

The same set of experiments were carried out while resonantly exciting the $8_{0,8}-7_{0,7}$ (9148.89 MHz) transition of E-PVN. Once again, a Tukey window with $r=0.3$ was used when generating the SFPs. Since edge effects were present when the transition was probed with a 250 ns SFP, in this case it was not possible to record a scan at this pulse length. Moreover, similar to Z-PVN, when the transition was probed with 1500 and 2000 ns SFPs there was no change in the number of modulated transitions, and the overall intensity decreased. As a cursory comparison of Figure 4.8a and 4.8b points out, for the same pulse length, the number of off-resonant transitions in E-PVN is significantly smaller than in Z-PVN. This is chase despite the fact that the transition dipole moment of the resonant transition in E-PVN is larger than the one used to study Z-PVN. A possible explanation for this observation is that Z-PVN has both *a*- and *b*- type transitions dipole-allowed, whereas E-PVN can only access *a*-type transitions. Once again, however, it must be recognized that, since the overall intensity of transitions due E-PVN are smaller due to its smaller concentration in the expansion, the experimental sensitivity is less.

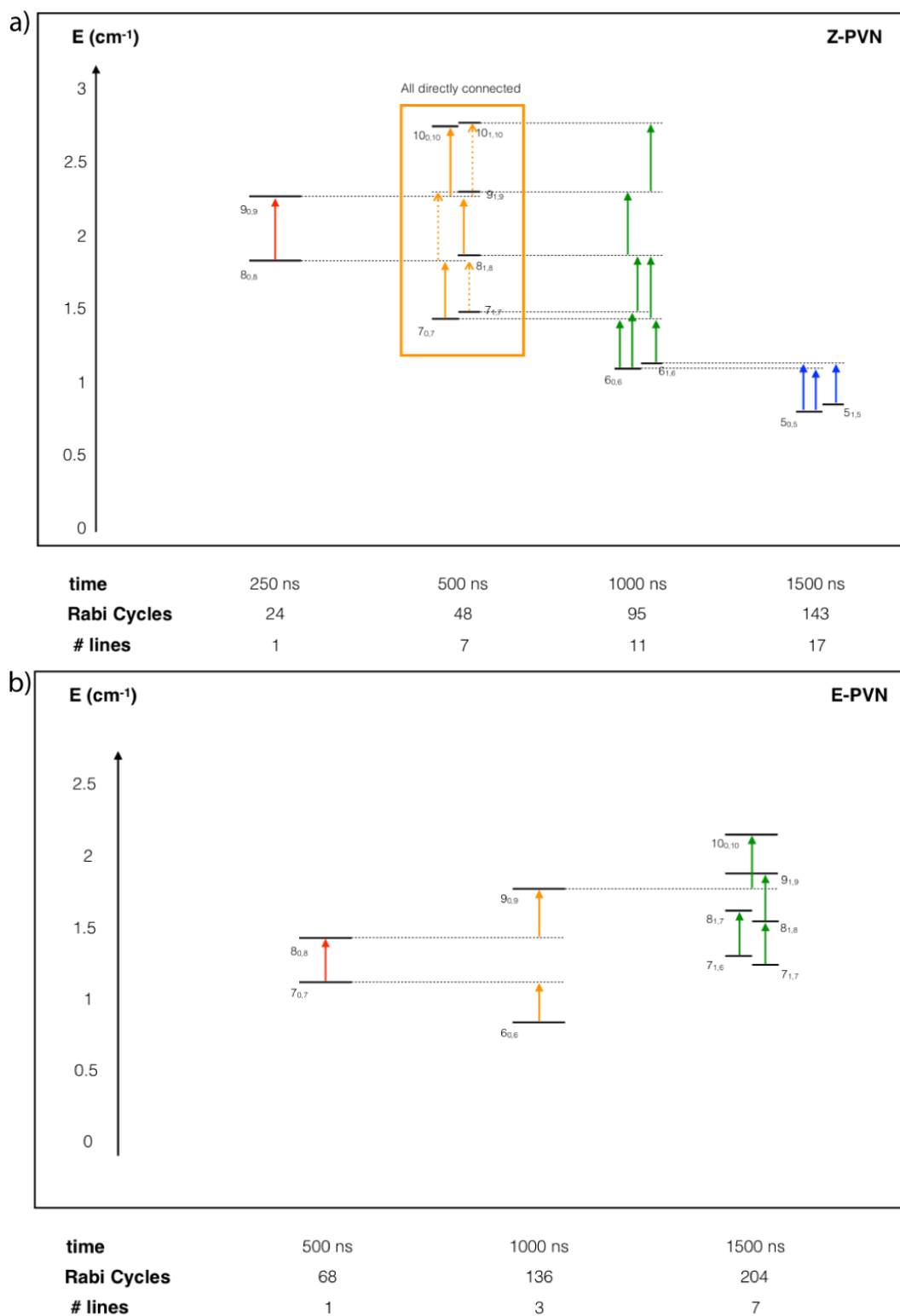


Figure 4.8: Energy diagrams for the off-resonant modulated transitions. a) Z-PVN energy diagram for the SFP at $8_{0,8}$ - $9_{0,9}$. b) E-PVN energy diagram for the SFP at $7_{0,7}$ - $8_{0,8}$.

4.3.3 Theoretical Models

In the hopes to develop a model that mimics the experimental results, different approaches have been tried. The programs described in this section were developed in collaboration with Dr. Francis Robicheaux. The program uses the following Hamiltonian:

$$\hat{H} = \hat{H}_{rot} + \hat{H}_{field}$$

where \hat{H}_{rot} describes the rotational eigenstates of an asymmetric top, and $\hat{H}_{field} = -\hat{D}_z E_0 W(t) \cos(\Omega_{MW} t)$ where \hat{D}_z is the electric dipole moment operator, F_0 is the microwave electric field strength, Ω_{MW} is the microwave frequency, and $W(t)$ is the window function. \hat{H}_{field} accounts for the coupling between different rotational states due to the microwaves. As a consequence of the coupling, the rotational eigenstates, $|\varphi_1\rangle, |\varphi_2\rangle \dots |\varphi_n\rangle$ are no longer stationary states, therefore transitions are induced between pairs of diabatic states. For notational simplicity in this section, we will label the rotational eigenstates with a single index which is understood to stand for all of the rotational quantum numbers.

We used two methods to solve for the time evolution of the superposition of rotational states. The first method gives a more accurate treatment while the microwaves have constant strength and frequency but can't easily be used to model the turn-on and -off of the microwaves or any chirp. This method is, essentially, a Floquet treatment of the Hamiltonian. The evolution of the wave function from time t_0 to time t can be represented as:

$$|\varphi, t_0; t\rangle \rightarrow U(t, t_0)|\varphi, t_0\rangle$$

$$i\hbar \frac{dU(t, t_0)}{dt} = \hat{H}U(t, t_0)$$

In the Floquet treatment, the time dependent Hamiltonian with $W(t) = 1$ is converted into a time independent Hamiltonian by using the Floquet eigenstates

$$|\psi_E(t)\rangle = \sum_m |\psi_{E,m}\rangle e^{-i(m\Omega_{MW} + \frac{E}{\hbar})t}$$

where m indicates the number of microwave photons absorbed or emitted. The energies E can be found by diagonalizing the Floquet Hamiltonian. This method is useful because the eigenstates and eigenvalues can be used to calculate $U(t, t_0)$ for any duration $t - t_0$.

The second method does not explicitly use $U(t, t_0)$ but instead directly solves for the time evolution of the eigenstate using the leapfrog algorithm:

$$|\psi, t_0; t + dt\rangle = \left| |\psi, t_0; t - dt\rangle - \left(\frac{2iH(t)dt}{\hbar} \right) \right| |\psi, t_0; t\rangle$$

where dt is the time step and the one step error is proportional to dt^3 . This method has the advantage of easily incorporating the window function and any chirp but has the disadvantage of needing more computational steps for larger durations. The other difficulty is that the time step needs to be smaller as the energy spread in the basis is increased. In the actual calculation, the wave function was expanded in the basis of eigenstates of the rotational Hamiltonian. Convergence was checked with respect to the time step and the number of basis functions that compose the wave function.

Finally, when the microwaves are off, there is an oscillating dipole $D(t)$ because the microwaves set coherences between the rotational states.

$$D(t) = \sum_{i,j} C_j^* C_i e^{i(E_j - E_i)t/\hbar} D_{ji}$$

This oscillating dipole depends on the initial state before the microwaves are turned on. We assume the molecules start in an incoherent superposition of rotational eigenstates weighted by the Boltzmann factor at temperature 1.43 K. We did not try to individually pick the possible initial states but included all of the possible states. The total $D(t)$ results from the weighted sum over the possible initial states.

The calculations reproduce the frequencies of test molecules (e.g., Z- and E-PVN) well by using the fit Hamiltonian for rotations and the fit dipoles for the transitions. Nonetheless, almost all of the non-resonant frequencies disappeared once there were more than ~ 20 cycles during the turn-on and -off of the window function, whereas the shortest turn on/off achieved experimentally was ~ 50 cycles. We also noticed that the presence or absence of the non-driven frequencies was not affected by the duration once the number of Rabi oscillations was larger than a few. The fact that a lot of the frequencies that are seen in the experiment are also in the unphysically short turn-on/off calculations might mean that the molecules behave like the microwaves are only present for a short time scale.

One of the written programs included a full density matrix, where an $N \times N$ matrix was propagated (N being the number of states), allowing the molecule to start in all of the states (up to $m=5$) with the appropriate Maxwell-Boltzmann weight. This program was compared with calculations that use single states and the results were qualitatively similar. However, none of the

programs were able to reproduce the increase in number of number of transitions that is observed in the experiment. Another approach was to take the states involved in the experimental off-resonant modulated transitions and solve the density matrix equation only for those states. For example, for the $9_{0,9}$ - $8_{0,8}$ (13069.37 MHz) transition of Z-PVN, the energies and dipoles of the states $7_{0,7}$, $7_{1,7}$, $8_{0,8}$, $8_{1,8}$, $9_{0,9}$, $9_{1,9}$, $10_{0,10}$, and $10_{1,10}$ were used. This is a simpler program that gave results similar to the full calculation and was used to quickly test ideas.

When larger molecules are put into a supersonic expansion for cooling their translational energies along the expansion axis are sped up by the buffer gas that is the majority of the expansion gas. However, it is possible that the heavy molecules are moving a bit more slowly than the buffer gas. The terminal velocity in a supersonic free jet of He is 1.8×10^5 cm/s. If a slip flow of PVN is assumed with a velocity of 10^4 cm/s slower than He, then for He atom to engage in an interaction with PVN that is stronger than the ΔE associated with a $\Delta k_a=1$ changing collision (for example), it needs to be within 12 Å of PVN. Under these conditions a ‘fly by’ collision occurs in 20 ps.

To check if rotational coherence transfer can occur during such a soft collision from one $J_{k_a k_c}$ level to another that is nearby in energy, without losing the phase information, some modifications were made to the original program. To explore collisions a random number generator was added to the program that solved for the density matrix, where at each step the code randomly decides whether a collision occurs, and it then randomly chooses between four different pairs of states, and these states were rotated by a small angle ($\cos(\theta)=0.95$). Although after one collision, different off-resonant transitions showed up, all the extra lines disappeared after averaging over many collisions. This is to be expected since each collision adds a term to $D(t)$ but with a phase that depends on the time when the collision occurs. That collisions do not contribute to the FID signal agrees with experiment. Besides collisions, we tested several possible mechanisms as the source for the extra lines:

- Collective polarization of the gas
- Resultant dipole-dipole interactions
- Superradiant spontaneous emission
- Microwave fields up to twice as strong as experimental estimates

However, none of these tests accounted for the off-resonant transitions.

4.4 Conclusions

A new phenomenon that involves monochromatic pulses, capable of driving resonant transitions and modulating off-resonant transitions, was observed. A series of tests using PVN were conducted to assess the conditions required to modulate off-resonant transitions. The effects of collisions were tested by changing the backing pressure of the carrier gas, the concentration of PVN in the gas mixture, and by testing different sections of the gas pulse. No real indication was uncovered that collisions contribute in a significant way in modulating the off-resonance transitions. Furthermore, it was determined that as the power of the electric field or the duration of the pulse increases, the number of modulated transitions increases. Therefore, it was surmised that the number of Rabi cycles was crucial to the appearance of off-resonant transitions in the molecular signal. Experimentally, to make sure that these effects were not constrained to the nature of the molecule, different molecules were tested as well, including benzonitrile, 4-pentynenitrile and allyl chloride. In each case the same behavior was observed.

In collaboration with Dr. Francis Robicheaux a theoretical model was developed to compare against the experimental results. However, to date, the model has been unsuccessful at accounting for the full suite of experimental observations, most notably in not predicting the intensity and growing number of off-resonant transitions with increasing pulse power and/or duration. It is clear that the model is missing a key factor, yet to be determined. One option could be that the effects from the microwave reflections within the experimental chamber could be playing a role. Another, less likely possibility is that up to now the electric field used in the simulations is distinctly smaller, for some reason, than anticipated based on the electronics specifications. Nonetheless, this experimental discovery, where a single frequency pulse in the strong field regime produces measurable coherent signals from other species-specific transitions is likely to speed the analysis of microwave spectra, since it not only helps deconvolute the spectrum but it also helps establish the connectivity of the transitions, which grow and spread with increasing power/pulse duration from the two levels initially involved in the resonant transition.

4.5 References

1. Grabow, J.-U., Fourier Transform Microwave Spectroscopy Measurement and Instrumentation. In *Handbook of High-Resolution Spectroscopy*, Wiley, Ed. 2011; p 723.
2. McGurk, J. C.; Schmalz, T. G.; Flygare, W. H., Fast passage in rotational spectroscopy: Theory and experiment. *The Journal of Chemical Physics* **1974**, *60*, 4181-4188.
3. McGurk, J. C.; Mäder, H.; Hofmann, R. T.; Schmalz, T. G.; Flygare, W. H., Transient emission, off-resonant transient absorption, and Fourier transform microwave spectroscopy. *The Journal of Chemical Physics* **1974**, *61*, 3759-3767.
4. Kasuga, T.; Amano, T.; Shimizu, T., Adiabatic Rapid Passage in Microwave-Microwave Double Resonance on a Three-Level System of the OCS Molecule. *Chem Phys Lett* **1976**, *42*, 278-282.
5. Hoke, W. E.; Bauer, D. R.; Flygare, W. H., Mdependence of T1 and T2 for the inversion doublets of ¹⁵NH₃. *The Journal of Chemical Physics* **1977**, *67*, 3454-3461.
6. Vogelsanger, B.; Bauder, A.; Mäder, H., Two-dimensional experiments with collision-induced transfer of populations in microwave Fourier transform spectroscopy. *The Journal of Chemical Physics* **1989**, *91*, 2059-2068.
7. Grabow, J. U., Fourier transform microwave spectroscopy: handedness caught by rotational coherence. *Angew Chem Int Ed Engl* **2013**, *52*, 11698-700.
8. Brown, G. G.; Dian, B. C.; Douglass, K. O.; Geyer, S. M.; Shipman, S. T.; Pate, B. H., A broadband Fourier transform microwave spectrometer based on chirped pulse excitation. *Rev Sci Instrum* **2008**, *79*, 053103.
9. Park, G. B.; Field, R. W., Perspective: The first ten years of broadband chirped pulse Fourier transform microwave spectroscopy. *J Chem Phys* **2016**, *144*, 200901.
10. Schmalz, T. G.; Flygare, W. H., *Coherent Transient Microwave Spectroscopy and Fourier Transform Methods*. Springer: 1978.
11. Schmitz, D.; Alvin Shubert, V.; Betz, T.; Schnell, M., Multi-resonance effects within a single chirp in broadband rotational spectroscopy: The rapid adiabatic passage regime for benzonitrile. *Journal of Molecular Spectroscopy* **2012**, *280*, 77-84.
12. Vitanov, N. V.; Halfmann, T.; Shore, B. W.; Bergmann, K., Laser-Induced Population Transfer by Adiabatic Passage Techniques. *Annu. Rev. Phys. Chem.* **2001**, *52*, 763-809.
13. Prozument, K.; Suleimanov, Y. V.; Buesser, B.; Oldham, J. M.; Green, W. H.; Suits, A. G.; Field, R. W., A Signature of Roaming Dynamics in the Thermal Decomposition of Ethyl Nitrite: Chirped-Pulse Rotational Spectroscopy and Kinetic Modeling. *J Phys Chem Lett* **2014**, *5*, 3641-8.
14. Abeysekera, C.; Joalland, B.; Ariyasingha, N.; Zack, L. N.; Sims, I. R.; Field, R. W.; Suits, A. G., Product Branching in the Low Temperature Reaction of CN with Propyne by Chirped-Pulse Microwave Spectroscopy in a Uniform Supersonic Flow. *J Phys Chem Lett* **2015**, *6*, 1599-604.
15. Park, G. B.; Womack, C. C.; Whitehill, A. R.; Jiang, J.; Ono, S.; Field, R. W., Millimeter-wave optical double resonance schemes for rapid assignment of perturbed spectra, with applications to the C(1)B(2) state of SO₂. *J Chem Phys* **2015**, *142*, 144201.
16. Schmitz, D.; Shubert, V. A.; Patterson, D.; Krin, A.; Schnell, M., Phase Dependence of Double-Resonance Experiments in Rotational Spectroscopy. *The Journal of Physical Chemistry Letters* **2015**, *6*, 1493-1498.
17. Patterson, D.; Doyle, J. M., Sensitive chiral analysis via microwave three-wave mixing. *Phys Rev Lett* **2013**, *111*, 023008.

18. Zhou, Y.; Grimes, D. D.; Barnum, T. J.; Patterson, D.; Coy, S. L.; Klein, E.; Muentner, J. S.; Field, R. W., Direct detection of Rydberg–Rydberg millimeter-wave transitions in a buffer gas cooled molecular beam. *Chemical Physics Letters* **2015**, *640*, 124-136.
19. Hernandez-Castillo, A. O.; Abeysekera, C.; Hays, B. M.; Zwier, T. S., Broadband multi-resonant strong field coherence breaking as a tool for single isomer microwave spectroscopy. *J Phys Chem A* **2016**, *145*.
20. Shternin, P. S.; Gericke, K.-H.; Vasyutinskii, O. S., The polarisation of two-photon excited fluorescence in rotating molecules. *Molecular Physics* **2010**, *108*, 813-825.
21. Shore, B. W.; Knight, P. L., The Jaynes-Cummings Model. *Journal of Modern Optics* **1993**, *40*, 1195-1238.
22. Grimes, D. D.; Coy, S. L.; Barnum, T. J.; Zhou, Y.; Yelin, S. F.; Field, R. W., Direct single-shot observation of millimeter wave superradiance in Rydberg-Rydberg transitions. *Phys Rev A* **2017**, *95*, 043818-043823.
23. Grimes, D. D.; Barnum, T. J.; Zhou, Y.; Colombo, A. P.; Field, R. W., Coherent laser-millimeter-wave interactions en route to coherent population transfer. *J Chem Phys* **2017**, *147*, 144201.
24. Martinis, J. M.; Nam, S.; Aumentado, J.; Urbina, C., Rabi oscillations in a large Josephson-junction qubit. *Phys Rev Lett* **2002**, *89*, 117901.
25. Park, G. B.; Field, R. W., Edge effects in chirped-pulse Fourier transform microwave spectra. *Journal of Molecular Spectroscopy* **2015**, *312*, 54-57.
26. Harris, F. J., On the Use of Windows for Harmonic Analysis with the DiscreteFourierTransform. *Proc. IEEE* **1978**, *66*, 51-83.
27. Kaiser, J. F., Nonrecursive Digital Filter Design Using the I0-Sinh Window Function. *Proc. IEEE* **1974**, 20-23.
28. Bloomfield, P., *Fourier Analysis of Time Series: An Introduction*. . New York: Wiley-Interscience: New York, 2000.
29. Pickett, H. M., The Fitting and Prediction of Vibration-Rotation Spectra with Spin Interactions. *J. Mol. Spec.* **1991**, *148*, 371-377.
30. Sakurai, J. J.; Napolitano, J., *Modern Quantum Mechanics*. 2nd edition ed.; Pearson Education: 2014.
31. Varsholovich, Chapter 8. In *Quantum Theory of Angular Momentum*., 1988.

CHAPTER 5. SPECTROSCOPIC CHARACTERIZATION OF MODEL AROMATIC SUBSTITUENTS OF LIGNIN BY BROADBAND CHIRPED-PULSE MICROWAVE SPECTROSCOPY

5.1 Introduction

The production of biofuels and bioenergy from lignocellulosic residues or energy crops constitutes one of the major solutions for providing an alternative to fossil fuels.¹ Since lignin is a major byproduct of second-generation bioethanol production it is considered as a potential source of aromatic feedstocks that could be used as biofuels.² Moreover, lignin is one of the three main components of biomass and one of the most abundant naturally occurring biopolymers on Earth, accounting for 15-25% (w/w) of herbaceous biomass,³ second only to cellulose and hemicellulose.⁴ Therefore, it is important to understand the properties of lignin in order to increase the efficacy with which it can be broken down during biofuel extraction. Lignin is an irregular biopolymer built from three closely-related phenolic monomers, the monolignols *p*-coumaryl, coniferyl, and sinapyl alcohol. These three monomers are composed of aromatic rings with varying numbers of hydroxyl and methoxy substituents. These monomers are held together by unique chemical linkages that determine the macroscopic properties of the lignin itself. Since lignin is formed by a free radical process, the detailed macromolecular structure of lignin, and how it varies from plant to plant, is still an active area of investigation.

Since lignin is an aromatic-rich polymer, several investigations of the UV spectra of model lignin compounds have been carried out previously, including work from our group on several phenol and alkyl phenol derivatives, guaiacol, syringol and its *para*-methylated derivatives, providing information on gas-phase structures in the electronic ground and excited states of these molecules. The ultraviolet spectra of guaiacol and syringol, which differ by a single methoxy group on the aromatic ring, were previously found to be surprisingly different, providing a basis for their spectroscopic recognition in lignin oligomers.⁵ While there are no previous reports of rotational spectroscopy of guaiacol, syringol, 4-methyl guaiacol and 4-vinyl guaiacol, there are previous high-resolution spectroscopy measurements on closely related molecules, such as: *p*-vinylphenol⁶,⁷ and *p*-coumaric acid⁸.

This chapter discusses the broadband CP-FTMW spectra of guaiacol, syringol, 4-methyl guaiacol, and 4-vinyl guaiacol, recorded under jet-cooled conditions over the 2-18 GHz frequency

range. Spectra of ^{13}C isotopomers of guaiacol were measured and assigned, allowing a detailed structure determination of this molecule. In the case of syringol, tunneling splitting due to OH hindered rotation was observed, from which the V_2 barrier was deduced. Comparison of this value with that for phenol provides evidence for the effect of the intramolecular $\text{OH}\cdots\text{OCH}_3$ H-bond present in syringol. For 4-methyl guaiacol, the barrier to internal rotation of the methyl group (V_3) was determined. This study provides a foundation for subsequent studies aimed at understanding the thermal decomposition of these molecules.

5.2 Experimental Methods

Guaiacol (98%), syringol (2,6-dimethoxyphenol, 99%), 4-methylguaiacol (98%), and 4-vinylguaiacol (98%) samples were all purchased from Sigma Aldrich and introduced into the gas phase by placing a small amount in a stainless-steel sample holder behind a solenoid-driven pulsed valve (Parker series 9). The solenoid valve was triggered at 10 Hz repetition rate using a home-made driver. To increase the vapor pressure of the samples, the sample holder in which they were kept was heated using a heating rope. These set of experiments were performed with the new chamber designed by Dr. Brian Hays. The experimental set up is described in section 2.3, and the arrangement of the microwave components is described in section 2.4.1.

All the geometry optimizations and harmonic vibrational frequency calculations were performed using the Gaussian09 program suite.⁹ Geometry optimizations for all four molecules were carried out using density functional theory (DFT) that employed the B2PLYP functional including Grimme's dispersion correction¹⁰ and Becke-Johnson damping¹¹, with a correlation consistent basis set, aug-cc-pVTZ. This level of theory has been shown to yield rotational constants that are in close agreement with experiment. The harmonic vibrational frequency calculations were performed at the afore-mentioned level of theory.

5.3 Results

5.3.1 Guaiacol

The microwave spectrum from 2-18 GHz is shown in Figure 5.1. This spectrum contains *a*- and *b*-type transitions belonging to *R* and *Q*-branches. The *a*-type transitions were the strongest in intensity, consistent with the calculated dipole moment components listed in Table 5.1.

Assignment of the spectrum was made using Pickett's SPFIT/SPCAT suite of programs¹². Watson's A-type reduced Hamiltonian in the I' representation was used to fit the spectra. Given the rigidity of the molecule, only the rigid rotor rotational constants were needed for a suitable fit at the present resolution. Attempts to determine the centrifugal distortion constants failed to improve the fit, which was already within the experimental uncertainty (~ 60 kHz) with an rms of 28.4 kHz.

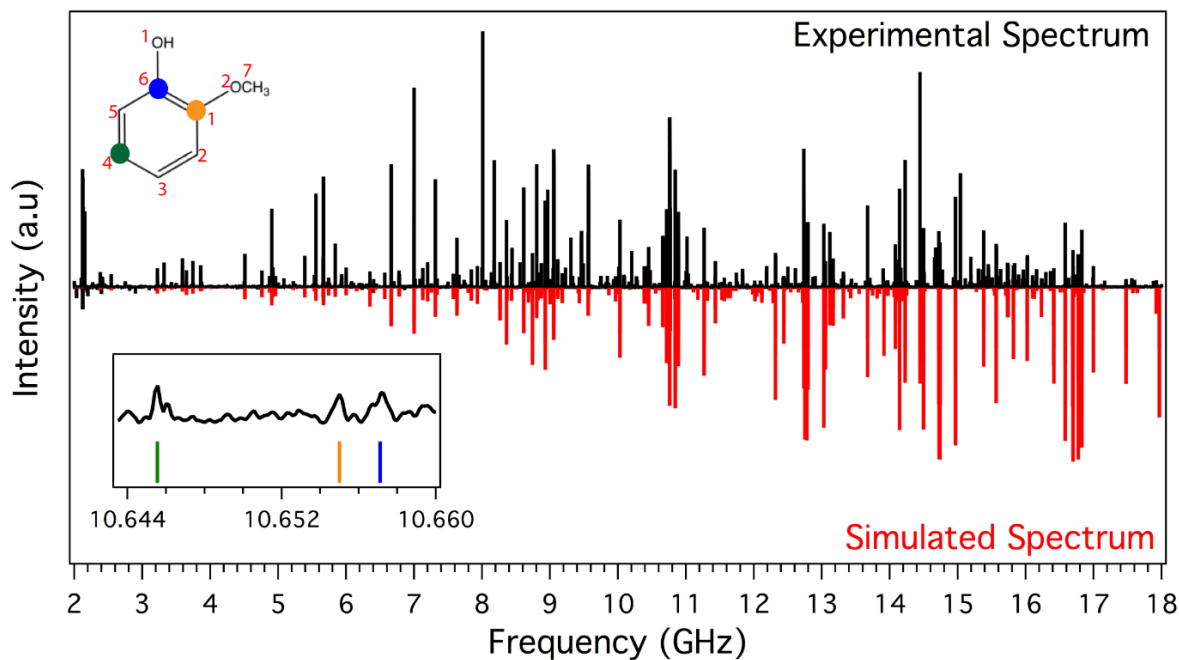


Figure 5.1: Broadband spectrum of guaiacol over the 2-18 GHz range. The 2-8 GHz frequency region was recorded heating the sample holder to 110 °C with the sample entrained in 1.03 bar of He, and 30 FIDs recorded per gas pulse. For the 8-18 GHz frequency region the sample was heated to 105°C. The rotational temperature was determined to be 1.56 ± 0.12 K. The blank subtracted experimental spectrum is shown in black and the simulated spectrum is illustrated in red. The inset show transitions due to the isotopic species in natural abundance.

The full set of spectroscopic parameters listed in Table 5.1 are in good agreement with the calculations, with the most significant error (0.38%) associated with the A rotational constant. When comparing the inertial defect of guaiacol (-3.46 uA^2) and anisole (-3.49 uA^2)¹³ one can see that the hydroxy group doesn't have a big effect on the planarity of the molecule in the electronic ground state. The magnitude of the inertial defect arises from the two out-of-plane hydrogens of the methoxy methyl group, with the OH hydrogen nearly in-plane so as to form an intramolecular

H-bond with the methoxy oxygen. In so doing, the oxygen lone pairs can engage in hyperconjugation with the aromatic ring, much as has been observed in previous studies of phenol¹⁴, anisole¹³, styrene¹⁵, and *p*-vinylphenol⁷.

Table 5.1: List of spectroscopic parameters used to fit guaiacol and its isotopomers. The atoms follow the numbering label showed in red in Figure 5.1.

	(CH ₃ O)C ₆ H ₄ OH	B2PLYP-D3BJ aug-cc-pVTZ	¹³ C(1) (CH ₃ O)C ₆ H ₄ OH	¹³ C(2) (CH ₃ O)C ₆ H ₄ OH	¹³ C(3) (CH ₃ O)C ₆ H ₄ OH
<i>A</i> (MHz)	2607.0533(266) ^d	2617.17475	2606.883(54)	2580.022(115)	2571.661(57)
<i>B</i> (MHz)	1560.7897(160)	1566.0881	1559.816(36)	1560.840(57)	1551.229(36)
<i>C</i> (MHz)	982.8693(142)	985.90801	982.4805(397)	979.0168(261)	974.0434(237)
μ_a (D)	-	2.051	-	-	-
μ_b (D)	-	-1.770	-	-	-
μ_c (D)	-	0.000	-	-	-
Δ (uA ²) ^a	-3.46	-3.19	-3.47	-3.45	-3.46
σ (kHz) ^b	28.4	-	39.6	54.4	35.5
N ^c	120	-	25	23	22

	¹³ C(4) (CH ₃ O)C ₆ H ₄ OH	¹³ C(5) (CH ₃ O)C ₆ H ₄ OH	¹³ C(6) (CH ₃ O)C ₆ H ₄ OH	¹³ C(7) (CH ₃ O)C ₆ H ₄ OH
<i>A</i> (MHz)	2602.775(100)	2600.015(116)	2594.845(116)	2599.051(70)
<i>B</i> (MHz)	1536.101(87)	1545.463(071)	1559.945(41)	1525.076(41)
<i>C</i> (MHz)	972.4424(311)	975.7752(280)	980.8160(249)	967.5178(312)
μ_a (D)	-	-	-	-
μ_b (D)	-	-	-	-
μ_c (D)	-	-	-	-
Δ (uA ²) ^a	-3.47	-3.46	-3.47	-3.48
σ (kHz) ^b	43.2	37.3	50.9	38.6
N ^c	21	23	22	22

^a Inertial defect $\Delta I = I_c - I_b - I_a$. ^b Number of transitions in the fit. ^c Root-mean-square deviation of the fit. ^d Standard error in parentheses in units of the last digit.

Given the high signal-to-noise (S/N) of the spectrum, it was possible to assign the ¹³C isotopologues in natural abundance. The sets of best-fit rotational constants are listed in Table 5.1. It wasn't possible to investigate the ¹⁸O isotopologues; therefore, it was not possible to determine the bond lengths and angles associated with these atoms. The experimentally derived inertial defects for the isotopic species are close in magnitude to one another and to that from the all ¹²C

guaiacol, ranging from -3.46 to -3.48 uA². This is a good indication that the experimental molecular parameters derived for the ¹³C isotopologues are correct.

The rotational constants determined could be used to determine the bond lengths and angles in the aromatic ring by applying Kraitchman's equations¹⁶. However, the r_s evaluation is subject to several inconsistencies, it is known that the addition of an asymmetric substituent onto the phenyl ring has the effect of introducing a small rotation between the ring and the inertial axes, thus degrading the accuracy of many of the reported r_s parameters.¹³ A global, least-squares fit to all available rotational constants usually can average over such problems. By using STRFIT¹⁷, it was possible to determine the carbon-carbon bond lengths and angles of the phenyl ring. Table 5.2 shows the experimental and the calculated parameters at the B2PLYP-D3BJ/aug-cc-pVTZ level of theory. While these are in good agreement, it is worth noting that the C-O bond lengths are especially sensitive to the rotational constants, as one might anticipate given that no isotopic data is available to pin down the O-atom position. As a result, without such data (e.g., from ¹⁸O isotopologues), it is not possible to extract a complete molecular geometry from the present data.

Table 5.2: Comparison of experimental and calculated geometrical parameters for guaiacol. The standard deviation of the fit was 0.0047 Å. The atoms follow the numbering label showed in red in Figure 5.1.

	Experimental	Calculation		Experimental	Calculation
Distances (Å)			Angles (°)		
C(1)-C(2)	1.388(3)	1.388	C(1)C(2)C(3)	119.75(36)	119.59
C(2)-C(3)	1.399(5)	1.396	C(2)C(3)C(4)	120.29(21)	120.20
C(3)-C(4)	1.390(4)	1.387	C(3)C(4)C(5)	120.23(12)	120.20
C(4)-C(5)	1.397(3)	1.394	C(4)C(5)C(6)	119.94(19)	119.92
C(5)-C(6)	1.386(4)	1.384	O(1)C(6)C(1)	-	120.07
C(1)-C(6)	1.408(3)	1.403	C(6)O(1)H	-	107.50
C(6)-O(1)	-	1.362	C(1)O(2)C(7)	-	117.42
C(1)-O(2)	-	1.371	O(2)C(1)C(2)	-	125.83
O(2)-C(7)	-	1.420			
O(1)-H	-	0.966			

There is a small, but clear, bond alternation in the ring; for example, $r(\text{C}(1)\text{-C}(2)) < r(\text{C}(4)\text{-C}(5))$, and $r(\text{C}(2)\text{-C}(3)) > r(\text{C}(3)\text{-C}(4))$, structural effects also captured by the calculations. It is important to notice that the distortion of the ring is similar to that present for anisole¹³, where the bonds most affected by the hyperconjugation of the oxygen lone pair with the aromatic ring shrinks relative to the 1.390 Å in benzene. In phenol this effect is less noticeable.¹⁴ The longest bond in guaiacol's aromatic ring is $r(\text{C}(1)\text{-C}(6))$ involving the two carbon atoms that hold a substituent group, and the adjacent bonds are the shortest, showing either the effects of the steric impedance between these two groups or the hyperconjugation of the oxygen lone pair with the aromatic ring. The hydrogen bond between the hydroxy and the methoxy groups doesn't seem able to compensate for the effect of the methoxy group on the ring.

5.3.2 2,6-dimethoxyphenol (Syringol)

The 2-18 GHz CP-FTMW spectrum of syringol is presented in Figure 5.2a. The calculated dipole moment components for syringol indicates that only *a*- and *b*- type transitions will be present in the microwave spectrum. A preliminary fit was obtained using the theoretical rigid-rotor spectrum predicted with the rotational constants calculated at B3PLYP-D3BJ/aug-cc-pVTZ (Table 5.3). As the magnified view of a small segment of the spectrum that shows that many of the rotational transitions appear as doublets arising from the hindered rotation of the OH group. Since syringol possesses a symmetric molecular frame with two methoxy groups, internal rotation of the OH group connects equivalent minima. Due to the OH group internal rotation the μ_a R-type transitions are split into doublets separated by approximately 0.9 MHz, while the *b*-type transitions were not split. Similar tunneling splittings have been observed in phenol^{18, 19}, propofol²⁰ and its symmetric para-derivatives²¹⁻²³. The rotational transitions were analyzed with a two-state Hamiltonian without coupling terms,

$$\begin{pmatrix} H_0 & 0 \\ 0 & H_1 + \Delta E_{10} \end{pmatrix}$$

where H_0 and H_1 are semirigid-rotor Hamiltonians and ΔE_{10} is the relative energy between the two torsional sub-states ($v=0^+$ and $v=0^-$).

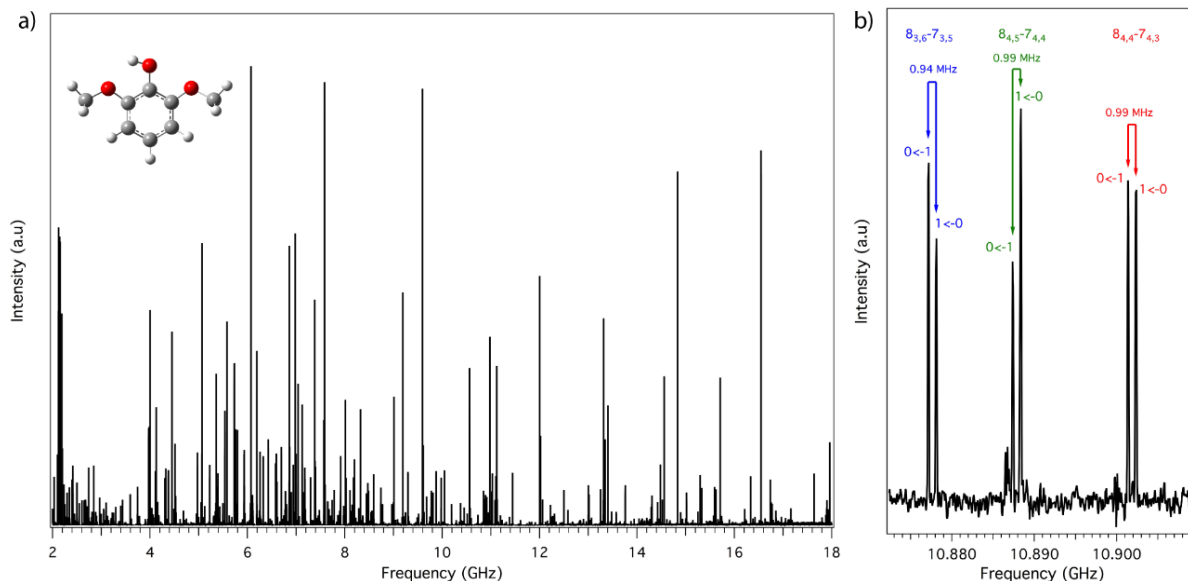


Figure 5.2: a) Broadband spectrum of syringol from 2-18 GHz. The 2-8 GHz frequency region was recorded heating the sample holder to 148 °C with the sample entrained in 2.75 bar of He, collecting 30 FIDs per gas pulse. For the 8-18 GHz frequency region the sample was heated to 130 °C. The rotational temperature of syringol following supersonic expansion was determined to be 1.7 ± 0.3 K. b) Close-up view of the $8_{3,6}-7_{3,5}$, $8_{4,5}-7_{4,4}$, and $8_{4,4}-7_{4,3}$ transitions showing their tunneling splitting due to the internal rotation of the hydroxyl group. See text for further discussion.

Table 5.3 lists the results of the fit using a Watson's A-reduction semirigid rotor Hamiltonian (I^r representation) for a set of 528 observed transitions. For this fit the Coriolis interaction between the two sub-states was neglected. These contributions tend to be appreciable in cases where the asymmetry and torsional splitting are accidentally close; nonetheless, similar to propofol²⁰, for syringol there was no significant deviation from semi-rigid behavior. Not surprisingly, as in guaiacol and other similar molecules there was no evidence of tunneling splittings associated with the internal rotation of the methyl groups.

The assignment of the ^{13}C -monosubstituted species in natural abundance was possible, and eight sets of molecular parameters were obtained. Due to its lower natural abundance (0.2%) the assignment of the spectrum of the ^{18}O species was not attempted. When the isotopic substitution was in any position off the b -axis the tunneling splitting was no longer present, since the symmetry was broken. However, the determination of the carbon-backbone structure was not possible due to the large amplitude motion arising from the OH internal rotation coordinate. The r_s structure contained several inconsistencies, such as imaginary coordinates. Usually, a global, least-squares

fit to all available rotational constants averages over such problems, however, in this case, it was not possible to derive a meaningful r_0 geometry.

Table 5.3: Experimental rotational parameters for syringol.

Syringol	Experimental	Calculated
A (MHz)	2267.066041(162) ^a	2280.7794
B (MHz)	768.348315(47)	769.21605
C (MHz)	578.479855(41)	579.43741
ΔE_{10} (MHz) ^b	0.47194(73)	-
V_2 (cm ⁻¹) ^c	1978(7)	1962
μ_a (D)	-	-1.36
μ_b (D)	-	-1.70
μ_c (D)	-	0.00
Δ (uA ²) ^d	-7.036	-6.398
σ (kHz) ^e	27.29	-
N^f	528	-

^a Standard error in parenthesis in units of the last digit
^b energy difference between the torsional tunneling substates $\sigma=1/0$. ^c Barrier height. ^d Inertial defect $\Delta I=I_c-I_b-I_a$. ^e Root-mean-square deviation of the fit. ^f Number of transitions in the fit.

In order to examine the structural changes associated with the OH torsion, a relaxed potential energy curve for OH internal rotation was calculated at the DFT B3LYP /def2tzvp level of theory, yielding a value of 1962 cm⁻¹. To get a quantitative description of the OH torsion the Meyer's one-dimensional flexible model²⁴ was applied to the ΔE splitting, thus determining the V_2 barrier using the following equation,

$$V(\tau) = \frac{1}{2}V_2(1 - \cos(2\tau))$$

where τ is the internal rotation angle of OH, assumed to be zero when OH lies in the plane of the phenyl ring. Using this model, the range 2π for τ was resolved with 37 mesh points and a barrier of 1978 cm⁻¹ was determined, a value fortuitously close to the DFT result. It is worth noticing that

since in the calculation the CCO angle only changes 0.003 degrees from 0° to 180°, structural relaxation was not considered.

The hydroxyl torsional barrier height can be compared to previous studies on phenolic molecules (Table 5.4). The experimental barrier height of syringol (1978 cm⁻¹) is greater than the barriers determined for phenol (1213(18) cm⁻¹), propofol(Gg) (905-940 cm⁻¹), and even *p*-hydroxypyridine (1513(10) cm⁻¹). The magnitude of the internal rotor barrier is affected by the electron donor/acceptor capabilities of the exocyclic substituent; for example, in 4-hydroxypyridine the electron-withdrawing effect of the nitrogen atom is responsible for increasing the barrier relative to phenol, whereas in propofol the electron-donation from the two isopropyl groups causes the barrier height to be reduced considerably. In syringol, the main reason for the significant increase in the barrier height is the additional stabilization at planar geometries from the intramolecular hydrogen bond that the OH group forms with the neighboring methoxy groups.

Table 5.4: Comparison of internal rotation barriers for the hydroxyl group in phenol derivatives.

	Torsional splitting ΔE_{10} (MHz)	Barrier height V (cm ⁻¹)
Propofol ²¹	104.0989(52)	905-940
Phenol ^{19, 20}	55.97	1213(18)
<i>p</i> -hydroxypyridine ²⁴	7.97(4)	1513(10)
Syringol	0.47194(73)	1978(7)

5.3.3 4-methyl guaiacol (4-MG)

4-MG has a methyl group on the phenyl ring *para* to the OH substituent. The addition of this methyl group raises the possibility that splittings due to methyl internal rotation will be present. This is indeed the case, as shown for the $7_{0,7}-6_{1,6}$ and $7_{1,7}-6_{0,6}$ transitions in Figure 5.3. As the labels show, we were able to assign transitions due to rotational levels in the $0a_1$ and $1e$ methyl rotor levels, labeled simply as A and E in the figure. Since the nuclear spin symmetries of these levels are different, collisional cooling does not efficiently remove population from the $1e$ level during the supersonic expansion.²⁵ In order to get some sense for the barrier height of the ring methyl group, we carried out a relaxed potential energy scan varying the dihedral angles for the

methyl hydrogens using a spacing of 10° . The result could be fit as a pure V_3 potential, which at the B3LYP-D3BJ/def2tzvp level of theory was calculated to be $V_3 = 63 \text{ cm}^{-1}$.

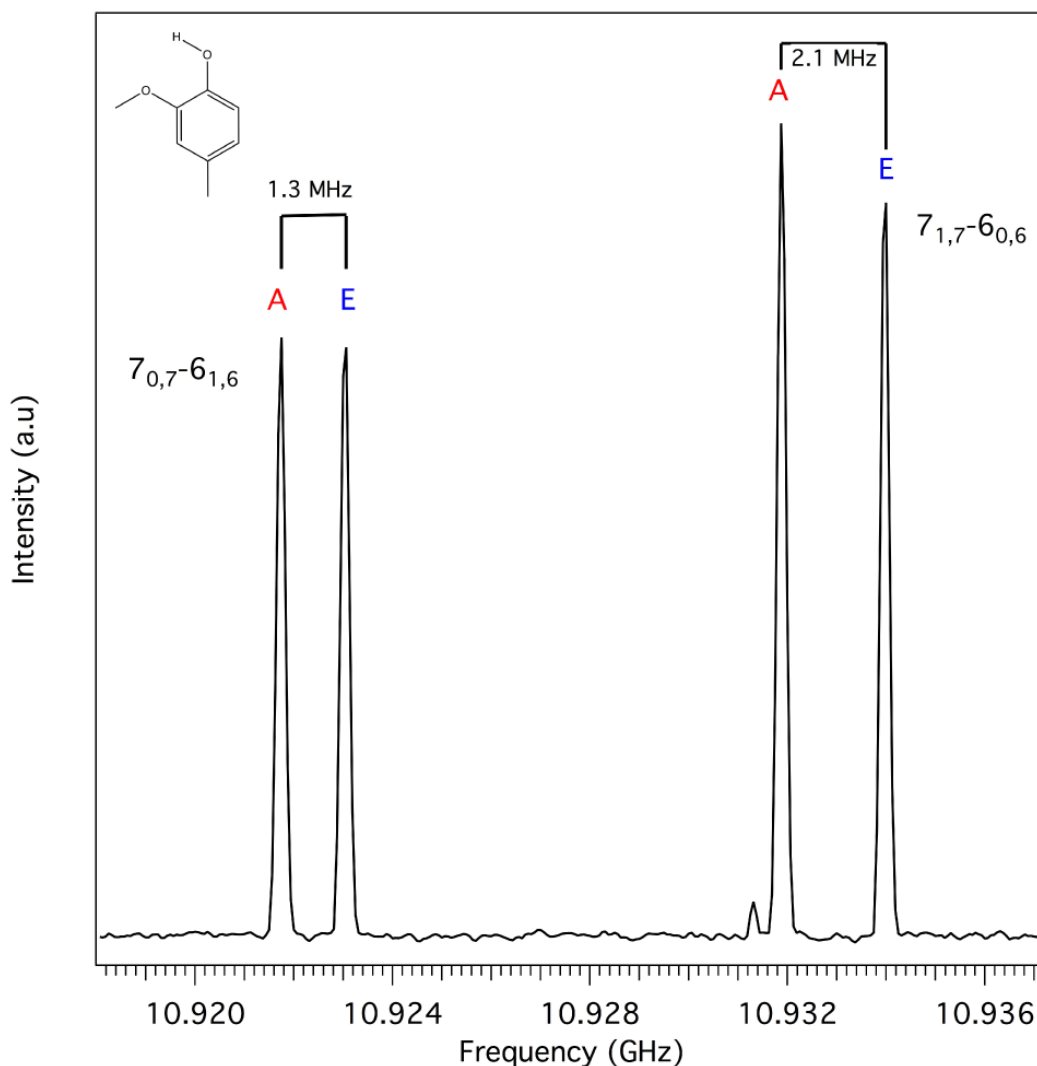


Figure 5.3: A window of about 20 MHz taken from the 8-18 GHz spectrum of 4-MG, highlighting the $7_{0,7}-6_{1,6}$ and $7_{1,7}-6_{0,6}$ transitions, which are split by 1.3 and 2.1 MHz, respectively, due to methyl internal rotation. The spectrum was recorded by heating the sample holder to 123°C with the sample entrained in 0.7 bar of He, accumulating 20 FIDs per gas pulse. The rotational temperature was determined to be $1.79 \pm 0.3 \text{ K}$.

As a first step in fitting the experimental spectrum for 4-MG, SPFIT/SPCAT¹² was used to obtain a fit excluding the effect of internal rotation. The assignment started with *b*-type *R*-branch transitions, because, the dipole moment components suggest a spectrum with intense *b*-type transitions. Transitions assigned preliminarily to A species often appeared as closely spaced

doublets, as in Figure 5.3, with the other member assigned to the E internal rotation symmetry species of the same rotational transitions. The program *XIAM*²⁶ was used to fit the full set of transitions including internal rotation-rotation coupling. Using the program, it was possible to assign 173 transitions, 120 of which belong to the A species and 53 to the E species, with a standard deviation of 46 kHz. The fitted molecular parameters are summarized in Table 5.5. The three linear combinations of the rotational constants $B_J=1/2(B+C)$, $B_K=A-1/2(B+C)$, $B_- = 1/2(B-C)$, the V_3 potential, and the angles δ and ε were determined. Because the frame of the aromatic ring in 4-MG is quite rigid, all centrifugal distortion constants are small; therefore, it was only possible to fit one centrifugal distortion constant (Δ_K) based on the jet-cooled data. In Table 5.5 the experimentally deduced rotational constants are compared with those from quantum chemical calculations, showing excellent agreement between the two. A V_6 contribution to the potential could generate additional splittings of the A and E torsional species of the threefold rotor if the lowest torsional level lies below the local maxima created by the 6-fold term. Since no additional splittings were observed experimentally this V_6 term is small or completely absent.

The barrier to methyl hindered rotation in 4-MG was previously determined by our group using fluorescence spectroscopy as $V_3 = 70 \text{ cm}^{-1}$, a value which is well reproduced by the present work using microwave splittings.⁵ The two methods are nicely complementary, since the fluorescence-based scheme determines the hindered rotor energy levels up to and through the barrier, while the microwave data on the jet-cooled molecules records high resolution data exclusively on the $0a_1$ and $1e$ levels, projecting via extrapolation to a barrier height well above the energies of the directly probed levels.

Given the positions of the OH, OCH₃, and methyl groups on the ring relative to one another, it is interesting to compare the methyl rotor barrier in 4-MG to these simpler analogs: *cis-m*-methyl anisole and *p*-cresol (or 4-methyl phenol). The ground state methyl rotor barriers are known for each of these simpler molecules based on previous work.^{27, 28} Note that the V_3 barrier we have derived for methyl hindered rotation in 4-MG ($V_3 = 68.8 \text{ cm}^{-1}$) is quite similar to that found for *cis-m*-methyl anisole studied by Ferres et al.,²⁷ ($V_3 = 55.7 \text{ cm}^{-1}$). Furthermore, *p*-cresol (4-methyl phenol) has a very low methyl rotor barrier with both 6-fold and 3-fold terms: $V_3 = 18 \text{ cm}^{-1}$ and $V_6 = -13.8 \text{ cm}^{-1}$.²⁸ Whether fortuitous or not, the barrier for 4-MG is approximately the sum of the barriers from the individual OH and OCH₃ constituents.

Table 5.5: Molecular parameters of 4-methyl guaiacol. All parameters refer to the principal axis system. Watson's A reduction and I^r representation were used. The rotational constant of methyl rotor, F₀, was fixed at 158 GHz.

4-MG	Experimental	Calculated
A (MHz)	1891.868633(1086) ^a	1897.0835
B (MHz)	1168.206007(366)	1173.5124
C (MHz)	729.233617(326)	731.6489
Δ_K (kHz)	0.2041(145)	0.2180
V_3 (cm ⁻¹)	68.7679(2)	63.64
s^b	5.737329	-
$\angle(i,a)$ (°)	32.2905(5)	35.346
$\angle(i,b)$ (°)	57.7095(5)	54.654
$\angle(i,c)$ (°)	90.0017(1)	89.993
μ_a (D)	-	0.296
μ_b (D)	-	-2.829
μ_c (D)	-	0.00
Δ (uA ²) ^c	-6.716	-6.398
σ (kHz) ^d	45.57	-
N _A /N _E ^e	120/53	-

^a Standard error in parentheses in units of the last digit ^b Reduced barrier, defined as $s=4V_3/9F$. ^c Inertial defect $\Delta I=I_c-I_b-I_a$. ^d Root-mean-square deviation of the fit. ^e Number of A and E species lines (N_A/N_E).

5.3.4 4-vinyl guaiacol (4-VG)

4-vinyl guaiacol places the vinyl group para to OH. has two stable conformations, labeled as *syn*- and *anti*-, which are defined by the orientation of the vinyl group with respect of the methoxy group. From previous studies on the monolignols this molecule was expected to be structurally quite rigid since the intramolecular H-bond between the OH and methoxy groups locks in their relative orientation.²⁹ An important experimental challenge was that in order to get the

sample into the gas phase, it was necessary to heat the sample to temperatures where polymerization occurred to some extent inside the heated sample cylinder. This constrained the number of averages that could usefully be taken for a given sample, reducing the over-all signal size in the final spectrum relative to the other molecules in this series.

The SFCB/MSE^{30,31} method was used in order to facilitate assignment of the intermingled transitions due to the two conformations. Using the most recent line picking scheme, described in section 3.3.1, it was possible to acquire a set of species-specific transitions associated with each conformer. This scheme identified a set of three MSE frequencies at 10632.625, 12267.313, and 15554.375 MHz for SFCB measurements. The final SFCB measurement was recorded with a 1 μ s broadband sweep followed by three 150 ns single-frequency pulses. A gap of 50 ns was employed between the broadband chirp and the first single frequency pulse, while 5 ns gaps were left between the three single frequency pulses in order to avoid beats between them. Using the Matlab routine described in Appendix A.2, a total of 22 transitions were identified as having their intensities modulated more than 30% compared to the 8-18 GHz sweep in the absence of MSE. Noting that the experimental conformer-specific transitions matched the pattern of the calculated 8-18 GHz microwave spectrum for the *syn*-4-VG, these transitions were used as a starting point for the rigid rotor fit.

Using Pickett's SPFIT and SPCAT programs¹², a total of 143 transitions were assigned in the final fit, with a standard deviation of 37.4 kHz. As Table 5.6 shows, the experimental rotational constants from the fit are in close agreement with the calculated values, with a largest error of just 0.33% associated with the A rotational constant. Even though *syn*-4-VG is a relatively rigid molecule, once the calculated centrifugal distortion constants were included in the fit the rms error decreased, a behavior that was not observed in guaiacol or syringol. This suggests that the vinyl group may contribute significantly to the centrifugal distortion. Unfortunately, it was not possible to get a good fit for these constants, therefore for the final fit these values were fixed to the theoretical ones. Figure 5.4(a) presents the SFCB/MSE difference spectrum, where the modulated lines are plotted against the fitted transitions.

For the *anti*-4VG conformer, the method was repeated for the remaining unassigned transitions using the same microwave settings. In this case, we chose a set of MSE frequencies at 9130.875, 13415.313, 16373.313 MHz. Following assignment these transitions were assigned as $5_{2,4}-4_{1,3}$, $6_{3,4}-5_{2,3}$, and $6_{4,3}-5_{3,2}$ transitions, respectively. This second set of MSE frequencies

modulated 16 transitions more than 50% relative to the original sweep taken in their absence. The modulated transitions are plotted in Figure 5.4(b) against the fitted transitions for this conformer.

Table 5.6: Molecular parameters for *syn*- and *anti*-4-vinyl guaiacol.

4-VG	<i>syn</i>		<i>anti</i>	
	Experimental	Calculated	Experimental	Calculated
<i>A</i> (MHz)	1646.753225(144) ^a	1652.1596	1867.786124 (158)	1874.2983
<i>B</i> (MHz)	872.490958 (82)	874.3385	779.970050 (75)	781.7989
<i>C</i> (MHz)	572.904936 (63)	573.8423	552.777238 (55)	553.6226
Δ_J (kHz)	<i>fixed</i>	0.02096	-	0.01160
Δ_K (kHz)	<i>fixed</i>	0.08358	-	0.16252
Δ_{JK} (kHz)	<i>fixed</i>	0.01149	-	0.03534
δ_j (kHz)	<i>fixed</i>	7.69×10^{-3}	-	3.75×10^{-3}
δ_k (kHz)	<i>fixed</i>	0.04726	-	0.04467
μ_a (D)	-	0.347	-	-0.979
μ_b (D)	-	2.400	-	2.475
μ_c (D)	-	0.000	-	0.000
ΔE_{rel} (cm ⁻¹)	-	0	-	136
% ^b	75(3)	60.4	24(4)	39.6
Δ (uA ²) ^c	-3.99	-3.21	-4.27	-3.21
σ (kHz) ^d	37.44	-	39.06	-
N ^e	143	-	154	-

^a Standard error in parenthesis in units of the last digit ^b Boltzmann distribution. ^c Inertial defect $\Delta I = I_c - I_b - I_a$. ^d Root-mean-square deviation of the fit. ^e Number of transitions in the fit.

The line frequencies obtained through the SFCB/MSE difference spectrum were used for the initial rigid rotor fit using Pickett's spectral fitting programs.¹² The rotational spectrum of *anti*-4-VG is composed exclusive of a- and b-type transitions, with a total of 154 transitions that were fit using a Watson's A-reduction (I^r representation), with a standard deviation on the fit of 39.06

kHz. The constants derived from the fit are shown in Table 5.6, where they are compared with calculations. As with the *syn* conformer, the experimental constants are in excellent agreement with those from the calculations. Interestingly, in this case, the fit did not improve when adding the centrifugal distortion constants.

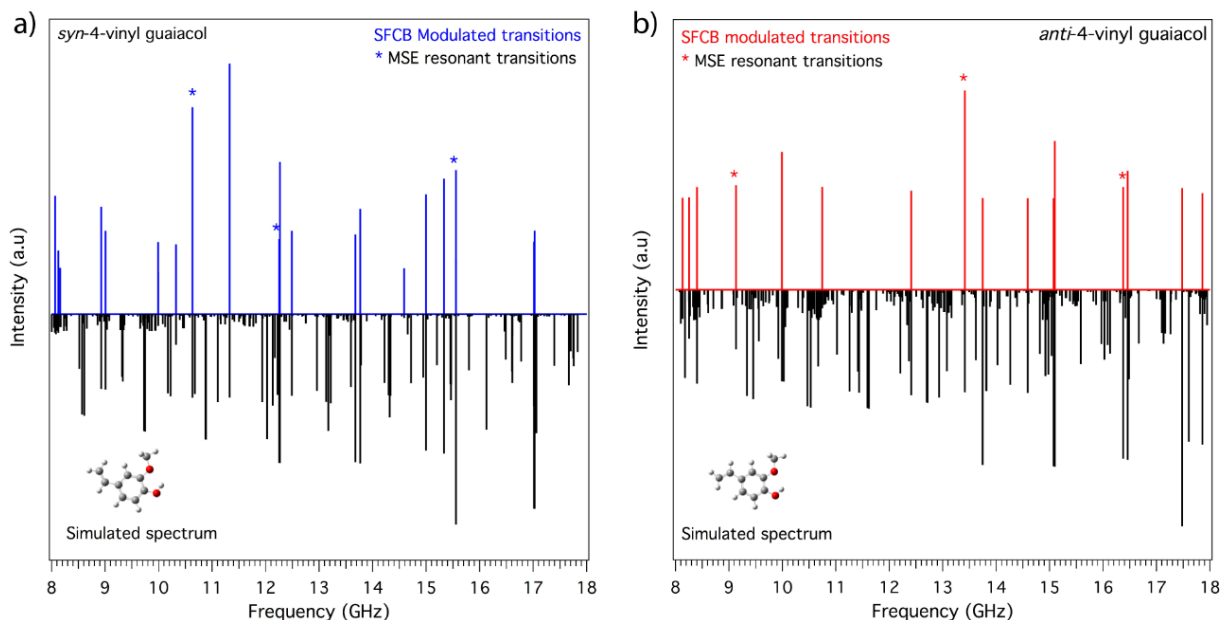


Figure 5.4: Experimental lines modulated in the SFCB difference spectrum compared to the simulated stick spectra for a) *syn*-4-VG and b) *anti*-4-VG. Experimental conditions: 1 μ s 8-18 GHz chirp, 50 ns gap and 3×100 ns single frequency pulses on frequencies labeled with asterisks, 100% TWTA gain level. The spectrum was recorded with the sample heated to 193 $^{\circ}$ C and entrained in 0.7 bar He. The timing of the experiment was set to record 30 FIDs per gas pulse.

Using the experimental rotational temperatures (1.7 ± 0.2 for *anti*-4-VG and 1.9 ± 0.2 for *syn*-4-VG) and the relationship between experimental integrated line intensities and column densities, it was possible to obtain percent abundances for the two conformers of $75 \pm 3\%$ *syn*-4-VG and $25 \pm 4\%$ *anti*-4-VG. The percent populations of the conformers at the pre-expansion temperature (466 K), calculated using the relative free energies are 60.4 and 39.6% for *syn*- and *anti*-4-VG respectively, which are relatively close to the experimental values. If the energetics from the calculations are accurate, this close correspondence would indicate that there is little collisional redistribution of population between the two conformers during the expansion.

5.4 Discussion

The microwave spectra of guaiacol, syringol, 4-MG, and 4-VG have been recorded and analyzed over the 2-18 GHz range under jet-cooled conditions, enabling the determination of the molecular rotational parameters. For all four molecules the calculated rotational constants at the B2PLYP-D3BJ/aug-cc-pVTZ level of theory are in excellent agreement with the experimental values. In guaiacol and syringol, data on the ^{13}C isotopologues in natural abundance provided a partial structural fit; however, the lack of ^{18}O data hindered determination of a full r_0 structure. Nevertheless, given the excellent correspondence between experiment and the B2PLYP-D3BJ calculations, it is worth looking in greater detail at the structures of guaiacol, syringol, 4-MG, and 4-VG to understand the structural changes induced by the addition of a methoxy group (in forming syringol), methyl group (in 4-MG) or vinyl group (4-VG) on the structures and bonding.

Figure 5.5 summarizes the calculated optimized structures for guaiacol, syringol, 4-MG, and the two conformers of 4-VG. Not surprisingly, in this set of five structures, the bond lengths and bond angles involving the hydroxy and methoxy substituents are nearly unchanged, and they distort the phenyl ring in similar ways. We surmise on this basis that these polar substituents are major factors in dictating any shift away from an unsubstituted aromatic ring.

The $\text{OH}\cdots\text{OCH}_3$ intramolecular H-bond lies in the plane of the phenyl ring and generally locks the molecule into a planar heavy-atom geometry. For these five molecules, the effect of this H-bond doesn't seem to have a significant impact on either the hydroxy or the methoxy bond angles. The $\text{C}(5)\text{C}(6)\text{O}(1)$ angle varies by less than 2 degrees for all molecules in the set compared to phenol, and the COH angle changes by less than one degree. When the bond lengths and angles of the methoxy substituent are compared to those in anisole, the change is less than one degree.

In guaiacol, the asymmetry of the single methoxy substituent propagates through the structure in subtle ways. As we have pointed out earlier, and as is apparent from Figure 5.5, the major effect of the methoxy group is to distort the phenyl ring away from six-fold symmetry, inducing clear alternation in bond lengths. The longest C-C bond in the phenyl ring is that which connects the two substituted carbons, calculated to be 1.403 Å. Whether this lengthening is a purely electronic effect or has some steric components associated with the crowding of the OH and methoxy substituents, is not clear. The bonds on either side shorten correspondingly to 1.384 and 1.388 Å. When combined with the shortened C(3)-C(4) bond on the opposite side of the ring (1.387 Å), this bond alternation indicates that this resonance structure, with double bond positions

shown in Figure 5.5a, gains in weight over its alternate, in which the single and double bonds are swapped in the ring.

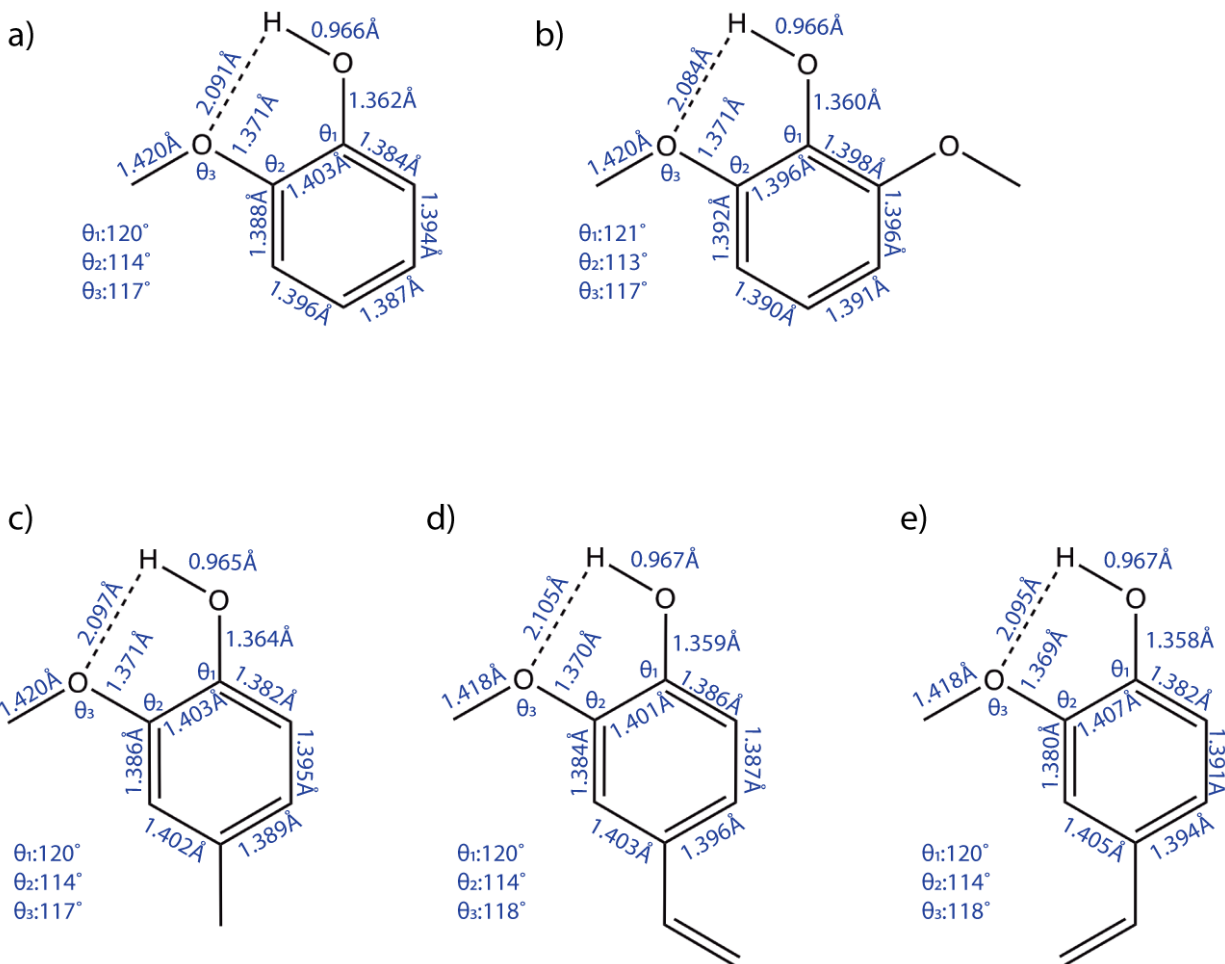


Figure 5.5: Summary of the calculated molecular geometries for: a) guaiacol, b) syringol, c) 4-MG, d) *anti*-4-VG, and e) *syn*-4-VG, all computed at the B2PLYP-D3BJ/aug-cc-pVTZ level of theory.

In syringol, the presence of the second methoxy group brings a near two-fold symmetry to the structure. Indeed, when tunneling of the OH group is considered, the molecule is effectively C_{2v} symmetry. Even in the optimized structure at one of the tunneling minima (as shown in Figure 5.5b), the C-C bond lengths in the aromatic ring are still nearly equivalent. From a dynamic and structural viewpoint, syringol's ability to undergo tunneling between the two in-plane OH torsional positions is most intriguing. In the microwave spectrum, we have resolved tunneling splittings in the b-type R-branch transitions due to the OH group tunneling through its torsional barrier between

equivalent in-plane geometries. The selection rules indicate that these involve lower-to-upper and upper-to-lower transitions, producing a splitting that is twice the energy separation between the 0^+ and 0^- tunneling levels (~ 1 MHz). A fit of this splitting to a one-dimensional, V_2 OH torsional potential predicts a barrier of 1960 cm^{-1} , more than 50% greater than in phenol, where no intramolecular H-bond exists.

This suggests that the stabilization of the in-plane geometry for the OH group is about two-thirds due to electronic effects of the OH group hyperconjugation with the ring, and one-third due to the stabilization of the H-bond itself. The effect of this increased barrier on the OH tunneling splitting is dramatic, since in phenol, the tunneling splitting is ~ 111 MHz,¹⁹ while in syringol, it drops to ~ 1 MHz. Given this small splitting, it is not surprising that zero-point shifts induced by the presence of even a single ^{13}C in an asymmetric position is sufficient to quench tunneling. One can also glean from the calculated structures a sense for the nature of the tunneling motion. Based on the optimized geometry for syringol in one of its tunneling minima (shown in Figure 5.5b), the most significant changes are in the C(ph)-O bond lengths and CCO bond angle of the two methoxy groups, which expand by 0.01 \AA and 2 degrees, respectively, when the OCH_3 is acting as H-bond acceptor.

5.5 Conclusions

The molecular rotational parameters of guaiacol, syringol, 4-MG, and 4-VG were determined experimentally using broadband microwave spectroscopy over the 2-18 GHz range. These values are in excellent agreement with those calculated at the B2PLYP-D3BJ/aug-cc-pVTZ level of theory. Spectra of ^{13}C isotopomers of guaiacol and syringol were measured and assigned; however, it was only possible to do a structural determination for guaiacol. In that case, the agreement between theoretically predicted structural parameters and those determined by experiment is better than 0.3% for both bond lengths and angles. Guaiacol has a small alternation in the C-C bond lengths in the aromatic ring. It is possible that the hyperconjugation of the oxygen lone pair with the aromatic ring shrinks the C(1)-C(2) and C(5)-C(6) bonds; however, this could also be due to steric impedance between the substituent groups.

In the case of syringol, tunneling splittings due to OH hindered rotation were observed. A simple 1D model for the process leads to a value of $V_2 = 1978\text{ cm}^{-1}$ for this barrier. This value is 50% greater than phenol's barrier, due to the presence of the methoxy groups that engage in

intramolecular H-bonding with the OH group. For 4-MG, the internal rotation barrier for the methyl group (V_3) was determined to be $68.7679(2) \text{ cm}^{-1}$ and seen to be consistent with the barrier deduced from LIF measurements by Dean et al.⁵

Furthermore, all the molecules studied in this chapter present a similar distortion of the phenyl ring, thus, it is possible to conclude that the polar substituents dictate the shifts from the unsubstituted aromatic ring. Of the two resonance structures in the aromatic ring, we see from the ring distortions that the ones shown in Figure 5.5 are more heavily weighted. Surprisingly, the vinyl group, which is asymmetrically conjugated with the phenyl ring, doesn't distort the ring in any significant way. The most significant change between the *cis* and *anti*-conformers is a slight modulation in the length of the C(1)-C(2) and C(5)-C(6) bonds.

Finally, the microwave data provided here can also be useful in subsequent pyrolysis studies of larger lignin oligomers, which may produce these molecules as pyrolysis intermediates. The pyrolysis of syringol is another important extension of previous work on the pyrolysis of guaiacol. The presence of two methoxy groups in syringol opens the way for a richer set of pyrolysis pathways via loss of one or two methyl groups.

5.6 References

1. Barakat, A.; Monlau, F.; Steyer, J. P.; Carrere, H., Effect of lignin-derived and furan compounds found in lignocellulosic hydrolysates on biomethane production. *Bioresour Technol* **2012**, *104*, 90-9.
2. Jiang, G.; Nowakowski, D. J.; Bridgwater, A. V., A systematic study of the kinetics of lignin pyrolysis. *Thermochimica Acta* **2010**, *498*, 61-66.
3. Buranov, A. U.; Mazza, G., Lignin in straw of herbaceous crops. *Industrial Crops and Products* **2008**, *28*, 237-259.
4. Huang, J.; Li, X.; Wu, D.; Tong, H.; Li, W., Theoretical studies on pyrolysis mechanism of guaiacol as lignin model compound. *Journal of Renewable and Sustainable Energy* **2013**, *5*.
5. Dean, J. C.; Navotnaya, P.; Parobek, A. P.; Clayton, R. M.; Zwier, T. S., Ultraviolet spectroscopy of fundamental lignin subunits: guaiacol, 4-methylguaiacol, syringol, and 4-methylsyringol. *J Chem Phys* **2013**, *139*, 144313.
6. de Groot, M.; Buma, W. J.; Gromov, E. V.; Burghardt, I.; Koppel, H.; Cederbaum, L. S., Combined experimental-theoretical study of the lower excited singlet states of paravinyl phenol, an analog of the paracoumaric acid chromophore. *J Chem Phys* **2006**, *125*, 204303.
7. Morgan, P. J.; Mitchell, D. M.; Pratt, D. W., High resolution electronic spectroscopy of p-vinylphenol in the gas phase. *Chemical Physics* **2008**, *347*, 340-345.
8. Smolarek, S.; Vdovin, A.; Perrier, D. L.; smit, J. P.; Drabbles, M.; Buma, W. J., High-Resolution Excitation and Absorption Spectroscopy of Gas-Phase p-Coumaric Acid: Unveiling an Elusive Chromophore. *J. Am. Chem. Soc.* **2010**, *132*, 6315–6317.
9. Frisch, M. J.; Trucks, G. W.; Schlegel, H. B.; Scuseria, G. E.; Robb, M. A.; Cheeseman, J. R.; Scalmani, G.; Barone, V.; Petersson, G. A.; Nakatsuji, H.; Caricato, X. L., M. ; Marenich, A.; Bloino, J.; Janesko, B. G.; Gomperts, R.; Mennucci, B.; Hratchian, H. P.; Ortiz, J. V.; Izmaylov, A. F.; Sonnenberg, J. L.; Williams-Young, D.; Ding, F.; Lipparini, F.; Egidi, F.; Goings, J.; Peng, B.; Petrone, A.; Henderson, T.; Ranasinghe, D.; Zakrzewski, V. G.; Gao, J.; Rega, N.; Zheng, G.; Liang, W.; Hada, M.; Ehara, M.; Toyota, K.; Fukuda, R.; Hasegawa, J.; Ishida, M.; Nakajima, T.; Honda, Y.; Kitao, O.; Nakai, H.; Vreven, T.; Throssell, K.; Montgomery, J. A.; Peralta, J., J. E. ; Ogliaro, F.; Bearpark, M.; Heyd, J. J.; Brothers, E.; Kudin, K. N.; Staroverov, V. N.; Keith, T.; Kobayashi, R.; Normand, J.; Raghavachari, K.; Rendell, A.; Burant, J. C.; Iyengar, S. S.; Tomasi, J.; Cossi, M.; Millam, J. M.; Klene, M.; Adamo, C.; Cammi, R.; Ochterski, J. W.; Martin, R. L.; Morokuma, K.; Farkas, O.; Foresman, J. B.; Fox, D. J., *Gaussian, Inc, Wallingford CT* **2016**.
10. Grimme, S., Semiempirical hybrid density functional with perturbative second-order correlation. *J Chem Phys* **2006**, *124*, 034108.
11. Grimme, S.; Ehrlich, S.; Goerigk, L., Effect of the damping function in dispersion corrected density functional theory. *J Comput Chem* **2011**, *32*, 1456-65.
12. Pickett, H. M., The Fitting and Prediction of Vibration-Rotation Spectra with Spin Interactions. *J. Mol. Spec.* **1991**, *148*, 371-377.
13. Desyatnyk, O.; Pszczółkowski, L.; Thorwirth, S.; Krygowski, T. M.; Kisiel, Z., The rotational spectra, electric dipole moments and molecular structures of anisole and benzaldehyde. *Phys. Chem. Chem. Phys.* **2005**, *7*, 1708-1715.
14. Larsen, N. W., Microwave Spectra of The Six Mono-¹³C-Substituted Phenols and of Some Monodeuterated Species of Phenol. Complete Substitution Structure and Absolute Dipole Moment. *J. Mol. Struct.* **1979**, *51*, 175-190.

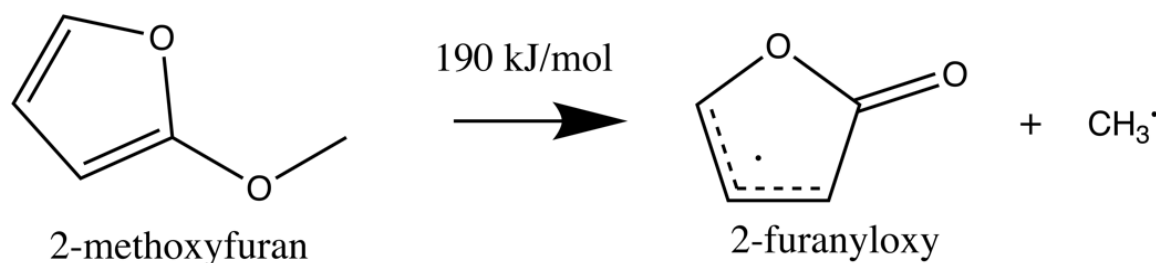
15. Syage, J. A.; Adel, A.; Zewail, A. H., Jet-Cooled Styrene: Spectra and Isomerization. *Chem Phys Lett* **1983**, *103*, 15-22.
16. Kraitchman, J., Determination of Molecular Structure from Microwave Spectroscopic Data. *American Journal of Physics* **1953**, *21*, 17-24.
17. Kisiel, Z., Least-Squares Mass-Dependence Molecular Structures for Selected Weakly Bound Intermolecular Clusters. *Journal of Molecular Spectroscopy* **2003**, *218*, 58-67.
18. Larsen, N. W.; Mathier, E.; Bauder, A.; Gunthard, H. H., Analysis of Microwave and Infrared Transitions of Phenol by Rotation-Internal Rotation Theory. Phenol-OD. *J. Mol. Spec.* **1973**, *47*, 183-188.
19. Mathier, E.; Welti, D.; Bauder, A.; Gunthard, H. H., Analysis of Microwave and Infrared Transitions of Phenol by Rotation-Internal Rotation Theory. *J. Mol. Spec.* **1971**, *37*, 63-76.
20. Lesarri, A.; Shipman, S. T.; Neill, J. L.; Brown, G. G.; Suenram, R. D.; Kang, L.; Caminati, W.; Pate, B. H., Interplay of Phenol and Isopropyl Isomerism in Propofol from Broadband Chirped-Pulse Microwave Spectroscopy. *J. Am. Chem. Soc* **2010**, *132*, 13417-13424.
21. Motoda, T.; Onda, M.; Yamaguchi, I., Barrier to internal rotation of 4-bromophenol by microwave spectrum and AB initio calculation. *Chem Lett* **1986**, *15*, 57-60.
22. Larsen, N. W., Microwave Spectra And Internal Rotation of 4-Fluorophenol, 4-Chlorophenol And 4-Bromophenol. *J. Mol. Struct.* **1986**, *144*, 83-99.
23. Sanchez, R.; Giuliano, B. M.; Melandri, S.; Caminati, W., Tautomeric equilibrium and hydroxyl group internal rotation in 4-hydroxypyridine. *Chemical Physics Letters* **2006**, *425*, 6-9.
24. Meyer, R., Flexible Models for Intramolecular Motion, a Versatile Treatment and Its Application to Glyoxal. *J. Mol. Spec.* **1979**, *76*, 266-300.
25. Zhao, Z. Q.; Parmenter, C. S.; Moss, D. B.; Bradley, A. J.; Knight, A. E. W.; Owens, K. G., p-fluorotoluene. I. Methyl (CH₃ and CD₃) internal rotation in the S₁ and S₀ states. *The Journal of Chemical Physics* **1992**, *96*, 6362-6377.
26. Hartwig, H.; Dreizler, H., The Microwave Spectrum of trans-2,3-Dimethyloxirane in Torsional Excited States. *Z. Naturforsch* **1996**, *51a*, 923-932.
27. Ferres, L.; Stahl, W.; Nguyen, H. V. L., Conformational effects on the torsional barriers in m-methylanisole studied by microwave spectroscopy. *J Chem Phys* **2018**, *148*, 124304.
28. Myszkiewicz, G.; Meerts, W. L.; Rätzer, C.; Schmitt, M., The structure of 4-methylphenol and its water cluster revealed by rotationally resolved UV spectroscopy using a genetic algorithm approach. *J Chem Phys* **2005**, *123*, 044304.
29. Rodrigo, C. P.; James, W. H., 3rd; Zwier, T. S., Single-conformation ultraviolet and infrared spectra of jet-cooled monolignols: p-coumaryl alcohol, coniferyl alcohol, and sinapyl alcohol. *J Am Chem Soc* **2011**, *133*, 2632-41.
30. Hernandez-Castillo, A. O.; Abeysekera, C.; Hays, B. M.; Zwier, T. S., Broadband multi-resonant strong field coherence breaking as a tool for single isomer microwave spectroscopy. *J Phys Chem A* **2016**, *145*.
31. Fritz, S. M.; Hernandez-Castillo, A. O.; Abeysekera, C.; Hays, B. M.; Zwier, T. S., Conformer-specific microwave spectroscopy of 3-phenylpropionitrile by strong field coherence breaking. *J. Mol. Spec.* **2018**, *349*, 10-16.

CHAPTER 6. BROADBAND MICROWAVE SPECTROSCOPY OF 2-FURANYLOXY RADICAL

6.1 Introduction

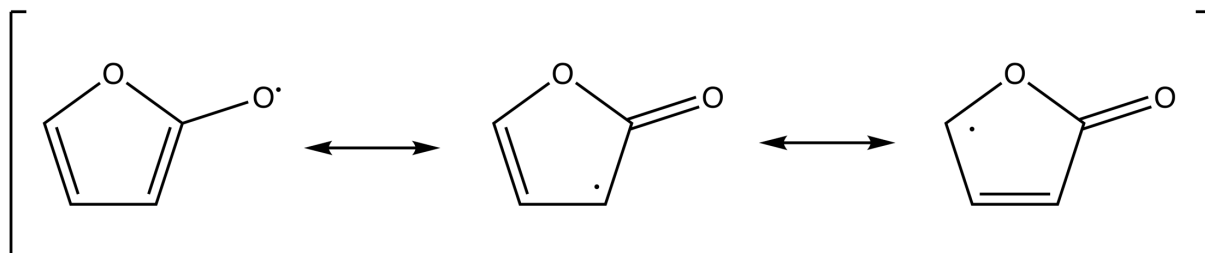
Alkylated furans and furanic ethers are among a variety of molecules derived from non-edible biomass that offer a renewable path to biofuels and other platform chemicals.¹ However, much remains to be learned about the combustion and pyrolytic behavior of these oxygenated species. Developing accurate combustion models requires experimental data on the kinetics and product branching ratios of their individual reaction steps. New spectroscopic tools and methods are needed to characterize this widening array of fuel components and reactive intermediates.²

The simplest furanic ether, 2-methoxy furan, is a common component in many biofuel synthesis processes.³ Due to the weak bond between the methyl group and the O atom, it is more highly reactive than other substituted heterocycles. The dissociation energy of the O-CH₃ bond was determined by Simmie et al. to be 190 kJ mol⁻¹, making the bond ~200 kJ mol⁻¹ weaker than the ring C-H bonds.⁴ Therefore, the dominant pathway from thermal decomposition would involve methyl loss, producing the resonant stabilized 2-furanyloxy radical, an allylic lactone.



Previous work by the Ellison group⁵ on the unimolecular thermal decomposition of 2-methoxy furan, provided direct experimental evidence based on VUV photoionization mass spectrometry that the 2-furanyloxy is indeed produced in the initial decomposition step. Previous computational studies have discussed the resonance-stabilized nature of the 2-furanyloxy radical, which has contributions from the three resonance structures shown below.^{4, 6} While the initial dissociation that produces the radical would tend to emphasize the radical as an alkoxy radical, the

allylic character of the carbon-centered radical resonance structures argues for their significant contributions.



Experimental data that allows a detailed structure of the 2-furanyloxy radical was the main goal of this work. Due to its resonance stabilization, 2-furanyloxy radical is a long-lived intermediate. Possessing a dipole moment of ~ 4 D, it is a good candidate to be investigated with microwave spectroscopy. As mentioned in previous chapters, rotational spectroscopy has the inherent characteristics of a near-ideal molecular shape detector, and it has been shown that the broadband capability and rapid spectral velocity at high resolution provided by CP-FTMW has enabled the detection and characterization of transient species created by laser excitation⁷ or electrical discharge⁸.

This work reports the first microwave detection and characterization of 2-furanyloxy radical, using a combination of CP-FTMW and flash pyrolysis. It presents accurate experimental rotational constants and a set of spin-rotation coupling constants, which are compared with state-of-the-art theory. Based on the close comparison between experiment and theory, the calculated spin densities on individual atoms are used to provide additional insight into the delocalization of the unpaired electron.

6.2 Experimental Methods

For this study, commercial sample of 2-methoxyfuran (97%, Sigma Aldrich) was used without further purification. The sample was inserted into a stainless-steel sample holder located outside the chamber. The solenoid valve was powered by a home-made pulsed valve driver triggered externally at a 10 Hz repetition rate. The experimental set up was performed with the chamber originally designed by Brian Dian described in section 2.3 and the arrangements of the main components is described in section 2.4.1.

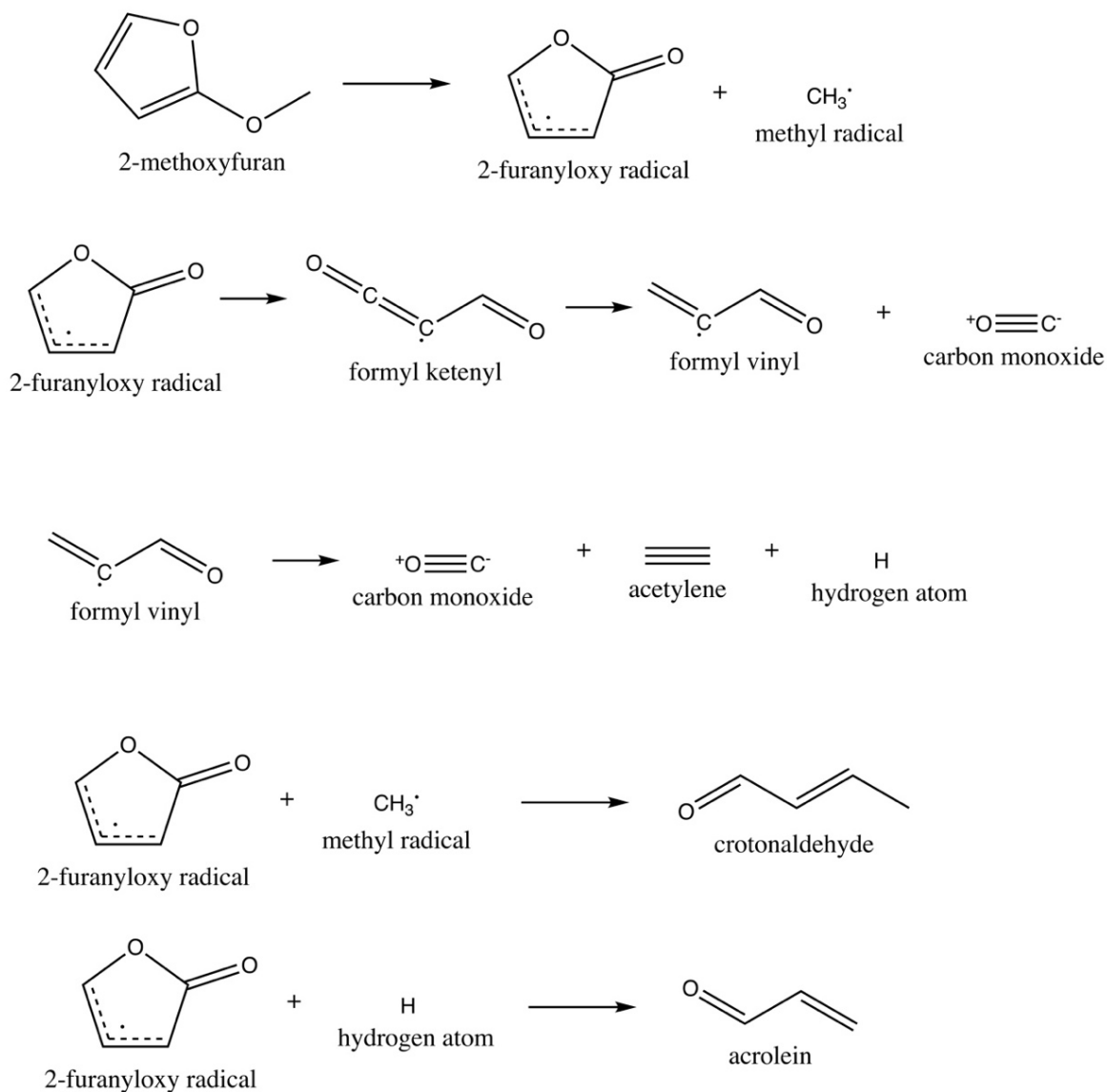
The experimental apparatus used for this work combines a flash-pyrolysis microreactor with a broadband CP-FTMW spectrometer operating in the 2-18 GHz frequency region. The micro-reactor assembly is described in section 2.2. For this work a temperature range 300-1600 K was used to detect reactive intermediates. The downstream pressure was maintained at approximately 10^{-3} mbar with an operating pressure of 0.1 mbar at a buffer gas flow rate of $0.68 \text{ bar} \cdot \text{cm}^3 \text{ sec}^{-1}$.

To selectively extract a set of transitions from the broadband microwave spectrum due to a single component in the gas mixture, and to aid the analysis of the broadband spectrum, the SFCB method⁹ described in Chapter 3 was employed. The method operates in the strong field coupling regime and uses a combination of CP-FTMW and multiple single frequency pulses. The magnitude of the difference between the CP-FTMW spectrum with and without the set of resonant single-frequency pulses produces a set of component-specific transitions.

The 2-furanyloxy radical was also studied computationally using coupled-cluster theory at the CCSD(T) level¹⁰. All calculations were done in collaboration with Prof. John Stanton using the CFOUR program system and the details of the calculations are described in section 2.5.

6.3 Results

Previous work shows that the dominant pathway for thermal decomposition of 2-methoxyfuran is the loss of CH_3 to produce the 2-furanyloxy radical (*o*- $\text{C}_4\text{H}_3\text{O}_2$).⁵ As shown in the following set of relevant reactions involved in the pyrolysis of 2-methoxy furan, in later stages of the process, 2-furanyloxy radical decomposes by ring opening to produce the formyl ketenyl radical, which then loses CO to give formyl vinyl radical. The latter decomposes to CO, H atom and acetylene. Even though the pyrolysis experiments were carried out under very dilute conditions, there were transitions due to products of radical recombination reactions in the spectrum at higher temperatures. Based on the work of Urness et al.⁵, these reactions involved H-atom and methyl radicals recombining with the 2-furanyloxy radical to produce acrolein ($\text{CH}_2=\text{CH}-\text{CHO}$) and crotonaldehyde ($\text{CH}_3-\text{CH}=\text{CH}-\text{CHO}$), respectively. In this work, these products were used to determine the best heating conditions, as their presence acts as an indicator for secondary reactions which it is important to minimize.



When the micro-reactor was held at temperatures below 620 K, only 2-methoxyfuran was present in the spectrum, while at temperatures above 700 K, there was clear evidence of thermal decomposition. As the temperature increased, crotonaldehyde transitions were first observed in the spectrum, while at still higher temperatures (~ 1100 K), a few transitions that belong to acrolein grew in, albeit weakly.

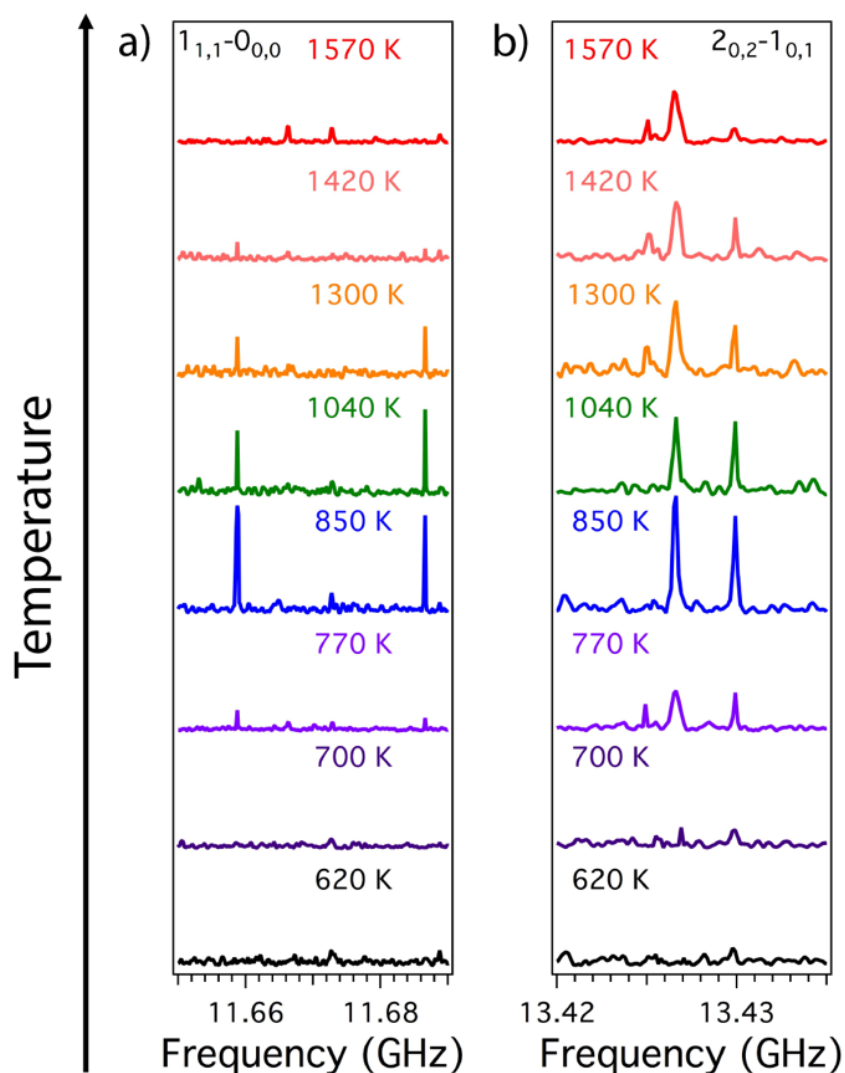


Figure 6.1: Intensities of the $1_{1,1}-0_{0,0}$ and $2_{0,2}-1_{0,1}$ rotational transitions of the 2-furanyloxy radical as a function of the micro-reactor wall temperature.

As mentioned earlier, in order to deconvolute the microwave spectrum and determine which of the transitions belong to the same species and thereby facilitate the assignment of the 2-furanyloxy radical spectrum, we implemented the SFCB protocol⁹. The SFCB scan used a 1.00 μ s long, linear broadband chirp (8-18 GHz), followed by a 50 ns gap before three 150 ns single-frequency pulses, which themselves were separated by 5 ns gaps. The frequencies chosen for the single-frequency pulses used in the MSE scheme were: 8568.776, 13426.633, and 16035.777 MHz. These frequencies were selected using the modified picking scheme¹¹ described in section 3.2.1,

and a custom Matlab routine describe in Appendix A.2 was used to extract six transitions where line intensities were modulated by the single frequency pulses by more than 20% of its original intensity.

Due to the moderate size of the 2-furanyloxy radical, only a few pure rotational transitions were observed in the 2-18 GHz frequency region. Nonetheless, as Figure 6.1 shows, using this set of transitions the optimal conditions for the 2-furanyloxy radical were found at a pyrolysis source temperature of ~ 900 K, through which a 0.7% mixture of 2-methoxyfuran in Ar was passed at a backing pressure of 2.7 bar. Using these conditions, the 2-18 GHz broadband microwave spectrum of 2-furanyloxy radical was recorded with a S/N of ~ 30 , as shown in Figure 6.2(a). The resonance-stabilized radical transitions were at most about 2% of the intensity of the precursor.

Despite careful searches, no transitions belonging to vibrationally excited states associated with the precursor or crotonaldehyde were observed in the spectrum. Their absence indicates that the molecules were cooled efficiently through collisions in the supersonic expansion that occurs when the gas exits the heated micro-reactor. The integrated line intensities of the precursor were used to fit to a Boltzmann plot based on the lower state energies E_l of the transitions, from which a rotational temperature of 2.1 ± 0.1 K was extracted. The rotational temperature of the 2-furanyloxy radical was determined to be 3.4 ± 1.2 K. However, it is not possible to acquire a good scan of the radical in the weak field regime, so it is likely that the Boltzmann distribution was altered to some degree by population transfer induced by the strong microwave field.

The modulated transitions from the SFCB method were used to get a preliminary rigid rotor fit for the radical. The a -component of the dipole moment, calculated at the ANO0/CCSD(T) level of theory (3.98 D), is predicted to be much larger than the b -component (1.12 D); therefore, the a -type R branch lines were searched for first (Figure 6.2(c)). Each transition has a splitting due to interaction of the unpaired electron spin with the molecular rotation (spin-rotation coupling). In the available frequency region, we only have R branch lines associated with $J=0,1,2$ and $K_a=0,1$. Nonetheless, once the a -type Q branch (Figure 6.2(d)) and b -type R and Q branch transitions were included in the fit, it was possible to determine accurate values for all three rotational constants, a set off three centrifugal distortion constants, and three spin-rotation coupling constants. Some transitions showed evidence of additional broadening and/or the presence of shoulders due to cross-terms of the spin-rotation tensor and/or Fermi contact hyperfine splittings. These patterns

were not sufficiently resolved to fit these parameters. Therefore, the standard deviation on the fit could not be brought below 124 kHz, a close value to the experimental resolution (150 kHz).

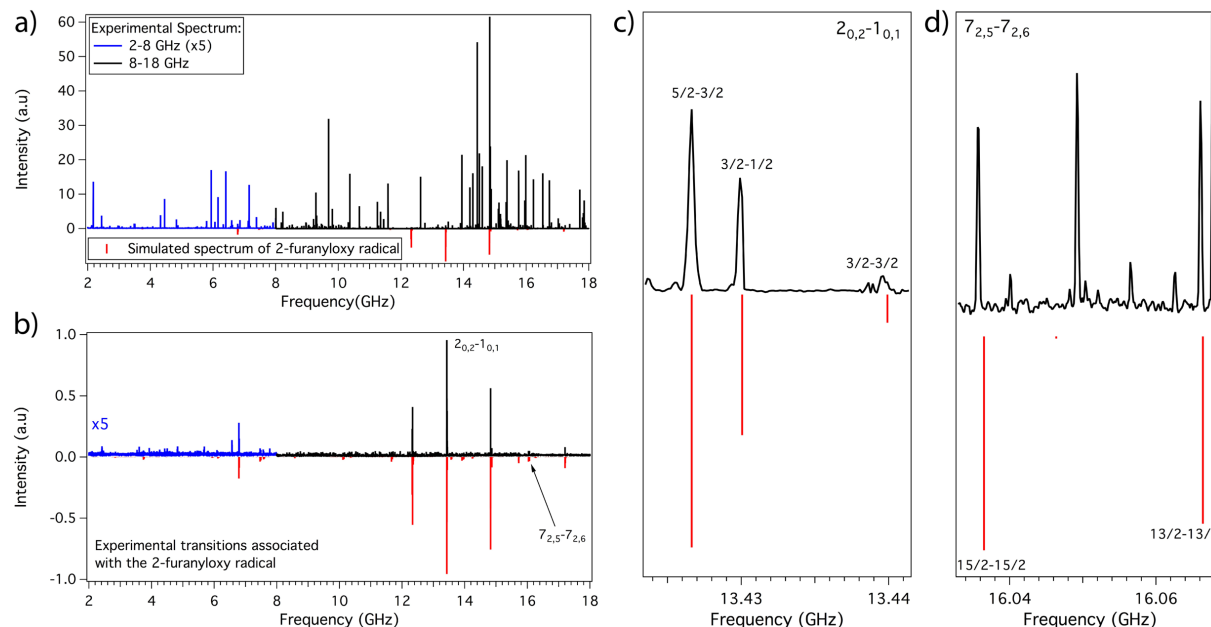


Figure 6.2: a) Broadband rotational spectrum of the 2-8 GHz (in blue) and 8-18 GHz (in black) regions of the pyrolysis of 2-methoxy furan, recorded at microtubular reactor temperatures of 850 K and 900 K, respectively. The simulated spectrum of the 2-furanyloxy radical at a rotational temperature of 2 K is shown as inverted sticks (red) below the rotational spectrum. b) Broadband spectrum with the precursor and other pyrolysis products removed in order to highlight the transitions of the radical and remaining transitions not assigned. c) Splitting of the $2_{0,2}-1_{0,1}$ transition due to spin-rotation coupling. A splitting of 3.4 MHz is observed between the $5/2-3/2$ and $3/2-1/2$ transitions. d) Spin-rotation splitting of the $7_{2,5}-7_{2,6}$ transition, with a splitting between $15/2-15/2$ and $13/2-13/2$ transitions of 9.8 MHz.

Using the CALPGM¹² program suite, a total of 59 spectral transitions were fit to the appropriate Hamiltonian for a doublet asymmetric top molecule with the centrifugal distortion constants expressed in Watson's A-reduced form. The best-fit spectroscopic constants are summarized in Table 6.1 along with those predicted at the CCSD(T) level of theory. The inertial defect ($\Delta = I_0^c - I_0^b - I_0^a$) was determined to be close to zero ($-0.09 \text{ u}\text{\AA}^2$), consistent with the radical possessing a planar equilibrium geometry. The experimentally determined rotational constants differ by no more than 0.6% from the calculated values. The centrifugal distortion constants and spin rotation coupling constants are in good agreement as well.

Table 6.1: Experimental best-fit and theoretical calculated spectroscopic parameters for 2-furanyloxy radical.

	Experimental	CCSD(T)	Exp-Calc
A (MHz)	8897.732(93) ^a	8847.92 ^e	49.81
B (MHz)	4019.946(24)	4014.46 ^e	5.49
C (MHz)	2770.321(84)	2760.85 ^e	9.47
Δ_{JK} (kHz)	1.232(33)	1.178 ^f	0.05
Δ_J (kHz)	0.345(33)	0.303 ^f	0.04
Δ_K (kHz)	2.81(79)	2.198 ^f	0.61
δ_j (kHz)	-	0.090 ^f	-
δ_k (kHz)	-	1.005 ^f	-
ε_{aa} (MHz)	-38.340(66)	-37.8 ^f	-0.5
ε_{bb} (MHz)	-14.786(253)	-14.8 ^f	0.0
ε_{cc} (MHz)	1.298(31)	1.2 ^f	0.1
μ_a (D)	-	3.98 ^f	-
μ_b (D)	-	1.12 ^f	-
μ_c (D)	-	0.00	-
Δ (uÅ ²) ^b	-0.09	0.04	-
σ (kHz) ^c	124	-	-
N^d	59	-	-

^a Standard error in parentheses in units of the last digit. ^b Zero-point inertial defect. ^c One sigma standard deviation on the fit. ^d Number of fitted transitions. The spectra were fit to a Watson-A reduced Hamiltonian including hyperfine interactions with the CALPGM program suite.¹² ^e See section 2.5 for further discussion. ^f ANO0 basis.

6.4 Discussion

The excellent agreement shown in Table 6.1 between theory and experimental rotational constants, inertial defect, centrifugal distortion constants, and spin-rotation coupling constants

indicates that the calculations are accurately predicting the structure and electronic effects of the radical. Therefore, the calculations can be used with some confidence to learn more about the chemical bonding, spin delocalization, and structural consequences of radical formation in this prototypical allylic lactone.

Table 6.2: Principal bond lengths and angles of the precursor (2-methoxy furan) and the 2-furanyloxy radical. Structures determined at ANO0/CCSD(T) level of theory.

	2-methoxy furan	2-furanyloxy radical
Distances (Å)		
r_{12}	1.388	1.359
r_{23}	1.365	1.398
r_{34}	1.453	1.396
r_{45}	1.372	1.463
r_{15}	1.358	1.432
r_{56}	1.347	1.209
Angles (°)		
C(5)O(1)C(2)	106.0	107.0
C(5)C(4)C(3)	104.8	107.8
O(1)C(5)O(6)	113.0	120.8

Table 6.2 compares select bond lengths and bond angles for the equilibrium structures of 2-methoxyfuran and the 2-furanyloxy radical, calculated at the ANO0/CCSD(T) level of theory. With a S/N of no more than 30 on the microwave transitions of the radical, it was not possible to observe the ^{13}C isotopes of the radical at natural abundance; limiting determination of experimental bond lengths and angles. However, the good agreement between experiment and theory on both the 2-furanyloxy radical (Table 6.1) and 2-methoxyfuran molecular parameters (Table 6.3) lends confidence in an analysis of the differences between the calculated r_e structures. Using the atom numbering scheme in Figure 6.3, the clear bond alternation of the furan ring in 2-methoxyfuran (Table 6.2) shows clear alteration in its C-C bond lengths, with $r_{34} \sim 0.1$ Å longer than r_{23} and r_{45} . The two C-O bonds in the ring (r_{12} and r_{15}) are similar to one another (1.388 and 1.358 Å, respectively) but inequivalent due to the presence of the electron-donating methoxy substituent at position 5. The C-O bond length r_{56} in 2-methoxyfuran is typical of a single bond.

By contrast, the 2-furanyloxy radical shows itself as an allylic lactone most notably in the large reduction in length of the pendant bond r_{56} of 1.209 Å reflective of a C=O double bond. This leads to substantial distortion of the furanic ring, where the adjacent C-O (r_{15}) and C-C bonds (r_{45}) are necessarily lengthened to be nearer to those of single bonds (1.432 and 1.463 Å). In addition, the O(1)-C(2)-O(6) angle widens from that typical in ethers ($\sim 113^\circ$) to a value more in keeping with an ester ($\sim 120^\circ$). Importantly, the two C-C bonds r_{23} and r_{34} are nearly equivalent (1.398 and 1.396 Å, respectively) at a length consistent with a bond order of 1.5 of an allylic radical.

Table 6.3: Spectroscopic constants (A-Reduction, I' representation) for 2-methoxy furan. The experimental constants were taken from the previous work of J.A. Beukes¹³.

	Experimental	ANO0/CCSD(T)	Exp-Calc
A_0 (MHz)	7613.1668(14)	7446.93619	166.23
B_0 (MHz)	2111.50975(40)	2072.87772	38.63
C_0 (MHz)	1671.35814(32)	1639.41791	31.94
Δ_{JK} (kHz)	0.0357(59)	0.02909	0.006
Δ_J (kHz)	0.14203(89)	0.1404	0.0016
Δ_K (kHz)	2.1805(19)	2.026	0.1545
δ_j (kHz)	0.034619(24)	0.0348	-0.0002
δ_k (kHz)	0.3981(97)	0.397	0.001
Δ (uÅ ²)	-3.35	-3.25	-
σ (kHz)	67	-	-
N	532	-	-

The delocalized radical electron density associated with the resonance-stabilized 2-furanyloxy radical can also be seen readily in the atomic spin densities predicted by the calculations. These atomic spin densities are defined as the difference in spin density between spin up (α) and spin down (β) at each atom i ; that is, $\rho_{net,i} = \rho_i(\alpha) - \rho_i(\beta)$, and is thus zero for all

atoms in a closed-shell molecule. In a radical such as the 2-furanyloxy radical, with a single unpaired electron, $\rho_{net,tot} = +1.00$.

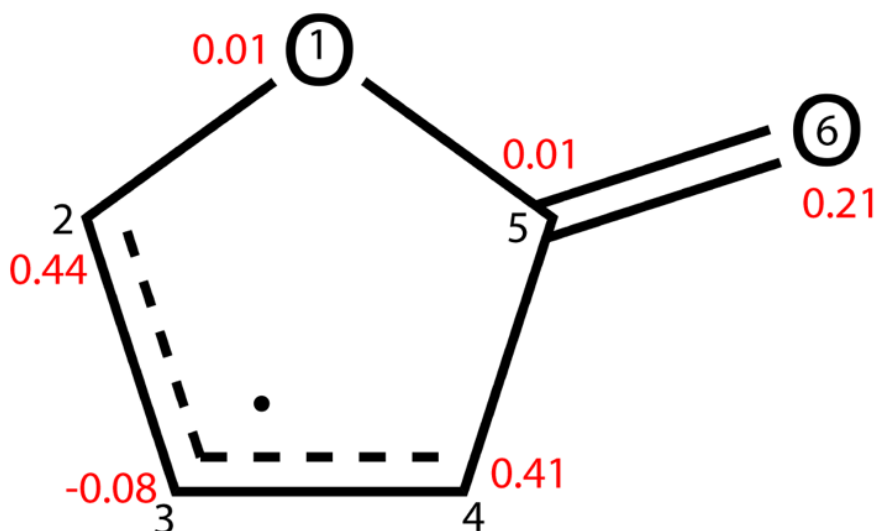


Figure 6.3: Heavy atom atomic spin densities calculated for 2-furanyloxy radical at the ANO1/CCSD(T) level of theory. Spin densities are indicated in red.

Recall that the calculations predict spin-rotation coupling constants (Table 6.1) in good quantitative agreement with experiment. While a more precise experimental characterization of the spin density would require fitting more elements of the spin-rotation tensor, the calculations themselves provide atomic spin densities that are centered almost entirely on the three atoms that would be anticipated to carry them: C atoms 2 and 4, and O(6), the oxygen atom exterior to the furanic ring. These calculated densities are included in Figure 6.3, showing that about 80% of the radical spin density is on the allylic carbons, and about 20% on O(6). Thus, it is proper to characterize this radical as an allylic lactone that is primarily carbon-centered rather than oxygen-centered. Furthermore, the asymmetry of the furanic ring has comparatively little effect on the C(2) versus C(4) spin densities, which are nearly equal (+0.44 versus +0.41). It seems appropriate to interpret these radical spin densities as measures of the weighting factors for the three resonance structures that contribute to delocalization. Such a connection has been made before in vibrational

spectroscopy¹⁴ and EPR studies¹⁵ of propargyl radical. Similarly, in past studies of phenoxy radical, EPR data confirmed that a significant portion of the spin density is localized at the *ortho* and *para* carbon atoms.¹⁶

6.5 Conclusion

The thermal decomposition of 2-methoxyfuran was carried out in a flash pyrolysis micro-reactor operating over the temperature range 300-1600 K. Using CP-FTMW spectroscopy, the broadband microwave spectrum of the 2-furanyloxy radical was recorded for the first time. High-level *ab initio* calculations provided further structural characterization and demonstrated accurate predictions of the rotational constants and spin-rotation coupling parameters compared to experiment. This resonance-stabilized radical, formed by methyl loss involving breaking an extraordinarily weak O-CH₃ bond (~ 190 kJ/mol)⁴ provided a means of forming the radical at modest temperatures (800-900 K), consistent with the unusually high reactivity of 2-methoxyfuran in combustion environments. Even so, in the flash pyrolysis source, a wall-temperature of 900 K produced line intensities in the radical that were only $\sim 2\%$ of those due to the precursor.

Based on the close correspondence between *ab initio* predictions and experiment, several structural aspects of the 2-furanyloxy radical were deduced. The structural data pointed to this radical being viewed most properly as an allylic lactone, with 80% of the electron spin density at the C(2) and C(4) allylic carbons in the furan ring, and only 20% at the O(6) site. Calculated bond lengths are also consistent with this picture of the radical.

6.6 References

1. Lange, J. P.; van der Heide, E.; van Buijtenen, J.; Price, R., Furfural--a promising platform for lignocellulosic biofuels. *ChemSusChem* **2012**, *5*, 150-66.
2. Prozument, K.; Barratt Park, G.; Shaver, R. G.; Vasiliou, A. K.; Oldham, J. M.; David, D. E.; Muentner, J. S.; Stanton, J. F.; Suits, A. G.; Barney Ellison, G.; Field, R. W., Chirped-Pulse millimeter-Wave spectroscopy for dynamics and kinetics studies of pyrolysis reactions. *Phys Chem Chem Phys* **2014**, *16*, 15739-15751.
3. Hudzik, J. M.; Bozzelli, J. W., Structure and Thermochemical Properties of 2-Methoxyfuran, 3-Methoxyfuran, and Their Carbon-Centered Radicals Using Computational Chemistry. *J. Phys. Chem.* **2010**, *114*, 7984-7995.
4. Simmie, J. M.; Somers, K. P.; Yasunaga, K.; Curran, H. J., A Quantum Chemical Study of the Abnormal Reactivity of 2-Methoxyfuran. *Int. J. Chem. Kinet.* **2013**, *45*, 531-541.
5. Urness, K. N.; Guan, Q.; Troy, T. P.; Ahmed, M.; Daily, J. W.; Ellison, G. B.; Simmie, J. M., Pyrolysis Pathways of the Furanic Ether 2-Methoxyfuran. *J Phys Chem A* **2015**, *119*, 9962-77.
6. Barckholtz, C.; Fadden, M. J.; Hadad, C. M., Computational Study of the Mechanisms for the Reaction of O₂(³Σ_g) with Aromatic Radicals. *J. Phys. Chem.* **1999**, *103*, 8108-8117.
7. Abeysekera, C.; Zack, L. N.; Park, G. B.; Joalland, B.; Oldham, J. M.; Prozument, K.; Ariyasingha, N. M.; Sims, I. R.; Field, R. W.; Suits, A. G., A chirped-pulse Fourier-transform microwave/pulsed uniform flow spectrometer. II. Performance and applications for reaction dynamics. *J Chem Phys* **2014**, *141*, 214203.
8. Karunatilaka, C.; Shirar, A. J.; Storck, G. L.; Hotopp, K. M.; Biddle, E. B.; Crawley, R.; Dian, B. C., Dissociation Pathways of 2,3-Dihydrofuran Measured by Chirped-Pulse Fourier Transform Microwave Spectroscopy. *J Phys Chem Lett* **2010**, *1*, 1547-1551.
9. Hernandez-Castillo, A. O.; Abeysekera, C.; Hays, B. M.; Zwier, T. S., Broadband multi-resonant strong field coherence breaking as a tool for single isomer microwave spectroscopy. *J Phys Chem A* **2016**, *145*.
10. Raghavachari, K.; Trucks, G. W.; Pople, J. A.; Head-Gordon, M., A Fifth-Order Perturbation Comparison of Electron Correlation Theories. *Chem Phys Lett* **1989**, *157*, 479-483.
11. Fritz, S. M.; Hernandez-Castillo, A. O.; Abeysekera, C.; Hays, B. M.; Zwier, T. S., Conformer-specific microwave spectroscopy of 3-phenylpropionitrile by strong field coherence breaking. *J. Mol. Spec.* **2018**, *349*, 10-16.
12. Pickett, H. M., The Fitting and Prediction of Vibration-Rotation Spectra with Spin Interactions. *J. Mol. Spec.* **1991**, *148*, 371-377.
13. Beukes, J. A.; Marstokk, K. M.; Mollendal, H., The structural and conformational properties of 2-methoxyfuran as studied by microwave spectroscopy and quantum chemical calculations. *J. Mol. Spec.* **2001**, *567-568*, 19-27.
14. Jochnowitz, E. B.; Zhang, X.; Nimlos, M. R.; Varner, M. E.; Stanton, J. F.; Ellison, G. B., Propargyl Radical: Ab Initio Anharmonic Modes and the Polarized Infrared Absorption Spectra of Matrix-Isolated HCCCH₂. *J. Phys. Chem. A.* **2005**, *109*, 3812-3821.
15. Kasai, P. H., Electron Spin Resonance Studies of Vinyl, Propargyl, and Butatrienyl Radicals Isolated in Argon Matrices. *J. Am. Chem. Soc* **1972**, *94*.
16. Fehir, R. J., Jr.; McCusker, J. K., Differential polarization of spin and charge density in substituted phenoxy radicals. *J Phys Chem A* **2009**, *113*, 9249-60.

CHAPTER 7. CHARACTERIZATION OF RESONANCE-STABILIZED RADICALS USING A MASS-CORRELATED BROADBAND MICROWAVE SPECTROMETER

7.1 Introduction

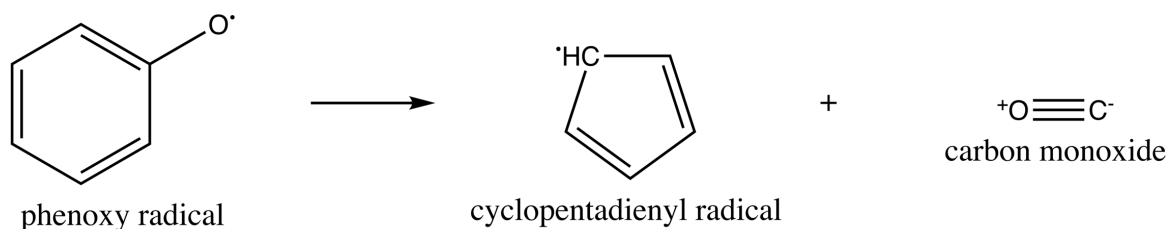
A spectrometer that combines the high-resolution provided by chirped pulse Fourier transform microwave (CP-FTMW) spectroscopy with vacuum ultraviolet (VUV) photoionization time-of-flight mass spectrometry (TOF-MS) has been built. The CP-FTMW/TOF spectrometer has been described in detail in section 2.3. In this chapter, the spectrometer capabilities are demonstrated by determining the molecular parameters of two important, closely-related resonance-stabilized radicals: phenoxy radical and *o*-hydroxy phenoxy radical. VUV photoionization TOF mass spectrometry provides the molecular formulae of the mixture components, as long as they have ionization potentials lower than the VUV photon energy (10.5 eV). CP-FTMW is a powerful tool to characterize chemical structures. The multiplexed approach for determining gas phase structures not only speeds the gas phase analysis of complex mixtures but, by recording a series of broadband microwave spectra under the same conditions, it is possible to detect and optimize conditions for characterizing the rotational spectra of transient species.

7.2 Structural Characterization of Phenoxy Radical

Phenoxy radical (C_6H_5O) is resonantly stabilized due to hyperconjugation of the oxyl radical moiety with the aromatic ring (Figure 7.1a).¹ As such, phenoxy is prototypical of radicals of type $C_6H_5X\cdot$, whose molecular structure is thereby important to characterize in detail. One of the intriguing aspects of the phenoxy radical is that, while one tends to think of the radical as oxygen-centered, resonance stabilization spreads the unpaired spin density over the *ortho* and *para* sites on the ring, thereby directing the reactivity of the radical (Figure 7.1b). This, in turn, will affect the structure of the radical, motivating high resolution studies seeking to determine its structure.

Beyond these fundamental structural questions, the phenoxy radical plays a significant role as a transient species in combustion and atmospheric chemistry, and thereby has attracted several previous studies investigating pathways to its formation and subsequent reactions, including its

thermal decomposition.²⁻⁵ Phenoxy is known to be a key intermediate in the combustion of aromatic compounds^{6,7}, such as benzene and toluene. More particularly, phenoxy radical stands at a critical juncture in the network of reactions that lead either toward or away from soot formation.⁸ On the one hand, the oxidation of the phenyl radical by reaction with molecular oxygen produces the phenoxy radical, an alternative to the all hydrocarbon-based structures that dominate polynuclear aromatic hydrocarbon (PAH) formation. By contrast, under fuel-rich conditions where oxidation is slow, these same phenyl radicals undergo reactions with other hydrocarbons leading ultimately to the efficient production of PAH. At the same time, the thermal decomposition of phenoxy radical produces cyclopentadienyl radical and CO, a pathway that itself could lead to naphthalene by radical recombination.^{2,3,9}



The phenoxy radical has been detected and characterized by a range of methods. Both electron-spin resonance (ESR)¹⁰ and ENDOR spectroscopies¹¹ probe the unpaired spin. Measurements of the ESR hyperfine coupling constants and related theoretical calculations¹² suggest that the unpaired electron is significantly delocalized from the oxygen atom onto the carbon ring; suggesting that the CO bond resembles a double bond. Electronic absorption spectra of phenoxy radical have been obtained both in gas and condensed phases.¹³⁻¹⁵ Vibrational spectroscopy studies based on Raman measurements¹⁶⁻¹⁸, matrix isolation Fourier transform infrared (FTIR) spectroscopy¹³, and IR linear dichroism (LD) measurements¹³ have enabled the near-complete assignment of the IR-active fundamental vibrational modes of this radical. Moreover, the combined measurement of infrared and electronic linear dichroism (LD) have enabled determination of absolute electronic transition moment directions.¹⁹ There are also multiple theoretical studies regarding its structure^{14,20}. What is missing from previous work are high resolution, rotationally-resolved spectroscopy that can be used to test theoretical predictions for its structure. This is the aim of the present work.

Phenoxy radical is a long-lived intermediate with a significant dipole moment (~ 4 D); therefore, it is an ideal candidate for detection via microwave spectroscopy, which can provide direct measure of the geometry through fitted rotational constants. This section presents a spectroscopic characterization of the gas-phase phenoxy radical, generated with a high-temperature flash pyrolysis source (described in section 2.2) coupled to a supersonic expansion. Using complementary data provided by VUV-TOF mass spectrometry and CP-FTMW spectroscopy, sets of rotational constants and spin-rotation coupling constants have been obtained for the all ^{12}C phenoxy radical, all six ^{13}C isotopic species in natural abundance, and the analogous all ^{12}C and the ^{13}C present in 2% natural abundance (C(2)/C(6) and C(3)/C(5)) data on the perdeuterated radical, $\text{C}_6\text{D}_5\text{O}$. For the isotopic species the hyperfine constants associated with the ^{13}C have been determined as well. These sets of molecular parameters coupled with high level of theory calculations are combined to provide a near-complete determination of the phenoxy radical structure, including all its C-C bond lengths, the C-O bond length, and an averaged C-H bond length, together with four angles that characterize the phenyl ring.

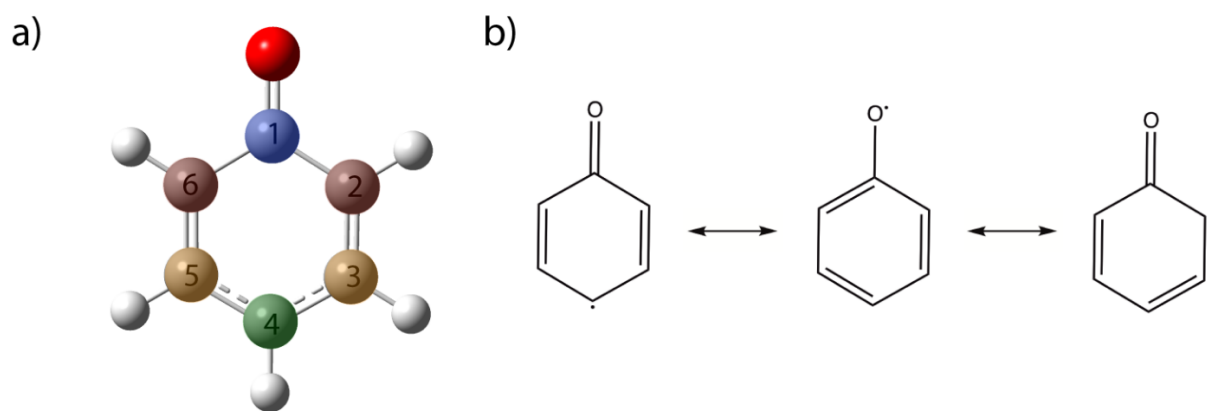


Figure 7.1: a) Optimized structure of phenoxy radical. The color and numbering scheme are consistent with those in Tables 7.1, 7.2, 7.3, and 7.4. b) Resonance structures of phenoxy radical.

7.2.1 Experimental Methods

For this study, commercial samples of anisole (Analytical Standard (99.9%), Sigma-Aldrich), allyl phenyl ether (99%, Sigma-Aldrich) and anisole-2,3,4,5,6- d_5 (98%, Sigma-Aldrich)

were used without further purification as precursors to make the phenoxy radical or its isotopologues. These samples were inserted in a stainless-steel sample holder heated via a heating rope to increase their vapor pressure (50 °C for anisole and deuterated anisole, and 130 °C for allyl phenyl ether). The samples were introduced into the SiC micro-reactor through a 1 mm diam. nozzle orifice via a pulsed valve (General Valve Series 9). The solenoid valve was triggered at 10 Hz repetition rate using a home-made driver to produce gas pulses ~500 μ s in duration. To generate the radical of interest the SiC micro-reactor described in section 2.2 was used, probing a temperature range from 300-1600 K to establish optimal conditions. The experimental apparatus that combines broadband CP-FTMW spectroscopy and TOF-MS has been described in section 2.3, while the microwave components are described in section 2.4.1.

The phenoxy radical was also studied computationally using coupled-cluster theory at the CCSD(T) level²¹. All calculations were done in collaboration with Prof. John Stanton using the CFOUR program suite. The details of the calculations are described in section 2.5.

7.2.2 Results

In order to optimize conditions for forming the phenoxy radical by pyrolysis of anisole, a series of TOF mass spectra and CP-FTMW spectra were recorded over a range of pyrolysis source temperatures ranging from 600-1500 K. The resulting mass and microwave spectra are shown in Figure 7.2. The pyrolysis of anisole has been studied previously by Friderichsen et al. using mass spectrometry and matrix isolation infrared spectroscopy as detection schemes.² This study proved that the phenoxy radical and cyclopentadienyl radical are important intermediates. The O-CH₃ is the weakest bond in the molecule with a bond dissociation of 268 kJ/mol.⁴ In the mass spectra of Figure 7.2, the anisole precursor peak (IP=8.2 eV $m/z=108$) doesn't decrease significantly with increasing temperature, as one might anticipate if pyrolysis is going towards completion. We ascribe this counter-intuitive result to anisole's increase in vapor pressure with temperature, since the sample holder temperature increases slowly as the SiC tube used for pyrolysis is heated to higher temperatures. While the TOF mass spectrum first shows evidence for formation of phenoxy radical + CH₃ at 1000 K, there is no evidence of this radical in the microwave spectrum until 1250 K. The optimal conditions for recording the microwave spectrum of phenoxy radical were found at a SiC wall temperature of 1350 K; however, the mass peak associated with cyclopentadienyl

radical (IP=8.41, $m/z=65$) grows in considerably at 1500 K. As a result, the phenoxy radical concentration never builds up significantly due to its subsequent decomposition to cyclopentadienyl + CO, limiting the signal size of the phenoxy radical rotational transitions in the microwave spectrum. Nevertheless, the data with anisole as precursor provided a preliminary fit for the phenoxy radical that was used to determine a set of microwave transitions that served as monitor transitions when finding the best conditions for forming phenoxy radical when phenyl allyl ether (PAE) was used as precursor. Moreover, the identified conditions also served to establish optimum conditions for studying the ring-deuterated phenoxy radical, which necessarily used $C_6D_5-OCH_3$ as precursor.

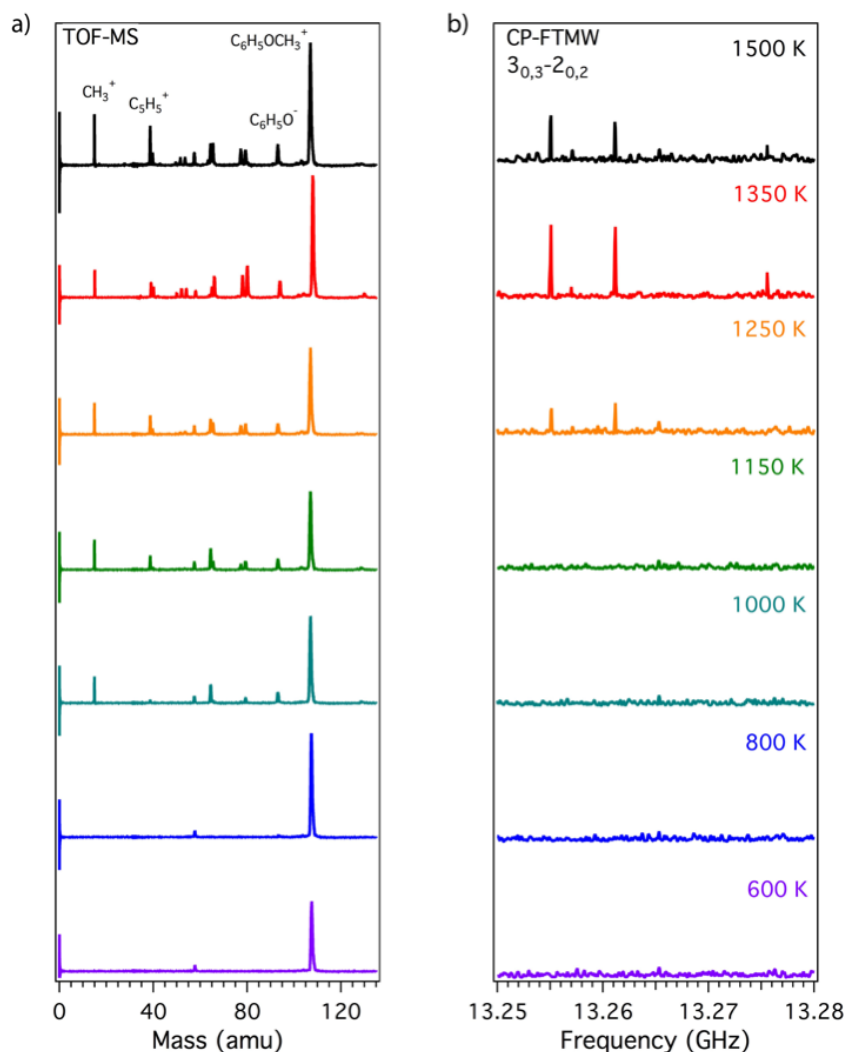


Figure 7.2: Unimolecular products from the pyrolysis of anisole using a pulsed flow heated SiC reactor, temperatures indicated are the measured reactor wall-temperature. a) Mass spectra recorded at different temperatures. b) $3_{0,3}-2_{0,2}$ rotational transition of phenoxy radical.

The thermal decomposition of PAE, studied before in a Knudsen quartz reactor²², leads to two resonant stabilized radicals (phenoxy and allyl); consequently, it is possible to make phenoxy radical at lower pyrolysis source temperatures where its subsequent decomposition is minimized. As before, the TOF-MS was used to determine the optimal conditions for detecting phenoxy radical when PAE was precursor. PAE was pyrolyzed at a series of SiC wall temperatures between 300-1000 K, with optimal signal found at ~ 850 K. At this pyrolysis source temperature, the rotational temperature for both conformers of allyl phenyl ether was determined to be ~ 1.4 K, demonstrating that even in the presence of the heated SiC tube, the pyrolysis precursor is still being collisionally cooled efficiently by the supersonic expansion that occurs as the gas mixture expands into vacuum. Since the microwave spectrum of phenoxy radical was taken in the strong field regime, it was not possible to determine an accurate rotational temperature for the radical; however, based on past experience, it is reasonable to assume that the radical is being efficiently cooled in the expansion, and its rotational temperature must be close to that of the precursor.

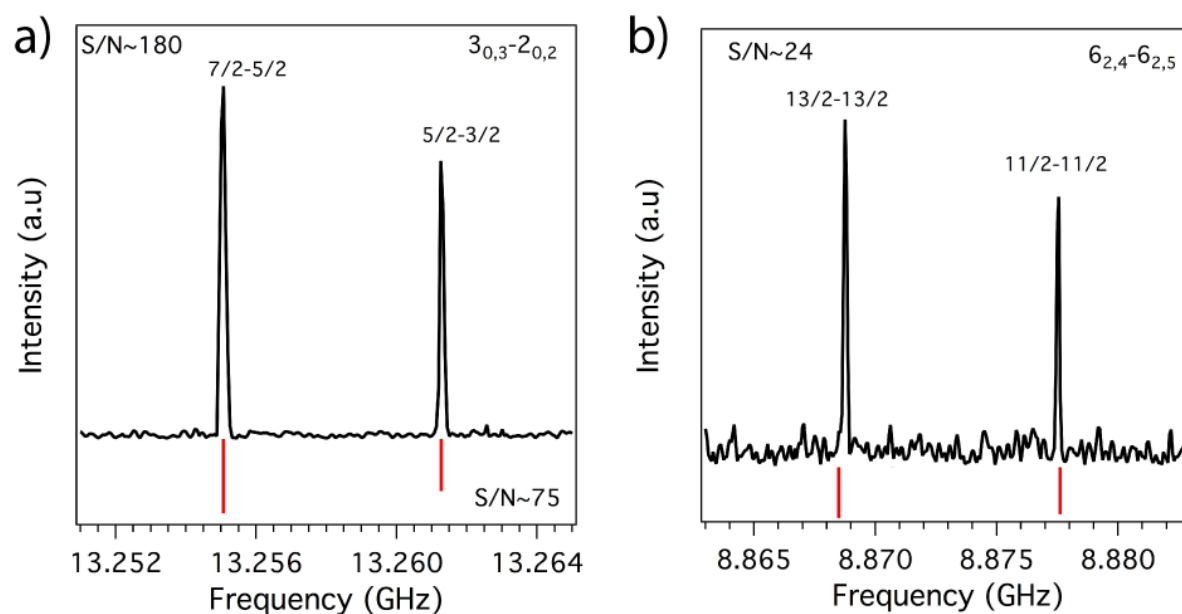


Figure 7.3: a) Spin-rotation splitting of the $3_{0,3}-2_{0,2}$ transition due to spin-rotation coupling. b) Spin-rotation splitting of the $6_{2,4}-6_{2,5}$ transition.

Table 7.1: Experimental best-fit and calculated spectroscopic parameters for phenoxy radical.

$\text{C}_6\text{H}_5\text{O}\cdot$	Experimental	CCSD(T)
A (MHz)	5539.22030(94) ^a	5522.0989 ^f
B (MHz)	2810.16659(39)	2800.397 ^f
C (MHz)	1864.75670(37)	1858.1048 ^f
Δ_J (kHz) ^b	<i>fixed</i>	0.146190 ^g
Δ_{JK} (kHz) ^b	<i>fixed</i>	0.195337 ^g
Δ_K (kHz) ^b	<i>fixed</i>	0.914182 ^g
d_J (kHz) ^b	<i>fixed</i>	0.050109 ^g
d_k (kHz) ^b	<i>fixed</i>	0.357747 ^g
ε_{aa} (MHz)	-99.3399(38)	-94.1 ^g
ε_{bb} (MHz)	-12.02894(206)	-13.04 ^g
ε_{cc} (MHz)	0.72801(155)	0.86 ^g
μ_a (D)	-	3.63 ^g
μ_b (D)	-	0.00 ^g
μ_c (D)	-	0.00 ^g
Δ (uA ²) ^c	-0.060	-
σ (kHz) ^d	14.7	-
N ^e	49	-

^a Standard error in parentheses in units of the last digit. ^b The values listed are the calculated values at ANO0/CCSD(T) level of theory. These were fixed for the fit. ^c Zero-point inertial defect. ^d One sigma standard deviation on the fit. ^e Number of fitted transitions.

Under optimum conditions using PAE as radical precursor, the transitions associated with the resonant stabilized radical were as large as 30% the size of those due to the precursor. Using the CALPGM program suite²³ a total of 49 transitions ($J=1-7$, $k_a=0,1,2$) were fit, including centrifugal distortion constants, in Watson's A-reduced form. Due to the interaction of the unpaired electron spin angular momentum with the radical's rotational angular momentum, each

of the rotational transitions is split into a set of closely spaced features, as illustrated for representative transitions in Figure 7.3a,b). Three rotational constants and three spin-rotation coupling constants were determined from the fit, while centrifugal distortion constants were fixed using the calculated values at ANO0/CCSD(T) level of theory. The fit has an average standard deviation of 14.7 kHz, which is below the experimental resolution (~60 kHz). The inertial defect ($\Delta = I_0^c - I_0^a - I_0^b$) was determined to be close to zero, corroborating that the radical has a planar equilibrium geometry. The experimental molecular parameters are listed in Table 7.1, and these are in good agreement with the calculated values.

In order to determine the spectroscopic constants of the ^{13}C isotopologues of the phenoxy radical in natural abundance, the 10 GHz frequency region (8-18 GHz) was divided into narrower segments of 2 GHz (5 segments) so as to increase the power delivered per unit frequency, in order to enhance the signal size on these low-abundance transitions. This effectively decreased the sweep rate (α) by a factor of five. With this approach the signal size was large enough to assign transitions associated with $J=1-4$ and $K_a=0$ for all the singly ^{13}C isotopomers of phenoxy. This led to preliminary assignment of rotational constants and spin-rotation coupling constants.

Subsequently, a series of seven scans over 1 GHz segments were chosen from the full 8-18 GHz frequency region (8-9, 9.8-10.8, 12.75-13.75, 13.5-14.5, 14.8-15.8, 16-17, 16.5-17.5 GHz) that covered regions of maximum interest for detection of the ^{13}C phenoxy radical transitions. This decreased the sweep rate even more (10^{15} s^{-2}), enabling assignment of additional ^{13}C isotopomer transitions, leading to the finally determined set of best-fit rotational constants and spin-rotation coupling constants for all the ^{13}C isotopomers. The fit required additional constants, the Fermi contact hyperfine term $b_F(^{13}\text{C})$, and the hyperfine components $T_{bb}-T_{cc}(^{13}\text{C})$ and $T_{aa}(^{13}\text{C})$. It was not possible to get a good fit for the centrifugal distortion constants; therefore, they were fixed to the calculated values. The values of the parameters determined in the final fit are given with their standard deviations in Table 7.2. The experimentally derived inertial defects for the isotopic species are close in magnitude to one another and to that from the all ^{12}C phenoxy radical, ranging from -0.060 to $-0.064 \text{ u}\text{\AA}^2$. This latter set of values provides additional evidence that the fitted rotational constants are self-consistent.

Table 7.2: Experimental best fit of the spectroscopic parameters for isotopomers of phenoxy radical.

	$^{13}\text{C}_{(2/6)} \text{C}_6\text{H}_5\text{O}^\bullet$	$^{13}\text{C}_{(3/5)} \text{C}_6\text{H}_5\text{O}^\bullet$	$^{13}\text{C}_{(1)} \text{C}_6\text{H}_5\text{O}^\bullet$	$^{13}\text{C}_{(4)} \text{C}_6\text{H}_5\text{O}^\bullet$
A (MHz)	5448.8102(175) ^a	5452.2705(178)	5539.2070(199)	5539.0068(102)
B (MHz)	2809.25391(100)	2790.31415(101)	2794.79586(111)	2759.65276(110)
C (MHz)	1854.01549(80)	1846.13338(80)	1857.98032(86)	1842.38289(58)
Δ_J (kHz) ^b	0.146190	0.145541	0.143558	0.145962
Δ_{JK} (kHz) ^b	0.195337	0.190822	0.195892	0.188588
Δ_K (kHz) ^b	0.914182	0.885825	0.878790	0.921159
d_J (kHz) ^b	0.050109	0.050197	0.049358	0.049938
d_k (kHz) ^b	0.357747	0.349796	0.350452	0.355772
ϵ_{aa} (MHz)	-97.8821(281)	-97.7947(301)	-99.331(52)	-99.298(45)
ϵ_{bb} (MHz)	-12.0504(144)	-11.9071(143)	-11.9458(195)	-11.7822(174)
ϵ_{cc} (MHz)	0.7450(64)	0.6040(59)	0.7283(74)	0.7304(69)
$T_{bb}-T_{cc}(^{13}\text{C})$ (MHz) ^b	-63.3539	23.5396	-	-
$T_{aa}(^{13}\text{C})$ (MHz)	-21.7347(215)	8.5209(228)	8.886(77)	-28.840(72)
$b_F(^{13}\text{C})$ (MHz)	18.983(53)	-24.287(38)	-34.621(93)	30.041(89)
Δ (uA ²) ^c	-0.062	-0.061	-0.060	-0.064
σ (kHz) ^d	15.41	16.14	13.7	16.4
N^e	39	39	27	26

^a Standard error in parentheses in units of the last digit. ^b The values listed are the calculated values at ANO0/CCSD(T) level of theory. These were fixed for the fit. ^c Zero-point inertial defect. ^d One sigma standard deviation on the fit. ^e Number of fitted transitions.

The broadband spectrum from 8-18 GHz of $\text{C}_6\text{D}_5\text{O}^\bullet$ was obtained from the pyrolysis of anisole-2,3,4,5,6- d_5 . Since this sample was a bit more expensive, the conditions for recording spectra were refined based on the previous studies. In these scans, the frequency region was divided into two segments, 7.5-13.5 GHz and 13-18.5 GHz. Furthermore, to decrease edge effects, the chirps included a Tukey window on the frequency amplitudes, with the ratio of cosine-tapered section length set to 0.3. Five million averages of each section were recorded, achieving a S/N for

the deuterated phenoxy radical of ~ 110 (Figure 7.4a) even with anisole as radical precursor. A total of 46 transitions were assigned with an rms deviation on the fit of 17.6 kHz. Table 7.3 shows the experimental and calculated values for the rotational constants and the three spin-rotational coupling constants that were determined. Given the higher signal-to-noise ratio, it was possible to obtain fits for the ^{13}C isotopomers that are in 2% natural abundance (Figure 7.4b&c). The determined molecular parameters are summarized in Table 7.3.

Table 7.3: Experimental best fit of the spectroscopic parameters for phenoxy-2,3,4,5,6-d5 radical and the ^{13}C isotopomers of phenoxy-2,3,4,5,6-d5 radical present in 2% natural abundance.

	$\text{C}_6\text{D}_5\text{O}\cdot$	$^{13}\text{C}_{(2/6)}\text{C}_6\text{D}_5\text{O}\cdot$	$^{13}\text{C}_{(3/5)}\text{C}_6\text{D}_5\text{O}\cdot$
A (MHz)	4601.47865(291) ^a	4538.9721(201)	4541.250891(297)
B (MHz)	2591.09909(33)	2589.97522(146)	2575.5698460(287)
C (MHz)	1658.09596(32)	1649.46810(97)	1643.9302299(124)
Δ_J (kHz) ^b	0.110938	0.110539	0.109056
Δ_{JK} (kHz) ^b	0.146235	0.142517	0.145975
Δ_K (kHz) ^b	0.486400	0.474942	0.470846
d_J (kHz) ^b	0.039038	0.039081	0.038456
d_K (kHz) ^b	0.242982	0.238076	0.238532
ϵ_{aa} (MHz)	-86.84299(297)	-85.484(98)	-84.85903(102)
ϵ_{bb} (MHz)	-11.21893(212)	-11.0688(258)	-10.55403(32)
ϵ_{cc} (MHz)	0.65812(166)	0.5919(86)	0.678511(153)
$T_{aa}(^{13}\text{C})$ (MHz)	-	-23.379(177)	9.86590(94)
$T_{bb}-T_{cc}(^{13}\text{C})$ (MHz)	-	-65.264(32)	-
$b_F(^{13}\text{C})$ (MHz)	-	19.430(89)	-24.69241(200)
Δ (uA ²) ^c	-0.079	-0.082	-0.085
σ (kHz) ^d	17.6	33.7	46.7
N^e	46	19	26

^a Standard error in parentheses in units of the last digit. ^b The values listed are the calculated values at ANO0/CCSD(T) level of theory. These were fixed for the fit. ^c Zero-point inertial defect. ^d One sigma standard deviation on the fit. ^e Number of fitted transitions.

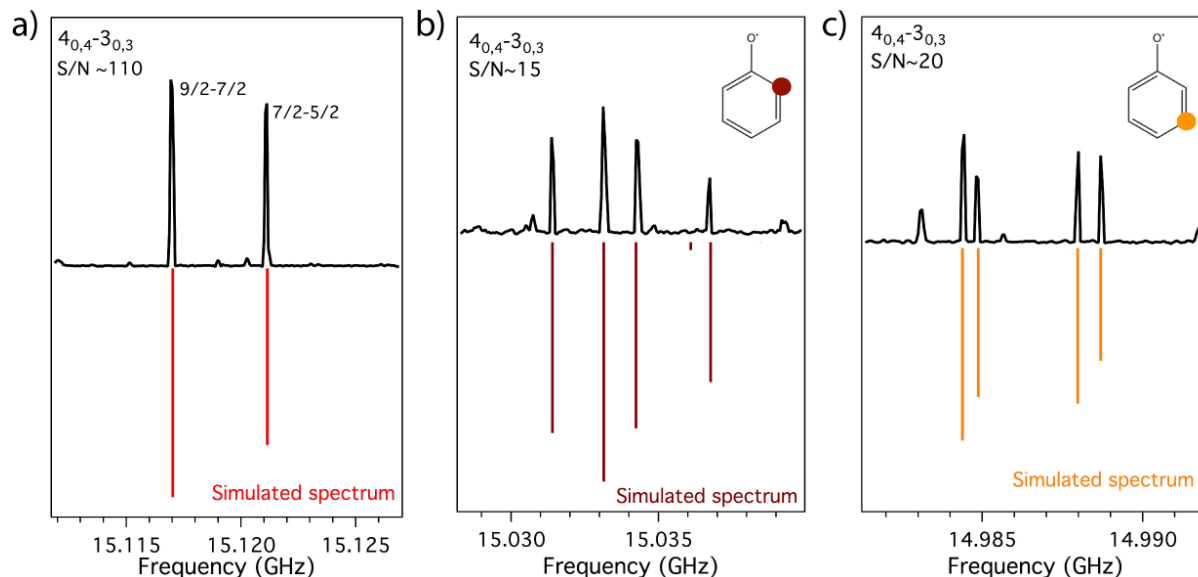


Figure 7.4: Spin-rotation splitting of the $4_{0,4}-3_{0,3}$ transition of fully deuterated phenoxy radical due to spin-rotation coupling: a) all ^{12}C phenoxy-2,3,4,5,6- d_5 radical. b) phenoxy-2,3,4,5,6- d_5 radical with ^{13}C in the C(2) or C(6) positions, and c) phenoxy-2,3,4,5,6- d_5 radical with ^{13}C in the C(3) or C(5) positions.

7.2.3 Molecular Structure

The full set of rotational constants from the eight isotopomers are sufficient to determine a semi-experimental molecular structure of the heavy atom backbone of phenoxy radical. By assuming that all C-H bonds have the same length and that the molecule has C_{2v} symmetry, it was possible to determine the nine unique structural parameters (five bond lengths and four bond angles) listed in Table 7.4. When comparing the r_0 structural parameters to those predicted by calculation, it is clear that they are in excellent agreement, with bond lengths and bond angles that differ by no more than 2 mÅ and 0.6° , respectively. Furthermore, all experimental values are within error with the calculated values.

Figure 7.5 shows a comparison of phenoxy radical, benzene, and phenol molecules. It is notable, first, that the distortion of the phenyl ring away from six-fold symmetry is considerably greater in phenoxy radical than it is for phenol. Indeed, in phenol, the structure of the phenyl ring deviates only slightly from benzene, and the C-O bond is only slightly shorter than a single bond (1.43 Å). For phenoxy radical the C-O bond has significantly more double bond character ($R_{\text{C3O}}=1.252$ Å), providing structural evidence that much of the unpaired spin density is carbon-centered rather than oxygen-centered. Furthermore, the phenyl ring itself in the phenoxy radical

shows evident alternations in its C-C bond lengths. More particularly, the r_{12} and r_{16} C-C bonds adjacent to the C-O moiety are ~ 0.10 Å longer than r_{23}/r_{56} which are closer in length to bonds with bond orders of 1.5, as in the allyl radical.

Table 7.4: Principal bond lengths and angles of phenoxy radical.

	Experimental	CCSD(T)
Distances (Å)		
C ₁ -C ₂ ^a	1.455(0.012)	1.453
C ₂ -C ₃ ^a	1.357(0.027)	1.371
C ₃ -C ₄ ^a	1.406(0.011)	1.408
C ₁ -O	1.252(0.018)	1.245
Average C-H ^b	1.076(0.017)	1.082
Angles (°)		
OC ₁ C ₂	121.7(0.7)	121.5
C ₁ C ₂ H ₂	117.1(8.3)	117.0
C ₁ C ₂ C ₃	121.1(0.7)	120.9
C ₂ C ₃ H ₃	120.9(5.0)	120.3

^a where C₁-C₂= C₁-C₆, C₂-C₃= C₅-C₆, and C₃-C₄= C₄-C₅.

^b The calculations bear the assumption that the C-H bond lengths are equal. They are within 0.0005 Å.

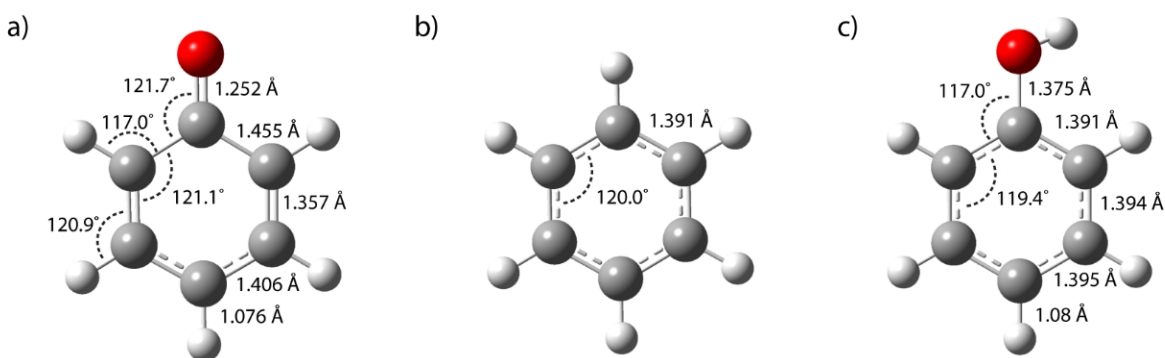


Figure 7.5: Molecular geometry of: a) phenoxy radical, b) benzene, and c) phenol²⁴.

In our recent study of the microwave spectroscopy of 2-furanyloxy radical²⁵, we used the close correspondence between experiment and theory to argue for the accuracy of atomic spin

densities calculated by theory, which reflect where the unpaired spin density resides in the structure. Figure 7.6 presents the calculated net atomic spin densities $\rho_{\text{net},i}$ for each of the heavy atoms i in the phenoxy radical, defined as the difference between spin-up (α) and spin-down (β) spin densities,

$$\rho_{i,\text{net}} = \rho_i(\alpha) - \rho_i(\beta).$$

As the figure shows, the atoms with large atomic spin densities are the same ones anticipated to have unpaired spin density based on the resonance structures in Figure 7.1. Indeed, these atomic spin densities indicate that 70% of the radical spin density is on the three carbon atoms anticipated based on the resonance structures of Figure 1, C(2), C(4), and C(6), while only 30% is found on the oxygen atom. Therefore, even though the phenoxy radical might be anticipated to be an oxygen-centered radical based on the bond being broken in its formation from phenol or anisole, the atomic spin densities indicate that it is much more aptly characterized as a carbon-centered radical. From a structural standpoint, it is important to notice that the bonds adjacent to those carbons that carry most of the spin density (r_{12}/r_{16} and r_{34}/r_{45}) are longer causing a deformation of the phenyl ring. An ESR study of the cyclohexadienyl radical show a similar distribution for the spin densities;²⁶ therefore, it will be interesting to compare the ring deformation of these two molecules. However, there are no high-resolution studies that determine the geometry of the cyclohexadienyl radical.

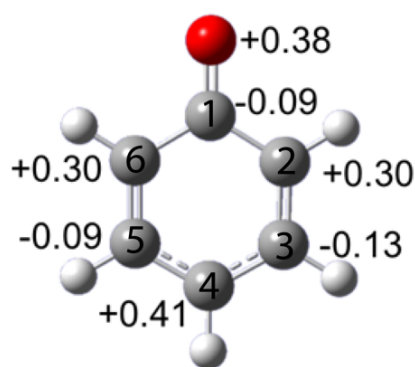


Figure 7.6: Heavy atom atomic spin densities calculated for phenoxy radical at the ANO0/CCSD(T) level of theory.

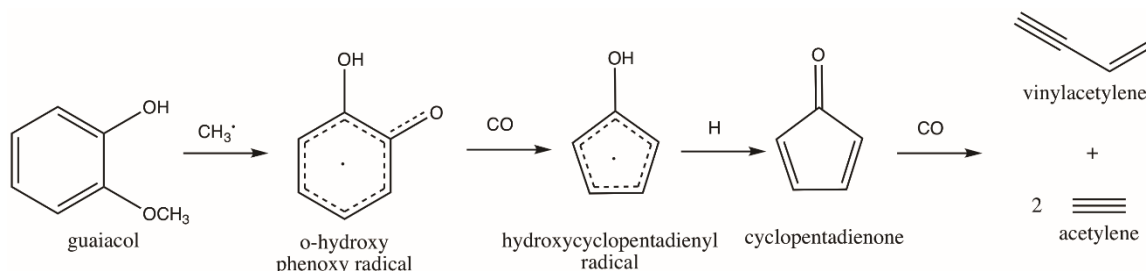
7.3 Molecular Parameters of *o*-Hydroxy Phenoxy Radical

Polycyclic aromatic hydrocarbon formation in the gasification of biomass for liquid fuels leads to tars and soot, and roughly a third of the biomass is comprised of lignin.²⁷ This complex heterogeneous polymer is formed from the copolymerization of the three monolignols *p*-coumaryl, coniferyl, and sinapyl alcohols, which are phenylpropene derivatives differing in the number of methoxy substituents on the aromatic ring.²⁸⁻²⁹ Of these, coniferyl alcohol is incorporated as a guaiacyl derivative, with OH and methoxy groups adjacent to one another. It is not surprising, then, that guaiacol, the fundamental aromatic, has been the subject of much previous work, including studies of its spectroscopy and pyrolysis.^{28, 30} Experimental and computational studies on lignin pyrolysis have shown that lignin initially mainly generates products characteristic of its syringol and guaiacol building blocks.³¹ Since the lignin biopolymer is quite complex, studying monomeric model compounds such as guaiacol and syringol, is a first step to deduce the decomposition mechanisms of lignin.³⁰

There are many reports of thermal degradation of guaiacol as a model aromatic component of lignin. In a study by Asmadi et al.³² the thermal reactions of guaiacol and syringol were compared in a closed ampule reactor. The unimolecular decomposition pathways for *o*-guaiacol (*o*-methoxyphenol) has previously been studied, showing that the first step in its pyrolysis is the formation of hydro phenoxy radicals.^{30, 33} Hosoya et al.³⁴ reported that the main products generated from guaiacol pyrolysis at 600 °C were phenolic compounds. Ellison group used 118 nm VUV TOF techniques, resonance-enhanced multiphoton ionization mass spectrometry (REMPI) and matrix isolation infrared spectroscopy as detection schemes to show that the O-CH₃ bond is the weakest bond in the molecule ($D_0 \sim 240 \text{ kJmol}^{-1}$)³⁵ and that the initial products of the thermal decomposition appear at $m/z=109$ and $m/z=15$ corresponding to *o*-hydroxy phenoxy radical (HOC₆H₄O) and CH₃ respectively.³⁰ There are also several computational studies regarding the pyrolysis of guaiacol that provide useful information for understanding the decomposition pathways and confirm the methoxy group as the principle site of initial decomposition.^{31, 36-37}

Suryan et al.³⁵ report that the higher reactivity of *o*-quinones is primarily due to the exceptional stability of the *o*-hydroxy phenoxy radical. Although this long-lived radical is a key intermediate in the pyrolysis of lignin, there are no high-resolution studies of it. Since it has a significant dipole moment, it is a good candidate for detection via microwave spectroscopy. In this work, we use the complementary data provided by VUV-TOF mass spectrometry and CP-FTMW

spectroscopy to obtain the rotational molecular parameters for *o*-hydroxy phenoxy radical. This set of molecular parameters are combined with high level *ab initio* calculations to provide high-resolution structural information for this important radical.



7.3.1 Experimental Methods

For this study, a commercial sample of guaiacol (Sigma Aldrich (98%)) was used without further purification as precursors to make the *o*-hydroxy phenoxy radical. The sample was inserted in a stainless-steel sample holder heated to 95 °C via a heating rope to increase the vapor pressure. Using a pulsed valve (General Valve Series 9) triggered at 10 Hz repetition rate (to produce gas pulses of ~500 μs) the sample was introduced into a 2mm silicon carbide (SiC) micro-reactor. Details of the microreactor are given in section 2.2. The *o*-guaiacol mass spectra were recorded from 320 to 1120 K to establish optimal conditions for formation of the radical. The experimental apparatus that combines broadband CP-FTMW spectroscopy and TOF-MS has been described in section 2.3, while the microwave components are described in section 2.4.1. The *o*-hydroxy phenoxy radical was also studied computationally using coupled-cluster theory at the ANO0/CCSD(T) level²¹. All calculations were done in collaboration with Prof. John Stanton using the CFOUR program suite.

7.3.2 Results

To optimize the conditions for forming the *o*-hydroxy phenoxy radical by pyrolysis of guaiacol, a series of TOF mass spectra were recorded at a series of pyrolysis source temperatures ranging from 320-1120 K. The mass-to-charge ratios and known chemical structures of the key

photoionizable components are labelled in Figure 7.7. At 820 K the *o*-hydroxy phenoxy radical is present at maximum concentration, with the TOF mass spectra guiding the choice of this temperature as the best one for recording a CP-FTMW spectrum with maximum S/N ratio.

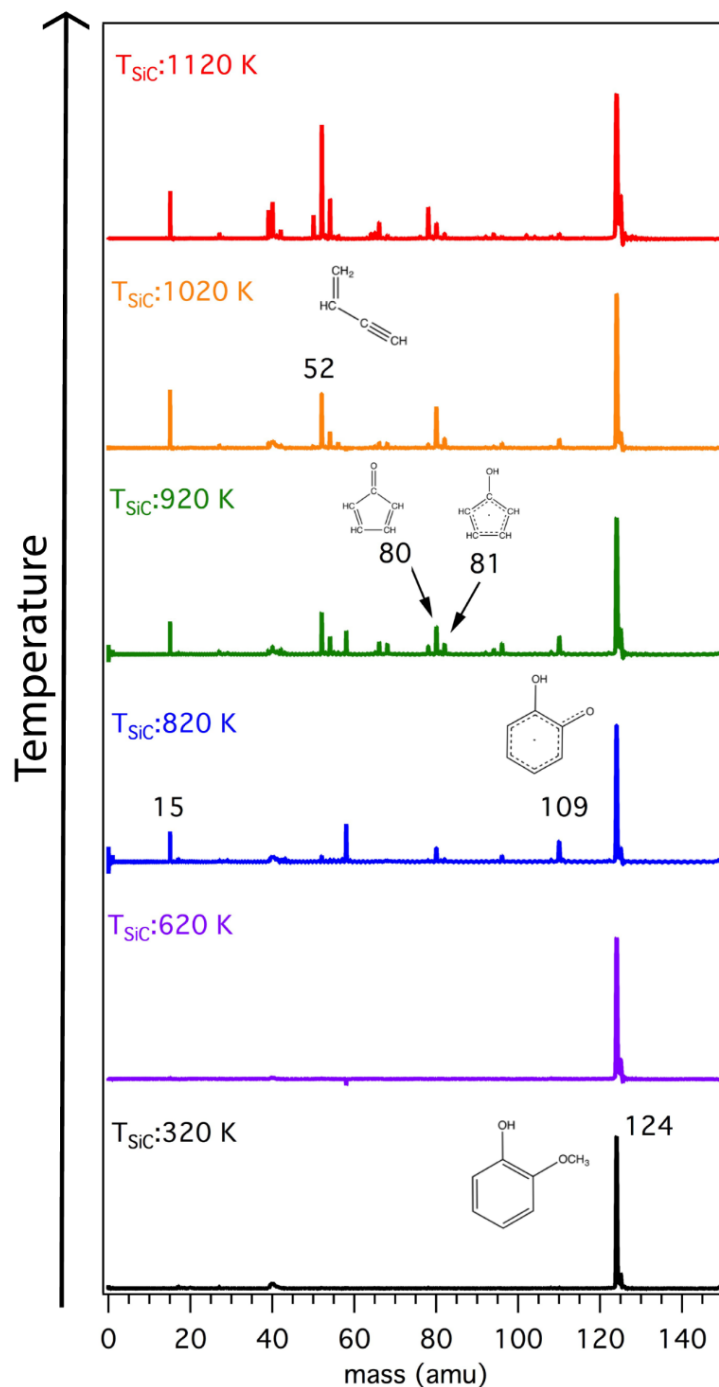


Figure 7.7: Mass spectra resulting from heating a mixture of *o*-guaiacol imbedded in Ar in a SiC micro-reactor. Temperatures indicated are the measured reactor wall-temperature.

Table 7.5: Experimental best fit of the spectroscopic parameters for *o*-hydroxy phenoxy radical.

OH-C₆H₅O[•]	Experimental	Calculations
<i>A</i> (MHz)	3505.8413(77) ^a	3445.5595 ^f
<i>B</i> (MHz)	2340.96389(86)	2292.8453 ^f
<i>C</i> (MHz)	1403.66652(58)	1376.7127 ^f
ϵ_{aa} (MHz)	-38.131(40)	-36.19 ^g
ϵ_{bb} (MHz)	-15.6082(206)	-16.00 ^g
ϵ_{cc} (MHz)	0.4173(70)	0.56 ^g
$\epsilon_{ab} + \epsilon_{ba}$ (MHz)	21.98(25)	16.57 ^g
$\epsilon_{ab} - \epsilon_{ba}$ (MHz)	-17.0(3)	-10.79 ^g
$T_{aa}(\text{H}(8))$ (MHz)	4.4435(309)	3.88 ^g
$T_{bb} - T_{cc}(\text{H}(8))$ (MHz)	-3.8944(174)	-2.96 ^g
$T_{ab}(\text{H}(8))$ (MHz)	-15.2(7)	-13.35 ^g
$b_{\text{F}}(\text{H}(8))$ (MHz)	-29.522(280)	-21.67 ^g
$b_{\text{F}}(\text{H}(10))$ (MHz) ^c	<i>fixed</i>	-10.69 ^g
$b_{\text{F}}(\text{H}(13))$ (MHz) ^c	<i>fixed</i>	-6.49 ^g
μ_a (D)	-	2.66 ^g
μ_b (D)	-	-1.06 ^g
μ_c (D)	-	0.00 ^g
Δ (uA ²) ^b	0.004	-
σ (kHz) ^c	15.4	-
N^{d}	40	-

^a Standard error in parentheses in units of the last digit. ^b Zero-point inertial defect. ^c One sigma standard deviation on the fit. ^d Number of fitted transitions. ^e Fixed to calculated values ^f Calculated at ANO0/CCSD(T) ^g Calculated at B2PLYP-B3DJ/aug-cc-pVTC

A portion of the CP-FTMW spectrum highlighting a series of transitions due to the radical are shown in Figure 7.8a, illustrating the high signal-to-noise ratio achieved. Guided by the predicted rotational constants and spin-rotation coupling constants from the calculations, we were

able to identify sets of transitions due to the *o*-hydroxyphenoxy radical. Using the CALPGM program suite,²³ a total of 40 transitions ($J=3-5$, $k_a=0-3$) were fit. Due to the interaction of the unpaired electron spin angular momentum with the radical's rotational angular momentum, each rotational transition of the radical is split into a set of transitions. The fit has an average standard deviation of 15.4 kHz and included 14 parameters, that included three rotational, five spin-rotational coupling constants, a set of hyperfine constants (T_{aa} , $T_{bb}-T_{cc}$, T_{ab}) and the Fermi contact hyperfine constant associated with H(8). In the final fit, the Fermi contact hyperfine constants of H(10) and H(13) were fixed to the calculated values. The experimental molecular parameters are listed in Table 7.5, along with the predictions of calculations. For this radical the inertial defect was also determined to be close to zero, corroborating that the radical has a planar equilibrium geometry.

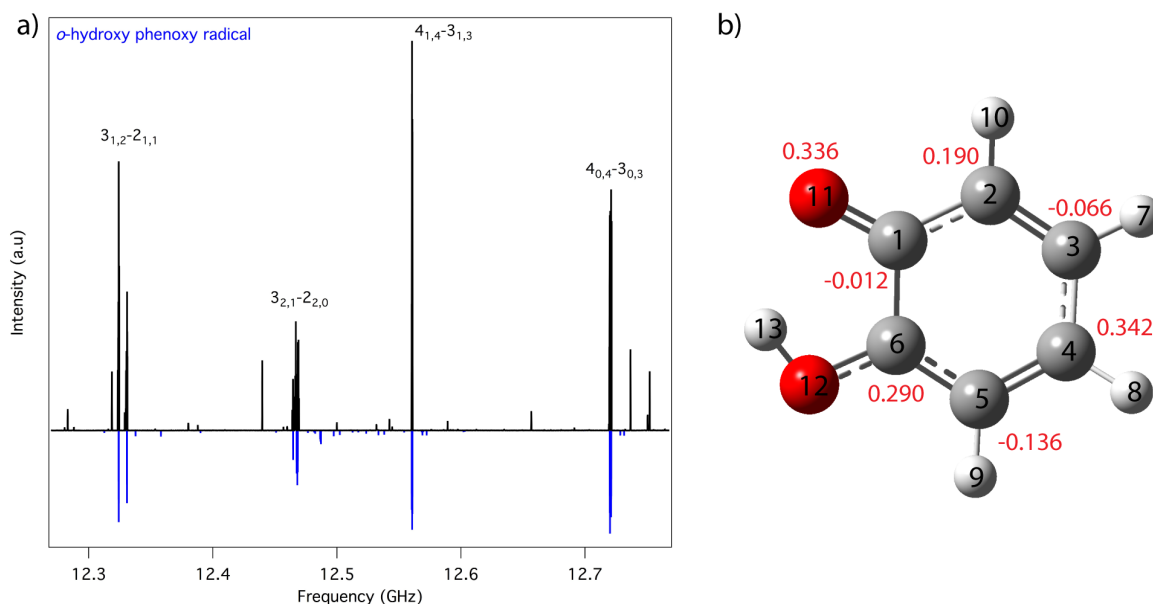


Figure 7.8: a) Section of the broadband rotational in the 8-18 GHz frequency region, recorded at microtubular reactor temperature of 820 K. The sample holder was heated to 95 °C with the sample entrained in 1.30 bar of He, and 30 FIDs recorded per gas pulse. The simulated spectrum of *o*-hydroxyphenoxy radical at a rotational temperature of 2 K is shown as inverted sticks (blue) below the rotational spectrum. b) Optimized structure of *o*-hydroxyphenoxy radical. Spin densities calculated at the ANO0/CCSD(T) level of theory are indicated in red.

As with the phenoxy radical, we see a close correspondence of the calculated rotational parameters and deduced structural features with the predictions of theory. We use the calculations then, to reflect on the effects of the OH group on the atomic spin densities and hence resonance

structures. Figure 7.8b presents the calculated net atomic spin densities $\rho_{\text{net},i}$ for each of the heavy atoms i in the *o*-hydroxy phenoxy radical. The calculations predict atomic spin densities that are centered almost entirely on the atoms that would be anticipated to carry them based on the resonance structures. These atomic spin densities indicate that 70% of the radical spin density is on the carbon atoms, while only 30% is found on the oxygen atom. Therefore, similar to phenoxy radical, the atomic spin densities indicate that *o*-hydroxy phenoxy radical is a carbon-centered radical. The carbon that carries most of the spin density (0.342) is C(4) and not surprisingly, its hydrogen (H(8)) is the hydrogen whose nuclear hyperfine constants and Fermi contact hyperfine term have a biggest effect on the fit.

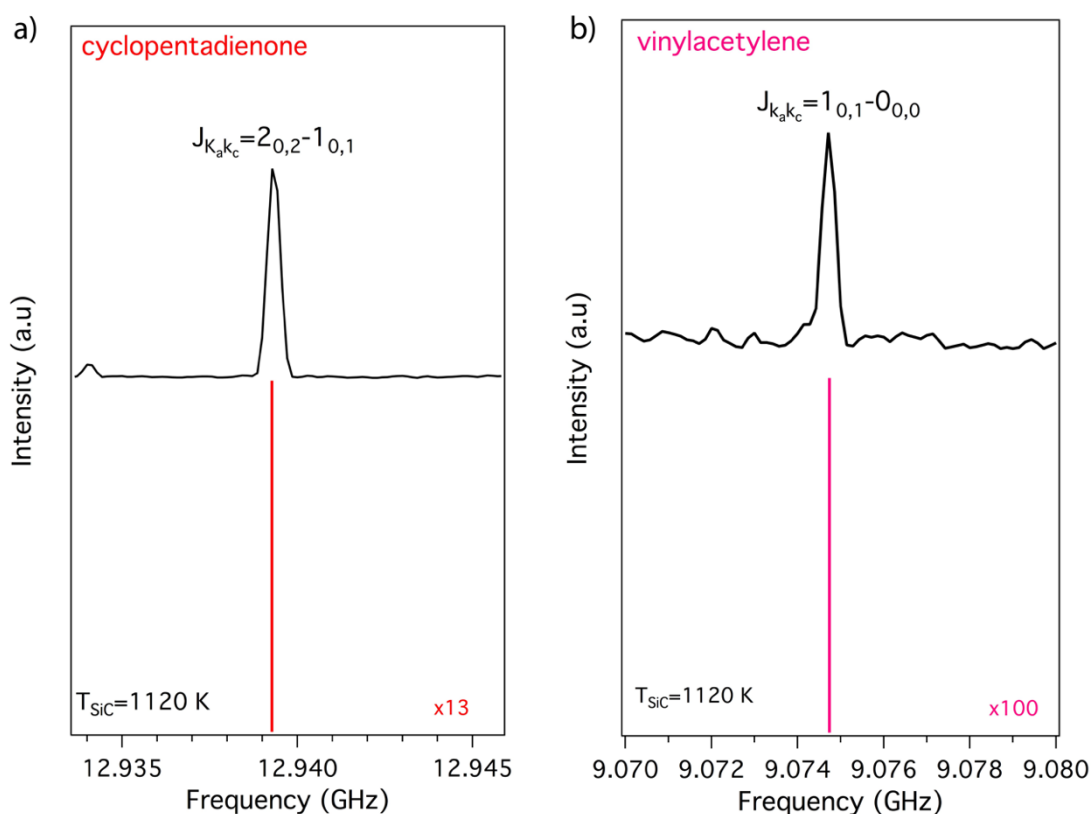


Figure 7.9: CP-FTMW spectra in small frequency regions around microwave transitions due to a) vinylacetylene and b) cyclopentadienone.

Decarbonylation of the *o*-hydroxy phenoxy radical generates the hydroxy-cyclopentadienyl radical ($m/z=81$), which has a total dipole moment of ~ 1.5 D. The maximum concentration of this radical is achieved at ~ 920 K but its VUV photoionization signal is never

very large. Despite a careful search, there was no evidence of this radical in the microwave spectrum at the present S/N ratio. The combination of the modest dipole moment and small concentration contribute to its signal being too small to detect. The hydroxy-cyclopentadienyl radical eliminates an H atom producing cyclopentadienone ($m/z=80$). Its microwave transitions are indeed observed, beginning at 820 K (Figure 7.9a). Further heating generates vinylacetylene ($m/z=52$), which only appeared in measurable concentration at 1120 K (Figure 7.9b). C_2H_2 has an ionization energy above 10.5 eV and has no dipole moment. As a result, its presence can only be surmised indirectly from the other products observed.³⁰ These observations are consistent with previous studies of Scheer et al.³⁰

7.4 Discussion and Conclusions

The present work on the phenoxy and ortho-hydroxy phenoxy radicals demonstrates how the correlation in signals between the VUV mass spectra and the microwave spectra can extend and speed the analysis of complex mixtures. VUV photoionization TOF mass spectrometry provides the empirical formulae of the mixture components, as long as they have ionization energies lower than the VUV photon energy (10.5 eV). On the other hand, the chemical structure of the molecular components is often not uniquely described by the empirical formulae. Moreover, free radicals and reactive intermediates often have chemical structures that have not been observed or characterized previously by high-resolution methods. CP-FTMW spectroscopy is a powerful tool for this characterization, relying only on the presence of a permanent dipole moment for detection. The combination of the two methods was put to particularly good use in identifying conditions under which particular pyrolysis intermediates are present with maximum intensity, leading to the determination of the molecular parameters of phenoxy and *o*-hydroxy phenoxy radicals.

There is a natural connection between the *o*-hydroxy radical and phenoxy radical. The presence of the OH group *ortho* to the phenoxy oxygen asymmetrizes the radical, reducing its C_{2v} symmetry to C_s symmetry. The presence of the OH group resulted in experimentally observing hyperfine splittings due to some of the H atoms.

A comparison of these spin densities shows a redistribution of the spin density due to the OH group. For both radicals 70% of their spin density is on the phenyl ring and only 30% is located on the oxygen atom. Nonetheless, the presence of the OH group *ortho* to the phenoxy

oxygen alters the spin density distribution significantly around the phenyl ring. For example, in phenoxy radical, the carbon atoms adjacent to the oxygen site (C(2) and C(6)) carry a similar percentage of the spin density; however, in the case of *o*-hydroxy phenoxy radical C(2) has a value of 0.290, similar to phenoxy, while C(6) has an atomic spin density lower by almost a factor of two (0.190). This is consistent with r_{23} possessing more double bond character in *ortho*-hydroxy phenoxy radical than its counterpart on the opposite side of the ring, r_{56} . Calculated bond lengths at ANO0/CCSD(T) are also consistent with this assessment of the radicals.

7.5 References

1. da Silva, G.; Chen, C.-C.; Bozzelli, J. W., Bond dissociation energy of the phenol OH bond from ab initio calculations. *Chemical Physics Letters* **2006**, *424*, 42-45.
2. Friderichsen, A. V.; Shin, E.-J.; Evans, R. J.; Nimlos, M. R.; Dayton, D. C.; Ellison, G. B., The pyrolysis of anisole (C₆H₅OCH₃) using a hyperthermal nozzle. *Fuel* **2001**, *80*, 1747-1755.
3. Lovell, A. B.; Brezinsky, K.; Glassman, I., The gas phase pyrolysis of phenol. *International Journal of Chemical Kinetics* **1989**, *21*, 547-560.
4. Arends, I. W. C. E.; Louw, R.; Mulder, P., Kinetic study of the Thermolysis of Anisole in a Hydrogen Atmosphere. *J. Phys. Chem.* **1993**, *97*, 7914-7925.
5. Liu, R.; Morokuma, K.; Mebel, A. M.; Lin, M. C., Ab Initio Study of the Mechanism for the Thermal Decomposition of the Phenoxy Radical. *J. Phys. Chem.* **1996**, *100*, 9314-9322.
6. Tao, Z.; Li, Z., A Kinetics Study on Reactions of C₆H₅O with C₆H₅O and O₃ at 298 K. *Int. J. Chem. Kinet.* **1999**, *31*, 65-72.
7. Brezinsky, K., The High-Temperature Oxidation of Aromatic Hydrocarbons. *Prog Energ Combust Sci* **1986**, *12*, 1-24.
8. Gu, X.; Zhang, F.; Kaiser, R. I., Crossed beam reaction of the phenyl radical, (C₆H₅, X₂A') with molecular oxygen: Observation of the phenoxy radical, (C₆H₅O, X₂A'). *Chemical Physics Letters* **2007**, *448*, 7-10.
9. Lin, C.-Y.; Lin, M. C., Thermal Decomposition of Methyl Phenyl Ether in Shock Waves: The Kinetics of Phenoxy Radical Reactions. *J. Phys. Chem.* **1986**, *90*, 425-431.
10. Dixon, W. T.; Murphy, D., Determination of the Acidity Constants of some Phenol Radical Cations by means of Electron Spin Resonance. *J. Chem. Soc., Faraday Trans. 2* **1976**, *72*, 1221-1230
11. Hurum, D. C.; Kreilick, R. W., Kinetics of Rapid Internal Subgroup Rotation of a Group of Phenoxy Radicals As Studied by ENDOR Spectroscopy. *J. Phys. Chem.* **1995**, *99*, 11813-11819.
12. Armstrong, D. R.; Cameron, C.; Nonhebel, D. C.; Perkins, P. G., Oxidative Coupling of Phenols. Part 7. Spin-density Calculations on the Phenoxy Radical. *J. Chem. Soc. Perkin Trans. 2* **1983**.
13. Spanget-Larsen, J.; Gil, M.; Gorski, A.; Blake, D. M.; Waluk, J.; Radziszewski, J. G., Vibrations of the phenoxy radical. *J. Am. Chem. Soc* **2001**, *123*, 11253-11261.
14. Johnston, L. J.; Mathivanan, N.; Negri, F.; Siebrand, W.; Zerbetto, F., Assignment and vibrational analysis of the 600 nm absorption band in the phenoxy radical and some of its derivatives. *Can. J. Chem.* **1993**, *71*.
15. Pullin, D.; Andrews, L., The Absorption Spectra of the Solid Argon. *J. Mol. Spec.* **1982**, *95*, 181-185.
16. Schnepf, R.; Sokolowski, A.; Muller, J.; Bachler, V.; Wieghardt, K.; Hildebrandt, P., Resonance Raman Spectroscopic Study of Phenoxy Radical Complexes. *J. Am. Chem. Soc* **1998**, *120*, 2352-2364.
17. Beck, S. M.; Brus, L. E., The resonance Raman spectra of aqueous phenoxy and phenoxy-d₅ radicals. *The Journal of Chemical Physics* **1982**, *76*, 4700-4704.
18. Tripathi, G. N. R.; Schuler, R. H., Resonance Raman Studies of Substituent Effects on the Electronic Structure of Phenoxy Radicals. *J. Phys. Chem.* **1988**, *92*, 5129-5133.

19. Radziszewski, J. G.; Gil, M.; Gorski, A.; Spanget-Larsen, J.; Waluk, J.; Mróz, B. a. J., Electronic states of the phenoxyl radical. *The Journal of Chemical Physics* **2001**, *115*, 9733-9738.
20. Chipman, D. M.; Liu, R.; Zhou, X.; Pulay, P., Structure and fundamental vibrations of phenoxyl radical. *The Journal of Chemical Physics* **1994**, *100*, 5023-5035.
21. Raghavachari, K.; Trucks, G. W.; Pople, J. A.; Head-Gordon, M., A Fifth-Order Perturbation Comparison of Electron Correlation Theories. *Chem Phys Lett* **1989**, *157*, 479-483.
22. Colussi, A. J.; Zabel, F.; Benson, S. W., The very low-pressure pyrolysis of phenyl ethyl ether, phenyl allyl ether, and benzyl methyl ether and the enthalpy of formation of the phenoxy radical. *International Journal of Chemical Kinetics* **1977**, *9*, 161-178.
23. Pickett, H. M., The Fitting and Prediction of Vibration-Rotation Spectra with Spin Interactions. *J. Mol. Spec.* **1991**, *148*, 371-377.
24. Larsen, N. W., Microwave Spectra of the Six mono-¹³C-Substituted Phenols and of Some Monodeuterated Species of Phenol. Complete Substitution Structure and Absolute Dipole Moment. *J. Mol. Struct.* **1979**, *51*, 175-190.
25. Abeysekera, C.; Hernandez-Castillo, A. O.; Stanton, J. F.; Zwier, T. S., Broadband Microwave Spectroscopy of 2-Furanyloxy Radical: Primary Pyrolysis Product of the Second-Generation Biofuel 2-Methoxyfuran. *J Phys Chem A* **2018**, *122*, 6879-6885.
26. Fessenden, R. W.; Schuler, R. H., ESR Spectrum of the Cyclohexadienyl Radical. *The Journal of Chemical Physics* **1963**, *38*, 773-774.
27. Reale, S.; Di Tullio, A.; Spreti, N.; De Angelis, F., Mass Spectrometry in the Biosynthetic and Structural Investigation Of Lignins. *Mass Spectrom. Rev.* **2004**, *23*, 87-126.
28. Kawamoto, H.; Horigoshi, S.; Saka, S., Pyrolysis reactions of various lignin model dimers. *Journal of Wood Science* **2007**, *53*, 168-174.
29. Kawamoto, H.; Saka, S., Role of Side-Chain Hydroxyl Groups in Pyrolytic Reaction of Phenolic β -Ether Type of Lignin Dimer. *Journal of Wood Chemistry and Technology* **2007**, *27*, 113-120.
30. Liu, C.; Zhang, Y.; Huang, X., Study of guaiacol pyrolysis mechanism based on density function theory. *Fuel Processing Technology* **2014**, *123*, 159-165.
31. Scheer, A. M.; Mukarakate, C.; Robichaud, D. J.; Nimlos, M. R.; Ellison, G. B., Thermal Decomposition Mechanisms of the Methoxyphenols: Formation of Phenol, Cyclopentadienone, Vinylacetylene, and Acetylene. *J. Phys. Chem. A.* **2011**, *115*, 1381-1389.
32. Asmadi, M.; Kawamoto, H.; Saka, S., Thermal reactions of guaiacol and syringol as lignin model aromatic nuclei. *Journal of Analytical and Applied Pyrolysis* **2011**, *92*, 88-98.
33. Custodis, V. B.; Hemberger, P.; Ma, Z.; van Bokhoven, J. A., Mechanism of fast pyrolysis of lignin: studying model compounds. *J Phys Chem B* **2014**, *118*, 8524-31.
34. Hosoya, T.; Kawamoto, H.; Saka, S., Role of methoxyl group in char formation from lignin-related compounds. *Journal of Analytical and Applied Pyrolysis* **2009**, *84*, 79-83.
35. Suryan, M. M.; Kafafi, S. A.; Stein, S. E., The Thermal Decomposition of Hydroxy- and Methoxy-Substituted Anisoles. *J Am Chem Soc* **1989**, *111*, 1423-1429.
36. Furutani, Y.; Dohara, Y.; Kudo, S.; Hayashi, J. I.; Norinaga, K., Theoretical Study on the Kinetics of Thermal Decomposition of Guaiacol and Catechol. *J Phys Chem A* **2017**, *121*, 8495-8503.
37. Huang, J.; Li, X.; Wu, D.; Tong, H.; Li, W., Theoretical studies on pyrolysis mechanism of guaiacol as lignin model compound. *Journal of Renewable and Sustainable Energy* **2013**, *5*.

APPENDIX

DESCRIPTION OF MATLAB PROGRAMS

A.1 Generating the Frequency Spectrum

A.1.1 spectra.m

This program takes the experimental free induction decay (FID), removes some of the spur lines from the digitizer using 'mhz250bkg.m' applies a Kaiser Bessel window and performs a fast Fourier transform (FFT). In order for it to run the 'mhz250bkg.m' needs to be in the same folder.

```
%FUNCTION VARIABLES
%m: Flag to establish the frequency range.
    % 0 --> 2-8 GHz: Without a mixer.
    % 1 --> 8-18 GHz: With a mixer.
%gd: This is the gate duration. Length of the FID. In microseconds.
%filedat: Name of the csv file that contains the raw data.
    %For example: '20420117.csv'

%OUTPUT OF THE PROGRAM
%freq: frequencies in GHz (full range).
%Intensities: Intensities of the spectrum.
function [freq,Intensities]=spectra(m,gd,filedat)

%Importing the file (raw data from the digitizer)
file=filedat;
delimiterIn='';
A=importdata(file,delimiterIn);
FID=A.data;

%Experimental parameters.
tstep=25e-12; %This variable is only needed to plot the FID.
25 ps is the time delay between ADC in the digitizer.
gate_duration=gd*1e-6; %Length of the FID in microseconds.
Sample_Rate=4e10; %This is the sampling rate of the digitizer, in
case you use another device with a different sampling rate it would need
to change.
mix=18.9; %This is the output frequency of the PLDRO. This
needs to be adjusted if the mixing frequency changes.
dig=0.0000625; %for 7us FID 1.4250e-04 should be the value (that
is the resolution).
mixdig=mix+dig;
T1=length(FID); %Length of the FID

%Plotting the FID
%To visualize the FID remove the percentage sign (%) from FID1, T0,
%"figure(2)" and "plot(T0,FID1)"
%FID1=Is generated to visualize the FID if needed. It is the raw data.
```

```

FID1=FID;
%Time domain x-axis
T0=(tstep:tstep:gate_duration)*1e6;
figure(2)
plot(T0,FID1)

%Removing the 250 MHz lines. This will run the mh250bkg.m program.
    %To visualize how the FID looks after running this program remove
    %the percentage sign(%) from FID2,"figure3" and "plot(T0,FID2)"
mh250bkg
%FID2=FID;
%figure(3)
%plot(T0,FID2)

%Applying the Kaiser-Bessel
%T1:Length of the FID
%The second variable is the beta of the window. Beta is the Kaiser window
%parameter that affects the sidelobe attenuation of the Fourier transform
of the window.
%Increasing beta widens the mainlobe and decreases the amplitude of the
sidelobes (i.e., increases the attenuation).
Wk=kaiser(T1,21.5);          %usually 11.5 is used for general 16us FID.
FID=Wk.*FID;                %Applying the window to the data.

%Performing the fast Fourier Transform
    %Here you perform a FFT then apply a shift due to the way Matlab
does
    %its FFT, take the absolute value and normalize.
Intensities=abs((fftshift(fft(FID)))/sqrt(T1));

%Calculating the frequencies
spec=1/gate_duration;
if m==0      % When you are not using a mixer
    freq=((spec:spec:Sample_Rate)-Sample_Rate/2)*1e-9-dig;          %
Sorting of frequency domain
elseif m==1  %Using a mixer
    freq=mixdig-((spec:spec:Sample_Rate)-Sample_Rate/2)*1e-9; % Sorting
of frequency domain
end

    %If you want to plot the full spectrum and not just the targeted
    %frequencies erase the percentage sign (%) from "figue(4)" and
    %"plot(freq,Intensities)"
%figure(4)
%plot(freq,Intensities)

end

```

A.1.2 freqcut.m

This program takes the whole frequency space and selects the frequency regime that was swept. In order to run this program 'spectra.m' and 'mhz250bkg.m' need to be in the same folder.

```
%FUNCTION VARIABLES
%m: Flag to establish the frequency range.
    % 0 --> 2-8 GHz: Without a mixer.
    % 1 --> 8-18 GHz: With a mixer.
%f1: Initial frequency (in GHz) that you want to look at in the spectrum.
%f2: Final frequency (in GHz) that you want to look at in the spectrum.
    %For example, if you sweep from 8-18 GHz then f1==8 and f2==18
%gd: This is your gate duration. Length of the FID. In microseconds.
%filedat: Name of the csv file that contains the raw data.
    %For example: '20420117.csv'
%filename: Name of the output file. This is also a csv file.
    %For example: 'Thisspectrumrocks.csv'
%OUTPUT OF THE PROGRAM
    %First Column: Frequencies (from fi to f2). These are in GHz in the
    Matlab output but in MHz in the csv file.
    %Second Column: Intensities.
%To run the program, you write in the command window:
    %name_of_the_file_in_matlab=function_name(variable); *The ";"
    is there so you don't get the output file displayed.

function [combine]=freqcut(m,f1,f2,gd,filedat,filename)

%Doing the data analysis. Here you are running the function "spectra"
[freq,Intensities]=spectra(m,gd,filedat);
%Select a frequency regime
Frequency=freq((freq>=f1) & (freq<=f2));
Spectrum=Intensities((freq>=f1) & (freq<=f2));

%plots the intensities vs frequency in GHz
figure(1)
plot(Frequency,Spectrum)

%convert from GHz to MHz and organize the data for the output csv file
%This is done so the output file is easy to read by other programs.
FreMHz=Frequency*1000;
FreqMHz=FreMHz(end:-1:1);
Spec=Spectrum(end:-1:1);

%output matlab file (frerquencies are in GHz)
combine=[Frequency',Spectrum];

%matrix for the output csv file (frequencies are in MHz)
GGG=[FreqMHz,Spec];
%convert to get the csv file.
dlmwrite(filename, GGG,'precision',13)
```

end

A.1.3 mhz250bkg.m

The digitizer consists of 160 separate internal ADC chips, which faces are not matched. This causes spur lines spaced by 250, 100, 50 and 10 MHz. In order to determine the offset of the individual ADC chips and adjust to a common zero, this program subtracts the average of the last 150 points (taken from each ADC chip) to its respective ADC chip.

```
numADC = 160; % number of ADC - see 'read me.docx' note 5
numTailSamples = 1000; % number of samples per ADC for tail calculation
tailLen = numADC * numTailSamples;

% Get the tail, reshape to get one row per ADC
bkgTail = FID(end-tailLen+1:end);
bkgTailMean = reshape(bkgTail, numADC, numTailSamples);
bkgTailStd = std(bkgTailMean, 0, 2);

% Take mean per ADC
bkgTailMean = mean(bkgTailMean, 2);

% Subtract offset from each ADC sample and reshape back to time series
bkgTimeMinusTailMean = reshape(FID, numADC, []);
bkgTimeMinusTailMean = bsxfun(@minus, bkgTimeMinusTailMean,
bkgTailMean);
FID = bkgTimeMinusTailMean(:);
```

A.2 Strong Field Coherence Breaking/ Extract Modulated Transitions

This is the primary program used to determine which transitions are modulated when using the SFCB method. It takes the difference spectrum and then finds the transitions that are modulated more than a given percentage. In order to run this program, the program 'mhz250bkg.m' needs to be in the same folder.

```
%FUNCTION VARIABLES
%m: Flag to establish the frequency range.
    % 0 --> 2-8 GHz: Without a mixer.
    % 1 --> 8-18 GHz: With a mixer.
%f1: Initial frequency (in GHz) that you want to look at in the spectrum.
%f2: Final frequency (in GHz) that you want to look at in the spectrum.
    %For example, if you sweep from 8-18 GHz then f1==8 and f2==18
%gd: This is your gate duration. Length of the FID. In microseconds.
%p: Percentage of modulation with respect of the sweep without the MSE.
    (percentage is arbitrary it is a selection criteria)
%th: Threshold. all frequencies lower than this would be send to zero
in
%the peak spectrum. Cannot exceed the experimental noise level.
```

```

%scans: This matrix contains the number of the scans that will be
analyzed.
%It has two columns:
    %First Column: Sweep without MSE. These scans will be subtracted
from
    %the ones in the second column.
    %Second Column: Sweep with MSE
%filedat: Usually the date in which the set of scans was taken.
%filename: Name of the output file. This is a csv file.
%OUTPUT OF THE PROGRAM
    %First Column: Frequencies (in GHz)
    %Second Column: Intensities of the transitions that were modulated
more than p% and are bigger than th threshold

```

```
function spectra=sfcb(m,f1,f2,gd,p,th,scans,filedat,filename)
```

```

%*****
%Experimental parameters.
%*****

```

```

gate_duration=gd*1e-6; %Length of the FID in microseconds.
Sample_Rate=4e10;      %This is the sampling rate of the digitizer, in
case you use another device with a different sampling rate it would need
to change.
mix=18.9;              %This is the output frequency of the PLDRO. This
needs to be adjusted if the mixing frequency changes.
dig=0.0000625;        %For 7us FID 1.4250e-04 should be the value (that
is the resolution).
mixdig=mix+dig;

```

```

%*****
%Take the experimental FID, remove the 250 spurs lines from the digitizer,
apply a Kaiser Bessel and performs a FFT to get the intensities. Selects
the regime that was swept.
%*****

```

```

S=vertcat(scans(:,1),scans(:,2));
T1=40000*gd;
%Calculating the frequencies
spec=1/gate_duration;
if m==0      %When you are not using a mixer
    freq=((spec:spec:Sample_Rate)-Sample_Rate/2)*1e-9-dig;    % Sorting
of frequency domain
elseif m==1 %Using a mixer
    freq=mixdig-((spec:spec:Sample_Rate)-Sample_Rate/2)*1e-9;    %
Sorting of frequency domain
end
%Select a frequency regime
Frequency=freq((freq>=f1) & (freq<=f2));
Spectrum=zeros(length(Frequency),length(S));

for n=1:length(S)

```

```

    name=[filedat, '_', num2str(S(n)), '.csv'];           %Importing the
file (raw data from the digitizer)
    file=name;
    delimiterIn='';
    A=importdata(file,delimiterIn);
    FID=A.data;
    mhz250bkg                                     %Removing the 250 MHz lines.
    Wk=kaiser(T1,11.5);                             %Applying the Kaiser-Bessel
    FID=Wk.*FID;
    fftspec=abs(fftshift(fft(FID)))/sqrt(T1); %Performing the fast
Fourier Transform
    Spectrum(:,n)=fftspec((freq>=f1) & (freq<=f2));
end

%*****
%Difference between two spectra.
%*****

%Difference between the intensities.
D=zeros(length(Frequency),length(scans));
for q=1:size(scans,1)
    D(:,q)=Spectrum(:,q+size(scans,1))-Spectrum(:,q);
end

%Average of the difference spectra
Davg=sum(D,2)/length(scans);
Davg=abs(Davg);

%Average of only the chirp spectra
A=Spectrum(:,1:length(scans));
Avg=sum(A,2)/length(scans);

%*****
%Take the intensities that are bigger than the p% of the original sweep
%*****

%A takes the percentage of the original line

p=p/100;
P=p.*Avg;
DD=zeros(length(Davg),1);
for n=1:length(Davg)
    DD(n)=(Davg(n)>=P(n)).*Davg(n)+(Davg(n)<P(n))*0;
end

%*****
%All frequencies lower than the threshold are send to zero. This is to
account for experimental fluctuations.
%*****

Dif=DD;
DD1=(Dif>th).*Dif+(Dif<=th).*0;

```

```

%*****
%Generate the peak spectrum
%*****

I1=DD1(end:-1:1);
F1=Frequency(end:-1:1);
if m==0
    [h,v]=findpeaks(DD1,Frequency); %h are the intensities & v are the
    frequencies
elseif m==1
    [h,v]=findpeaks(I1,F1); %h are the intensities & v are the frequencies
end

%Plots the peak spectrum
figure(1)
stem(v,h,'Marker','none')

spectra=[v',h']; % Matrix of frequencies in GHz and peaks that are
modulated more than p% and bigger than th threshold

dlmwrite(filename, spectra,'precision',13) %it converts from a matrix
in matlab to a csv file with a precision of 8 digits.

end

```

A.3 Transition Dipole Moment

A.3.1 tdm.m

This program extracts the frequencies, energies, transition dipole moments, and quantum numbers from the '.str' and '.cat' files from the SPFIT/SPCAT suite of programs. To run the program is necessary to have 'dip.m', 'ener.m', and 'clebschgordan.m' in the same folder.

```

%FUNCTION VARIABLES
%filestr: filename is the .str output file from SPCAT but in .txt format
and the frequencies are sorted.
    %Example: 'file.txt'
        %First column: frequencies
        %Second column: dipole moment
        %Third column: format of the quantum numbers
        %Fourth to Sixth column: quantum numbers
        %Seventh column: number of dipole
%filecat: name of the cat file ('test.cat'). Normal output from SPCAT.
%outputfile: name of the csv output file.
%m1: m can go from -j to j. Usually it is 0.

%OUTPUT
%The output matrix has 10 columns:
    %1: Frequencies (MHz)
    %2: Energies

```

```

%3: Reduced matrix element of the transition dipole moment
%4: Transition dipole moment
%5-7: quantum numbers associated with J2
%8-10: quantum numbers associated with J1

function output=tdm(filestr,filecat,outputfile,m1)
%*****
%Read files
%*****

%read str file
strmt=dip(filestr);

%read cat file
ctmat=ener(filecat);

%select energies, transition dipole moments, frequencies and quantum
numbers
qnumbs=ctmat(:,3:8)*[1e5;1e4;1e3;1e2;10;1];
qnumbs1=strmt(:,3:8)*[1e5;1e4;1e3;1e2;10;1];

%The str file does not necessarily have the same length as the cat file.
Here it selects the shared frequencies.
A1=ismember(qnumbs1,qnumbs);
B1=strmt(:,2);
C1=B1(A1==1);

%generate tdp matrix. tdp has 9 columns.
%First Column: Frequencies
%Second Column: Reduced matrix element of the transition dipole
moment
%Third Column: Energies
%4-6 quantum numbers J2, and 7-9 quantum numbers J1
A=[ctmat(:,1),C1,ctmat(:,2),ctmat(:,3),ctmat(:,4),ctmat(:,5),ctmat(:,6
),ctmat(:,7),ctmat(:,8)];

%select the rows with J equal or higher than m1
tdp=A(~sum(A(:,[4,7])<m1,2),:);

%*****
%Calculate clebsch-gordan coefficients
%*****

j=1;
m=0; %comes from q and it is zero due to the z direction
%for the m quantum number, m can go from -j to j but then we would have
to calculate a lot of elements, so for now we are only calculating with
specific m.

L=length(tdp(:,1));
C=zeros(L,3);
sc=zeros(L,1);

```



```

fileID = fopen(filename, 'r');

% Read columns of data
dataArray = textscan(fileID, formatSpec, endRow(1)-startRow(1)+1,
'Delimiter', ',', 'WhiteSpace', ' ', 'HeaderLines', startRow(1)-1,
'ReturnOnError', false);

for block=2:length(startRow)
    frewind(fileID);
    dataArrayBlock = textscan(fileID, formatSpec,
endRow(block)-startRow(block)+1, 'Delimiter', ',', 'WhiteSpace', ' ',
'HeaderLines', startRow(block)-1, 'ReturnOnError', false);
    for col=1:length(dataArray)
        dataArray{col} = [dataArray{col};dataArrayBlock{col}];
    end
end

% Close the text file.
fclose(fileID);

% Convert the contents of columns containing numeric strings to numbers.
Replace non-numeric strings with NaN.
raw = repmat({''}, length(dataArray{1}), length(dataArray)-1);

for col=1:length(dataArray)-1
    raw(1:length(dataArray{col}), col) = dataArray{col};
end

numericData = NaN(size(dataArray{1}, 1), size(dataArray, 2));

% Convert the contents of columns containing numeric strings to numbers.
Replace non-numeric strings with NaN.
for col=[1,2,3,4,5,6,7,8,9,10]
    rawData = dataArray{col};
    for row=1:size(rawData, 1);
        regexstr =
'(?<prefix>.*?)(?<numbers>([-]*(\d+[\,]*)+[\.]{0,1}\d*[eEdD]{0,1}[-
+]*\d*[i]{0,1})|([-]*(\d+[\,]*)*[\.]{1,1}\d+[eEdD]{0,1}[-
+]*\d*[i]{0,1}))(?<suffix>.*)';
        try
            result = regexp(rawData{row}, regexstr, 'names');
            numbers = result.numbers;
            invalidThousandsSeparator = false;
            if any(numbers==' ');
                thousandsRegExp = '^(\d+?(\,\d{3})*\.\{0,1\}\d*$)';
                if isempty(regexp(thousandsRegExp, ' ',
'once'));
                    numbers = NaN;
                    invalidThousandsSeparator = true;
                end
            end
        end

        if ~invalidThousandsSeparator;

```

```

        numbers = textscan(strrep(numbers, ',', ''),
'%f');
        numericData(row, col) = numbers{1};
        raw{row, col} = numbers{1};
    end
catch me

end

end

end

end
% Replace non-numeric cells with NaN
R = cellfun(@(x) ~isnumeric(x) && ~islogical(x),raw);
raw(R) = {NaN};

% Create output variable
strmt = cell2mat(raw);
strmt=strmt(:,[1,2,4:9]);

end

```

A.3.3 ener.m

This program reads the '.cat' file from SPCAT and outputs a matrix with the frequencies, energies, and quantum numbers.

```

%INPUT
%filename: name of the cat file ('test.cat').

function ctmat=ener(filename)

formatSpec = '%21s%8s%2s%10s%3s%7s%4s%2s%2s%2s%8s%2s%2s%s%[\n\r]';

startRow = 1;
endRow = inf;

fileID = fopen(filename,'r');

dataArray = textscan(fileID, formatSpec, endRow(1)-startRow(1)+1,
'Delimiter', ',', 'WhiteSpace', '', 'HeaderLines', startRow(1)-1,
'ReturnOnError', false);
    for block=2:length(startRow)
        frewind(fileID);
        dataArrayBlock = textscan(fileID, formatSpec,
endRow(block)-startRow(block)+1, 'Delimiter', ',', 'WhiteSpace', '',
'HeaderLines', startRow(block)-1, 'ReturnOnError', false);
        for col=1:length(dataArray)
            dataArray{col} = [dataArray{col};dataArrayBlock{col}];
        end
    end
end

```

```

fclose(fileID);

raw = repmat({' '},length(dataArray{1}),length(dataArray)-1);

    for col=1:length(dataArray)-1
        raw(1:length(dataArray{col}),col) = dataArray{col};
    end

numericData = NaN(size(dataArray{1},1),size(dataArray,2));

for col=[1,2,3,4,5,6,7,8,9,10,11,12,13,14]
    rawData = dataArray{col};

    for row=1:size(rawData, 1);
        regexstr
        '(?<prefix>.*?)(?<numbers>([-]*(\d+[\,]*)+[\.]{0,1}\d*[eEdD]{0,1}[-
+]*\d*[i]{0,1})|([-]*(\d+[\,]*)*[\.]{1,1}\d+[eEdD]{0,1}[-
+]*\d*[i]{0,1}))(?<suffix>.*)';
        =
        try
            result = regexp(rawData{row}, regexstr, 'names');
            numbers = result.numbers;
            invalidThousandsSeparator = false;
            if any(numbers==' ');
                thousandsRegExp = '^(\d+?(\,\d{3})*\.{0,1}\d*$)';
                if isempty(regexp(thousandsRegExp, ' ',
'once'));
                    numbers = NaN;
                    invalidThousandsSeparator = true;
                end
            end
            if ~invalidThousandsSeparator;
                numbers = textscan(strrep(numbers, ',', ' '),
'%f');
                numericData(row, col) = numbers{1};
                raw{row, col} = numbers{1};
            end

        catch me

    end

end

R = cellfun(@(x) ~isnumeric(x) && ~islogical(x),raw);
raw(R) = {NaN};

% Create output variable
ctmat = cell2mat(raw);

```

```
ctmat=ctmat(:,[1,4,8:13]);
end
```

A.3.4 clebschgordan.m

This program computes the Clebsch-Gordan coefficients. It doesn't take into account hyperfine couplings.

```
% Inputs:
% j1 : A scalar giving the first total angular momentum.
% m1 : A scalar giving the projection of the first total angular
%      momentum.
% j2 : A scalar giving the second total angular momentum.
% m2 : A scalar giving the projection of the second total angular
%      momentum.
% j   : A scalar giving the coupled total angular momentum.
% m   : A scalar giving the projection of the coupled total angular
%      momentum.
% Outputs:
% C   : A scalar giving the required Clebsch-Gordan coefficient.

function C = clebschgordan(j1,m1,j2,m2,j,m)

assert(isscalar(j1) && isscalar(m1) && isscalar(j2) && isscalar(m2) &&
isscalar(j) && isscalar(m),'All inputs must be scalars.')
```

```
*****
%Check conditions
*****
if j1 < 0 || j2 < 0 || j < 0 || ...
    mod(2*j1,1) ~= 0 || mod(2*j2,1) ~= 0 || mod(2*j,1) ~= 0 || ...
    mod(2*m1,1) ~= 0 || mod(2*m2,1) ~= 0 || mod(2*m,1) ~= 0 || ...
    abs(m1) > j1 || abs(m2) > j2 || abs(m) > j || ...
    j1+m1 < 0 || j2+m2 < 0 || j+m < 0 || j1+j2+j < 0 || ...
    mod(j1+m1,1) ~= 0 || mod(j2+m2,1) ~= 0 || mod(j+m,1) ~= 0 || ...
    mod(j1+j2+j,1) ~= 0

elseif m1+m2-m ~= 0 || j < abs(j1-j2) || j > j1+j2

    C = 0;
    return
end

*****
%Compute valid k values for summation
*****
k = max([0,j2-j-m1,j1-j+m2]):min([j1+j2-j,j1-m1,j2+m2]);

*****
%Check for stability
```

```

%*****
if j+j1-j2 > 21 || j+j2-j1 > 21 || j1+j2-j > 21 || j1+j2+j+1 > 21 || ...
    j+m > 21 || j-m > 21 || j1+m1 > 21 || j1-m1 > 21 || ...
    j2+m2 > 21 || j2-m2 > 21 || any(k > 21) || ...
    any(j1+j2-j-k > 21) || any(j1-m1-k > 21) || ...
    any(j2+m2-k > 21) || any(j-j2+m1+k > 21) || any(j-j1-m2+k > 21)

%If the argument to one or more of the factorials used in the computation
of the requested Clebsch-Gordan coefficient is greater than 21, this can
result in inaccuracies.
end

%*****
%Compute coefficient
%*****

C = sqrt((2*j+1)*factorial(j+j1-j2)*factorial(j+j2-j1)*factorial(j1+j2-
j)/factorial(j1+j2+j+1))*...
    sqrt(factorial(j+m)*factorial(j-m)*factorial(j1+m1)*factorial(j1-
m1)*factorial(j2+m2)*factorial(j2-m2))*...
    sum((-1).^k./(factorial(k).*factorial(j1+j2-j-k).*factorial(j1-
m1-k).*factorial(j2+m2-k).*factorial(j-j2+m1+k).*factorial(j-j1-
m2+k)));
end

```

VITA

Alicia O. Hernández Castillo was born on January 17th, 1990 to Silvia Castillo. She attended The National and Autonomous University of Mexico (UNAM) to study Chemistry. During this time, she adopted a coonhound puppy and named him Hooke. She received her B.S. in Chemistry graduating with honors in 2014. While at the UNAM, Alicia participated in undergrad research under Professor Renato Lemus Casillas using group theory to determine the symmetry group of an impenetrable cubic well potential. She wrote her undergrad thesis on this topic. In the fall of 2014, Alicia moved to the United States with Hooke to start graduate school at Purdue University. She joined the research group of Professor Timothy S. Zwier in the spring of 2015. There she focused on detection and characterization of pyrolysis intermediates using molecular spectroscopy. Alicia received her Ph.D. in Physical Chemistry in 2018 and joined the research group of Professor Gerard Meijer under the supervision of Dr. Sandra Eibenberger as a postdoctoral researcher at the Fritz Haber Institute of Max Planck Society in Berlin, Germany.

PUBLICATION

THE JOURNAL OF CHEMICAL PHYSICS **145**, 114203 (2016)

Broadband multi-resonant strong field coherence breaking as a tool for single isomer microwave spectroscopy

A. O. Hernandez-Castillo, Chamara Abeysekera, Brian M. Hays, and Timothy S. Zwier^{a)}
Department of Chemistry, Purdue University, 560 Oval Drive, West Lafayette, Indiana 47907, USA

(Received 13 July 2016; accepted 29 August 2016; published online 20 September 2016)

Using standard hardware available in chirped-pulse Fourier transform microwave (CP-FTMW) spectroscopy, an experimental method is introduced to selectively extract from the microwave spectrum of an otherwise complicated multicomponent mixture a set of transitions due to a single component, thereby speeding spectral assignment. The method operates the broadband chirped-pulse used to excite the sample in the strong-field limit through a combination of high power and control of the sweep rate. A procedure is introduced that leads to selection of three transition frequencies that can be incorporated as a set of resonant sequential single-frequency microwave pulses that follow broadband chirped-pulse excitation, resulting in a reduction in the coherent signal from a set of transitions ascribable to the component of interest. The difference in the CP-FTMW spectrum with and without this set of multi-resonant single-frequency pulses produces a set of transitions that can confidently be assigned to a single component of the mixture, aiding the analysis of its spectrum. The scheme is applied to (i) selectively extract the spectrum of one of five singly ¹³C-substituted isotopologues of benzonitrile in natural abundance, (ii) obtain the microwave spectra of the two structural isomers (E)- and (Z)-phenylvinyl nitrile, and (iii) obtain conformer-specific microwave spectra of methylbutyrate. *Published by AIP Publishing.* [<http://dx.doi.org/10.1063/1.4962505>]

I. INTRODUCTION

In many important circumstances (e.g., photochemical product analysis, pyrolysis, and combustion), complex gas-phase mixtures are produced that have a number of unique molecular components whose identities and abundances must be determined. Even in pure samples containing a single chemical component, if the molecule is large enough, it can possess several distinct conformational and/or structural isomers, each with their own unique properties and spectral signatures.¹ These each contribute to the spectrum via transitions that are interspersed amongst one another, presenting a considerable challenge to attempts to assign individual transitions to particular components of the mixture. This has fueled much effort towards the development of methods for conformer- or isomer-specific spectroscopy.

Double resonance methods in the optical and infrared regions have been used for many years to carry out isomer-specific spectroscopy, with one light source tagging a ground state level of a single isomer by selectively removing population from it, while a second tuned light source probes the changes induced in the spectral intensities by the first. In the gas phase, optical-optical,² IR-IR,³ and IR-optical methods^{1,4-6} have been devised.

The direct relationship between molecular structure and rotational frequencies makes rotational spectroscopy highly structurally specific and an important tool for analyzing chemically complex structures and mixtures. The rotational transitions of a molecule can be fit to obtain highly accurate rotational constants, while intensities report on the populations

of the levels and the projections of the permanent dipole moment on the inertial axes of the molecule.⁷ Shifts and splittings due to centrifugal distortion, nuclear quadrupole coupling, tunneling, or other large amplitude motions of specific functional groups all add to the richness of the structural data.

The development of the Chirped-Pulse Fourier transform microwave (CP-FTMW) technique⁸ brought a rapid spectral velocity^{9,10} to high resolution rotational spectroscopy. The success of chirped-pulse, linear sweep excitation rests on delivering sufficient microwave power to the sample to maximize coherence between pairs of rotational energy levels resonant in the swept frequency range.¹¹ However, population of rotational levels can be significantly altered during a strong field linear sweep. These pronounced multi-resonance excitations in microwave spectroscopy¹² have been generally avoided in CP-FTMW operation.

Rotational transitions due to different components of a mixture show up interspersed amongst one another, presenting a challenge to assignment, especially when the determination of the chemical composition of the gas mixture is itself the research problem of primary interest. The broadband capability and rapid data acquisition of CP-FTMW techniques has enabled many advances in microwave double-resonance techniques that can facilitate the analysis of congested rotational spectra.¹³ For example, microwave three-wave mixing can differentiate two chiral enantiomers;¹⁴ infrared-microwave (IR-MW)¹⁵ double resonance is used to study kinetics of conformational isomerization,¹⁶ and UV-microwave (UV-MW) techniques can extract single-species rotational spectra using rotationally resolved electronic spectra.^{17,18} Coherence transfer techniques like microwave-

^{a)}Author to whom correspondence should be addressed. Electronic mail: zwier@purdue.edu

radio frequency (MW-RF) double-resonance gives information about the connectivity of rotational energy levels, by modulating the MW transitions with an interacting RF pulse.^{19,20} The coherence-breaking null scheme, in which laser excitation out of a single rovibronic level occurs between two oppositely phased composite millimeter-wave pulses, has successfully demonstrated the ability to rapidly analyze dense, congested regions in an optical spectrum of a small molecule.²¹ Recently, McCarthy and co-workers have introduced a powerful method for “spectral taxonomy” of multi-component mixtures that combines broadband microwave spectroscopy with fast acquisition of line-by-line double resonance spectra that determine line connectivity, using a computer-controlled cavity microwave spectrometer.¹³ Finally, two-dimensional CP-FTMW spectroscopy holds promise as an ultimate solution for tracking the global connectivity of rotational energy levels; however, acquisition of 2D microwave spectra in its full broadband implementation is still a formidable challenge.²² One drawback of many of these techniques is that they require additional equipment for their implementation beyond that required for CP-FTMW, generating another level of experimental complexity. Therefore, a new approach that takes full-advantage of the multi-pulse capabilities of CP-FTMW instrumentation using only this instrumentation would be ideal and cost effective.

In the last several years broadband microwave techniques focused mainly on reducing the data acquisition time¹⁶ and expanding the bandwidth to higher frequency regions.^{23–27} The massive data output rate of these spectrometers and the scarcity of compatible high speed broadband data analysis procedures make their spectral interpretation time consuming. Therefore, methods that can reduce the assignment time for complex congested spectra will contribute to making rotational spectroscopy an ever-more powerful analytical tool.^{27,28}

Here, a new method is introduced, using the same CP-FTMW hardware to extract from a congested spectrum subsets of transitions ascribable to single-components of the mixture, thereby greatly simplifying line assignments. In discovering,

exploring, and developing the multi-resonance strong field method, benzonitrile was used as a simple single-component sample, and is used here to introduce the method and illustrate various aspects of the technique. Several examples of the method’s application follow. As a test of the method’s detection sensitivity and selectivity, we apply it first to a singly ¹³C isotope of benzonitrile (2-¹³C), present in natural abundance at ~2% of the all ¹²C molecules. Next, to illustrate its application to samples containing structural isomers, a sample containing a mixture of (E)- and (Z)-phenylvinyl nitrile is interrogated. Finally, results from studies of methyl butyrate demonstrate the ability of a refined version of the method to obtain single-conformer microwave spectra even in a sample with modest dipole moment (~1.5 D).

II. EXPERIMENTAL

A. CP-FTMW spectrometer

The main components of the CP-FTMW spectrometer are shown in Figure 1. The 10 GS/s arbitrary waveform generator (AWG; Tektronix AWG7101) can be programmed to produce single frequency pulses or linear frequency sweeps up to 5 GHz in $\leq 2 \mu\text{s}$. The AWG output is directed through a 5 GHz low-pass filter (Lorch 10LP-5000-S, (164 MHz)) and leveled in a preamplifier (Mini-Circuits ZX60-6013E-S+ 6000 MHz, +14.2 dB gain). The pre-amplifier output is then multiplied with a quadrupler (Phase One PS06-0161) to obtain an 11 GHz bandwidth pulse and/or any variety of selected single frequency pulses within the 7.5-18.5 GHz range. Final waveforms are power controlled with a step attenuator (Weinschel AF117A-69-11) and fed into a 200 W traveling wave-tube amplifier (TWTA; Amplifier Research 200T8G18A), where the pulses are amplified and sent into a vacuum chamber through a broadcasting horn (Amplifier Research model AT4004, 8-18 GHz).

Details of the current vacuum chamber configuration are explained elsewhere.²⁹ The chamber is maintained at an

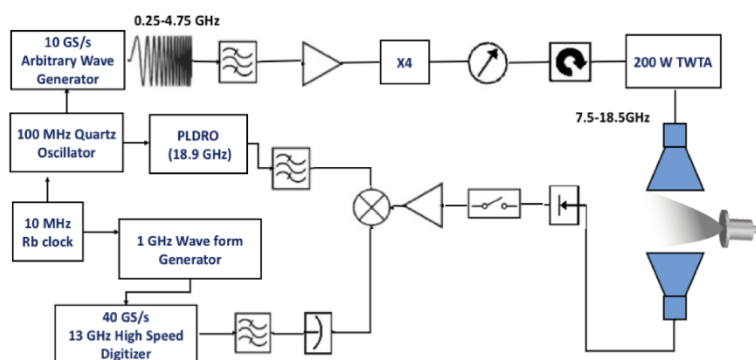


FIG. 1. Schematic diagram of the CP-FTMW spectrometer. The arbitrary wave form generator (AWG) produces linear frequency sweeps from 0.25 to 4.75 GHz. The resulting frequencies are up converted to the 7.5–18.5 GHz range using a quadrupler and amplified by a 200 W traveling wave-tube amplifier (TWTA). The microwave radiation is transmitted into the vacuum chamber using a broadcasting horn. The sample is introduced into the chamber using a pulsed valve that creates a supersonic expansion that cools the molecular sample to low rotational temperatures. The polarized molecules will emit a molecular free induction decay (FID), which is collected using a receiving horn. The molecular signal is amplified by a +45 dB active gain amplifier. The FID is phase coherently averaged and digitized with a real time digitizer.

unloaded pressure of 1×10^{-6} mbar and average operating pressure of $\sim 3 \times 10^{-5}$ mbar when the sample is introduced. The broadcasted high power microwave pulse polarizes the sample molecules, which then undergo free induction decay (FID). The FID signal is collected with a second broadcasting horn and passed through a PIN diode limiter (Advanced Control Components ACLS 4619F-C36-1K) and a reflective single pole single throw switch (Advanced Technical Materials S1517D isolation 80 dB, 2-18 GHz). This combination protects the amplifier and high speed digitizer from the high-power polarizing chirp. The FID collection is initiated ~ 60 ns after the high power chirp, which incorporates the switching speed of the switch and a buffer. The collected molecular FID is amplified by a +45 dB gain low noise amplifier (Miteq AMF-6F-06001800-15-10P) and down-converted using a triple-balanced mixer (Miteq TB0440LW1) with a phase-locked dielectric resonator oscillator (PLDRO, Microwave Dynamics PLO-2000-18.90) operating at 18.9 GHz. For mixing purity the PLDRO output is filtered with an 18.9 GHz cavity bandpass filter (Lorch 7CF7-18900/100S, (50 MHz at 3 dB)). The mixed low-frequency band (0.4-11.4 GHz) is transmitted through a DC block (MCL 15542 BLK-18) and a 12 GHz low pass filter (Lorch 7LA-12000-S, (92.54 MHz)). Finally, the molecular free induction decay (FID) is phase coherently averaged and digitized in the time domain with a 13 GHz, 40 GS/s real-time digitizer (Guzik ADC6131). In order to average in the time domain the PLDRO and the AWG are synchronized to a 100 MHz phase-locked loop (Wenzel Associates 501-10137B). This loop is driven by a 10 MHz Rb-disciplined crystal oscillator (Stanford Research Systems FS725). The phase drift of the oscillators and the amplifiers is controlled through water cooling.

The real-time digitizer achieves its 40 GS/s digitization rate using 160 separate internal ADC chips interleaved with one another, where each individual chip makes an acquisition every 4 ns. These ADC chips are not perfectly matched, causing the appearance of spurious lines at 250 MHz intervals in the frequency domain. Therefore, a custom Matlab routine was written to attenuate these lines. This routine determines the offset of each individual ADC chip by calculating the average of the last 150 points acquired by each respective ADC chip in the data set, and then subtracts each ADC's offset from all points acquired by that ADC to obtain a properly baseline-corrected FID. After performing the Matlab routine, the data are filtered with a Kaiser-Bessel function^{8,30} to discriminate against the TWTA noise present at early time in the FID collection, before Fourier transforming the time-domain signal to obtain the final frequency domain (8-18 GHz) spectrum.

The general experimental timing scheme is controlled by the two marker channels of the AWG, enabling multiple chirp/FID detections in a single gas pulse ($\sim 500 \mu\text{s}$ in duration). The AWG output is routed through two pulse-delay generators (Berkeley Nucleonics Corp. Model #555 and 577), one of which is used to control the delays between the gas pulse and the chirp sequence. The other delay generator sets the timings of the TWTA amplification and the fast PIN switch.

For this study, commercial samples of the molecules (benzonitrile (98%, Sigma-Aldrich), a commercial mixture

of (E)- and (Z)-PVN (97%, Alfa Aesar), and methyl butyrate (99%, Sigma-Aldrich)) were used without any further purification. The liquid samples were inserted into a stainless steel sample holder, located immediately behind a pulsed valve (Parker General Valve, Series 9) with a 1 mm diameter nozzle orifice. The (E)- and (Z)-PVN mixture was heated to $\sim 80^\circ\text{C}$ to obtain sufficient vapor pressure. The samples were entrained in helium gas at a 10 psig backing pressure. The solenoid valve was powered by a home-made pulsed valve driver triggered externally at a 10 Hz repetition rate. The experimental timing scheme was matched to the width of the gas pulse in order to collect a set of 25 FIDs for a single gas pulse, each $16 \mu\text{s}$ long and separated by $20 \mu\text{s}$.

B. Computational methods

Ab initio or Density Functional Theory (DFT) calculations on (E)/(Z)- phenylvinyl nitrile (PVN) and methyl butyrate (MB) were performed using the Gaussian 09 suite at the MP2/aug-cc-pVTZ and M06-2X/6-311 + g(d) levels of theory for PVN and MB, respectively.³¹ The calculated rotational constants were used to predict the line frequencies and compared directly to experimental observations (see Section IV).

III. STRONG FIELD COHERENCE BREAKING (SFCB)

Fast passage excitation in chirped pulse spectroscopy can be considered as a transient absorption during the excitation pulse and a subsequent transient emission.^{8,32} The development of equations describing the mechanism that governs chirped-pulse FTMW spectroscopy has been provided in detail elsewhere.³³⁻³⁵ Here, we summarize only the essentials necessary to understand the unique aspects of the new strong field coherence breaking scheme.

Consider a simple case in which the frequency of a pulse of microwave radiation is swept from well below to well above a single molecular rotational transition. The Rabi frequency for the transition between the two energy levels is given by

$$\Omega_0 = \left[\left| \frac{\vec{\mu} \cdot \vec{E}_{\text{pulse}}}{\hbar} \right|^2 + \Delta^2 \right]^{\frac{1}{2}},$$

where μ is the transition dipole moment, E_{pulse} is the electric field strength of the microwave field, and Δ is the detuning of the excitation pulse from resonance frequency. If the linear sweep rate ($\alpha = \frac{d}{dt} \Delta\omega_{ab}$) is much faster than the Rabi frequency ($\alpha \gg \Omega_0^2$), the coupling between the molecules and the polarizing electric field via the rotational transient dipole moment is small. In this weak coupling limit, referred to as the linear fast passage (LFP) regime, radiation that sweeps from low-to-high or high-to-low frequencies produces a coherence between the two rotational states.³⁶ The maximum coherence is achieved with a $\pi/2$ excitation pulse in the Bloch sphere representation. The observed transition signal at a resonance frequency ω , $S(\omega)$, scales according to³²

$$S \propto \omega \cdot \mu^2 \cdot E_{\text{pulse}} \cdot \Delta N_0 \cdot \left(\frac{\pi}{\alpha} \right)^{1/2},$$

where ΔN_0 is the population difference between the two energy levels involved in the transition prior to the excitation pulse. Population analysis is possible in this regime because the signal scales linearly with this population difference, which is often governed by a Boltzmann distribution associated with the rotational levels. This is the regime in which almost all past FTMW studies have been carried out.

However, as Schnell and co-workers have recently highlighted, the high power TWTA's used in CP-FTMW spectrometers have allowed the exploration of rapid adiabatic passage (RAP) effects in rotational spectroscopy.¹² In this regime, a strong coupling (large Ω_0) is created,^{37,38} inducing significant population transfer between two diabatic states, leading in the RAP limit to a π -pulse excitation in the Bloch sphere representation that creates a population inversion between the two states. Therefore, a linear broadband excitation sweep in the strong field limit can alter the relative line intensities from what would be expected based on a Boltzmann distribution.

A linear excitation sweep from low to high frequency will excite low-J states at the beginning of the sweep and higher J states later. If a near π -pulse excitation is achieved, the population transfer induced in the two rotational states will propagate up the ladder in subsequent excitations, moving population to higher-J levels that are subsequently involved in transitions at higher frequency, leading to multi-resonance excitation effects.^{12,33,39,40}

Techniques like selective-excitation CP-FTMW⁴¹ have demonstrated the ability to selectively modulate intensities of rotational transitions that share a common rotational energy level. The technique uses a broadband chirp to create the molecular transient absorption, and a narrowband pulse to selectively disrupt specific coherences between rotational transitions that share common energy levels in the molecular free induction decay. The strong field coherence breaking (SFCB) method we introduce here combines both strong field coupling and selective-excitation schemes to modulate the populations and coherences of a specific set of single conformer/isomer transitions. Subtraction of the CP-FTMW spectrum without the selective excitation pulses, from the spectrum with them present, then effectively highlights a subset of transitions ascribable to a single conformer/isomer in what is otherwise a complex, congested spectrum.

A. Method development

Strong coupling ($\alpha \ll \Omega_0^2$) between the polarizing electric field (E_0) and the molecular rotational dipole is a primary prerequisite for the SFCB method. As demonstrated in previous work,¹² operation in either of the two coupling regimes can be achieved by controlling the polarizing electric field strength of the microwave radiation via the gain on the TWT amplification stage. In the linear fast passage regime, the line intensities will be independent of the direction of the chirp (low-to-high frequency, or high-to-low); however, in the RAP regime, population transfer during the chirp will be significant, resulting in different intensities when the chirp occurs in one direction or the other. As Figure 2(a) illustrates for benzonitrile, a CP-FTMW spectrum recorded with 1%

TWTA gain, in the LFP regime, shows no difference between spectra recorded with an $8 \rightarrow 18$ GHz or an $18 \rightarrow 8$ GHz sweep. However, at 100% TWTA gain, large differences in intensity between the two scans are observed, indicating effects characteristic of the RAP regime. Thus, it is possible to access the weak and strong-field limits for the test molecule, benzonitrile, with its substantial permanent dipole moment ($\mu = 4.5152$ D).⁴²

In its simplest form, the SFCB method involves three fundamental steps.

1. A high power broadband linear chirp is used to record a CP-FTMW spectrum.
2. A second spectrum is recorded after excitation with the same high power linear broadband chirp (8-18 GHz), followed by a single-frequency pulse (or pulses), also at high power, whose frequency is resonant with a transition(s) in the CP-FTMW spectrum, delayed from the chirped pulse by a fixed time. The resultant molecular FID is collected at the end of the selective frequency pulse.
3. A difference spectrum is constructed between scans 1 and 2 in the frequency domain. When the difference is taken, some of the transitions increase in intensity and some decrease, so the absolute value of the intensities is plotted.

In order to obtain difference spectra of highest sensitivity and selectivity, we explored a range of time delays and pulse durations for the single-frequency pulse(s) in benzonitrile, to establish parameters that work best. The $J_{\text{kak}} = 4_{0,4}-3_{0,3}$ ($\nu = 10\,855.233$ MHz) rotational transition of benzonitrile was chosen for the selective single-frequency pulse. The effect of varying pulse duration was investigated by using single-frequency pulses ranging from 10 to 100 ns and 500 to 2000 ns in 5 and 500 ns increments, respectively, while monitoring the integrated intensity of the resonant transition. Our studies showed an initial rise in signal, followed by a 70%-80% reduction in the pulsed transition intensity with longer pulse durations. It was noticed, however, that after a 70% depletion the final number of modulated rotational transitions in the difference spectrum did not change significantly. However, using longer pulse durations can reduce edge effects.⁴³

The time delay between the linear broadband chirp and the single frequency pulse was also varied from 3 ns up to 25 ns in 2 ns increments, with its optimized value also occurring at the minimum intensity of the pulsed transition in the difference spectrum. Both the time delay and single pulse(s) duration must be on time scales fast compared to the relaxation times (T_1 , T_2) of the pulsed transition in order to create multi-level modulation in the FID from the broadband pulse.

For benzonitrile, the method was tested in both coupling regimes, with its optimal selective frequency pulse duration and gap. The difference spectra obtained under weak coupling (LFP) and strong coupling (RAP) regimes are shown in Figures 2(c) and 2(d), respectively. The resulting difference spectrum in the LFP regime (Figure 2(c)) is just as anticipated, based on the selective-excitation CP-FTMW technique,⁴¹ with intensity changes induced in $2_{02}-3_{03}$ and $4_{04}-5_{05}$ transitions that share a rotational level with the $3_{03}-4_{04}$ transition on which the single-frequency coherence-breaking pulse is resonant.

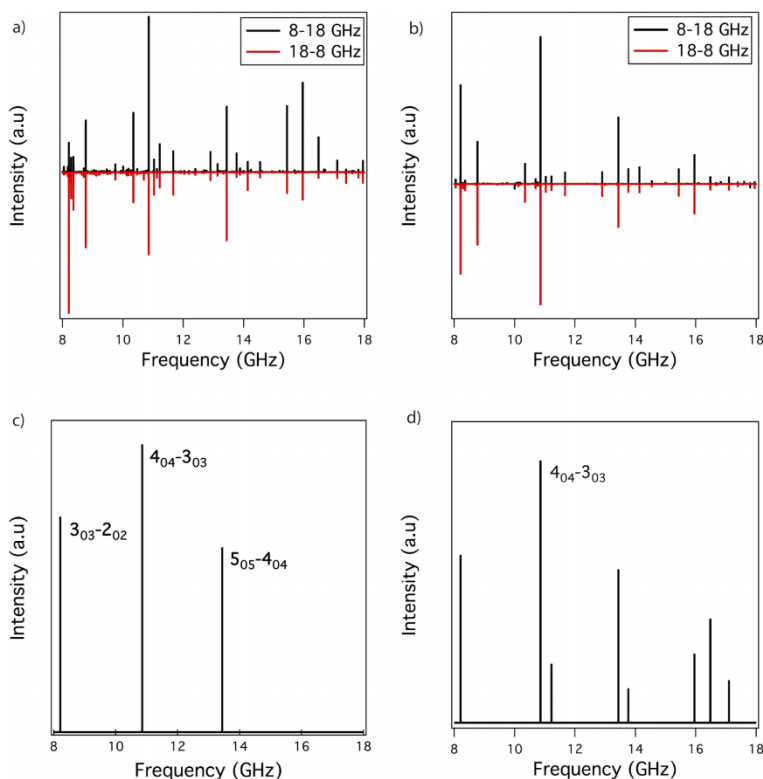


FIG. 2. ((a) and (b)): Broadband CP-FTMW spectra of benzonitrile over the 8-18 GHz region, comparing the spectra following 900 ns chirps with the frequency swept up from 8 to 18 GHz (black) and down from 18 to 8 GHz (red), with TWTA gain at (a) 1% and (b) 100% of full power. ((c) and (d)): Difference spectrum from an 8-18 GHz chirp (800 ns duration) with and without a resonant pulse (100 ns) following the broadband sweep, centered in frequency at the $J_{KaKc} = 4_{0,4}-3_{0,3}$ transition (10 855.233 MHz). The TWTA gain in (c) is 1% and (d) 100% of full power. Only the directly connected $3_{0,3}-2_{0,2}$ and $5_{0,5}-4_{0,4}$ transitions appear in (c), while additional transitions appear under SFCB conditions in (d). The transitions shown here are above the median noise level.

Meanwhile, in the RAP regime (Figure 2(d)), many more transitions had their intensities modulated, even those that have no shared rotational energy level with the $4_{04}-3_{03}$ transition used for the single-frequency pulse. The stability and the reproducibility were checked between scans to make sure the modulation was not due to flow fluctuations or any experimental uncertainty.

The ability to create modulation of a large fraction of the rotation transitions of the molecule in the 8-18 GHz region, by just placing a single selective excitation pulse after the broadband chirp is unique and demonstrates the advantage of operating in the strong field limit when seeking to obtain isomer-specific spectra.

B. Multiple selective-excitation (MSE)

The test molecule benzonitrile has its total dipole moment (μ_a) fixed along a single rotational axis, the “a”-axis. Since a-type rotational transitions therefore dominate the spectrum in its 8-18 GHz range, most of these transitions can be modulated with the SFCB method by exciting a single a-type transition (Figure 2(d)). However, most molecules of more general interest do not have this advantage. Therefore, the SFCB method was modified by implementing a refinement involving a Multiple Selective-Excitation (MSE) sequence, where instead of a single selective pulse, multiple successive

single-frequency pulses are used to disrupt coherences involving a wider range of rotational levels and transition types (a-, b-, or c-).

A new line picking sequence was developed to find the frequencies required for the MSE scheme that would sensitively modulate the intensities of a large fraction of the rotational transitions due to a single isomer or molecular component in a mixture. During this development, it became clear that the single-frequency pulses themselves modulate a number of connected and non-connected transitions due to the isomer selected by the resonant pulse, even in the absence of the broadband chirped-pulse. Careful tests were carried out to ensure that these modulations were not due to any noise associated with the microwave electronics or the high power TWTA. Optimum operating conditions were chosen by varying the input power to the TWTA to make sure that no transition was modulated in intensity when the frequency of the resonant pulse was shifted 10 MHz off-resonance from the most intense transition chosen for MSE.

As the duration of the pulse was increased, more isomer specific transitions were modulated. Therefore, for this study we used 1 μ s long single frequency pulses to select the frequencies needed for the MSE scheme. Further work is on-going to explore the effects produced through these single-frequency microwave pulses. Here, we use them simply as a means of selecting the frequencies for the MSE scheme.

In the MSE sequence as it is currently implemented, it was found that sequential application of single frequency pulses at three frequencies (ν_1 , ν_2 , ν_3) produced a difference spectrum that modulated a sufficient number of lines in a particular isomer to greatly aid assignment. Faced with a broadband CP-FTMW spectrum with anticipated contributions from several components, the three frequencies in the MSE sequence can be chosen using a selection algorithm illustrated in Figure 3. In step 1 the most intense line in the LFP spectrum is chosen as the first frequency (ν_1) pulse, and a FID is collected following a single-frequency selective pulse at frequency ν_1 , leading to the appearance of multiple transitions as just discussed.

In step 2 the spectrum from step 1 is compared to the LFP broadband spectrum, and a transition that is intense in the broadband spectrum but comparatively weak in the ν_1 spectrum is chosen as ν_2 . This choice for ν_2 imparts some complementarity to the transitions that will be modulated in the ultimate SFCB spectrum, thereby increasing the number of transitions that appear in it. Having made this choice for ν_2 , a single-frequency spectrum at ν_2 is obtained as in step 1.

In step 3 the same two criteria are used to choose an initial transition at frequency ν_3^i that appears weakly in the ν_2 spectrum but is relatively intense in the broadband spectrum. This frequency ν_3^i is subsequently used as the basis for a single-frequency pulse spectrum at ν_3^i . Since selective excitation of transitions due to a single isomer is key to the proper choice of frequencies ν_1 , ν_2 , and ν_3^i , the final choice of ν_3 is made after viewing all three single-frequency excitation spectra. The final value for the frequency ν_3 is then chosen by identifying a transition that is the most intense line in the broadband spectrum modulated in all three single-frequency spectra.

This step-wise routine increases the probability of picking frequencies capable of modulating larger number of transitions in the final difference spectrum. It also provides a tier of

validation that all the selected frequencies for the MSE scheme are exciting energy levels of the same species irrespective of their relative abundance.

Having made this choice of frequencies, the single-isomer microwave spectrum for the component in the mixture originally identified with the transition at frequency ν_1 is carried out using a broadband chirp followed by three sequential single-frequency pulses, as shown schematically in the upper right-hand corner of Figure 3. As already outlined, the difference between this spectrum and the corresponding broadband spectrum with no single-frequency pulses produces a set of rotational transitions due to the isomer of interest.

Having obtained this difference spectrum, the same series of steps can be carried out beginning with the next-most intense transition not appearing in the initial SFCB/MSE spectrum. This process can be continued until all transitions of interest have been accounted for.

C. Tailored sequential chirps (TSC)

As previously described, creating a strong coupling between the molecular transitions and the electric field is vital for the SFCB method. However, in most CP-FTMW spectrometers the maximum attainable electric field is limited by the available amplification power of the TWTA. Therefore, for the same linear broadband sweep rate (α) a low dipole molecule will only have a few transitions that experience a sufficiently strong coupling with the electric field ($\alpha \ll \Omega_0^2$) to be in the RAP regime. To circumvent this experimental limitation, and still implement SFCB, a new Tailored Sequential Chirps (TSC) scheme was introduced into the broadband step. Employing TSC the entire 8-18 GHz frequency range is swept in segments, with different tailored linear sweep rates chosen to vary the sweep rate (α) in each segment. Region(s) of the spectrum in which a majority

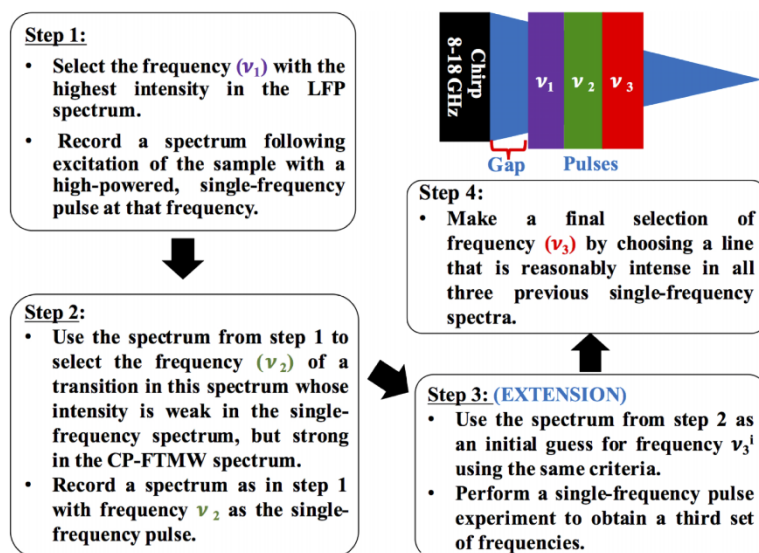


FIG. 3. Line picking scheme to establish the multiple pulse sequence employed in the SFCB-MSE method.

of the transitions are comparatively weak are candidates for interrogation at a slower sweep rate. In addition, more congested regions of the spectrum, where assignment is challenging, also benefit from a slower sweep rate, as this brings a larger number of transitions in that region into the strong coupling regime so they gain intensity in the SFCB-MSE spectrum, which in turn facilitates line assignments.

D. Method summary

The SFCB method can be summarized as follows: Operating in the strong coupling limit, a high power linear broadband chirp or a tailored sequential chirp is used in combination with a series (usually three) of single-frequency selective excitation pulses chosen according to the algorithm presented in Figure 3. Then the same chirp without the selective pulses is used to irradiate the sample under otherwise identical experimental conditions. The figures report the transitions that appear in the difference spectrum with a percent modulated intensity greater than or equal to the indicated percentage of the transition intensity in the absence of a resonant frequency pulse, thereby showing a set of rotational transitions due to the molecular component of interest. By keeping the percentage of modulation value initially high, only a few transitions appear in the difference spectrum, which can subsequently be lowered until background peaks due to reflections begin to appear. From this a broader set of transitions can be subsequently identified in the LFP spectrum based on this preliminary assignment, leading to a refinement of the assigned rotational constants.

IV. RESULTS AND DISCUSSION

A. ^{13}C -benzonitrile

While benzonitrile has no conformational or structural isomers, it does have in natural abundance the presence of

a set of five isotopologues, differing from the all ^{12}C parent in having a single ^{13}C atom in any of the six positions (four inequivalent) in the aromatic ring, or a seventh in the nitrile group. These isotopologues have different rotational constants than the all ^{12}C molecules, appearing just to the lower-frequency side of those main transitions, as illustrated by the dotted lines and inset in Figure 4(a). In benzonitrile, by symmetry, ^{13}C substitution at the 2- and 6- positions has equivalent rotational constants, as do the 3- and 5-substituted pair. Since the ^{13}C isotope is present in 1% natural abundance compared to ^{12}C , the transitions due to the isotopologues are often difficult to identify with certainty in the spectrum since they appear with such low intensity. Their identification is valuable in that it pins down the positions of the ^{13}C -substituted atoms in the molecular framework to high accuracy via Kraitchman analysis.⁴⁴

We chose the $[2-^{13}\text{C}]$ isotopologue to illustrate the technique's sensitivity and capability to selectively identify low intensity transitions in a dense spectrum. The initial signal intensity of the transitions due to $[2-^{13}\text{C}]$ benzonitrile was $\sim 2\%$ of those due to the parent molecule. The SFCB scheme was implemented with MSE using three transitions due to the $[2-^{13}\text{C}]$ isotopologue chosen as outlined above. The resulting difference spectrum with the modulated ^{13}C lines is shown in Figure 4(b). As anticipated by symmetry, only a-type rotational transitions were observed for $[2-^{13}\text{C}]$ benzonitrile. The SFCB scan used a linear broadband chirp (8-18 GHz) of 1000 ns duration, with a 50 ns gap followed by three 150 ns selective pulses. The selected frequencies for the MSE scheme were 15 900.31, 13 399.19, and 10 828.94 MHz. A custom Matlab routine was used to extract from the experimental difference spectra those transitions that were modulated more than 40% compared to the original 8-18 GHz sweep, to overcome the experimental errors ($\sim 4\%$) associated with gas flow fluctuations. The method selectively modulated 10 transitions due to the $[2-^{13}\text{C}]$ isotopologue, with no interference from transitions due to the all ^{12}C

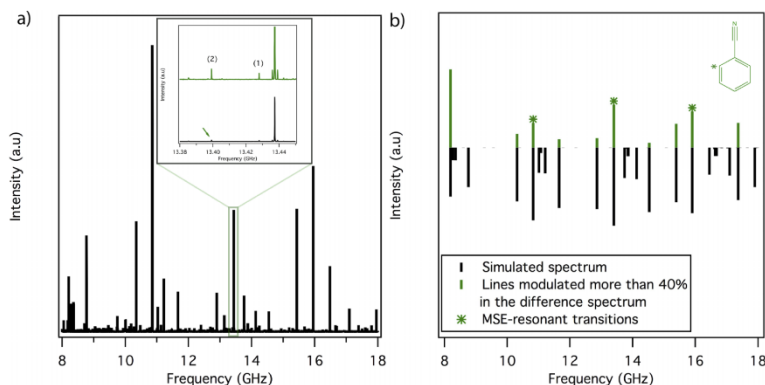


FIG. 4. (a) The 8-18 GHz pure rotational spectrum of benzonitrile recorded with a 900 ns chirped pulse at 100% TWTA gain level. The inset is an expanded view (13.35-13.45 GHz) illustrating the relative line intensities of the ^{13}C and parent transitions. The arrow indicates the transition due to $[2-^{13}\text{C}]$ benzonitrile used for excitation via the resonant pulse. The green spectrum is scaled $7\times$ with the labels identifying the isotopologues present in the expanded region, (1) $[1-^{13}\text{C}]$ benzonitrile and (2) $[2-^{13}\text{C}]$ benzonitrile. Transitions due to other ^{13}C isotopologues are outside the frequency range shown. (b) Experimental lines modulated more than 40% in the SFCB difference spectrum using the MSE sequence (green) with single-frequency pulse frequencies marked with an asterisk, compared to the simulated stick spectra (black). The rotational constants used in the simulation in black were taken from Casado and co-workers.⁴⁴

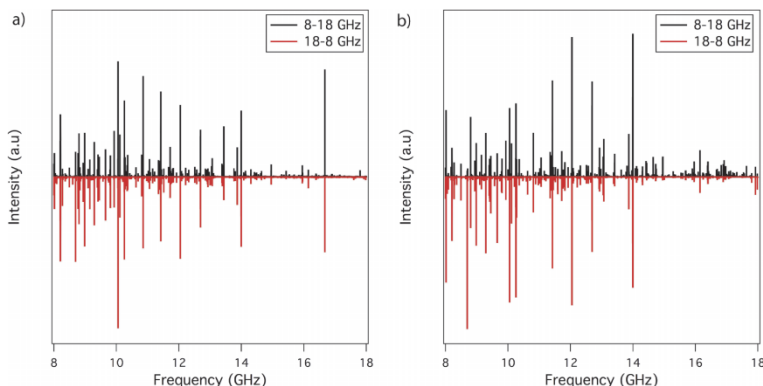


FIG. 5. Broadband CP-FTMW spectra over the 8-18 GHz region of (E)- and (Z)-PVN, comparing the spectra with the frequency swept up from 8 to 18 GHz (black) and down from 18 to 8 GHz (red), with TWTA gain at (a) 10% and (b) 100% of full power. Experimental conditions: 1 μ s long chirped pulse, 25 000 averages, 16 μ s molecular FID collection, PVN sample heated to 78 $^{\circ}$ C.

isotopologue, despite the fact that these transitions were 50 times more intense. This demonstrates the SFCB's future potential to selectively modulate low abundance isotopes, or minor isomers/conformers concealed in a highly congested spectrum (Figure 4).

B. (E)- and (Z)-phenylvinyl nitrile

(E)- and (Z)-PVN are structural isomers of one another, and of the simplest polyaromatic nitrogen heterocyclic quinoline. These molecules have extensive absorption cross sections in UV, and have been postulated as intermediates along photochemical pathways that lead to nitrogen heteroaromatics.^{45,46} Their isomer-specific vibronic spectroscopy has been studied recently by our group in some detail in the ultraviolet, motivated by their potential relevance to such heteroaromatic formation in Titan's atmosphere, one of the moons of Saturn.^{45,46} As a first demonstration of the SFCB-MSE method involving structural isomers, (E)- and (Z)-PVN is interesting in that the two isomers have very different dipole moments that are distributed along more than one rotational axis, making their rotational spectra more complex. The microwave spectra of these isomers have not been recorded previously, offering an opportunity to implement the method "blind" to the carriers of the transitions.

Figure 5 compares the rotational spectra of (E)- and (Z)-PVN recorded in the frequency range 8-18 GHz sweeping up (black) or down (red) in frequency, in both the strong and weak field coupling regimes. The spectrum recorded with the TWTA gain level at 10% is shown in Figure 5(a), demonstrating operation in the LFP regime, with relative intensities maintained irrespective of the sweep direction. However, at 100% TWTA gain level, Figure 5(b) clearly shows the line intensity patterns change with the direction of the linear frequency sweep. These asymmetric line intensities indicate the ability to operate in the strong field regime. The line picking sequence illustrated in Figure 3 was implemented to determine the selective frequencies required for the MSE scheme. Step 1 was initiated using the most intense line (10 052.50 MHz) in the 8-18 GHz linear fast passage spectrum (10%, TWTA). Performing steps 2-4 led to the selection of the following set of frequencies for MSE: 10 052.50, 16 400.12, and 8203.63 MHz.

Since the end result of the SFCB method is a difference spectrum, it is important to assess the level of stability of intensities of transitions in the CP-FTMW spectrum. In PVN, these intensity fluctuations ($\pm 1.5\%$) were assessed via single 8-18 GHz chirp scans immediately before and after the SFCB scans. Using the same custom Matlab routine mentioned above, 93 transitions were identified as having their intensities modulated more than 10% compared to the 8-18 GHz sweep

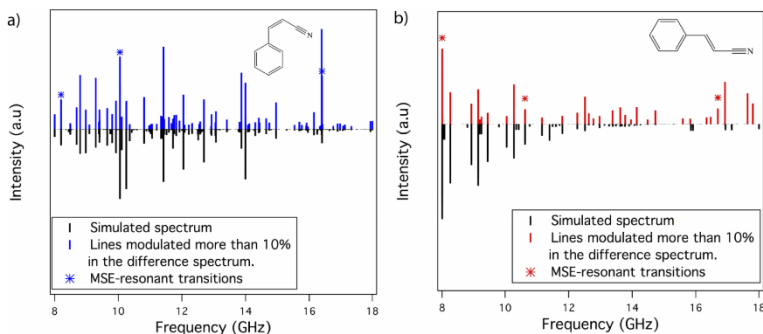


FIG. 6. Experimental lines modulated more than 10% in the SFCB difference spectrum compared to the simulated stick spectra for (a) (Z)-PVN and (b) (E)-PVN. Experimental conditions: 1 μ s 8-18 GHz chirp, 50 ns gap and 3×100 ns single frequency pulses on frequencies labeled with asterisks, 100% TWTA gain level.

in the absence of the MSE, shown in blue in Figure 6(a). The transitions are compared to the spectrum predicted for the (Z)-PVN isomer, demonstrating the method's ability to selectively modulate a large fraction of the transitions in the single isomer's spectrum.

The rotational transitions obtained through the initial SFCB/MSE run were compared with the 8-18 GHz LFP rotational spectrum and the method was implemented a second time on the remaining unassigned lines, using the same pulse durations and time delay conditions. The second set of selective frequencies was 10 624.97 MHz, the strongest line in the LFP spectrum not previously modulated, 16 697.08 MHz and 8016.88 MHz. Similarly, the difference spectrum was plotted and a set of 32 lines were identified by the Matlab routine, and matched with the (E) isomer predictions, as shown in Figure 6(b).

The line frequency sets obtained through the SFCB/MSE difference spectra were used for the initial rigid rotor fits of both isomers. The clear differentiation between the two frequency sets drastically reduced the spectral fitting time, as anticipated. The method's isomer specificity enabled the assignment of transitions and provided an extra level of confidence when assigning transitions from higher-J levels with low transition intensities.

The ^{14}N nuclei possess a quadrupole moment arising from its nuclear spin I being greater than $1/2$ ($I = 1$). This causes splitting of the rotational transitions. The SFCB/MSE method identified a significant number of nuclear quadrupole transitions for both isomers. The spectral transitions were fit to Watson's semi-rigid Hamiltonian⁴⁷ (A-reduction, I-representation) while accounting for hyperfine interaction using the CALPGM⁴⁸ program suite, with the PIFORM program used to format outputs from the spectral fitting. The experimental rotational constants, centrifugal distortion constants, and nuclear quadrupole coupling constants are listed in Table I, where they are compared to the predictions of calculations at the MP2/aug-cc-pVTZ level of theory. The calculated values are in good agreement with the constants obtained experimentally. The fit for both isomers is reported with one sigma uncertainty for the last digit and overlaid on the 8-18 GHz, LFP spectrum in Figure 7. Remaining features in the spectrum were identified as arising from incomplete

TABLE I. Experimental best-fit and theoretical calculated spectroscopic parameters for E/Z-PVN.

	Z-PVN experimental	Z-PVN theoretical	E-PVN experimental	E-PVN theoretical
A (MHz)	3122.882 6(13) ^a	3124.3392	5102.410 8(20)	5125.1298
B (MHz)	873.251 09(62)	880.2379	607.514 35(69)	608.1963
C (MHz)	683.730 89(43)	687.7546	543.210 36(62)	543.6783
D _J (kHz)	0.079 0(33)	...	0.011 8(17)	...
D _{JK} (kHz)	-0.288
D _K (kHz)	0.738(88)
d _J (kHz)	0.018 5(14)
d _K (kHz)	0.257(80)
χ_{aa} (MHz)	2.580(30)	2.31	-8.639	-7.83
$\chi_{bb}-\chi_{cc}$ (MHz)	-0.330 7(12)	-0.313	-0.012	-0.022
μ_A (D)	...	2.68	...	-5.01
μ_B (D)	...	2.83	...	0.63
μ_C (D)	...	0.00	...	0.00
σ (MHz) ^b	0.035	...	0.036	...
Δ (u A ²) ^c	-1.415	-1.070	-0.571	0.000
N ^d	321	...	204	...

^aStandard error in parenthesis in units of the last digit.

^bStandard deviation of the fit.

^cZero-point inertial defect.

^dNumber of fitted transitions. The spectra were fit using a Watson-A reduced Hamiltonian including hyperfine interactions with the CALPGM program suite and PIFORM program to format the outputs from the spectral fitting.

subtraction of spurious lines arising from electronic noise and reflections were identified from a blank run in the absence of the gas pulse.

Previous LIF and UV-UV hole burning studies⁴⁶ of the ground S_0 and S_1 excited states of (E)- and (Z)-PVN showed both isomers to be planar in the S_0 state, based on selection rules in the vibronic transitions involving out-of-plane vibrations. The inertial defect ($\Delta = I_c^c - I_0^a - I_0^b$, where I is the moment of inertia) is a spectroscopic test for planarity,⁴⁹ and was calculated here for both isomers. The experimental inertial defects (Δ) (Table I) for both isomers are negative but small. Similar molecules that are planar on a vibrationally averaged basis also show non-negligible negative inertial defects in the ground vibrational state, due to the presence of a low-frequency out-of-plane vibration.^{49,50} In (E)- and

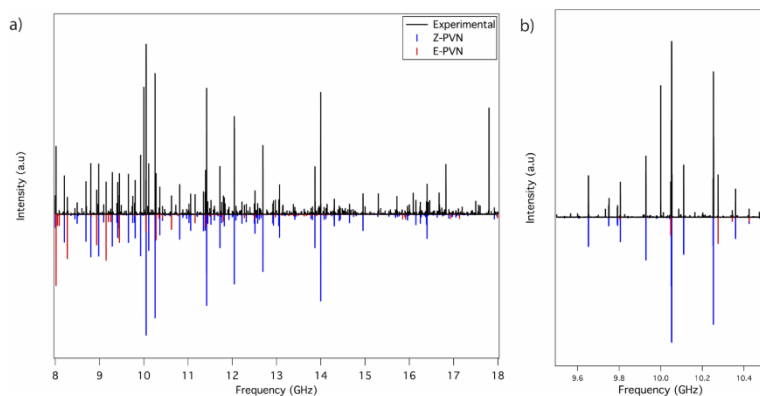


FIG. 7. (a) The experimental 8-18 GHz broadband microwave spectrum of a mixture of (E)- and (Z)-PVN (black), and the final fit for both structural isomers, overlaid on top of one another. (b) Expanded view of 9.5-10.5 GHz with the assignments overlaid.

(Z)-PVN, the lowest frequency vibrational mode involves an out-of-plane torsion of the vinylcyanide substituent relative to the ring, with frequencies of 18.5 and 48 cm^{-1} , respectively, consistent with the molecule being planar but floppy.⁴⁶

C. Methyl butyrate

To demonstrate application of the SFCB method to molecules with more modest-sized dipole moments than those found in the nitriles, and also to extend the method to molecules containing conformational isomers, the method was implemented on methyl butyrate, $\text{CH}_3\text{—CH}_2\text{—C(=O)—O—CH}_3$. This application stimulated the development of tailored sequential chirps (TSC) as a refinement of the excitation scheme. Four stable conformers of methyl butyrate, each with a total dipole moment less than 1.7 D, were predicted using MacroModel software suite with a MM2* force field.

The first set of TSC was designed focusing on the congested Q-branch region in the 13-15 GHz region, which contained many weak transitions (Figure 8(a)). To bring this region into the RAP regime, bandwidths of 8-13, 13-15, and 15-18 GHz were chosen, with duration of 350, 1000, and 140 ns, respectively. This set of conditions resulted in relative sweep rates of 7:1:10 in the three frequency regions. Achievement of strong-field conditions is demonstrated in Figure 8(b), where the spectrum chirping up (black) is compared with that chirping down (red), clearly demonstrating intensity changes indicative of RAP in all three frequency regions. The TSC set covered the entire 8-18 GHz region, promoting strong coupling of the maximum number of rotational transitions with the polarizing electric field. The selective frequencies, for the MSE scheme, were determined using the same line picking scheme illustrated in Figure 3. Step 1 was initiated with the most intense line, at 10 059.87 MHz; the following steps of the scheme output the set of frequencies 10 059.87, 12 682.25, and 15 264.19 MHz, denoted with asterisks in the spectrum of Figure 9(a), with one in each frequency region of the TSC.

The difference spectrum obtained from the SFCB(TSC)/MSE method with 100% TWTA gain (Figure 9(a)) employed a modulation level above 20% as threshold, producing a set of 47 lines. These lines were correlated with the frequency predictions for the *gauche* conformer, which has a total

TABLE II. Experimental preliminary fit and theoretical calculated spectroscopic parameters for the low energy conformers of methyl butyrate.

	Conformer 1 experimental	Conformer 1 theoretical	Conformer 2 experimental	Conformer 2 theoretical
A (MHz)	8349.75(23) ^a	8165.5225	6059.56(17)	6211.4006
B (MHz)	1197.675(38)	1208.5613	1421.341(25)	1435.1202
C (MHz)	1076.441(35)	1081.5471	1333.318(35)	1335.6117
μ_A (D)	...	0.255	...	0.445
μ_B (D)	...	-1.677	...	-1.474
μ_C (D)	...	0.00	...	0.511
σ (MHz) ^b	0.556	...	0.263	...
N^c	9	...	21	...

^aStandard error in parenthesis in units of the last digit. The spectra were fit using a Watson-A reduced Hamiltonian using the CALPGM program suite and PIFORM program to format the outputs from the spectral fitting.

^bStandard deviation of the fit.

^cNumber of fitted transitions.

dipole moment of 1.474 D and a mixed set of a- and b-type transitions.

The second set of TSCs focused on the remaining intense unassigned lines, with chosen frequency bandwidths of 8-9.5, 9.5-16.5, and 16.5-18 GHz with a duration of 100, 1300, and 100 ns, respectively. The frequencies used in the MSE sequence were 9427.38, 11 578.06, and 13 671.63 MHz. For this TSC set the SFCB(TSC)/MSE method was implemented under the same experimental conditions, and the difference spectrum shown in Figure 9(b) was obtained. The Matlab routine with 20% modulation threshold level outputs 18 lines, that could be fit with rotational constants corresponding to the *trans* conformer, with a total dipole moment of 1.677 D, and a nearly pure a-type spectrum. Flow fluctuations between scans were less than 1% for both experiments.

The two sets of frequencies facilitated the preliminary assignments (Table II), providing a list of conformer-specific transitions with no cross-over between the sets. Moreover, high accuracy of the initial predictions from the calculations was not required for this system. Therefore, the SFCB method essentially eliminated the requirement for accurate prior predictions of rotational constants, and therefore reduced the requirements on the level of theory required for the initial fit. More details of the assignment and chemical analysis of the methyl butyrate conformers will be presented in a future publication.⁵¹

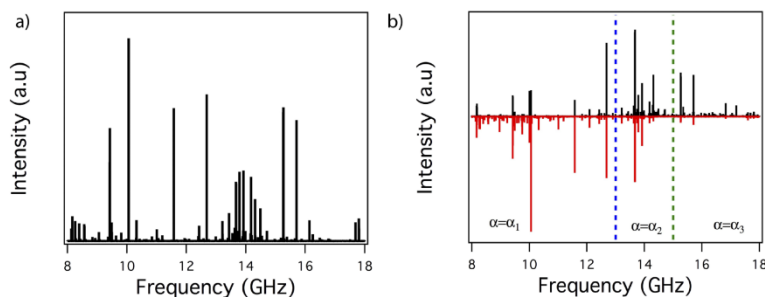


FIG. 8. 8-18 GHz CP-FTMW rotational spectrum of methyl butyrate. (a) 10% TWTA gain level and 1 500 000 acquisitions. (b) 100% TWTA gain and 75 000 acquisitions using Tailored Sequential Chirps (TSCs) with different sweep rates (α) covering 8-18 GHz sweeping up (black) or down (red) in frequency, where $\alpha_1 = 14.3$ GHz/ μs for the 8.0-13.0 GHz region, $\alpha_2 = 2.0$ GHz/ μs for the 13.0-15.0 GHz region, and $\alpha_3 = 20.0$ GHz/ μs for the 15.0-18.0 GHz region.

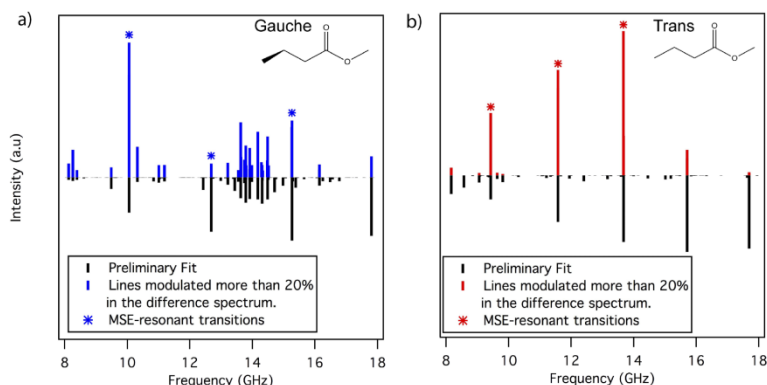


FIG. 9. Experimental lines modulated more than 20% in the SFCB(TSE)-MSE difference spectrum compared with the simulated stick spectra for the two most abundant conformers of methyl butyrate. Experimental conditions: 8-18 GHz tailored sequential chirps as in Figure 8, 50 ns gap and 3×150 ns single frequency pulses on selected frequencies labeled with asterisks at 100% TWTA gain level.

V. CONCLUSIONS AND FUTURE OUTLOOK

A new SFCB analysis method is introduced to dissect congested rotational spectra into sub-sets of transitions due to particular components of a mixture, simplifying line assignments. The method incorporates a unique combination of broadband CP-FTMW and multiple selective-excitations while operating in the strong field coupling regime to differentiate conformer/isomer transitions. Isomer-specific microwave spectra are demonstrated for isotopomers, structural isomers, and conformational isomers, illustrating a range of circumstances in which the method will be useful. Future applications in circumstances where transitions due to different reaction products created by a discharge, photolysis source, or pyrolysis source are likely to further expand its applicability.

The method's high selectivity even in the face of potential interferences from transitions more than 50 times more intense was demonstrated on [2- ^{13}C] benzonitrile as a proof of concept. Next, the SCFB/MSE method was used to differentiate and assign the microwave spectra of the two structural isomers (E)- and (Z)-PVN. The isomer-specific output frequencies were used as starting points for the line assignments, which greatly reduced the analysis time. Finally, in order to extend the method and create strong field coupling with transitions that have a low transient dipole moment, TSCs were introduced to reach the RAP regime on weak transitions that potentially have smaller transition dipole moments, by slowing the sweep rate that interrogates them. The SFCB(TSC)/MSE method successfully produced sets of conformer specific rotational lines for the two observed methyl butyrate conformers.

In many ways, the broadband CP-FTMW technology has revolutionized the field of rotational spectroscopy by introducing rapid data acquisition time. Nevertheless, for chemists to fully utilize the technology, high-speed, cost-effective analysis techniques are vital, that enable its practitioners to quickly identify transitions due to single components of complex gas-phase mixtures and draw structural inferences about them. The SFCB method makes use of tailored excitation pulses using standard CP-FTMW

hardware, and incorporates them into a scheme that produces single-isomer microwave spectra with a sufficient number of transitions so that preliminary assignments are possible on short time scales.

Future refinement of the method is likely to further expand its capabilities. The choice of transition frequencies for the single-frequency pulses can at times lead to cross-talk between components of the mixture if transitions due to another component are within ~ 10 MHz of the transition(s) chosen for selective excitation. This is mainly due to microwave power "leakage" out of the single-frequency applied by the arbitrary waveform generator due to the sharp edges of the excitation pulse. This leakage can be minimized by applying specific window functions to the excitation pulses. Furthermore, since the number of transitions that can be modulated is greatly expanded by operation in the RAP regime, we anticipate difficulty using the method (in its current implementation with typical TWTA powers of 200 W), for mixture components with total permanent dipole moments below about 0.5 D. Of course, these components are also difficult to detect in standard implementations of CP-FTMW spectroscopy. In general, using microwave components with small noise and optimal efficiency is recommended to minimize the effects of noise/harmonics, which can cause false, off-resonance modulations.

Taken as a whole, it is hoped that the SFCB method will be a useful tool in modern high-speed rotational spectroscopy to selectively "light up" conformer/isomer transitions in a highly congested system, speeding line assignments, and providing the ability to address chemically challenging environments in a more effective way.

ACKNOWLEDGMENTS

The authors gratefully acknowledge support for this research from the Department of Energy Basic Energy Sciences, Chemical Sciences Division under Grant No. DE-FG02-96ER14656. Acknowledgment is also made to the Donors of the American Chemical Society Petroleum Research Fund for partial support of this research through a New Directions Grant No. PRF #55152-ND6.

- ¹T. S. Zwier, *J. Phys. Chem.* **105**, 8827 (2001).
- ²R. A. Bernheim, L. P. Gold, P. B. Kelly, C. Kittrell, and D. K. Veirs, *Phys. Rev. Lett.* **43**, 123 (1979).
- ³B. M. Elliott, R. A. Relph, J. R. Roscioli, J. C. Bopp, G. H. Gardenier, T. L. Guasco, and M. A. Johnson, *J. Chem. Phys.* **129**, 094303 (2008).
- ⁴T. Walther, H. Bitto, T. K. Minton, and J. R. Huber, *Chem. Phys. Lett.* **231**, 64 (1994).
- ⁵R. H. Page, Y. R. Shen, and Y. T. Lee, *J. Chem. Phys.* **88**, 5362 (1988).
- ⁶M. Hippler, R. Pfab, and M. Quack, *J. Phys. Chem. A* **107**, 10743 (2003).
- ⁷C. H. Townes and A. L. Schawlow, *Microwave Spectroscopy* (Dover Publications, 1975).
- ⁸G. G. Brown, B. C. Dian, K. O. Douglass, S. M. Geyer, S. T. Shipman, and B. H. Pate, *Rev. Sci. Instrum.* **79**, 053103 (2008).
- ⁹C. Abeysekera, L. N. Zack, G. B. Park, B. Joalland, J. M. Oldham, K. Prozument, N. M. Ariyasingha, I. R. Sims, R. W. Field, and A. G. Suits, *J. Chem. Phys.* **141**, 214203 (2014).
- ¹⁰G. B. Park and R. W. Field, *J. Chem. Phys.* **144**, 200901 (2016).
- ¹¹G. G. Brown, B. C. Dian, K. O. Douglass, S. M. Geyer, and B. H. Pate, *J. Mol. Spectrosc.* **238**, 200 (2006).
- ¹²D. Schmitz, V. Alvin Shubert, T. Betz, and M. Schnell, *J. Mol. Spectrosc.* **280**, 77 (2012).
- ¹³K. N. Crabtree, M.-A. Martin-Drumel, G. G. Brown, S. A. Gaster, T. M. Hall, and M. C. McCarthy, *J. Chem. Phys.* **144**, 124201 (2016).
- ¹⁴D. Patterson and J. M. Doyle, *Phys. Rev. Lett.* **111**, 023008 (2013).
- ¹⁵S. Twagirayezu, T. N. Clasp, D. S. Perry, J. L. Neill, M. T. Muckle, and B. H. Pate, *J. Phys. Chem. A* **114**, 6818 (2010).
- ¹⁶B. C. Dian, G. G. Brown, K. O. Douglass, and B. H. Pate, *Science* **320**, 924 (2008).
- ¹⁷G. Berden, W. L. Meerts, and W. Kreiner, *Chem. Phys.* **174**, 247 (1993).
- ¹⁸M. Nakajima, Y. Sumiyoshi, and Y. Endo, *Rev. Sci. Instrum.* **73**, 165 (2002).
- ¹⁹N. Heineking, W. Stahl, and H. Dreizler, *Z. Naturforsch., A: J. Phys. Sci.* **43**, 280 (1988).
- ²⁰F. J. Wodarczyk and E. B. Wilson, *J. Mol. Spectrosc.* **37**, 445 (1971).
- ²¹G. B. Park, C. C. Womack, A. R. Whitehill, J. Jiang, S. Ono, and R. W. Field, *J. Chem. Phys.* **142**, 144201 (2015).
- ²²D. S. Wilcox, K. M. Hotopp, and B. C. Dian, *J. Phys. Chem. A* **115**, 8895 (2011).
- ²³G. B. Park, A. H. Steeves, K. Kuyanov-Prozument, J. L. Neill, and R. W. Field, *J. Chem. Phys.* **135**, 024202 (2011).
- ²⁴D. P. Zaleski, J. L. Neill, M. T. Muckle, N. a. Seifert, P. Brandon Carroll, S. L. Widicus Weaver, and B. H. Pate, *J. Mol. Spectrosc.* **280**, 68 (2012).
- ²⁵A. L. Steber, B. J. Harris, J. L. Neill, and B. H. Pate, *J. Mol. Spectrosc.* **280**, 3 (2012).
- ²⁶J. L. Neill, B. J. Harris, A. L. Steber, K. O. Douglass, D. F. Plusquellic, and B. H. Pate, *Opt. Express* **21**, 19743 (2013).
- ²⁷E. Gerecht, K. O. Douglass, and D. F. Plusquellic, *Opt. Express* **19**, 8973 (2011).
- ²⁸N. R. Walker, *Philos. Trans. R. Soc., A* **365**, 2813 (2007).
- ²⁹A. J. Shirar, D. S. Wilcox, K. M. Hotopp, G. L. Stork, I. Kleiner, and B. C. Dian, *J. Phys. Chem. A* **114**, 12187 (2010).
- ³⁰F. Harris, *Proc. IEEE* **66**, 51 (1978).
- ³¹D. J. Frisch, M. J. Trucks, G. W. Schlegel, H. B. Scuseria, G. E. Robb, M. A. Cheeseman, J. R. Scalmani, G. Barone, V. Mennucci, B. Petersson, G. A. Nakatsuji, H. Caricato, M. Li, X. Hratchian, H. P. Izmaylov, A. F. Bloino, J. Zheng, and G. Sonnenb, GAUSSIAN 09, Revision E.01, Gaussian, Inc., Wallingford CT (2009).
- ³²J. C. McGurk, T. G. Schmalz, and W. H. Flygare, *J. Chem. Phys.* **60**, 4181 (1974).
- ³³J.-U. Grabow, *Handbook of High-Resolution Spectroscopy* (Wiley, 2011), p. 723.
- ³⁴F. Wolf, *J. Phys. D: Appl. Phys.* **27**, 1774 (1994).
- ³⁵V. V. Khodos, D. A. Ryndyk, and V. L. Vaks, *Eur. Phys. J.: Appl. Phys.* **25**, 203 (2004).
- ³⁶T. G. Schmalz and W. H. Flygare, *Coherent Transient Microwave Spectroscopy and Fourier Transform Methods* (Springer, 1978).
- ³⁷N. V. Vitanov, T. Halfmann, B. W. Shore, and K. Bergmann, *Annu. Rev. Phys. Chem.* **52**, 763 (2001).
- ³⁸C. Liedebaum, S. Stolte, and J. Reuss, *Phys. Rep.* **178**, 1 (1989).
- ³⁹P. Balling, D. J. Maas, and L. D. Noordam, *Phys. Rev. A* **50**, 4276 (1994).
- ⁴⁰D. Maas, C. Rella, P. Antoine, E. Toma, and L. Noordam, *Phys. Rev. A* **59**, 1374 (1999).
- ⁴¹S. T. Shipman and B. H. Pate, in *Handbook of High-Resolution Spectroscopy* (Wiley, 2011), pp. 801–827.
- ⁴²K. Wohlfart, M. Schnell, J. U. Grabow, and J. Kupper, *J. Mol. Spectrosc.* **247**, 119 (2008).
- ⁴³G. B. Park and R. W. Field, *J. Mol. Spectrosc.* **312**, 54 (2015).
- ⁴⁴J. Casado, L. Nygaard, and G. O. L. E. Srensen, *J. Mol. Struct.* **8**, 211 (1970).
- ⁴⁵M. L. Cable, M. H. Sarah, R. Hodyss, P. M. Beauchamp, M. A. Smith, and P. A. Willis, *Chem. Rev.* **112**, 1882 (2012).
- ⁴⁶D. N. Mehta-Hurt, J. A. Korn, P. Navotnaya, A. P. Parobek, R. M. Clayton, and T. S. Zwier, *J. Chem. Phys.* **143**, 074304 (2015).
- ⁴⁷J. K. G. Watson, *Vib. Spectra Struct.* **6**, 1 (1977).
- ⁴⁸M. Pickett, *J. Mol. Spectrosc.* **377**, 371 (1991).
- ⁴⁹J. K. G. Watson, *J. Chem. Phys.* **98**, 5302 (1993).
- ⁵⁰T. Oka, *J. Mol. Struct.* **2860**, 225 (1995).
- ⁵¹A. O. Hernandez-Castillo, C. Abeysekera, B. M. Hays, and T. S. Zwier, "Conformational Preferences of Methyl Butyrate by Broadband Microwave Spectroscopy" (unpublished).